University of Strathclyde
Department of Electronic and Electrical Engineering

Low Voltage Ride-Through of Permanent Magnet Synchronous Generator Wind Energy Systems

Rania Assem Elsayed Ibrahim
B.Eng, M.Sc

A thesis presented in fulfilment of the requirements for the Degree of Doctor of Philosophy.

2014

This thesis is the result of the author's original research. It has been composed by the author and has not been previously submitted for examination which has led to the award of a degree.

Signed: *Rania Assem Ibrahim* Date: January 2015

Acknowledgement

All praise to Allah for his guidance and blessing through this experience.

I would like to express my gratitude and sincerest respects to my supervisors Prof. B.W.Williams and Prof. S. Finney for their guidance, insight throughout this study and most of all believing in me.

Special thanks and appreciation goes to Prof. Y.G. Dessouky and Dr. M.S. Hamad for their continuous support, fruitful discussions and encouragement to make a dream come true.

I express my warm thanks to Dr. K.H. Ahmed and Dr. A.A. Abushadi for their good advice and their friendly assistance.

Personal thanks are due to my friends, particularly Prof. A. Hanafi, Dr. A. Kadry, Eng. N. Zakzouk and Eng. M. Ibrahim. You have been there for me through good and bad times and I wish you all the best in your research and life.

The assistance of the valuable academic and technical staff in the Arab Academy for Science and Technology (AAST) and Strathclyde University is gratefully acknowledged. Particular appreciation is accorded to my lab partner Mr. A. Alalfi in the Electrical and Control Department in the AAST.

Finally, last but not least, I would like to thank my family and my parents. Special thanks goes to my husband and my son for their understanding, endless support and tolerance.

Dedication

To my family

Table of Contents

Abstract

Low Voltage Ride-Through (LVRT) capability is considered a critical feature that should be implemented within a Wind Energy Conversion System (WECS). The mismatch produced between the generated active power and the power delivered to the grid during any dip incidence at the Point of Common Coupling causes a dc link voltage rise, an increase in grid currents and generator speed-up. Failure to ride-through grid voltage dips would lead to converter failures within the WECS.

This thesis focuses on enhancing LVRT capability of PMSG based WECS using magnetic amplifiers. LVRT techniques vary according to the turbine and utility grid variables. A survey of the state-of-art LVRT techniques highlighting the merits and demerits of each approach is carried out. A 1.5 MW wind turbine system is modelled, which includes the wind turbine, PMSG, and power converters. Also PMSG control, maximum power point extraction, and grid active and reactive power control are investigated. System performance is studied in compliance with British grid codes for active and reactive power sudden changes, frequency excursion, and grid voltage phase angle jump. The model is tested for LVRT capability under symmetrical network dips.

Magnetic amplifiers have been used in various applications such as instrumentation, fault current limiting, and battery chargers. In this thesis, magnetic amplifiers are proposed as part of a LVRT capability enhancing technique. Two possible configurations are proposed; 3-phase and dc-side configurations. LVRT capability enhancement is investigated for the 1.5 MW WECS using the two magnetic amplifier configurations. The 3-phase topology is able to reduce the dc link voltage rise; however, it causes an increase in the stored rotor inertia accompanied by an increase in generator speed. The dc-side magnetic amplifier topology is able to limit the dc-link voltage rise which in turn protects the power converters without affecting generator performance.

In addition to simulations, a scaled prototype with the dc side magnetic amplifier configuration is used to verify the effectiveness and applicability of the proposed technique during steady state and transient behaviour under various operating conditions.

List of Symbols

A	Blades swept area, m^2
A_1, A_2	Magnetic amplifier primary and secondary windings cross sectional area, m^2
a	turns ratio representing $N_{1T}: N_{2T}$
a_m	Magnetic amplifier turns ratio
B_m	Damping coefficient
B_{sat}	Saturating magnetic flux density, T
C, L	TCSC compensating capacitor, F and bypass inductance, H
$[c_1 \ldots\ldots c_9]$	Characteristic constants for each wind turbine
C_{dc}	Rectifier output filter capacitor, F
$C_{dc-link}$	DC- link capacitor, F
C_p	Power coefficient
D, k	Buck and boost chopper duty cycles respectively
D'_{abc}, D''_{abc}	3-phase magnetic amplifier main winding diodes
D_b	Boost chopper diode
D_m	Buck chopper diode
D_c	Magnetic amplifier control winding diode
E	Generator phase electromotive force, V
E_{ac} , E_{dc}	Magnetic amplifier main and control winding supply voltages respectively, V
E_{gen} , E_{grid}	Energy supplied by generator and energy injected in the grid respectively, J
E_{ke}	Stored kinetic energy, J
ΔE_{Lg} , $\Delta E_{Cdc-link}$	Energy exchanged in the AC inductor and DC-link capacitor connected with the grid respectively, J
E_{PMSG}	Tacho-generator induced voltage, V
E_{Rg}	Energy consumed by equivalent grid resistor, J
E_t	Magnetic amplifier emf per turn, V
f	Supply frequency, Hz
f_c	Inverter carrier triangular signal frequency, Hz

f_{ch}	Chopper carrier frequency, Hz
$f_{gen(nom)}$, f_{gen}	Generator rated frequency at 1500 rpm and operating frequency respectively, Hz
f_{grid} , θ_u	Grid frequency Hz and phase angle of the utility-voltage vector, ° respectively
H	Magnetic field intensity, AT/m
i'_{abc}, i''_{abc}	3-phase magnetic amplifier main winding currents, A
i_{abcgen}	3-phase stator currents, A
$i_{abcgrid}$, $\overline{i_{grid}}$	3-phase grid currents and grid current vector respectively, A
i_c	DC-link capacitor current, A
I_{ch}	Input buck chopper current, A
I_D	Boost chopper diode current, A
I_d^* , I_d	Reference and actual active grid current respectively, A
i_{Dl}	Diode rectifier D_l current, A
I_{dc}^*, I_{dc}	Boost chopper inductor current reference and actual respectively, A
i_{dq0}	Grid currents in *dq0* rotating reference frame, A
i_{dq0gen}	Generator currents in *dq0* rotating reference frame, A
I_L	Chopper load current, A
I_m	Magnetic amplifier magnetizing current, A
I_r	6 pulse diode rectifier output current, A
I_{sc}, I_{fl}	Short circuit current and full-load current, A
i_{SMES}	SMES Current, A
i_{w1abc}	3-phase magnetic amplifier main winding currents, A
I_{w2}	Magnetic amplifier control winding current, A
J	Moment of inertia, kg/m^2
K_e	Machine co-efficient
k_1, k_2	Grid current PI controller constants
k_{abcL} , k_{abcH}, k_c	Low voltage, high voltage side and control winding contactors respectively

k_u	Magnetic amplifier window utilization factor
L_{gen}	PMSG line filter inductance, H
L_{grid}, R_{grid} , Z_{grid}	Grid filter inductance H, grid resistance Ω, grid impedance Ω
l_{aa}, l_{bb}, l_{cc}	Self inductances of phase *abc,* H
l_{ab}, l_{ba}	Mutual inductance between phase *a* and *b,* H
l_{ac}, l_{ca}	Mutual inductance between phase *a* and *c,* H
l_{bc}, l_{cb}	Mutual inductance between phase *b* and *c,* H
L_{dc}	Boost chopper inductance*,* H
L_{SC}	SC series inductance*,* H
L_{SMES} , E_{SMES}	SMES coil H, SMES stored energy, J
m_a	Inverter modulation index
N_1, N_2	Magnetic amplifier main and control winding turns, turns
$N_{1abc}^{'}$, $N_{1abc}^{''}$	3-phase magnetic amplifier main winding coils
$N_{2abc}^{'}$, $N_{2abc}^{''}$	3-phase magnetic amplifier control winding coils, turns
N_{1T}, N_{2T}	Grid coupling transformer primary and secondary number of turns, turns
n	Generator speed, rpm
P	Number of pole pairs
P_c	Power stored in the capacitor, W
P_{dc}	Maximum dc-side electric power, W
P_e,	Electromechanical power, W
P_{gen}, Q_{gen}	Active generator power W, reactive generator power, VAr
P_{grid}, Q_{grid}	Active grid power W, reactive grid power, VAr
P_{ig}	Instantaneous power input to the generator, W
P_{Rg}	Power dissipated by equivalent grid resistor, W
P_w	Extracted power by wind turbine, W
P_{wind}	Kinetic power of air stream, W
R	Windmill blade radius, m

R_a	3-phase stator windings resistance, Ω
R_{ex}	External rotor resistance for WRIG, Ω
R_{ns} , $R_{nc}(t)$	SFCL stabilizer resistance of *n*-th unit and the *n*-th unit superconducting resistance, Ω
S_{abc}, S_{dq0}	Variables (current, voltage, and flux linkage) in the *abc* frame and the *dq0* frame respectively
S_b	Buck chopper switch
SW_1	Boost chopper switch
T_1, T_2	TCSC bi-directional thyristors
T_e, T_L	Electromechanical and load torque respectively, Nm
t_{on} , t_{oFF} , T	Switch ON, OFF times and total switching period respectively, s
V_{ch}	Supply voltage for the buck chopper, V
V_{dc}, $\overline{V_{dc}}$,	Rectifier output voltage and mean value respectively, V
$V_{dc-link}$, $\Delta v_{dc-link}$	DC-link capacitor voltage and voltage ripple respectively, V
$V_{dc-link(0)}$, $V_{dc-link(f)}$	DC-link voltage before and during fault respectively, V
V_{dc-opt}	Optimum rectified dc voltage at a given wind speed, V
V_{grid} , $\overline{v_{grid}}$	RMS and Grid voltage vector respectively, V
V_{LL}	RMS value of the line-to-line supply voltages, V
$\left(\hat{V}_{LLinv}\right)_{max}$	Maximum amplitude of the line-to-line inverter voltage, V
V_{nl}, $\hat{V}_{nl}$	PMSG no-load line-to-line rms voltage and its maximum respectively, V
V_{PCC}	Point of common coupling voltage, V
V_{PH}	RMS phase supply voltages, V
V_q^* , V_q	Actual and reference reactive grid voltage respectively, V
V_s , I_s	Voltage V and current A applied to the PMSG terminals in DC- test
v_{ab}	Line-to-line voltage between phase *a* and *b*, V
$\widehat{v_{ab}}$	Maximum line-to-line inverter voltage, V
$v_{abcgrid}$	Phase-to-neutral grid voltages, V
v_{an}, v_{cn}, v_{cn}	Phase-to-neutral supply voltages, V

$v_c, \hat{V}_c$	Inverter carrier triangular signal and amplitude respectively, V
v_{di}, v_{qi}	The *dq*-axes output of the decoupled grid controller, V
v_{dq0gen}	Generator voltages in *dq0* rotating reference frame, V
$v_{gen(nom)}$, v_{abcgen}	Rated voltage at 1500 rpm and operating 3-phase generator voltages, V
$\hat{v}_{grid}$, V_{grid}	Peak mains and RMS grid voltage respectively, V
$v_m, \hat{V}_m$	Inverter reference phase voltage and amplitude respectively, V
v_{ma}, v_{mb}, v_{mc}	3-phase sinusoidal modulating signals, V
v_{magamp}	Control winding voltage for scaled down system magnetic amplifier, V
v_r^*, v_c	Reference signal and carrier triangular signals respectively
v_{W1}, v_{W2}	Magnetic amplifier main and control winding voltages respectively, V
W_1 , W_2	Magnetic amplifier primary and secondary winding
W_c	Total copper wire area in window of magnetic amplifier, m^2
X_1	Main winding inductive reactance, Ω
β, ω, λ	Pitch blades angle °, blade tip speed m/s, tip speed ratio
δ	Load angle, °
η_{MPP} , ΔP_{MPP}	Efficiency of the MPPT and power oscillations at maximum power point, W
θ	Angle between phase *a*-axis to the *d*-axis, °
$\theta_{V_{grid}}$, $\theta_{I_{grid}}$	Phase grid voltage and current angle respectively, °
ρ, V	Wind density kg/m^3, wind speed, m/s
φ	Magnetic flux linkage, V/rad/s
φ_{abc}	3-phase stator flux linkages, V/rad/s
φ_{dq}	Generator flux linkages in *dq* reference frame, V/rad/s
φ_f	Permanent magnet flux linkage, V/rad/s
φ_{grid}	Grid power factor angle, °
φ_m , $\Delta\varphi_m$	Magnetic amplifier flux and change in magnetic amplifier flux level respectively, V/rad/s
ω_{opt}	Optimized rotational speed, rad/s

ω_r , ω_e	PMSG rotor angular and electrical velocity respectively, rad/s
ω_s , ω_u	Supply and grid angular frequency, rad/s

List of Abbreviations

ANN	Artificial neural network algorithm
BPA	Blade pitch angle
CSC	Current source converter
DG	Distributed generation
DVR	Dynamic Voltage Restorer
EESM	Excited synchronous machine
EMF	Electromotive force
FES	Flywheel energy storage
GSC	Grid-side converter
HCS	Hill climbing search technique
IGBT	Insulated gate bipolar transistor
IPMSG	Interior permanent magnet synchronous generator
LAB	Lead-Acid Batteries
LV	Low voltage
LVRT	Low voltage ride through
MERS	Magnetic Energy Recovery Switch
MPPT	Maximum power point tracking
MSC	Machine side converter
MV	Medium voltage
NPC	Neutral point clamped
ORB	Optimum relationship-based control
OTT	Optimal torque technique
P&O	Perturb and observe control
PCC	Point of common coupling
PI	Proportional and integral
PLL	Phase-lock loop
PM	Permanent magnet
PMDD	Permanent magnet direct drive
PMSG	Permanent magnet synchronous generators
PR	Proportional resonant
PSF	Power Signal Feedback
PWM	Pulse width modulation
RMS	Root mean square
SCC	Short circuit capacity, Super Conductor Coil
SCIG	Squirrel-cage induction generator
SFCL	Short Circuit Fault Current Limiter
SFCL- MES	Short Circuit Fault Current Limiter Magnetic Energy Storage
SG	synchronous generators
SMES	Super Magnetic Energy Storage
SPWM	Sinusoidal pulse width modulation
SSSC	Static Synchronous Series Compensator
TCSC	Thyristor controlled series capacitor
THD	Total harmonic distortion
TSR	Tip speed ratio control
UPFC	Unified power flow controller
VOC	Voltage oriented control
VRB	Vanadium Redox flow Battery
VSI	Voltage source inverter
WECS	Wind energy conversion systems

WRSG	Wound-rotor synchronous generators
WT	Wind turbines

Preface

Grid disturbances such as severe voltage dips can lead to disconnection of power-generating units from the grid, which may in turn cause instability in the power grid. To avoid this, the grid code requires power-generating units to remain connected and continuously in operation even with severe voltage dips. The research objective is to improve the performance of PMSG based WECS to fulfil grid code requirements for LVRT.

The thesis is presented in nine chapters:

Chapter one outlines wind penetration growth and introduces LV WECS topologies, configurations for the MV level, and the objective of this research. Grid integration issues are outlined.

Chapter two commences with an overview of WECS and includes modelling of PMSG WECS. Mathematical modelling for the PMSG, wind turbine, ac-dc-ac power converters, and grid and interfacing filters is presented. WECS control aspects are presented which includes MSC and GSC control.

Chapter three studies a modelled 1.5 MW WT system to meet grid interconnection requirements for continuous operation. The system is analyzed and studied for active and reactive power sudden changes, frequency excursion, and phase jump. The modelled system performance is compared with UK grid code technical requirements. Also, this chapter provides an explanation for the LVRT capability requirement in technical grid codes as well as its impact on WECS systems. Furthermore, a study of 1.5 MW WT performance to sudden grid voltage dips is carried out and the system is tested for LVRT capability.

Chapter four overviews state-of-art LVRT capability enhancement technologies, which covers their main control schemes, classification, merits, and demerits. The chapter covers solutions applicable to individual wind turbines as well as techniques suitable for wind farms. The chapter is extended to explain the theory of operation, connection, characteristics, and control aspects of magnetic amplifiers. The use of magnetic amplifiers as a method for improving the ride-through capability of wind turbines is proposed using two possible configurations, namely 3-phase and dc-side configurations.

Chapter five investigates the use of 3-phase and dc-side configurations when applied to the 1.5 MW WECS for LVRT capability enhancement. The performance of both configurations is compared through simulation.

In **Chapter six, p**ractical validation of the proposed dc-side configuration is carried out. Simulation of a scaled down system are compared with results obtained from the experimental test rig.

Finally, **Chapter seven** presents the conclusions, the author's contribution, and suggested future research.

CHAPTER ONE

Introduction

With the growing concerns for conventional energy sources consumption, increasing environmental concerns and interest in technology for generating electricity from renewable energy sources, wind power has emerged as the most promising renewable resource. With more than 35 GW of wind power capacity added in 2013 and a total above 318 GW, wind power capacity by the end of 2013 was enough to meet an estimated 2.9% of total electricity consumption [1.1]. Accordingly, turbine designs continue to evolve to increase yields with trends towards larger machines, and shifts in technologies to improve the economics of wind power in wider operating conditions. This chapter overviews wind turbine technologies. Various wind turbine trends are highlighted and grid code fundamentals are presented to emphasis their importance in the integration of grid connected wind energy.

1.1 Wind Penetration Growth

Installed wind power capacity has been steadily growing over the last two decades. Figure 1.1 shows the evolution of cumulative installed capacity worldwide from 2000 to 2013. The installed capacity of global wind power has increased exponentially from a total capacity of 48 GW in 2004 to 318 GW by the end of 2013, and capacity is expected to achieve 760 GW in 2020 based on a moderate scenario, with an average annual growth rate of 21.4% since 2008. This growth has been fostered by the continuous cost increase of traditional energy sources, cost reduction of wind turbines (WT), governmental incentive programs, and public demand for cleaner energy sources [1.2].

In addition to the rapid growth in total installed capacity, the size of individual wind turbines is also increasing substantially to obtain a reduced price per generated kilowatt

hour. In 2013, the average turbine size delivered to the market was 1.9 MW, among which the average offshore turbine has achieved a size of 4 MW [1.1].

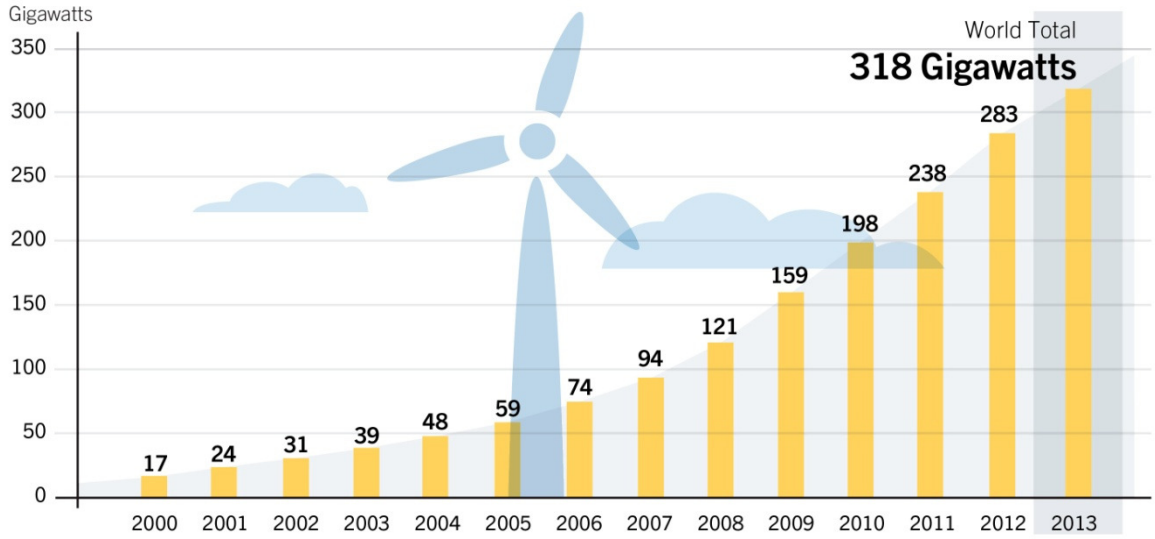

Figure 1.1 Worldwide wind power capacity growth. [1.1]

1.2 Wind Energy Conversion Systems Configurations

A variety of wind energy conversion system (WECS) configurations have been developed in an attempt to reduce the cost, increase reliability, and improve efficiency and performance. A classification of the most common configurations is shown in figure 1.2, where the WT can be generally classified into the fixed and variable speed turbines. The selection of variable speed or fixed speed wind generators for a specific site is determined by several factors: wind speed distribution of the site, reliability and maintenance concerns, system cost, and profit by the electricity generation [1.3].

Fixed-speed turbines incorporate a squirrel-cage induction generator (SCIG) connected directly to the grid which is inherently a fixed-speed machine [1.4], as for the variable-speed WT, it can be divided into direct and indirect drive turbines. In direct-drive turbines, low-speed synchronous generators (SGs) with a large number of poles are employed. Both wound-rotor synchronous generators (WRSGs) and permanent-magnet synchronous generators (PMSGs) are suitable for direct-drive turbines, where a full-scale power converter system is required [1.5]. The converter system serves as an interface between the generator and the power grid.

Indirect-drive turbines require a gearbox to match the low turbine speed to the high generator speed. WRSG, PMSG, and SCIG equipped with full-capacity power converters have all been used in practical wind energy systems. In addition, doubly fed induction generators (DFIGs) with reduced-capacity converters and wound-rotor induction generators (WRIGs) with converter-controlled variable rotor resistance have also been reported [1.2].

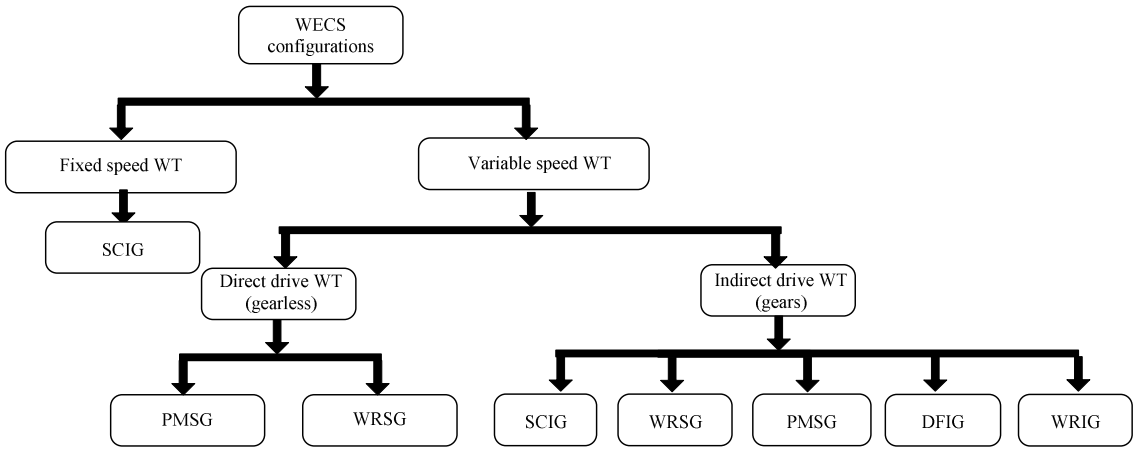

Figure 1.2. Wind energy conversion systems configurations.

1.3 Fixed-Speed WECS

Fixed-speed turbines can be classified into single-speed WECS, in which the generator operates at only one fixed speed; and two-speed WECS, in which the generator can operate at two fixed speeds [1.6].

A typical configuration for a megawatt (MW) fixed-speed wind energy system is shown in figure 1.3. A squirrel cage induction generator is exclusively used where it is commercially called Type-1 WT. A practical example of this configuration is the V82-1.65 rated at 1.65MW, manufactured by Vestas. To assist turbine start-up, a soft starter is used to limit the inrush current in the generator winding, which is undesirable particularly in the case of weak grids and can also cause severe torque pulsation and probably damage the gearbox [1.7]. The soft starter is essentially a three-phase AC voltage controller composed of three pairs of thyristors. To start the system, the firing angles of thyristors are gradually adjusted such that the voltage applied to the generator is increased gradually from zero to the grid voltage level, thereby effectively limiting the stator currents. The soft-start operates over a

short time interval and thereafter is by-passed via a contactor in order to eliminate thyristor losses and the WECS is then connected to the grid through a transformer [1.8].

Since the system does not need power converter interface during normal operation, it is classified as a WECS without power converters. To compensate for the inductive reactive power consumed by the induction generator, a capacitor-based power-factor compensator is normally used. In practice, the compensator is composed of multiple capacitor banks, which can be switched into or out of the system to provide optimal compensation according to the operating conditions of the generator.

Due to the use of a cost-effective and robust squirrel-cage induction generator with an inexpensive soft starter, the fixed-speed WECS features simple structure, low cost, and reliable operation. However, compared to a variable-speed WECS, its major disadvantage is that it almost never captures the wind energy at peak efficiency in terms of the power coefficient C_p. Wind energy is wasted when the wind speed is higher or lower than the specific value selected as the optimum[1.9]. Fixed speed WECS also exist where two-speed operation can be achieved by changing the number of poles or by using a two generator set [1.2].

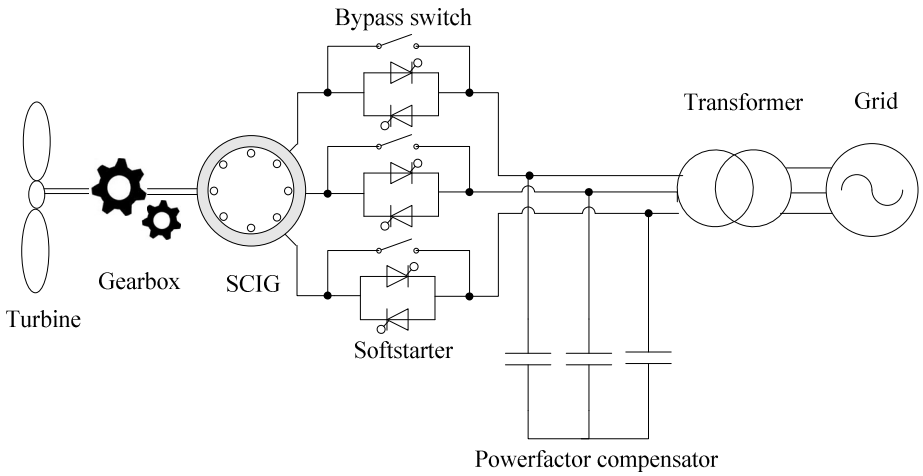

Figure 1.3. Fixed speed WECS using a soft starter.

1.4 Variable-Speed Induction Generator WECS

Variable-speed operation of a wind energy system can be realized by a WRIG, in which the rotor is connected to external variable resistance, or by a DFIG with a reduced-capacity power converter in the rotor circuit. The former is one of the earliest commercial variable-speed WECS, and the latter is one of the most widely used WECS to date [1.2].

1.4.1 Wound-Rotor Induction Generator with External Rotor Resistance

Figure 1.4 shows the simplified configuration for a variable-speed WRIG wind energy system with converter-controlled external rotor resistance which is regarded as the earliest commercial variable–speed WT. The system configuration is the same as that of the fixed-speed wind energy system except that the SCIG is replaced with a WRIG. The external rotor resistance R_{ex} is made adjustable by a converter composed of a diode bridge and an IGBT chopper [1.10]. The equivalent value of R_{ex} seen by the rotor varies with the duty cycle of the chopper. With different values of R_{ex}, the generator can operate at different operating points with different torque-slip characteristics. The main advantage of this configuration compared to the variable-speed WECS is low cost and simplicity. One of the disadvantages to this technique is the lack of control of reactive power consumption independent of the real power. Another is the high rotor losses, which increase with slip and limit the speed variation to approximately 10% [1.11]. Commercially, this type of WECS is known as a Type-2 WT, such as OptiSlip from Vestas.

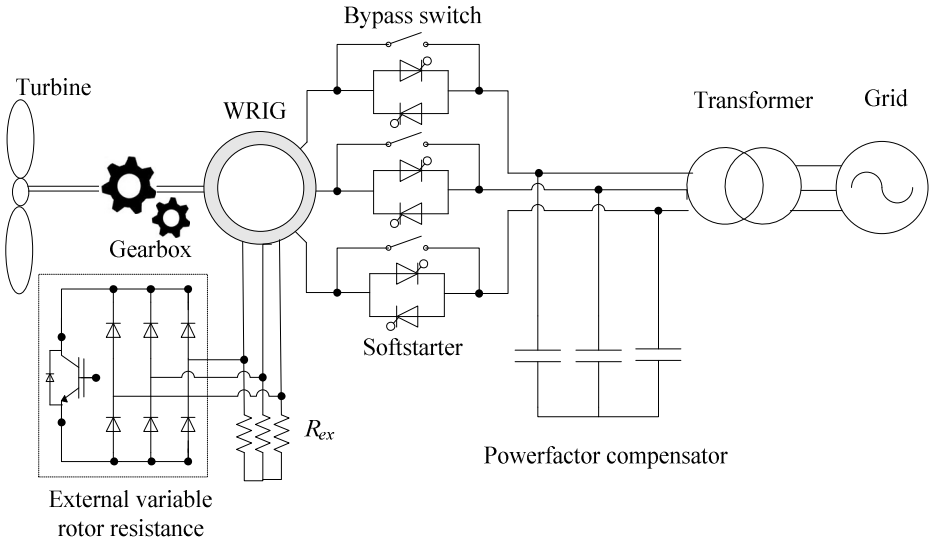

Figure 1.4. Variable speed WECS using a WRIG.

1.4.2 Doubly-Fed Induction Generator Wind Turbine

The variable-speed DFIG wind energy system is one of the main WECS configurations in today's wind power industry. As shown in figure 1.5, the stator is connected to the grid directly, whereas the rotor is connected to the grid via reduced-capacity power converters [1.12]. The rotor-side converter (RSC) controls the torque or active/reactive power of the generator while the grid-side converter (GSC) controls the dc-link voltage and its ac-side

reactive power. External reactive power compensation is not needed since the system has the capability to control reactive power. The power flow in the rotor circuit is bidirectional: it can flow from the grid to the rotor or vice versa thus requiring a four-quadrant converter system as shown in figure 1.5, which also enables decoupled control of generator active and reactive powers. However, the converter system needs to process only around 30% of the rated power while the speed range is ±33% around the synchronous speed [1.12]. The use of reduced-capacity converters results in reduced cost, weight, and compact size of the converter as well as the inverter filters and EMI filters [1.13]. Also, the configuration offers smoother grid connection and maximum wind power extraction. Compared with the fixed-speed systems, the energy conversion efficiency of the DFIG wind turbine is greatly enhanced. Examples of commercial DFIG WECS are the 2.5 MW Nordex 100, 3 MW Vestas V90, and the 5 MW Repower 5M [1.2]. This type of configuration is commercially known as Type-3 WT.

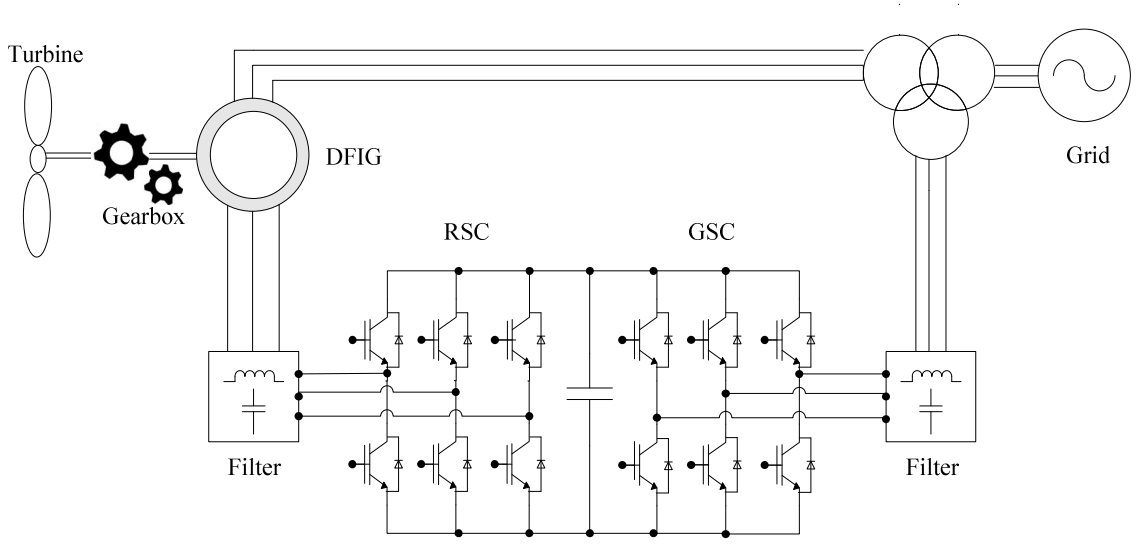

Figure 1.5. Configuration of the DFIG.

1.4.3 Squirrel-cage Induction Generator Wind Energy Systems with Full-Capacity Power Converters

A typical voltage source converter configuration for SCIG wind energy systems is shown in figure 1.6, where a two-level voltage source rectifier (VSR) and voltage source inverter (VSI) using IGBT devices are employed [1.14]. The two converters are linked by a common dc-link capacitor. The converter power rating can be increased by parallel connecting IGBT modules [1.2].

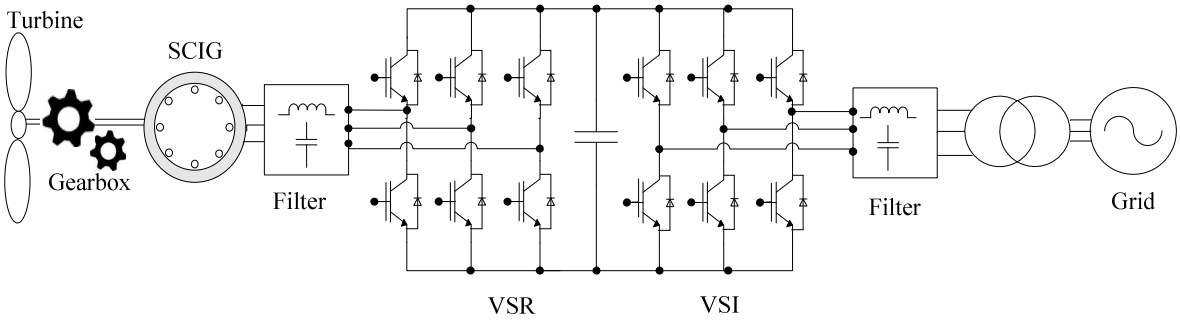

Figure 1.6. VSI WECS using a SCIG.

1.4.4 Variable-Speed Synchronous Generator Wind Turbines

i- Configuration with Full-Capacity Back-to-Back Power Converters

Synchronous generator wind energy systems offer more configurations than the induction generator WECS [1.15]. This is mainly due to the fact that the synchronous generator provides the rotor flux by itself through permanent magnets or a rotor field winding and, thus, diode rectifiers can be used as generator-side converters. Also, it is cost-effective for synchronous generators to have multiple-pole (e.g., 72 poles) and multiple phase (e.g., six phases) configurations. WTs employing full capacity back-to-back power converter configurations are known as Type-4 WT and include examples such as the 2.5 MW geared PMSG Clipper Liberty 2.5, the gearless 3 MW PMSG Siemens SWT 3.0-101, and the 2.5 MW direct drive PMSG Goldwind 2.5 PMDD.

A typical configuration for SG wind energy systems with full-capacity power converters are shown in figures 1.7 and 1.8, where back-to-back two-level voltage source converters are employed in low-voltage wind energy systems and 3-level neutral point clamped (NPC) converters are used in medium voltage WT respectively. Similar to the SCIG system presented previously, parallel modules or converter channels are required in the LV systems for higher power rating, whereas in MV systems a single NPC converter can handle powers up to a few megawatts. The 3-level NPC back-to back configuration shown in figure 1.8 is one of the most commercialized multilevel converters on the market as it achieves one more output voltage level and less *dv/dt* stress than the 2-level converter, and has a smaller filter [1.16]. Other configurations such as a 3-Level H-bridge back-to-back topology and a 5-Level H-bridge back-to-back topology have been reported [1.17, 1.18].

Not all SG WTs need a gearbox, as when a low-speed generator with high number of poles is employed, the gearbox can be eliminated. The gearless wind turbine is attractive due to reduced cost, weight, and maintenance; with a market share of 28% in 2013 compared to 12% in 2008 [1.1].

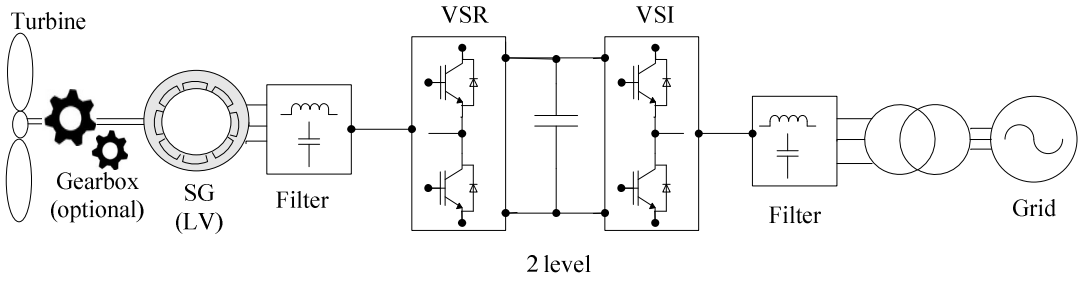

Figure 1.7. 2-level based WECS using back-to-back converters.

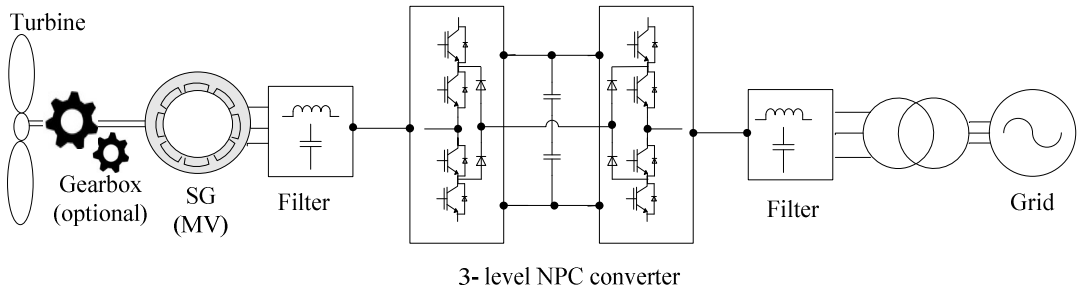

Figure 1.8. 3-level SG based WECS using NPC converters.

ii- Configuration with PWM Current Source Converters.

Figure 1.9 shows a typical configuration for a medium-voltage SG wind energy system using current source converter technology. The current source converter has a number of advantages over its voltage counterpart due to its simple converter topology, near sinusoidal waveforms, and reliable short circuit protection. It is particularly suitable for high-power applications such as megawatt variable-speed drives and wind energy conversion systems. It is a promising converter topology for large SG WECS at the medium-voltage level of 3-4 kV [1.19].

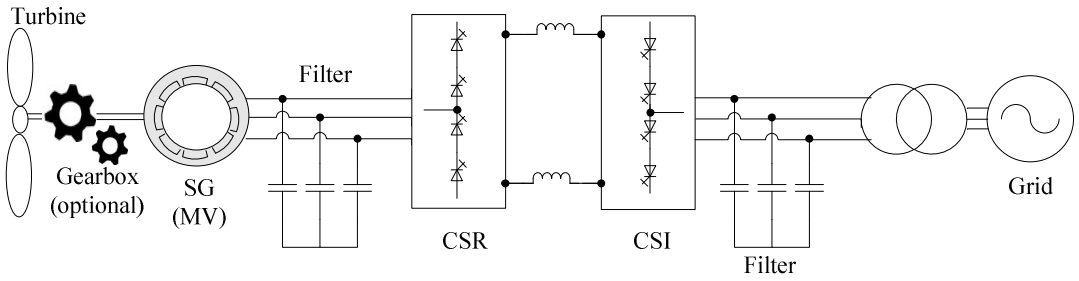

Figure 1.9. WECS with PWM current source converters.

iii- Configuration with Diode Rectifier and DC/DC Converters

To reduce wind energy system costs, the two-level voltage source rectifier in figure 1.7 can be replaced by a diode rectifier and a boost converter as shown in figure 1.10 [1.20]. This converter configuration cannot be used for SCIG WTs since the diode rectifier cannot provide the magnetizing current needed by the induction generator. The diode rectifier converts variable generator voltage to a dc voltage, which is boosted to a higher dc voltage by the boost converter. It is required that the generator voltage at low wind speeds be boosted to a sufficiently high level for the inverters, which ensures the delivery of the maximum captured power to the grid over the full wind speed range. Compared with the PWM voltage source rectifier, the diode rectifier with a boost converter is simpler and more cost-effective [1.21]. However, the stator current waveform is distorted due to the use of the diode rectifier, which increases generator losses and causes torque ripple.

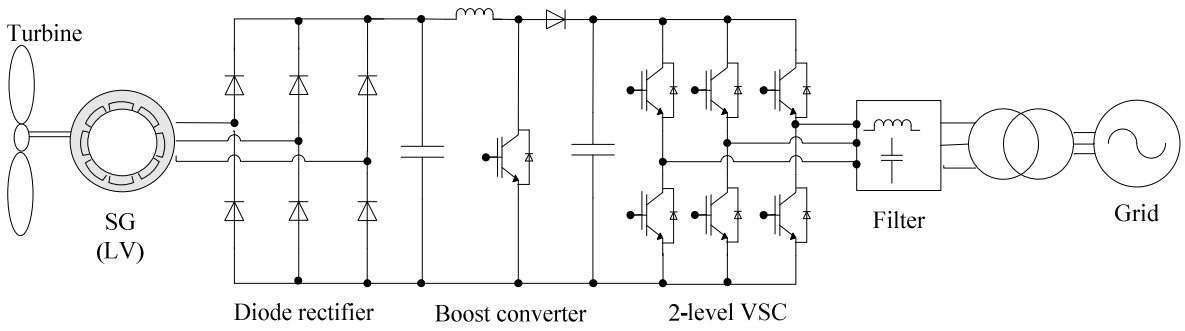

Figure 1.10. Single channel boost converter.

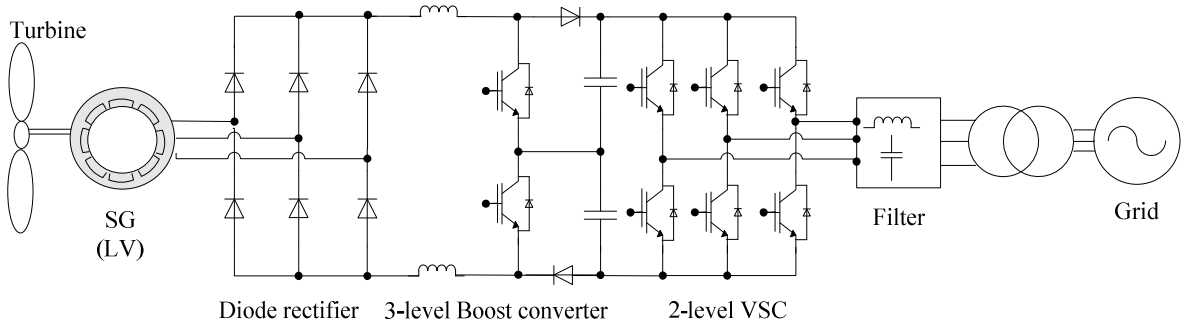

Figure 1.11. A 3-level boost converter.

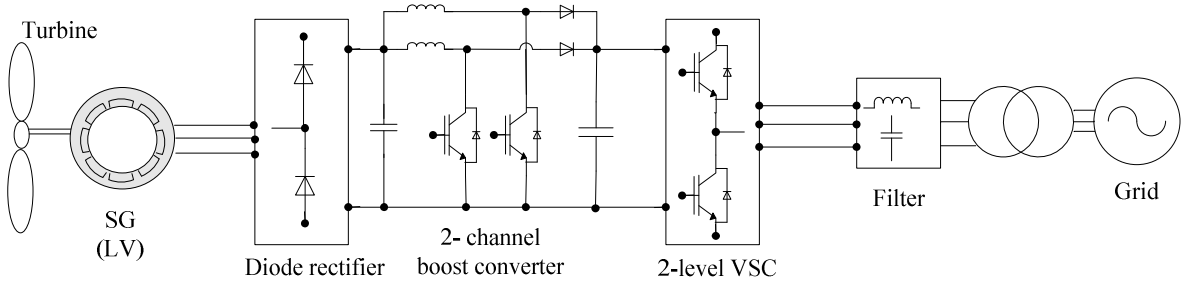

Figure 1.12. A 2-channel boost converter.

The configuration can be extended to a 3-level boost converter which is composed of two single-boost converters in a cascaded arrangement as in figure 1.11. This alternative has found practical application with a power rating up to 1.2 MW [1.2]. Another method of increasing the power rating of this configuration is to use a two-channel or three-channel interleaved boost converter as shown in figures 1.12.

1.5 Configurations with Multiple Cells Power Converters

Parallel and series connecting devices or converters to increase the WTs power level includes matrix converters, cascaded topologies, neutral point clamp, flying capacitor as well as hybrid configurations [1.18]. Also, it is possible to increase the power rating of wind energy systems by using distributed converters for a generator with multiple windings or for multiple generators. Correspondingly, the grid-side transformer can also be designed with multiple windings. This configuration has a number of advantages, such as

low torque ripple and harmonic distortion, use of low power converters for a MW WT and no power de-rating of converters because of the absence of circulating currents [1.2].

The multi-winding generator approach is illustrated in figure 1.14, where a six-phase generator is used and the power is delivered to the grid through two distributed converter channels [1.22]. Each converter channel is composed of two-level voltage source converters and filters.

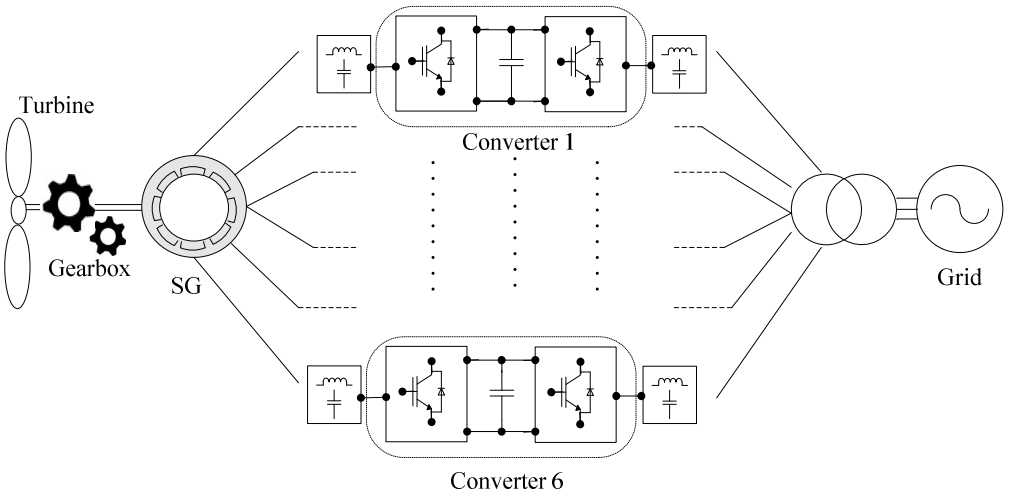

Figure 1.13. WECS multiple cells power converters.

1.6 Wind Generator Grid Integration Issues

Since wind power production is dependent on the wind, the output power of a wind turbine varies over time under the influence of meteorological fluctuations. This raises challenges for the integration of large power into electricity grids, consequently several design and operation issues must be addressed [1.20]. To ensure power system stability, grid operators issue technical guidelines which wind power plants have to comply with to be able to merge the production of conventional power plants with renewable energy plants which have different performance [1.23]. To safeguard the electrical power system under liberalized electricity markets, grid codes were written in different countries specifying the technical and operational characteristics of plants owned by the different parties involved in the production, transport and consumption of electric power. This is necessary in order to ensure a certain level of quality of supply which must be delivered to the end users [1.24].

The most common requirements include steady state performance ratings such as voltage, frequency, active and reactive power; power quality parameters such as flicker, in-rush current damping, negative phase sequence voltage, voltage and current total harmonic distortion, and current inter-harmonics levels. The technical grid codes also include regulations for grid dynamic performance such as low voltage ride through, frequency and power ramps, islanding, active power control, reactive power and voltage control [1.25].

1.7 Low Voltage Ride-through

The main objective of this thesis is to focus on the low voltage ride through capability of PMSG based WECS. Grid disturbances such as severe voltage dips caused by short-circuit faults can lead to power-generating units disconnected from the grid. Grid faults in the form of voltage sags or swells can typically lead to tripping of wind power plant, which can unbalance the grid and may yield blackouts and instability in the grid. To avoid these problems, it is required that wind power plants continue to operate even at very low voltage dips, support the voltage recovery by injecting reactive current and restore active power after fault clearance with limited ramp values [1.26]. All these features are defined as fault ride-through (FRT) capability and vary from one country to another. FRT is defined in terms of minimum and maximum voltage ride-through (low and high VRT) and recovery slope for symmetrical and asymmetrical faults that the wind power plant must be able to withstand without being disconnected from the utility grid.

1.8 Research Motivation and Objectives

Variable speed operation and grid interconnection through a full scale power converter are the main trends of modern WTs. However, large wind installations are requested to behave similar to conventional power plant due to their high impact on grid stability. Accordingly, wind power plant control needs to be carefully designed to meet the system operator's requirements in terms of grid code compliance and control in both normal operation and in response to disturbances.

In this research, low voltage ride-through capability enhancement for PMSG based WECS is the prime factor under investigation. The research analyzes the possibility of enhancing the ride-through capability of PMSG wind turbines in response to symmetrical voltage dips through the use of magnetic amplifiers.

The thesis main objectives are:

- Model and simulate a 1.5 MW PMSG wind turbine for grid interconnection.
- Investigate the system's performance for compliance with UK grid codes for active and reactive powers, frequency and phase changes.
- Outline the different methods used for LVRT capability enhancement for PMSG WECS.
- Investigate the performance of magnetic amplifiers as a method for LVRT enhancement through simulation analysis using Matlab, for the 1.5 MW full sized system.
- Practical validation for enhancing the LVRT capability of a scaled down system prototype using magnetic amplifiers and comparing the experimental results with the scaled down system simulation.

References

[1.1] REN21—Renewables 2014 Global Status Report [Online] [Online]. Available: http://www.ren21.net

[1.2] B. Wu, *et al.*,'Power Conversion and Control of Wind Energy Systems', Wiley, 2011.

[1.3] D. Yao and R. G. Harley, 'Present and Future Trends in Wind Turbine Generator Designs', IEEE Power Electronics and Machines in Wind Applications, (PEMWA), June 2009. pp. 1-6.

[1.4] L. Mihet-Popa and I. Filip, 'Modeling and Simulation of a Soft-Starter for Large Wind Turbine Induction Generators', International Joint Conference on Computational Cybernetics and Technical Informatics (ICCC-CONTI), May 2010. pp. 465-470.

[1.5] H. Polinder, *et al.*, 'Comparison of Direct-Drive and Geared Generator Concepts for Wind Turbines', IEEE Transactions on Energy Conversion, Vol. 21, 2006. pp. 725-733.

[1.6] M. R. Patel,'Wind and Solar Power Systems: Design, Analysis, and Operation, Second Edition', Taylor & Francis, 2005.

[1.7] S. Tunyasrirut, B. Wangsilabatra, and T. Suksri, 'Phase Control Thyristor based Soft-Starter for a Grid Connected Induction Generator for Wind Turbine System', International Conference on Control Automation and Systems (ICCAS) May 2010. pp. 529-534.

[1.8] G. Quinonez-Varela and A. Cruden, 'Modelling and Validation of a Squirrel Cage Induction Generator Wind Turbine during Connection to the Local Grid', IET Generation, Transmission & Distribution, Vol. 2, 2008. pp. 301-309.

[1.9] M. R. Patel,'Wind and Solar Power Systems', Taylor & Francis, 1999.

[1.10] M. Arifujjaman, M. T. Iqbal, and J. E. Quaicoe, 'A Comparative Study of the Reliability of the Power Electronics in Grid Connected Small Wind Turbine Systems', Canadian Conference on Electrical and Computer Engineering (CCECE) May 2009. pp. 394-397.

[1.11] D. J. Burnham, S. Santoso, and E. Muljadi, 'Variable Rotor-Resistance Control of Wind Turbine Generators', IEEE Power & Energy Society General Meeting (PES) May 2009. pp. 1-6.

[1.12] S. Muller, M. Deicke, and R. W. De Doncker, 'Doubly Fed Induction Generator Systems for Wind Turbines', IEEE Industry Applications Magazine, Vol. 8, 2002. pp. 26-33.

[1.13] D. Ehlert and H. Wrede, 'Wind Turbines with Doubly-Fed Induction Generator Systems with Improved Performance due to Grid Requirements', IEEE Power Engineering Society General Meeting, June 2007. pp. 1-7.

[1.14] B. Kedjar and K. Al-Haddad, 'Optimal Control of a Grid Connected Variable Speed Wind Energy Conversion System based on Squirrel Cage Induction Generator', 38th Annual Conference on IEEE Industrial Electronics Society (IECON), Oct 2012. pp. 3560-3565.

[1.15] H. Ahuja, G. Bhuvaneswari, and R. Balasubramanian, 'Performance comparison of DFIG and PMSG based WECS', IET Conference on Renewable Power Generation (RPG), Sep 2011. pp. 1-6.

[1.16] F. Blaabjerg, M. Liserre, and M. Ke, 'Power Electronics Converters for Wind Turbine Systems', IEEE Transactions on Industry Applications, Vol. 48, 2012. pp. 708-719.

[1.17] M. Ke, F. Blaabjerg, and X. Dehong, 'Power Devices Loading in Multilevel Converters for 10 MW Wind Turbines', IEEE International Symposium on Industrial Electronics (ISIE), June 2011. pp. 340-346.

[1.18] S. Kouro*, et al.*, 'Recent Advances and Industrial Applications of Multilevel Converters', IEEE Transactions on Industrial Electronics, Vol. 57, 2010. pp. 2553-2580.

[1.19] B. Wu,'High-Power Converters and AC Drives', Wiley, 2006.

[1.20] M. H. Ali,'Wind Energy Systems: Solutions for Power Quality and Stabilization', Taylor & Francis, 2012.

[1.21] J. A. Baroudi, V. Dinavahi, and A. M. Knight, 'A Review of Power Converter Topologies for Wind Generators', IEEE International Conference on Electric Machines and Drives, May 2005. pp. 458-465.

[1.22] M. J. Duran*, et al.*, 'Six-phase PMSG Wind Energy Conversion System based on Medium-Voltage Multilevel Converter', Proceedings of the 14th European Conference on Power Electronics and Applications (EPE) Sep 2011. pp. 1-10.

[1.23] S. A. Pastromas, ‘Grid Support by Wind Turbines and Future Trends’, IEEE Transmission and Distribution Conference and Exposition (PES), July 2010. pp. 1-7.

[1.24] C. E. Stephan and Z. Baba, ‘Specifying a Turbogenerator's Electrical Parameters Guided by Standards and Grid Codes’, IEEE International Electric Machines and Drives Conference, (IEMDC) 2001. pp. 63-68.

[1.25] EWEA. Generic Grid Code Format for Wind Power Plants [Online]. Available: www.ewea.org

[1.26] R. Teodorescu, M. Liserre, and P. Rodríguez,‘Grid Converters for Photovoltaic and Wind Power Systems’, Wiley, 2011.

CHAPTER TWO

Modelling of a Permanent Magnet Synchronous Generator based Wind Energy Conversion System

Wind energy is the most promising renewable energy source, with a fast growing capacity. In addition to the growth in total installed capacity, the size of individual wind turbines is also increasing dramatically, starting with a few tens of kilowatt of rated power in the 1980s and now reaching 8 MW. As grid penetration and power levels of the WT increase steadily, wind power has started to have significant impact on the power grid. Moreover, advanced generators, power electronic systems, and control solutions have been introduced to improve the characteristics of wind power plant integration into the power grid [2.1]

Variable speed WECS employing PMSG are a popular wind energy configuration owing to their extended speed operating range, high power density, full decoupling between generation and the grid, and maximum energy capture at different wind speeds. Also, the ability to be directly driven from the turbine without the use of a gearbox, gives directly driven PMSG systems a competitive advantage in terms of high energy yield, noise reduction, low maintenance and high efficiency. Large amounts of variable generated power from distributed generation (DG) units create power system operation issues; dynamic and steady state stability forcing the need for analysis and modelling of the WECS for proper control.

In this chapter, a mathematical model of the WECS employing a multi-pole PMSG is developed and analyzed. The model includes the wind turbine, PMSG, ac-dc –ac converters employed, and grid coupling. The chapter further investigates WECS control methodologies.

2.1 Wind Energy Conversion System Overview

Variable speed WT operation requires a power electronic system that is capable of matching the generator frequency and voltage with that of the electrical grid. By utilizing a full-scale power converter in the PMSG WT case, to interconnect to the power grid, all the generated power from the wind turbine can be regulated with good speed control and grid support features. Figure 2.1 shows a basic PMSG wind turbine system configuration, which is also known as a Type-4 WECS [2.2]. The system consists of a wind turbine coupled to a PMSG where the stator terminals of the PMSG are connected to the constant voltage and frequency grid through a two stage power conversion unit (ac-dc-ac), grid coupling filter, and a step-up transformer.

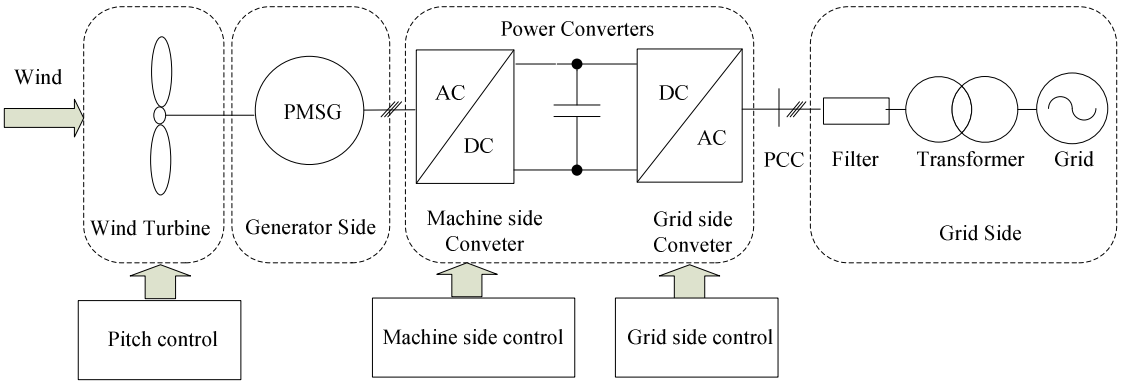

Figure 2.1. PMSG WECS.

The following sections contain full system description and modelling of the PMSG WECS shown in figure 2.1. Mathematical modelling is carried out for the system components of figure 2.1 which includes the mechanical wind turbine, PMSG, ac-dc-ac conversion units as well as the grid side representation. Machine side and grid side control for WT operation are also outlined.

2.2 Wind Turbine Model

WTs use the blades to convert kinetic energy into rotational and then electrical energy. The kinetic power of air stream, P_w, can be represented as:

$$P_{wind} = \frac{1}{2}\rho A V^3 \tag{2.1}$$

where ρ is the wind density, A is the blades swept area, and V is the wind speed. The swept area of the blades, A is equal to πR^2, where R is the wind turbine blade radius.

The power that can be extracted from the wind can be expressed as [2.3]:

$$P_w = \frac{1}{2}\rho\pi R^2 C_p(\lambda,\beta)V^3 \tag{2. 2}$$

where the power coefficient, C_p, varies as a function of the tip speed ratio, λ, and the pitch blade angle β. For every fixed β there is a corresponding ($C_p - \lambda$) curve, where each has a peak C_p value corresponding to an optimum λ. Maximum C_p is achieved at optimized rotational speed when β is equal to zero.

For lossless systems, the maximum C_p is equal to 0.59; accordingly it is possible to only extract 59% of the wind energy [2.3]. The value for C_p can be computed as [2.4]:

$$C_p(\lambda_1,\beta) = c_1\left(\frac{c_2}{\lambda_1} - c_3\beta - c_4\beta^{c_5} - c_6\right)e^{\frac{-18.4}{\lambda_1}} \tag{2.3}$$

$$\text{where } \lambda_1 = \frac{1}{\left(\frac{1}{\lambda - c_8\beta} - \frac{c_9}{\beta^3+1}\right)}, \text{ and} \tag{2.4}$$

$$\lambda = \frac{R\omega}{V} \tag{2.5}$$

where $[c_1 \ldots\ldots\ c_9]$ are characteristic constants for each wind turbine.

The tip speed ratio, λ, is defined as the ratio between the blade tip speed ω, wind turbine blade radius R and the wind speed V, while β and λ are related in equation (2.5) to obtain the value of λ_1. Figure 2.2 shows the mathematical model of a wind turbine.

Typical wind turbine characteristic curves are shown in figure 2.2. Assuming that β is zero to achieve maximum C_p, figure 2.3 shows the wind turbine output power variation with its rotary speed, ω_r, with respect to wind speed V. If the generator is running at rated speed at a wind speed of 12 m/s, the maximum extracted power from the wind turbine will only be approximately 70% of its nominal output. The effect of changing β is illustrated in figure 2.4. If β moves slightly, by an angle of 2°, the output power from the turbine will drop to a value below 0.7 per unit of the nominal output power.

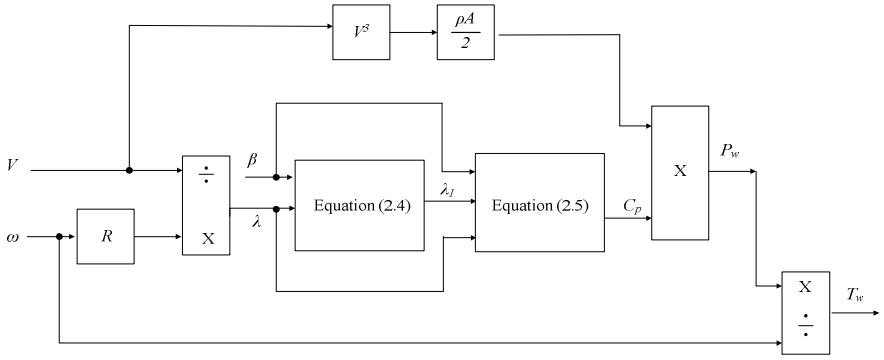

Figure 2.2. Wind turbine model.

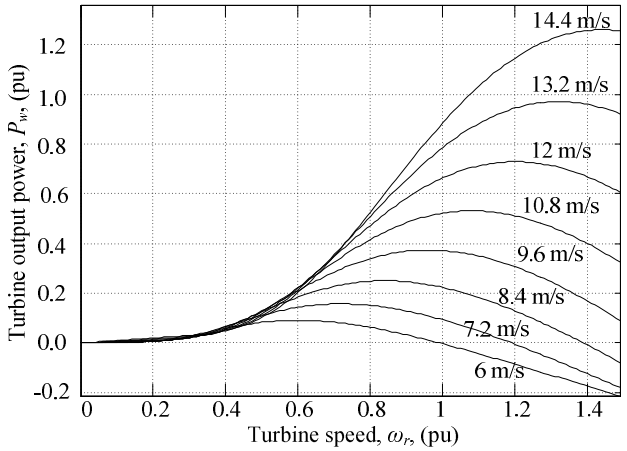

Figure 2.3. Turbine output power versus generator speed at different wind speeds, at β =0°.

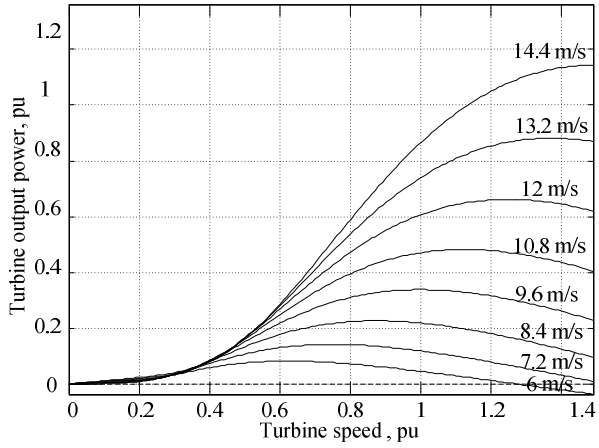

Figure 2.4. Generator output power versus generator speed at different wind speeds, at β =2°.

2.3 Generator Model

The electrical generator is required to convert the mechanical energy from the wind turbine prime mover to electrical energy that is transferred to the electrical grid. The PMSG is favoured in recent turbine designs, since it is characterized by high efficiency and with no need for any external excitation current, making it superior in offshore wind applications since it requires minimum maintenance and has a reduced likelihood of mechanical failures due to the absence of a gearbox [2.5].

Park transformation transforms the rotating stator variables to a fixed rotor frame [2.6]. Let *S* represent any of the variables (current, voltage, and flux linkage) to be transformed from the *abc* frame to the *dq0* rotor frame. The transformation in matrix form is given by

$$\begin{bmatrix} S_d \\ S_q \\ S_0 \end{bmatrix} = \frac{2}{3} \begin{bmatrix} cos\theta & cos\left(\theta - \frac{2\pi}{3}\right) & cos\left(\theta + \frac{2\pi}{3}\right) \\ -sin\theta & -sin\left(\theta - \frac{2\pi}{3}\right) & -sin\left(\theta + \frac{2\pi}{3}\right) \\ ½ & ½ & ½ \end{bmatrix} \begin{bmatrix} S_a \\ S_b \\ S_c \end{bmatrix} \tag{2.6}$$

where the S_O component is the zero sequence component and in balanced 3-phase system this component is zero. The $\frac{2}{3}$ constant in (2.6) is introduced to make the transformation power variant [2.7]. Due this choice the values of the time independent variables, such as *dq* axes currents will be equal to their corresponding peak values. The inverse of the transformation is [2.6]:

$$\begin{bmatrix} S_a \\ S_b \\ S_c \end{bmatrix} = \begin{bmatrix} cos\theta & -sin\theta & 1 \\ cos\left(\theta - \frac{2\pi}{3}\right) & -sin\left(\theta - \frac{2\pi}{3}\right) & 1 \\ cos\left(\theta + \frac{2\pi}{3}\right) & -sin\left(\theta + \frac{2\pi}{3}\right) & 1 \end{bmatrix} \begin{bmatrix} S_d \\ S_q \\ S_0 \end{bmatrix} \tag{2.7}$$

The essential features of a 3-phase synchronous machine from the analytical point of view are shown in figure 2.4, where the co-ordinate system used in modelling is presented in part (a). On the stator are the three distributed windings *a, b* and *c* and on the rotor is the permanent magnet as indicated in figure 2.4 part (b). The PMSG model is similar to the standard wound synchronous machine except for the absence of dc-field excitation and instead the excitation is provided by the permanent magnet giving a constant flux φ_f.

The PMSG rotor has two axes of symmetry, direct axis and quadrature axis, *d* and *q* respectively. The *dq* axes revolve with the rotor, while the magnetic axes of three stator

phases are stationary and the angle θ is the angle between phase *a*-axis and the *d*-axis. As the rotor turns, θ varies with time, with a constant rotor angular velocity ω_r.

The electrical dynamic voltage equations in terms of phase variables are

$$[v_{abcgen}] = [R_a][i_{abcgen}] + p[\varphi_{abc}] \quad (2.8)$$

$$[\varphi_{abc}] = [L_{abc}]\,[i_{abcgen}] + [\varphi'_f] \quad (2.9)$$

where v_{abcg} , i_{abcg} , φ_{abc} are the three phase stator voltages, currents and flux linkages for phase *a,b,c* respectively and R_a is the resistance of the three phase stator windings which is equal in the three phases.

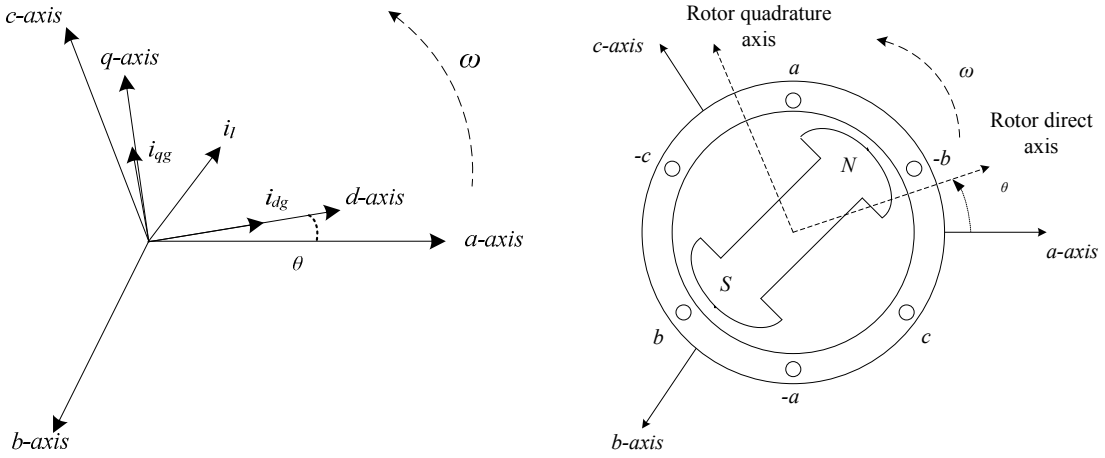

Figure 2.5. The synchronous machine: (a) co-ordinate system and (b) idealized machine.

The inductance matrix $[L_{abc}]$ is given by:

$$[L_{abc}] = \begin{bmatrix} l_{aa} & l_{ab} & l_{ac} \\ l_{ba} & l_{bb} & l_{bc} \\ l_{ca} & l_{cb} & l_{cc} \end{bmatrix} \quad (2.10)$$

where l_{aa}, l_{bb}, l_{cc} are the self inductances of phase *abc,* $l_{ab} = l_{ba}$ are the mutual inductance between phase *a* and *b*, $l_{bc} = l_{cb}$= mutual inductance between phase *b* and *c*, $l_{ac} = l_{ca}$= mutual inductance between phase *a* and *c*.

Neglecting the change due to loading and air gap variation, the flux-linkage in the stator winding due to the permanent magnet rotor is given by

$$[\varphi_f'] = \begin{bmatrix} \varphi_a \\ \varphi_b \\ \varphi_c \end{bmatrix} = \begin{bmatrix} \varphi_f \sin\theta \\ \varphi_f \sin\left(\theta - \frac{2\pi}{3}\right) \\ \varphi_f \sin\left(\theta + \frac{2\pi}{3}\right) \end{bmatrix} \tag{2.11}$$

where φ_f is the amplitude of the flux linkages established by the permanent magnet, viewed from the stator phase windings.

The equivalent *dq*-axes stator windings are transformed to the reference frame that is revolving at the rotor speed. The consequence is zero speed differentials between the rotor and stator magnetic fields. Also, the stator *d* and *q*-axis windings will have a fixed phase relationship with the rotor magnet axis, which is the *d*-axis in the modelling. Applying Park's transformation (2.6) and its inverse (2.7) to voltage equation (2. 8), and the flux linkage equation of (2.11), the voltage-current relations of the PMSG in *dq* terms are

$$v_{dgen} = R_a i_{dgen} + p\varphi_d - \varphi_q \omega_e \tag{2.12}$$

$$v_{qgen} = R_a i_{qgen} + p\varphi_q + \varphi_d \omega_e \tag{2.13}$$

where ω_e is the electrical angular frequency and can be related to rotor mechanical angular frequency ω_r as

$$\omega_e = \frac{P}{2}\omega_r \tag{2.14}$$

The flux linkage equations in *dq* terms are

$$\varphi_d = L_d i_{dgen} + \varphi_f \tag{2.15}$$

$$\varphi_q = L_q i_{qgen} \tag{2.16}$$

Substituting (2.15) and (2.16) into (2.12) and (2.13), and since φ_f is constant, then $p\varphi_f$ = 0, and

$$v_{dgen} = (R_a + pL_d) i_{dgen} - \omega_e L_q i_{qgen} \tag{2.17}$$

$$v_{qgen} = (R_a + pL_q) i_{qgen} + \omega_e L_d i_{dgen} + \varphi_f \omega_e \tag{2.18}$$

For dynamic simulation, the PMSG model can be expressed as:

$$pi_{dgen} = \frac{\left(v_{dggen} - R_a i_{dgen} + L_q i_{qgen} \omega_e\right)}{L_d} \tag{2.19}$$

$$pi_{qgen} = \frac{\left(v_{qgen} - R_a i_{qgen} + L_d i_{dgen} \omega_e - \varphi_f \omega_e\right)}{L_q} \tag{2.20}$$

The instantaneous power input to the 3-phase stator will be

$$P_{igen} = v_{agen} i_{agen} + v_{bgen} i_{bgen} + v_{cgen} i_{cgen} \tag{2.21}$$

Using (2.6) for voltages and currents and neglecting the zero sequence component, the power equation is

$$P_{igen} = \frac{3}{2}\left(v_{dgen}i_{dgen} + v_{qgen}i_{qgen}\right) \tag{2.22}$$

$$P_{igen} = \frac{3}{2}\left(R_a\left(i_{dgen}^2 + i_{qgen}^2\right) + i_{qgen}\frac{d\varphi_q}{dt} + i_{dgen}\frac{d\varphi_d}{dt} + \omega_e\left(\varphi_d i_{dgen} - \varphi_q i_{dgen}\right)\right) \tag{2.23}$$

The ohmic term represents the ohmic losses while the rate of change term represents the magnetic energy and therefore, it can be concluded that the electromechanical power P_e is given by

$$P_e = \frac{3}{2}\omega_r\left(\varphi_d i_{qgen} - \varphi_q i_{dgen}\right) \tag{2.24}$$

The electromechanical torque is produced by the interaction between the rotor poles P and the poles resulting from the rotating air gap mmf established by currents flowing in the stator windings as in (2.25). The electromechanical developed torque T_e is obtained as [2.8]

$$T_e = \frac{3}{2}\left(\frac{P}{2}\right)\left(\varphi_d i_{qgen} - \varphi_q i_{dgen}\right) \tag{2.25}$$

The torque and speed may also be related using equation (2.26), where J is the moment of inertia and T_L is the load torque:

$$T_e = J\left(\frac{2}{P}\right)\frac{d\omega_r}{dt} + \omega_r\left(\frac{2}{P}\right) + T_L \tag{2.26}$$

Substituting (2.15) and (2.16) into (2.25), the electromagnetic torque equation of an interior permanent magnet synchronous generator (IPMSG) is obtained

$$T_e = \frac{3}{2}\left(\frac{P}{2}\right)\left(\varphi_f i_{qgen} + \left(L_d - L_q\right)i_{qgen}i_{dgen}\right) \tag{2.27}$$

Figure 2.6 represents the PMSG model using equations (2.6) to (2.26).

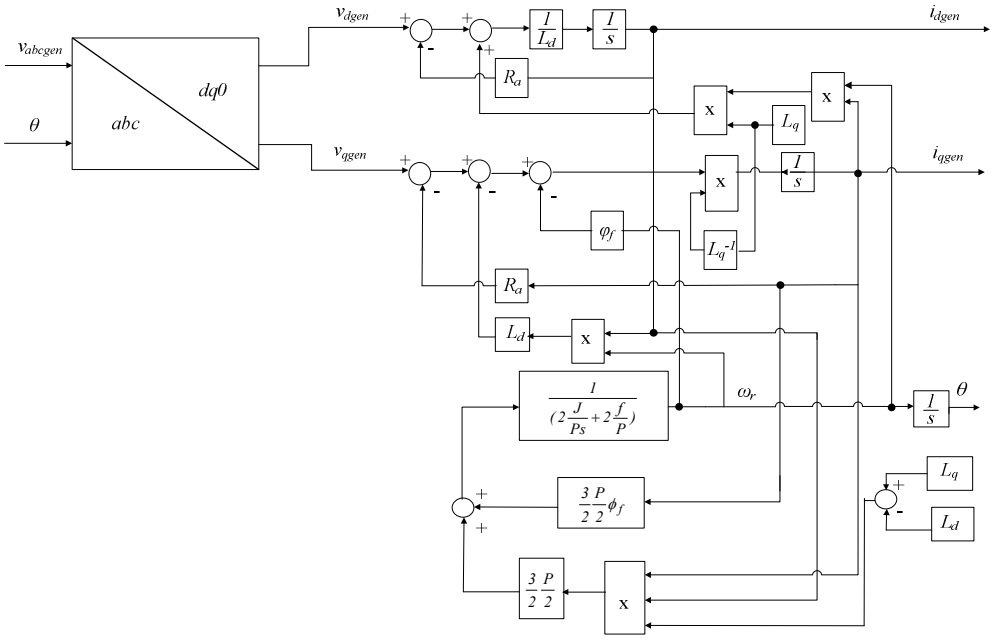

Figure 2.6. Mathematical model of a PMSG.

2.4 AC-DC Conversion Unit

The main function of the ac-dc conversion unit is to control the wind turbine generator, and decouple the generator from the electrical grid. Since the generator output voltage and frequency do not match those of the grid, the ac-dc conversion unit transforms the generator voltage and current to dc-values, which become frequency independent. Several ac-dc topologies can be used depending on the power range, and type of wind turbine generator employed, as well as grid conditions.

A widely used scheme is to use a pulse width modulated (PWM) VSI as the grid-side converter (GSC) [2.9], although other topologies exist. PWM-VSI configurations require that the dc-link voltage, $V_{dc-link}$ be higher than the peak of the grid voltage, $\hat{v}_{grid}$ for controlled power flow operation. Figure 2.7 shows two popular configurations for the ac-dc conversion unit, one using a PWM voltage source rectifier shown in part (a); and the other utilizing a diode rectifier with a boost chopper circuit as indicated in part (b) [2.10]. The former topology, also known as the back-to-back configuration when connected to a PWM VSI, is more expensive, has higher switching losses because of the six switches and has a more complex control system. However, it offers better generator control, such as

torque ripple, speed and bidirectional power flow control [2.11, 2.12]. Other circuit configurations exist, including multilevel converters and the matrix converter [2.13, 2.14]. The converter topology employing a diode bridge rectifier and a boost chopper in figure 2.7 (b) instead of a controlled PWM rectifier, offers a low cost solution with high reliability. The main disadvantage of the diode-rectifier based system is that the generator stator currents are uncontrolled. It can, however, be used in small scale wind power systems. Analysis in the following sections will be carried out for the diode rectifier-boost configuration where the ac-dc conversion stage will be referred to as the machine side converter (MSC) as indicated in figure 2.1.

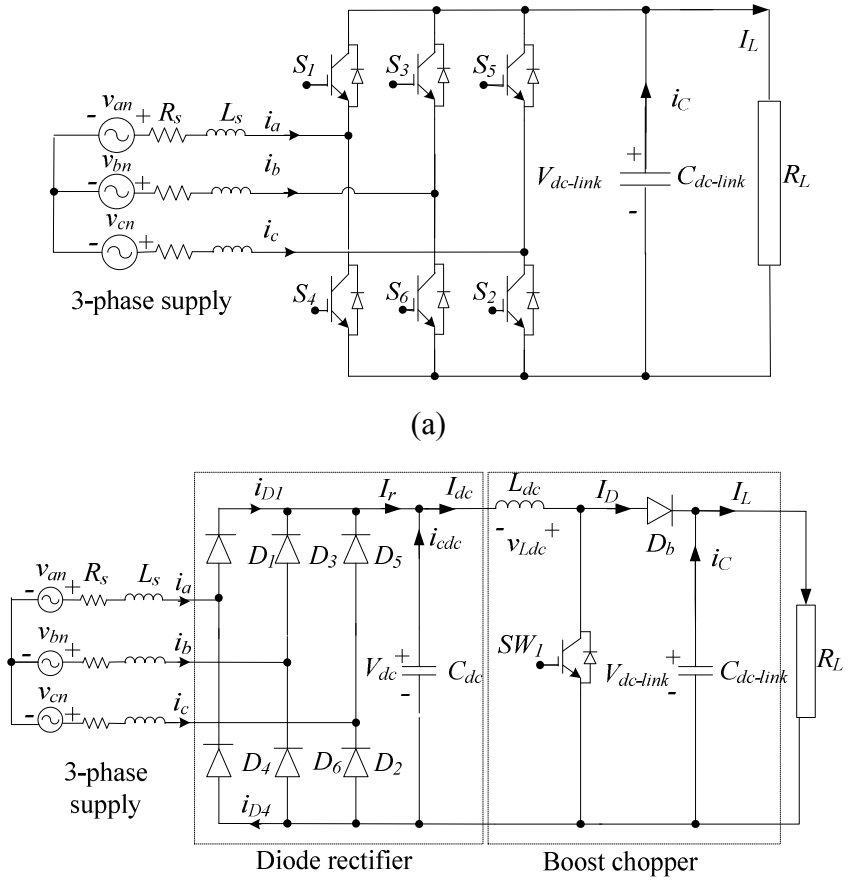

Figure 2.7. Machine side converter: (a) voltage-source PWM rectifier and (b) diode rectifier with boost.

In analyzing the diode rectifier part without the boost chopper of figure 2.7 (b), assume the phase-to-neutral supply voltages in figure 2.5 are defined as

$$v_{an} = \sqrt{2}\, V_{PH}\, sin(\omega_s t)$$
$$v_{bn} = \sqrt{2}\, V_{PH}\, sin\left(\omega_s t - \frac{2\pi}{3}\right) \quad (2.28)$$
$$v_{cn} = \sqrt{2}\, V_{PH}\, sin\left(\omega_s t + \frac{2\pi}{3}\right)$$

V_{PH} is the rms value of the phase voltage and ω_s is the supply voltage angular frequency given by $2\pi f$, where f is the supply frequency. The line-to-line voltage v_{ab} can be calculated as:

$$v_{ab} = v_a - v_b = \sqrt{2}\, V_{LL}\, sin\left(\omega_s t + \frac{\pi}{6}\right) \quad (2.29)$$

where V_{LL} is the rms value of the line-to-line voltage.

The full bridge diode rectifier waveforms connected to a resistive or highly inductive load are presented in figure 2.8 (a) to (f). The waveform for the rectifier output voltage, V_{dc}, is shown in figure 2.8 (b), while the rectifier load current response, I_{dc} is demonstrated in part (c). The rectifier load current I_{dc} is continuous with six pulses per cycle of the supply frequency; where each diode conducts for $\frac{2}{3}$ π and experiences a maximum reverse voltage of the peak line voltage $\sqrt{2}\, V_{LL}$ [2.15]. Diode currents, i_{D1} and i_{D4} waveforms are illustrated in part (d) and (e), while the supply current, i_a, is shown in part (f).

The mean output dc voltage $\overline{V_{dc}}$, is continuous as shown in (b) and can be calculated as:

$$\overline{V_{dc}} = \frac{1}{\pi/3}\int_{\pi/6}^{\pi/2} \sqrt{2}\, V_{LL}\, sin\left(\omega_s t + \frac{\pi}{6}\right) d(\omega_s t) = \frac{3\sqrt{2}}{\pi} V_{LL} \approx 1.35\, V_{LL} \quad (2.30)$$

Having an unregulated output voltage is regarded as the main disadvantage for the rectifier-boost topology despite its low complexity. Moreover, since the supply current (or generator stator currents in the case of the PMSG) contains serious harmonic content, relatively large electromagnetic torque ripple results, caused by the low frequency generator stator harmonic current [2.16]. The torque ripple may cause detrimental effects on the turbine and shaft life time [2.17]. Although it is acceptable for small power rating systems, torque ripple reduction enhances system reliability and also the applicability at higher power. The inductance L_s found in figure 2.8 (a) and (b), represents the inductance of a three-phase reactor that is often added to the system in practice for the reduction of

current and torque ripple [2.18]. A reduction in the rectifier output dc-voltage, V_{dc} takes place in the AC side filtering due to the voltage drop across L_s.

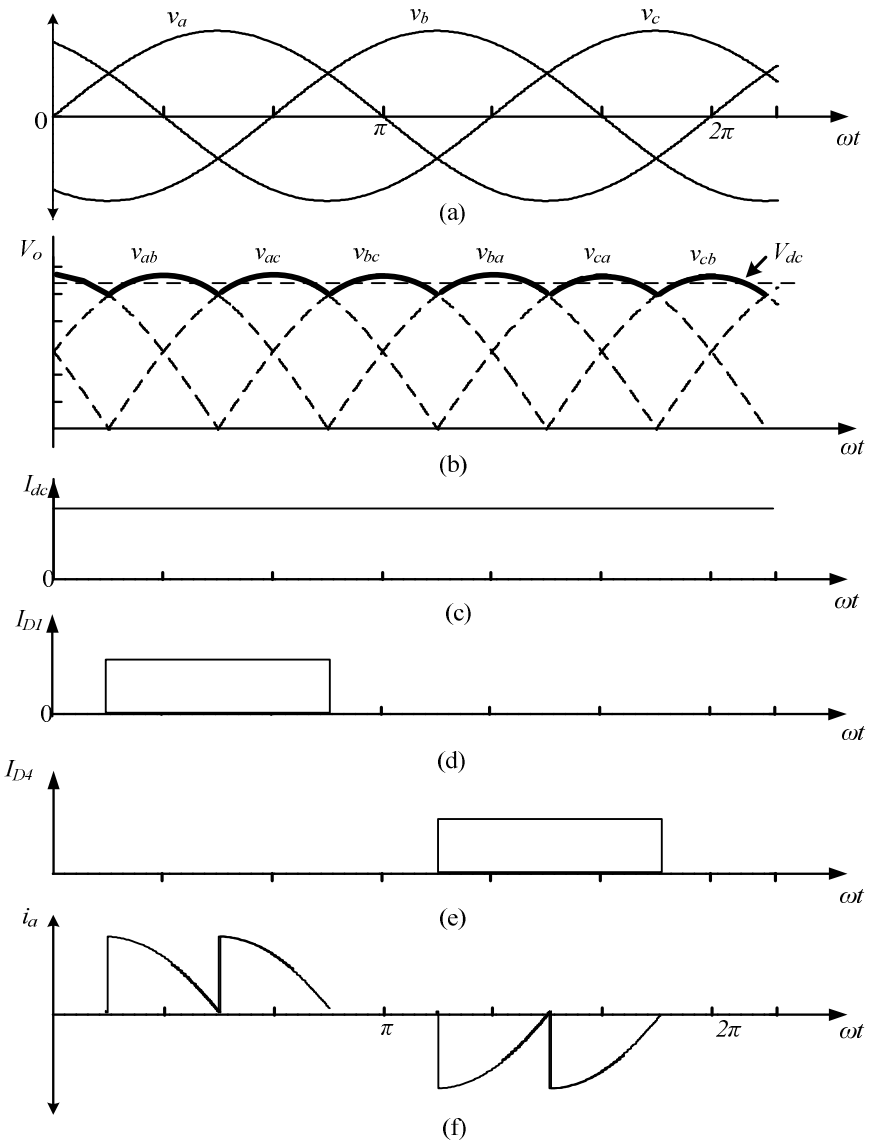

Figure 2. 8. Three-phase full-wave bridge rectifier waveforms: (a) 3-phase voltage, v_s, (b) line voltage, V_s, and output voltage, V_{dc}, (c) load current, I_{dc}, (d) diode D_1 current, I_{D1}, (e) diode D_4 current, I_{D4}, and (f) supply current, i_a.

The boost chopper in figure 2.7 (b) transforms the rectifier output voltage, V_{dc}, to dc-voltage $V_{dc-link}$ that is greater in magnitude but has the same relative polarity as the input. As the transistor SW_1 is switched off, the output capacitor $C_{dc-link}$ is charged to the rectifier voltage V_{dc}; thus the output voltage $V_{dc-link}$ can never be less than the input

voltage level. When the transistor switch SW_1 is turned on, V_{dc} is applied across the inductor L_{dc} and the diode D_b is reverse-biased by the output voltage, $V_{dc-link}$. Energy is transferred from the supply to L_{dc} and when the transistor is turned off energy is transferred to the load and dc-link capacitor $C_{dc-link}$ through D_b. While L_{dc} is transferring stored energy to $C_{dc-link}$ and the load, energy is also being drawn from the input source. The diode current I_D is always discontinuous, but the input current can be either continuous or discontinuous.

Assuming continuous inductor current, the output voltage $V_{dc-link}$ and output current I_L relation is

$$\frac{V_{dc-link}}{V_{dc}} = \frac{I_L}{I_{dc}} = \frac{1}{1-k} \tag{2. 31}$$

where k is the duty cycle, defined as:

$$k = \frac{t_{on}}{T} \tag{2. 32}$$

where t_{on} is the switch ON time, T is the switching period and t_{off} is the switch OFF time.

Typical waveforms for the boost converter circuit in figure 2.7 when connected to a resistive load R_L are shown in figure 2.9 (a) to (f). For the applied gating in part (a) to switch SW_1, the output voltage $V_{dc-link}$ and inductor current, I_{dc} are shown in parts (d) and (f) respectively. Part (c) shows the inductor voltage, v_{Ldc} while (e) shows the diode D_1 current I_{D1}. The switch SW_1 voltage, v_{SW1} is illustrated in (b).

To calculate the ripple current in the inductor, L_{dc}, the inductor current ripple Δi_{dc} can be expressed as

$$\Delta i_{dc} = \frac{\Delta v_{Ldc}}{L_{dc}}\,\Delta t = \frac{(V_{dc-link} - V_{dc})}{L_{dc}}\,t_{off} = k\,(1-k)\,\frac{V_{dc-link}\,T}{L_{dc}} \tag{2. 33}$$

For continuous inductor current, the constant output current I_L is provided solely from the capacitor during the period t_{on} when the switch is on thus the output ripple voltage is the capacitor ripple voltage $\Delta v_{dc-link}$, defined by

$$\Delta v_{dc-link} = \frac{1}{C_{dc-link}} \int i\,dt = \frac{1}{C_{dc-link}}\,\Delta Q$$
$$= \frac{1}{C_{dc-link}}\,t_{on}\,\frac{v_{dc-link}}{R_L} \tag{2. 34}$$

Rearranging gives the percentage (peak-to-peak) output voltage ripple:

$$\frac{\Delta v_{dc-link}}{v_{dc-link}} = \frac{kT}{R_L C_{dc-link}} \tag{2. 35}$$

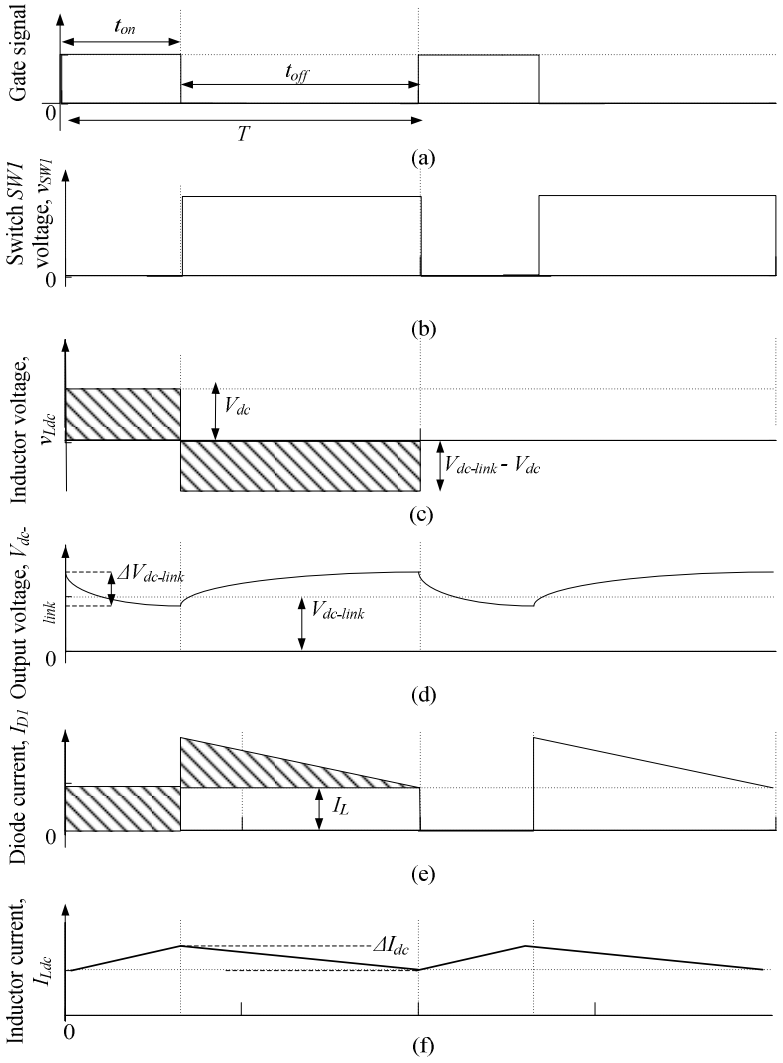

Figure 2. 9. Boost converter waveforms in continuous mode (a) gate signal, (b) SW_1 voltage v_{SW1}, (c) inductor voltage v_{Ldc}, (d) output voltage $V_{dc-link}$, (e) D_1 current I_{D1}, and (f) inductor current I_{Ldc} .

As previously mentioned, the main purpose of the MSC employing a rectifier-boost converter unit is to extract maximum power from the wind turbine at any given wind speed. To show the control algorithm for the MSC, figure 2.7 (b) is modified to include the control system block diagram as illustrated in figure 2.10. From figure 2.10, MSC operation is based on controlling the boost chopper current I_{dc}. A PI-controller is used to control the chopper inductor current I_{dc}, at a given reference value I_{dc}^{*}. The command

signal for the inductor current I_{dc}^{*} is chosen to satisfy the maximum power extraction criterion from the wind turbine. The on and off states of the chopper switch are determined using the output of the PI-controller. PWM is used to control the chopper switch duty cycle, k, varying from 0 to 1, assuming an ideal switch, with a constant carrier frequency, f_{ch}.

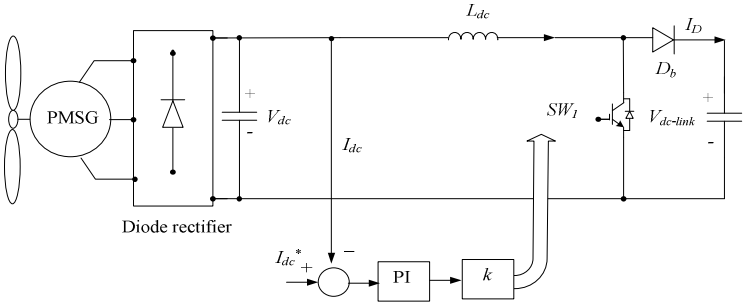

Figure 2. 10. WECS with rectifier and boost chopper.

2.5 DC-AC Conversion Unit

The dc-ac conversion unit is responsible for delivering the PMSG extracted power to the grid with regulations and conditions specified by grid operators. This stage reconstructs variable-amplitude and variable-frequency waveforms from the generator for grid matching purposes. The dc-ac conversion unit; also known as grid side converter (GSC), has different technologies to improve control and increase the reliability of the system.

GSCs can be divided into voltage and current source inverters [2.14]- [2.19]. Voltage source inverters are classified as either two-level VSI or multilevel inverters. Multilevel inverters have attracted research attention, where several topologies have been introduced and commercially established. Among them, the neutral point clamped, cascaded H-bridge, and flying capacitor inverters are the most common configurations [2.14]. The two-level VSI is applicable to MV drives. Extended voltage and power capabilities can be achieved by series connection of semiconductors. Figure 2.11(a) shows the topology of the two-level VSI [2.20] - [2.21]. Current source inverters (CSI) illustrated in figure 2.11 (b) are common in high-power applications and can be divided into two topologies, load commutated inverters (LCIs) and PWM CSIs [2.19]. The impedance source inverter (ZSI) is a new approach to dc-ac conversion technology. The ZSI circuit diagram shown in figure 2.11 (c) consists of an x-shaped impedance network formed by two capacitors and

two inductors, and provides unique buck– boost characteristics. The ZSI is characterized by robustness during bridge arm shoot-through, no need for dead time in switch commands, and low harmonic distortion in the output voltage [2.22].

A two level PWM VSI topology has been adopted in this research due to stable open-loop operation using constant V/Hz control, ease of control, and low cost [2.23].

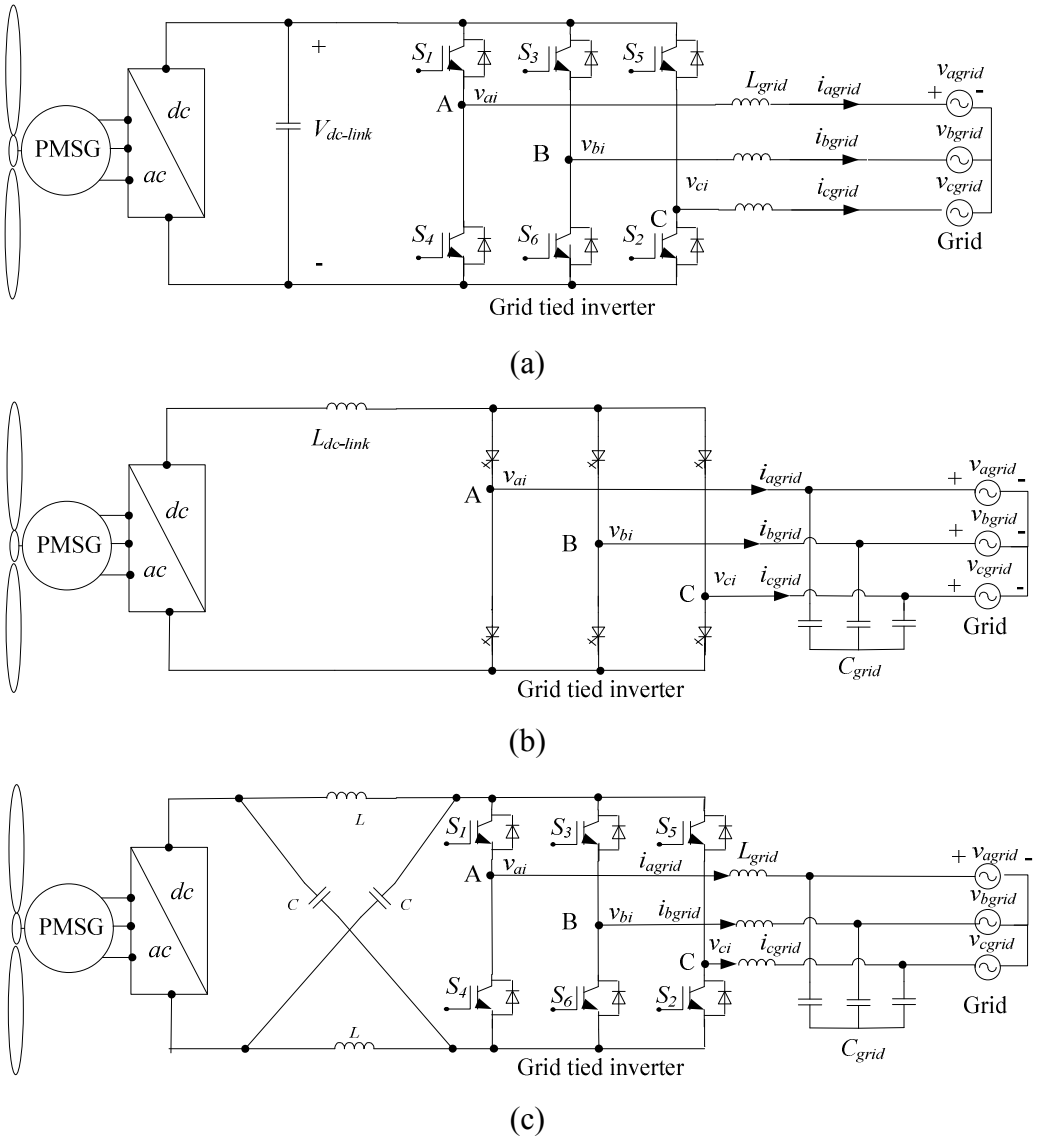

Figure 2.11. Grid-connected inverter in a WECS: (a) VSI, (b) CSI, and (c) ZSI.

The PWM VSI produces modulated ac output voltage from a constant or controlled dc-voltage source that maps a given reference signal by properly generating the switching functions of the semiconductor devices. Three PWM techniques are widely used, namely,

carrier-based PWM, space-vector modulation, and selective harmonic elimination [2.20]. In this thesis, the carrier based PWM technique is used.

The on and off states of the switches in a VSI leg are defined by comparing a modulating signal with a carrier signal. The resultant pulse width is proportional to the amplitude of the modulating signal. The modulating signal is the inverter reference phase voltage, v_m, while the carrier signal is a triangular waveform, v_c at frequency f_c. Referring to the inverter topology shown in figure 2.11 (a), each inverter leg has two switches, the upper switch for instance, S_1, is on when $v_m > v_c$ and the complementary switch in the same leg, S_2, is off. Similarly, when $v_m < v_c$, switch S_1 is off and switch S_2 is on. The inverter operates in the linear region provided the modulation index, m_a, is less than 1. The modulation index is defined as [2.24]

$$m_a = \frac{\hat{V}_m}{\hat{V}_c} \tag{2.36}$$

where $\hat{V}_m$ and $\hat{V}_c$ are the amplitude of the modulating and carrier signals respectively.

The sinusoidal PWM (SPWM) scheme is a special case of the carrier-based PWM technique when the modulating signal v_m is a pure sinusoidal at frequency f_c and amplitude $\widehat{V_m}$. Figure 2.12 shows the principle of operation of SPWM where v_{ma}, v_{mb}, v_{mc} are the three phase sinusoidal modulating signals and v_c is the triangular carrier wave.

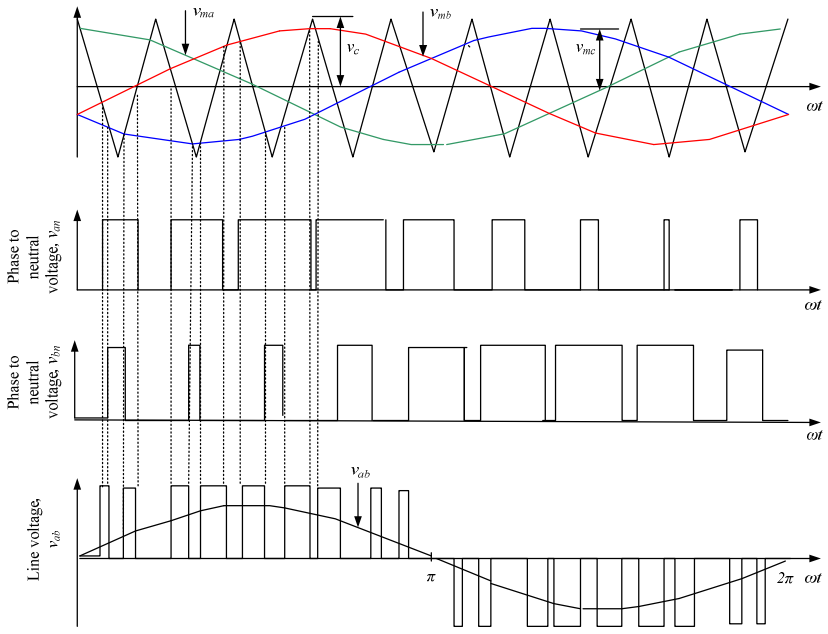

Figure 2. 12. Sinusoidal pulse-width modulation (SPWM).

Carrier-based PWM can be classified according to the sampling method, as natural sampled, and symmetrical and asymmetrical regular sampled PWM. It can also be classified as synchronous and asynchronous PWM. Synchronous PWM means that the carrier signal frequency f_c is synchronized with the modulating signal frequency f_m, and asynchronous PWM means that the two are not synchronized [2.15].

It can be concluded that the maximum amplitude of the line-to-line voltage, $\left(\hat{V}_{LLinv}\right)_{max}$ in SPWM is limited to [2.25]:

$$\left(\hat{V}_{LLinv}\right)_{max} = \frac{\sqrt{3}}{2} V_{dc-link} \approx 0.867\, V_{dc-link} \tag{2.37}$$

2.6 Grid and Interfacing Filter

A grid can be characterized by different parameters. Besides the grid voltage level and its total power capability, the short circuit capacity (SCC) can be defined as the amount of power flowing at a given point during a short circuit. It is mainly dependent on the rated voltage and the absolute value of grid impedance which can be measured at this point. The grid impedance is the sum of impedances of many grid components and typically differs from region to region. The grid impedance Z_{grid} takes into account the distribution lines, transformer and/or filter impedance for the reduction of line current distortion. In some cases, part of Z_{grid} can be due to the addition of reactive power compensation devices and/or large loads connected to this grid. The line resistance has been negligible as it has no impact on the system performance.

Passive filters are used in DG systems employing inverters to reduce voltage harmonics and current distortion, where each category harmonic must be sufficiently and appropriately attenuated. The current harmonics generated, if injected into the grid, can cause the malfunction of sensitive apparatus connected to the same bus. Passive filter configurations used with grid connected VSI have been extensively surveyed in reference [2.26]. A first order L- filter has been employed in this thesis for grid current smoothing.

For simulation purposes, the transformer and distribution line impedances have been neglected and only the effect of the filter impedance is taken into account. The voltage equation per phase can be written as:

$$v_{grid} = R_{grid} i_{grid} + L_{grid} \frac{di_{grid}}{dt} + V_{PCC} \tag{2.38}$$

where v_{grid} , i_{grid} are the grid voltage and injected grid current respectively, R_{grid}, L_{grid} are the equivalent resistance and inductance of distribution lines, filter and/or short circuit level grid representation. V_{PCC} is the voltage at the point of common coupling (PCC).

2.7 PMSG WECS Control

Figure 2.13 shows the block diagram of a typical wind energy system interfaced using a dc-dc boost converter. Four control variables need to be tightly controlled: dc-link voltage, generator active power, and grid active and reactive powers. The dc-voltage, V_{dc} produced by the diode rectifier varies with generator speed n as will be demonstrated in the following sections. The input inverter dc-voltage $V_{dc-link}$, however, is maintained at a constant value.

The following sections will describe two distinct control features used with PMSG WECS for controlling the four subject control variables. The two control algorithms achieved by the MSC and GSC include maximum power point tracking of the wind, as well as grid interconnection

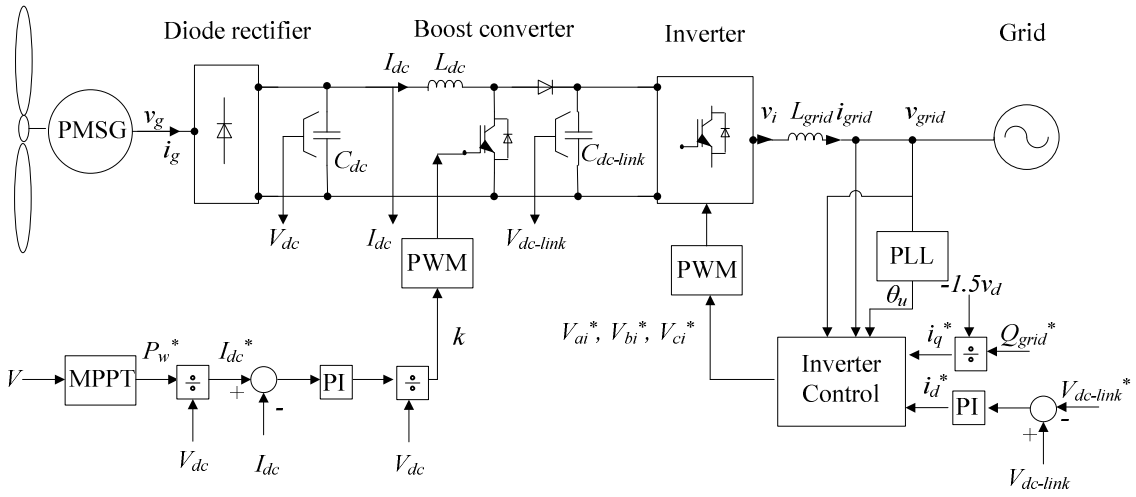

Figure 2.13. PMSG WECS employing rectifier and dc-dc boost converter.

2.7.1 MSC Control

The wind power system design must optimize the annual energy capture at a given site. Maximum power point tracking (MPPT) is one of the inherent characteristics of a variable speed wind turbine generator for optimal operation of wind power systems. There are three types of MPPT algorithms, namely, tip speed ratio (TSR) control, perturb and observe

(P&O) control (which is also known as hill-climbing searching control), and optimum relationship-based (ORB) control.

Tip speed ratio control is one of the oldest methods utilized in optimal power extraction. This method directly regulates the turbine speed to keep the TSR at an optimal value, at which the rotational speed is optimum and the power extracted maximum through measuring wind speed and turbine speed [2.27]. This method has good performance with fast response and high efficiency, however, the anemometer presence makes the controller costly especially for small sized WTs and reduces overall system robustness [2.28].

With the Perturb and Observe Method, also known as the hill climbing search (HCS) technique, the strategy for optimizing power output is to take continuous samples of the rotor speed $\Delta\omega_r$ and observe whether at the present sample the output power is greater or less than the previous one [2.29, 2.30]. There are three main types of HCS techniques that differ according to the step size $\Delta\omega_r$ and can be classified as fixed step size, variable step size, and dual step size [2.31]. HCS control does not require any prior knowledge and is independent of the turbine, generator and the wind characteristics, and therefore is the most the robust and generic of all the MPPT strategies. However, oscillations around the MPP operating point at steady state give rise to the waste of some available energy [2.32]. Hence a trade-off between control efficiency and tracking speeds should be considered [2.33]. P&O techniques are most commonly used with small-scale WECSs.[2.34] [2.35].

2.7.2 Optimum Relationship Based techniques:

Look up table techniques (also known as ORB techniques) are the most commonly used MPPT approach where wind speed measurement is not required and the response to wind speed change is fast. Therefore, it can be used with applications of different power ratings using Power Signal Feedback (PSF), Optimal Torque Technique (OTT) or sensorless techniques employing rectifier dc-voltage versus dc-current relationship. These are all methods used for MPPT using the ORB technique.

The PSF uses a 2D look-up table where the optimal powers versus the rotating-speed characteristics are recorded either through offline experimental tests, simulations of wind turbine or datasheets. A block diagram of a PSF based WG control system is shown in figure 2.14 (a). The turbine speed is measured then the optimal output power is obtained from a turbine speed versus optimal power look-up table which is then compared with the actual load power [2.29].

In the OTT technique, MPPT control using the OT technique is the same as the PSF technique but it utilizes the quadratic optimal torque curve, as shown in figure 2.17 (b), instead of the optimal power curve [2.36]. The same performance is achieved with the same implementation complexity as the PSF method.

As for the sensorless technique, instead of relying on mechanical sensors to measure wind and generator speeds, parameters are calculated from available electrical parameters at the generator output terminals. For every wind speed, there is a value of dc-voltage V_{dc} that achieves the MPP from the turbine as seen from the maximum power curves formed in figure 2.14 (c). A 2D lookup table with the maximum output dc-power versus dc-voltage is constructed and the maximum power is derived from the turbine's output voltage, current and frequency, corresponding to the dc-voltage [2.37]. Generally, the accuracy of lookup table techniques is affected by aging of the mechanical sensors, electrical and thermal stresses, drifting system parameters and consequently power coefficient curve changes. Also, OT and PSF responses to rapid wind change are slower than the TSR method which relies on direct wind speed measurement via an anemometer. The sensorless ORB technique in [2.28], is implemented in the WECS under investigation.

From (2. 2), it is concluded that the power extracted from the wind is proportional to the cubic function of wind speed and is thus proportional to the cubic function of the generator speed (2.39) where

$$P_{W-max} \propto V^3 \propto \omega_{r-opt}^3 \tag{2.39}$$

For a PMSG with a constant flux, the phase back electromotive force E is a linear function of generator rotor speed [2.8]

$$E = K_e \varphi_f \omega_r \tag{2.40}$$

where φ_f is the generator flux and K_e is a coefficient depending on the number of turns per pole per phase as well as the winding factor of the machine and is considered constant.

The phase terminal voltage function for a non-salient PMSG is

$$V_{agen} = E - I_{gen}(R_a + j\omega_e L_a) \tag{2.41}$$

$$\omega_e = P\omega_r$$

where V_{agen} is the phase terminal voltage, I_{gen} is the phase current, R_a is the stator resistance, L_a is the stator inductance, ω_e is the electrical angular frequency, and P is the number of pole pairs. Due to the diode bridge rectifier, the rectifier ac-side voltage amplitude V_{a-amp} and the dc-side voltage V_{dc} are related as in (2.29) [2.24]

Accordingly, when the system is at MPP

$$V_{dc-opt} \propto \omega_{r-opt} \tag{2.42}$$

where V_{dc-opt} is the optimum rectified dc-voltage at a given wind speed. Then the maximum dc-side electric power at a given wind speed can be expressed as

$$P_{dc} = \eta P_{max} = V_{dc-opt} I_{dc-opt} \tag{2.43}$$

where η is the conversion efficiency from the generator to the dc-side and is assumed to be a fixed value and I_{dc-opt} is the optimum dc-side current.

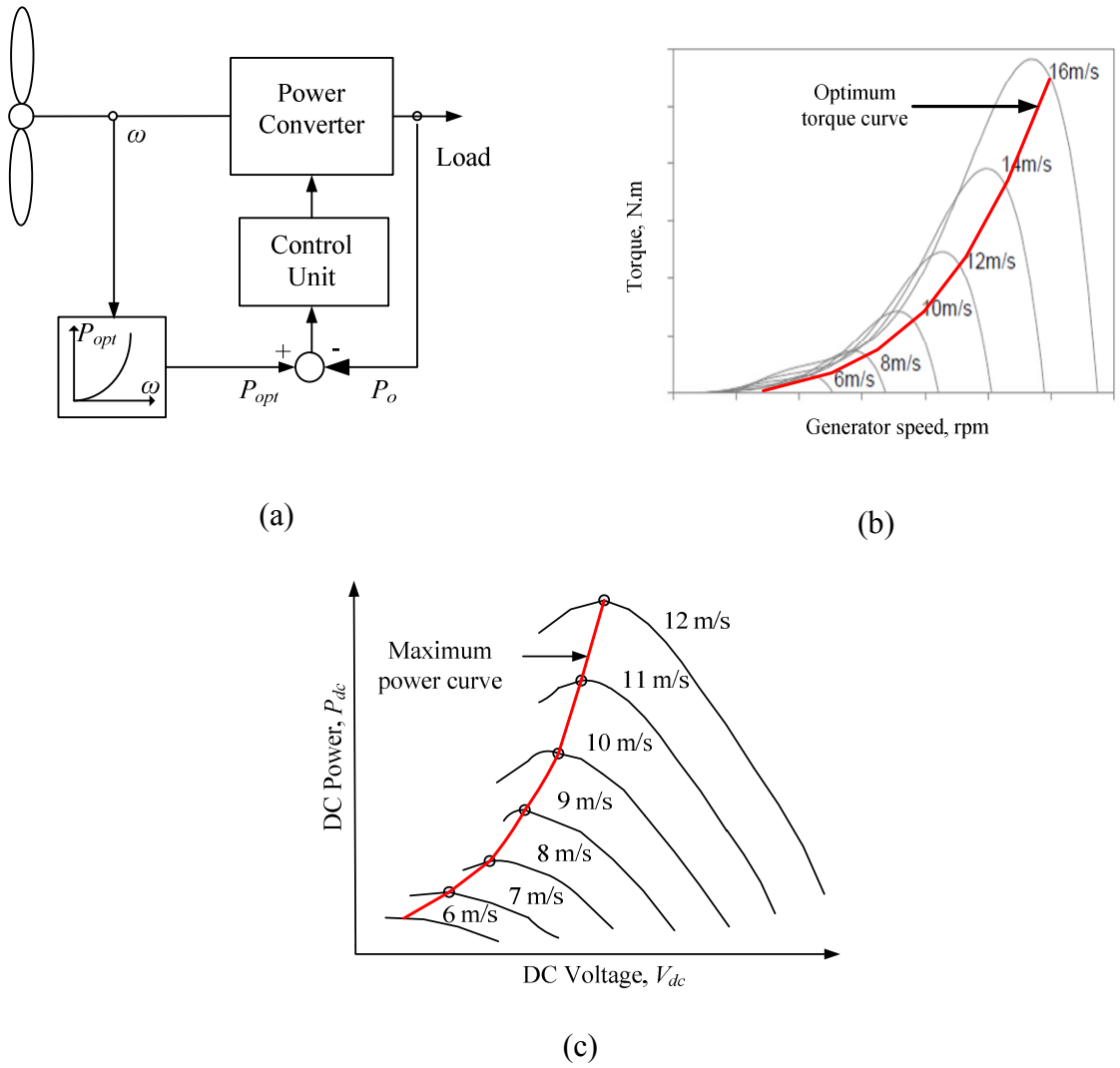

Figure 2.14. ORB techniques: (a) PSF (b) OTT and (c) sensorless.

Thus using the sensorless ORB technique, the optimum relationship between the rectifier output voltage V_{dc}, boost chopper and the dc-power P_{dc} is recorded for different wind

speeds. The I_{dc}^{*} values corresponding to maximum power are extracted from the V_{dc} versus P_{dc} relationship and recorded in a 2D lookup table according to the corresponding V_{dc} as seen in figure 2.18.

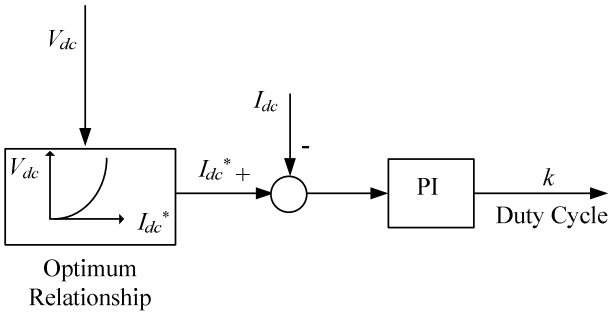

Figure 2. 15. System control block diagram for sensorless ORB.

As mentioned previously, sensorless techniques have an advantage over the other look up table techniques as they take into account the converter and generator efficiency while obtaining the optimal characteristics. However, parameter variation due to aging will reduce the efficiency of this technique in MPP extraction.

2.7.3 GSC Control

For grid interconnection, the WECS has to satisfy the grid requirements for proper interconnection. GSC has to fulfil following major tasks [2.38]:

- Grid synchronization.
- Control of dc-link voltage;
- Control of active power generated to the grid;
- Control of reactive power transfer between the PMSG and the grid; and
- Ensure high quality of the injected power.

Different GSC control strategies have been introduced in [2.39, 2.40] and can be classified depending on the reference frame used in the control. There are three vector control techniques; in the synchronous reference frame, stationary frame and natural reference frame.

dq synchronous reference frame control, also known as voltage oriented control (VOC) uses a reference frame transformation, from $abc \rightarrow dq$ to transform the grid current and

voltage waveforms into a reference frame that rotates synchronously with the grid voltage using the Park's and Clark's transformations presented in (2.6) and (2.7). Transforming the ac quantities into dc values leads to easier filtering and control.

In stationary frame control, the grid currents are transformed using Clark's transformation from $abc \rightarrow \alpha\beta$ transform where the control variables are sinusoidal. It is not advisable to use PI controllers with stationary frame control due to its limited capabilities in eliminating the steady-state error when controlling sinusoidal waveforms. Proportional resonant (PR) control has been used with stationary frame control and has gained popularity in grid connected system current control [2.41].

In natural frame control, components are controlled in the *abc* frame. Nonlinear controllers are usually employed with natural frame control, such as hysteresis or dead beat control are preferable due to their high dynamic capability [2.42, 2.43].

Figure 2.19 shows the block diagram for GSC using synchronous reference frame control which is used in this thesis. GSC control is responsible for controlling the dc-link voltage $V_{dc-link}$ and for controlling the grid currents i_{grid} in synchronism with the grid voltage v_{grid}. The control algorithm of the PWM VSI operating with GSC is explained in the following sections.

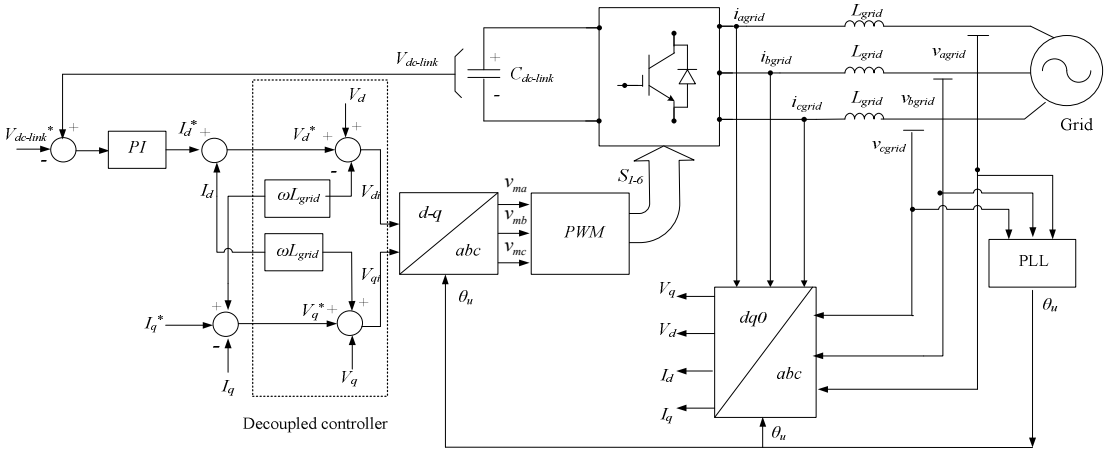

Figure 2.16. General structure for stationary reference frame control strategy.

i- Phase Locked Loop (PLL) and Grid Synchronization:

Phase-lock loops (PLLs) have been extensively used in power system and power electronics applications for the generation of thyristor firing angles, active filters and distributed generation systems [2.23]. In grid connected power converters, the phase angle

of the utility-voltage vector θ_u, is the basic information for most grid-connected power conditioning equipment. This information may be used to synchronize the turning on/off of power devices, to calculate and control the flow of active/reactive power or to transform the feedback variables to a reference frame suitable for control purposes [2.44].

The conventional three-phase PLL topology is illustrated in the block diagram of figure 2.17 (a). The instantaneous grid voltage phase-angle θ_u is detected by synchronizing the PLL rotating reference frame to the utility-voltage vector. The PLL model implemented in the dq synchronous reference frame requires the Park transform. The transformation from the $abc - dq0$ frame is applied to the PCC voltage as follows:

$$\begin{bmatrix} v_d \\ v_q \end{bmatrix} = T_{dq-\alpha\beta} C_{abc-\alpha\beta} \begin{bmatrix} v_a \\ v_b \\ v_c \end{bmatrix} \tag{2.44}$$

Assuming three phase balanced voltages and given that the angle of the reference frame exactly matches that of the grid voltage:

$$v_d = |v_{dq}| = |v_{\alpha\beta}| = \sqrt{v_\alpha^2 + v_\beta^2} \tag{2.45}$$

where v_a, v_b, v_c are the instantaneous three, phase-to-neutral grid voltages, and v_α, v_β are the $\alpha\beta$ frame voltages as shown in figure 2.17.

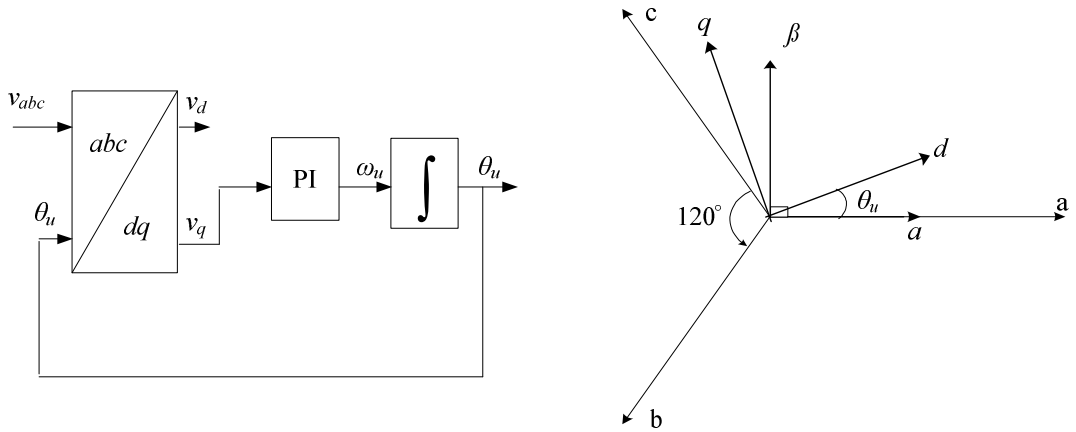

(a) (b)

Figure 2.17. PLL (a) block diagram and (b) coordinate system.

The magnitude of the controlled variable v_q determines the phase difference between the grid voltage and the PLL angle. Thus a PI controller sets the q-axis reference voltage to zero to lock to the utility-voltage vector phase angle. For a balanced supply, the controller

output is the supply voltage angular frequency ω_u which, after integration, gives the supply voltage phase θ_u. This angle is fed back as the transformation angle to perform the $abc - dq0$ transformation of the PCC voltage. This conventional technique is simple but can be affected in the presence of disturbances such as phase unbalance, harmonics, and offset [2.45]. However, the parameters of the PI controller can be adjusted to minimize those effects at the expense of slower dynamics. Hence, this structure is widely used and, specifically, it is also used in the present thesis.

ii- DC- link voltage and Grid Current Control:

As shown in figure 2.16, the PWM VSI control employs two control loops; the inner loop is for the grid current, i_{grid} control while the outer loop is for the dc-link voltage $V_{dc-link}$ control. Decoupling the grid currents in the dq-axes frames provides means for controlling the active grid current at unity power factor by setting the q-axis current to zero. The dc-link voltage controller is designed for balancing the power flow in the system thus usually the controller has slow dynamics.

The active power of the system delivered to the grid is calculated from:

$$P_{grid} = 3\, V_{grid}\, I_{grid}\, cos(\varphi_{grid}) \tag{2. 46}$$

where P_{grid} is the active power injected into the grid and φ_{grid} is the grid power factor angle, defined by:

$$\varphi_{grid} = \theta_u - \theta_{I_{grid}} \tag{2. 47}$$

where $\theta_{I_{grid}}$ is the grid current angle. The grid power factor can be unity, leading, or lagging, as shown in figure 2.18

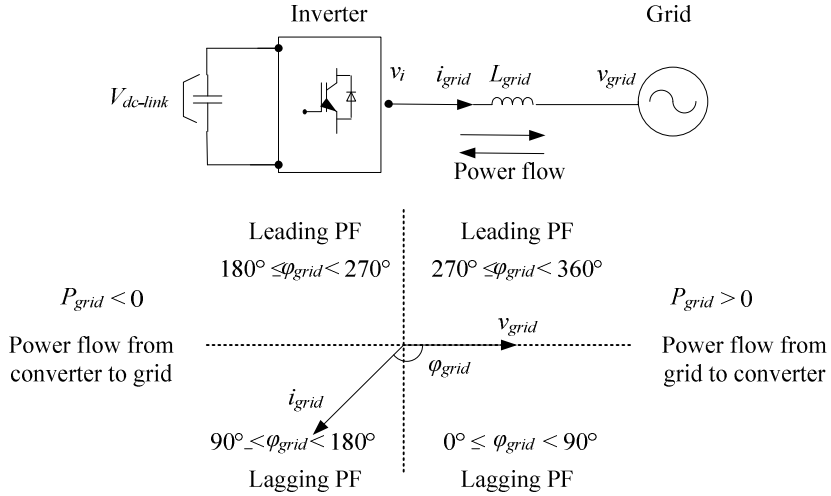

Figure 2.18. Simplified diagram and phasor diagram and PF [2.46].

Using the VOC transformations, the instantaneous power in a three phase system is:

$$P_{grid} = v_{agrid} i_{agrid} + v_{bgrid} i_{bgrid} + v_{cgrid} i_{cgrid} \tag{2.48}$$

Using the *dq* transformations, the *d*-axis of the synchronous frame is aligned with the grid voltage vector, therefore the *d*-axis grid voltage, v_d is equal to its magnitude, where:

$$v_d = v_{grid} \tag{2.49}$$

and the resultant *q*-axis voltage, v_q is then equal to zero:

$$v_q = \sqrt{v_{grid}^2 - v_d^2} = 0 \tag{2.50}$$

from which the active and reactive powers of the system can be calculated by:

$$P_{grid} = \frac{3}{2}\left(v_d i_d + v_q i_q\right) = \frac{3}{2} v_d i_d \tag{2.51}$$

$$Q_{grid} = \frac{3}{2}\left(v_q i_d - v_d i_q\right) = -\frac{3}{2} v_d i_q \tag{2.52}$$

where Q_{grid} is the reactive power injected into the grid.

The *q*-axis current reference, i_q^* can then be obtained from:

$$i_q^* = \frac{Q_{grid}^*}{-1.5\, v_d} \tag{2.53}$$

where Q_{grid}^* is the reference for the reactive power, which can be set to zero for unity power factor operation, a negative value for leading power factor operation, or a positive value for lagging power factor operation.

The *d*-axis current reference i_d^*, which represents the system active power, is generated by the PI controller for dc-voltage control as shown in figure 2.19. When the inverter operates in steady state, the inverter dc-voltage $V_{dc-link}$ is kept constant at a value set by its reference voltage $V_{dc-link}^*$. The PI controller generates the reference current, i_d^* according to the operating conditions. Neglecting inverter losses, the active power on the ac-side of the inverter is equal to the dc-side power, that is,

$$P_{grid} = \frac{3}{2} v_d i_d = v_{dc-link}\ I_D \tag{2.54}$$

When the active power is delivered from the grid to the dc-circuit, the inverter operates in a rectifying mode ($P_{grid} > 0$), whereas when the power is transferred from the dc-circuit to the grid ($P_{grid} < 0$), the inverter is in an inverting mode.

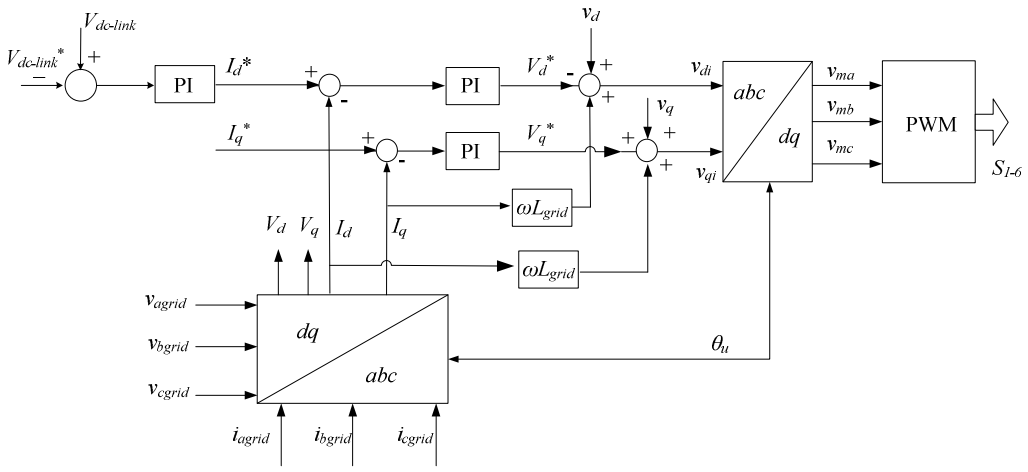

Figure 2.19. Control diagram of GSC.

Cross-coupling terms and voltage feed-forward are added to improve system response:

$$v_{di} = v_d - v_d^* + \omega_u L_{grid} i_q \tag{2.55}$$

$$v_{qi} = v_q + v_q^* + \omega_u L_{grid} i_d \tag{2. 56}$$

where v_{di} and v_{qi} are the output of the decoupled controller in the dq-axes respectively. Assuming PI controllers are used, the terms v_d^* and v_q^* can be expressed as:

$$v_d^* = \left(k_1 + \frac{k_2}{s}\right)(i_d^* - i_d) \tag{2.57}$$

$$v_q^* = \left(k_1 + \frac{k_2}{s}\right)(i_q^* - i_q) \tag{2.58}$$

where $\left(k_1 + \frac{k_2}{s}\right)$ is the transfer function of the PI controller.

2.8 Summary

Modelling of PMSG based WECS is essential to predict the system behaviour and response for grid interconnection during normal and abnormal conditions. In this chapter, a model for a PMSG based WECS has been presented which included the wind turbine model, PMSG dynamic equations as well as state-of-art power converters. The chapter also highlighted the important control aspects for WT which include wind maximum power extraction as well as grid active and reactive power control and dc-link voltage control. Special focus on an ORB technique for MP tracking and GSC control using synchronous frame control have been explained as they will be incorporated in the following chapters. The next chapter will investigate system behaviour and compliance with utility

interconnection requirements to meet national grid codes for normal operation as well as with the presence of grid voltage disturbance.

References

[2.1] F. Blaabjerg and M. Ke, 'Future on Power Electronics for Wind Turbine Systems', IEEE Journal of Emerging and Selected Topics in Power Electronics, Vol. 1, 2013. pp. 139-152.

[2.2] M. Chinchilla, S. Arnaltes, and J. C. Burgos, 'Control of Permanent-Magnet Generators Applied to Variable-Speed Wind-Energy Systems Connected to the Grid', IEEE Transactions on Energy Conversion, Vol. 21, 2006. pp. 130-135.

[2.3] M. R. Patel,'Wind and Solar Power Systems', Taylor & Francis, 1999.

[2.4] S. Heier,'Grid Integration of Wind Energy Conversion Systems', Wiley, 1998.

[2.5] N. P. W. Strachan and D. Jovcic, 'Dynamic Modelling, Simulation and Analysis of an Offshore Variable-Speed Directly-Driven Permanent-Magnet Wind Energy Conversion and Storage System (WECSS)', OCEANS, Oct 2007. pp. 1-6.

[2.6] R. H. Park, 'Two-Reaction Theory of Synchronous Machines Generalized Method of Analysis- Part I', Transactions of the American Institute of Electrical Engineers, Vol. 48, 1929. pp. 716-727.

[2.7] N. N. Hancock,'Matrix Analysis of Electrical Machinery', Pergamon Press, 1964.

[2.8] A. E. Fitzgerald, C. Kingsley, and S. D. Umans,'Electric Machinery', McGraw-Hill, 2003.

[2.9] K. Nishida, T. Ahmed, and M. Nakaoka, 'Development of Grid-Connected Wind Energy System Employing Interior PM Synchronous Generator and Multi-Pulse Rectifier', IEEE Energy Conversion Congress and Exposition (ECCE), Sep 2010. pp. 3374-3381.

[2.10] J. M. Carrasco*, et al.*, 'Power-Electronic Systems for the Grid Integration of Renewable Energy Sources: A Survey', IEEE Transactions on Industrial Electronics, Vol. 53, 2006. pp. 1002-1016.

[2.11] A. M. El-Tamaly*, et al.*, 'Low cost PWM Converter for Utility Interface of Variable Speed Wind Turbine Generators', 14th Annual Applied Power Electronics Conference and Exposition, (APEC) Sep 1999. pp. 889-895.

[2.12] Y. Y. Xia*, et al.*, 'Torque Ripple Analysis and Reduction for Wind Energy Conversion Systems using Uncontrolled Rectifier and Boost Converter', IET Renewable Power Generation, Vol. 5, 2011. pp. 377-386.

[2.13] Z. Chen, J. M. Guerrero, and F. Blaabjerg, 'A Review of the State of the Art of Power Electronics for Wind Turbines', IEEE Transactions on Power Electronics, Vol. 24, August 2009. pp. 1859-1875.

[2.14] J. Rodriguez, *et al.*, 'Multilevel Voltage-Source-Converter Topologies for Industrial Medium-Voltage Drives', IEEE Transactions on Industrial Electronics, Vol. 54, 2007. pp. 2930-2945.

[2.15] B. W. Williams,'Principles and Elements of Power Electronics : Devices, Drivers, Applications, and Passive Components', MacMillan, 2005.

[2.16] Y. Y. Xia, *et al.*, 'Torque ripple analysis and reduction for wind energy conversion systems using uncontrolled rectifier and boost converter', Renewable Power Generation, IET, Vol. 5, 2011. pp. 377-386.

[2.17] L. Dessaint, H. Nakra, and D. Mukhedkar, 'Propagation and Elimination of Torque Ripple in a Wind Energy Conversion System', IEEE Transactions on Energy Conversion, Vol. EC-1, 1986. pp. 104-112.

[2.18] J. W. Kolar and T. Friedli, 'The Essence of Three-Phase PFC Rectifier Systems; Part I', IEEE Transactions on Power Electronics, Vol. 28, 2013. pp. 176-198.

[2.19] W. Bin, *et al.*, 'Current-Source Converter and Cycloconverter Topologies for Industrial Medium-Voltage Drives', IEEE Transactions on Industrial Electronics, Vol. 55, 2008. pp. 2786-2797.

[2.20] N. Mohan and T. M. Undeland,'Power Electronics: Converters, Applications, and Design', Wiley India, 2007.

[2.21] M. Rashid,'Power Electronics Handbook', Elsevier Science, 2011.

[2.22] H. Delesposte Paulino, P. J. Mello Menegaz, and D. S. Lyrio Simonetti, 'A Review of the Main Inverter Topologies Applied on the Integration of Renewable Energy Resources to the Grid', Power Electronics Conference (COBEP), Sep 2011. pp. 963-969.

[2.23] B. Wu,'High-Power Converters and AC Drives', Wiley, 2006.

[2.24] M. H. Rashid,'Power Electronics: Circuits, Devices, and Applications', Pearson Education, 2004.

[2.25] N. Mohan,'Electric Power Systems: A First Course', Wiley, 2012.

[2.26] K. H. Ahmed, S. J. Finney, and B. W. Williams, 'Passive Filter Design for Three-Phase Inverter Interfacing in Distributed Generation', Compatibility in Power Electronics, (CPE '07), 2007. pp. 1-9.

[2.27] D. Rekioua,'Wind Power Electric Systems Modeling, Simulation and Control', Springer, 2012.

[2.28] Y. Xia, K. H. Ahmed, and B. W. Williams, 'A New Maximum Power Point Tracking Technique for Permanent Magnet Synchronous Generator Based Wind Energy Conversion System', IEEE Transactions on Power Electronics, Vol. 26, 2011. pp. 3609-3620.

[2.29] E. Koutroulis and K. Kalaitzakis, 'Design of a Maximum Power Tracking System for Wind-Energy-Conversion Applications', IEEE Transactions on Industrial Electronics, Vol. 53, 2006. pp. 486-494.

[2.30] I. K. Buehring and L. L. Freris, 'Control Policies for Wind-Energy Conversion Systems', IEE Proceedings Generation, Transmission and Distribution, Vol. 128, 1981. pp. 253-261.

[2.31] K. Raza*, et al.*, 'A Novel Algorithm for Fast and Efficient Maximum Power Point Tracking of Wind Energy Conversion Systems', 18th International Conference on Electrical Machines, 2008. ICEM 2008. , 2008. pp. 1-6.

[2.32] N. Femia*, et al.*, 'Optimization of Perturb and Observe Maximum Power Point Tracking Method', IEEE Transactions on Power Electronics, Vol. 20, 2005. pp. 963-973.

[2.33] S. M. Raza Kazmi*, et al.*, 'A Novel Algorithm for Fast and Efficient Speed-Sensorless Maximum Power Point Tracking in Wind Energy Conversion Systems', IEEE Transactions on Industrial Electronics, Vol. 58, 2011. pp. 29-36.

[2.34] W. Wenkai*, et al.*, 'DSP-based Multiple Peak Power Tracking for Expandable Power System', 18th Annual IEEE Applied Power Electronics Conference and Exposition, (APEC) 2003. pp. 525-530.

[2.35] J. M. Mauricio*, et al.*, 'An Adaptive Nonlinear Controller for DFIM-Based Wind Energy Conversion Systems', IEEE Transactions on Energy Conversion, Vol. 23, 2008. pp. 1025-1035.

[2.36] S. Morimoto, *et al.*, 'Sensorless Output Maximization Control for Variable-Speed Wind Generation System Using IPMSG', IEEE Transaction on Industry Applications, Vol. 41, January 2005. pp. 60-67.

[2.37] M. Abdel-Salam, A. Ahmed, and M. Abdel-Sater, 'Maximum Power Point Tracking for Variable Speed Grid Connected Small Wind Turbine', IEEE International Energy Conference and Exhibition, (EnergyCon), 2010. pp. 600-605.

[2.38] F. Blaabjerg, *et al.*, 'Overview of Control and Grid Synchronization for Distributed Power Generation Systems', IEEE Transactions on Industrial Electronics, Vol. 53, 2006. pp. 1398-1409.

[2.39] A. Hamadi, *et al.*, 'A New Maximum Power Point Tracking with Indirect Current Control for a three-phase Grid-Connected Inverter used in PMSG-based Wind Power Generation Systems', 38th Annual Conference on IEEE Industrial Electronics Society (IECON), 2012. pp. 916-923.

[2.40] L. Shuhui, *et al.*, 'Optimal and Direct-Current Vector Control of Direct-Driven PMSG Wind Turbines', IEEE Transactions on Power Electronics, Vol. 27, 2012. pp. 2325-2337.

[2.41] N. Thanh-Hai and L. Dong-Choon, 'A Novel Current Control Scheme of Grid Converters for Small PMSG Wind Turbines under Grid Voltage Distortion', IEEE Power Electronics and Machines in Wind Applications (PEMWA), 2012. pp. 1-6.

[2.42] A. I. Maswood, N. Sarangan, and A. Venkataraman, 'Comparison of Current Control Methods for a Near Unity Power Factor Converter in a Wind Generator System Feeding Stand-alone loads', IEEE Industry Applications Society Annual Meeting (IAS) 2011. pp. 1-8.

[2.43] T. Kawabata, T. Miyashita, and Y. Yamamoto, 'Dead Beat Control of three phase PWM Inverter', IEEE Transactions on Power Electronics, Vol. 5, 1990. pp. 21-28.

[2.44] A. M. Salamah, S. J. Finney, and B. W. Williams, 'Three-phase Phase-Lock Loop for Distorted Utilities', IET Electric Power Applications, Vol. 1, 2007. pp. 937-945.

[2.45] S. K. Chung, 'Phase-Locked Loop for Grid-Connected three-phase Power Conversion Systems', IEE Proceedings Electric Power Applications, Vol. 147, 2000. pp. 213-219.

[2.46] B. Wu, *et al.*,'Power Conversion and Control of Wind Energy Systems', Wiley, 2011.

CHAPTER THREE

Performance Investigation of a 1.5 MW PMSG based WECS

The penetration of wind power into the power system continues to increase, which implies large wind farms are changing from being simple energy sources to having power plant status with grid support characteristics. One major challenge is the connection and optimized integration of large wind farms into electrical grids. With increased wind power capacity, transmission system operators (TSOs) have become concerned about the impact of high levels of wind power generation on power systems. To handle large-scale integration of wind power, TSOs have issued grid codes and grid requirements for wind turbine connection and operation [3.1].

This chapter studies the performance of a 1.5 MW PMSG WECS and its behaviour for proper grid interconnection using simulation analysis. The study includes tests for continuous grid operation such as active and reactive power step changes, frequency excursion and grid phase jumps; as well as abnormal grid operation for severe symmetrical grid voltage dips.

3.1 System description

Modelling for a PMSG based WECS has been reported in the previous chapter which included the mathematical representation of the wind turbine, PMSG, power converters, and the electrical grid. The control methodologies for the power converters, responsible for optimal power extraction from the wind as well as grid interconnection, were presented for PWM-VSI topologies. Finally, a block diagram of a case study for a 1.5 MW PMSG WECS was introduced, as shown in figure 3.1 and a MATLAB model has been constructed to investigate system performance.

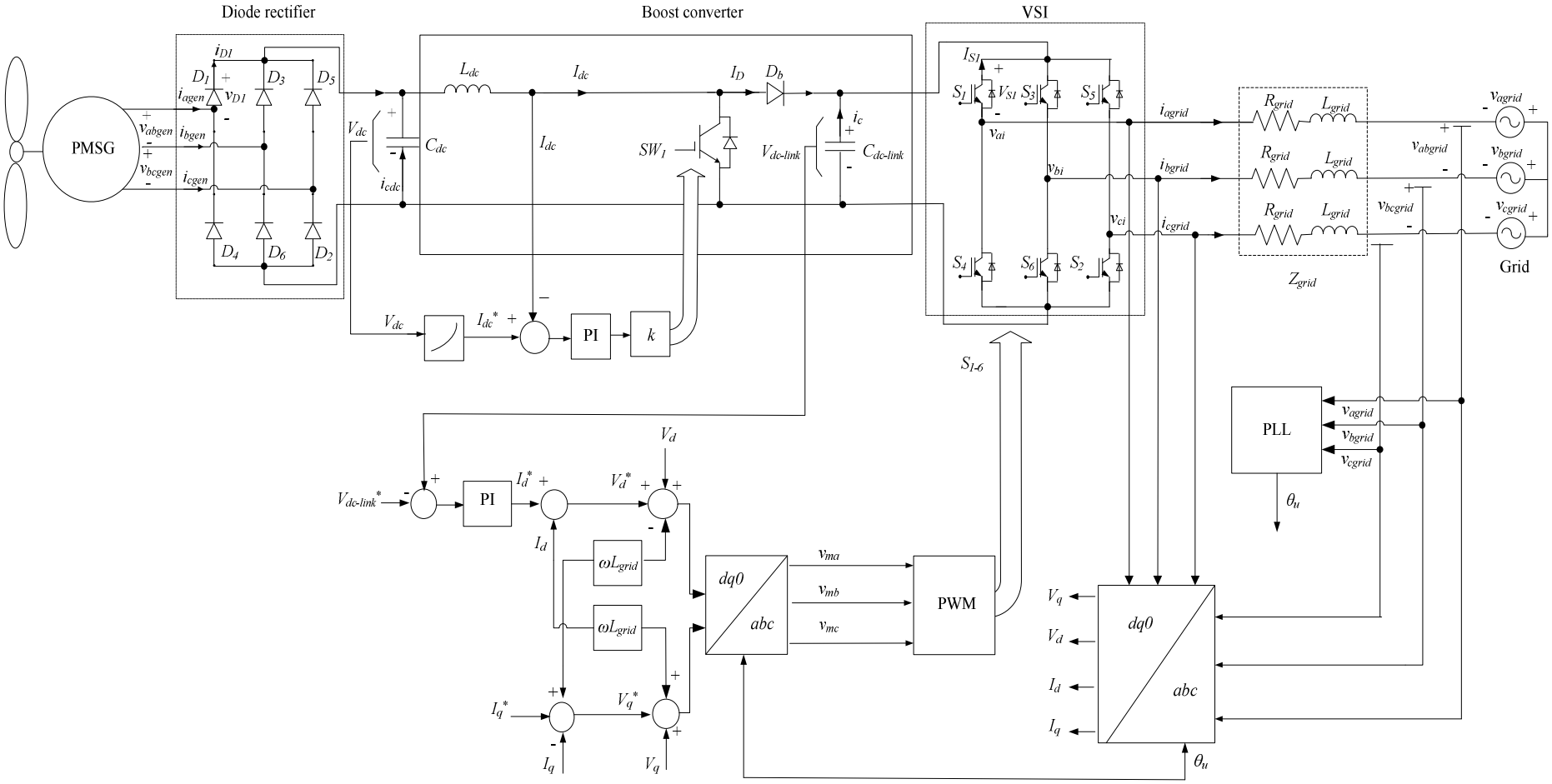

Figure 3.1. PMSG based WECS.

For the system presented in figure 3.1, the parameters used for simulation purposes are defined in table 3.1. A 1.5 MW wind turbine is selected with parameters listed in Appendix (A). The turbine curves are shown in figures 2.2 and 2.3. For simulation purposes, the wind turbine is driven at a constant wind speed, V, of 12 m/s, at a fixed blade pitch angle, $\beta = 0$ where the output power corresponds to approximately 800 kW. The turbine drives a 1.5 MVA, 80 pole, 690 V, 11.5 Hz gearless PMSG with parameters listed in Appendix (B-1) [3.2]. The mechanical wind turbine drives the PMSG at its fixed rated speed, ω_r, of 1.8 rad/s, and produces a balanced 3-phase, line-to-line voltage, v_{abcgen} of 690 V at a frequency, f_{gen} of 11.5 Hz at no load.

Table 3.1. Rated WECS parameters.

Parameter	Variable name	Value
Turbine mechanical output power (MVA)	P_w	1.5
Rated wind speed (m/s)	V	13
Generator power (MW)	P_{gen}	1.5
Generator voltage (V)	v_{gen}	690
Generator frequency (Hz)	f_{gen}	11.5
Pole pairs of PMSG	P	40
Rectifier output capacitor (μF)	C_{dc}	5000
Boost chopper switching frequency (Hz)	f_c	5000
Boost chopper inductor (mH)	L_{dc}	10
Boost chopper reference current (A)	I_{dc}^*	800
DC-link capacitor (μF)	$C_{dc-link}$	6000
DC-link voltage (V)	$V_{dc-link}^*$	5500
PWM-VSI switching frequency (Hz)	f_c	5000
Grid voltage (V)	v_{grid}	480
Grid frequency (Hz)	f_{grid}	50
Grid resistance (Ω)	R_{grid}	0.05
Grid inductance (mH)	L_{grid}	10

For a given wind speed of 12 m/s and generator speed of 1.8 rad/s, the PMSG peak line current, $\widehat{\imath_{abcgen}}$ is 800 A and the peak generator line-to-line voltage, $\widehat{v_{gen}}$ becomes 600 V, thus the output generator power, P_{gen} corresponds to approximately 877 kW. The operating conditions of the WECS were selected as to establish a stable operating condition where the system is successfully grid connected for further LVRT study.

The generator terminals are connected to a three phase diode rectifier unit then a boost converter circuit. The diode rectifier converts the variable generator ac-voltage, v_{gen} to a

dc-voltage which is then increased to $V_{dc-link}$ by the boost converter with a switching frequency, f_c of 5 kHz. It is important that the generator voltage at low wind speeds is boosted to a sufficiently high level for the proper operation of the grid tied inverter, which ensures delivery of the maximum captured power to the grid over the full wind speed range. For the extraction of i_{gen}, the boost inductor current reference, I_{dc}^{*} is set to 800A.

The two-level PWM inverter operates at a carrier frequency of 5 kHz and controls $V_{dc-link}$ and the grid-side active and reactive powers P_{gen} and Q_{gen} respectively. The GSC is required to export the generator power, to the utility grid whose line-to-line voltage, v_{grid} is 480 V at a frequency f_{grid} of 50 Hz. Due to the large value of selected grid impedance, which is a very common practice in low voltage distribution systems, the dc-link voltage $V_{dc-link}$ is regulated at a high reference value of 5500 V to ensure proper operation of the GSC, as well as the injection of 800A peak grid current i_{gen} at unity power factor. Accordingly, taking into account the grid and power converters losses, the power delivered to the grid is approximately 765 kW.

3.2 Performance of PMSG WECS and Grid Interconnection

Technical regulations for wind farms (WFs) connected to a power system vary considerably from country to country. The differences in requirements depend on the wind power penetration level, on the robustness of the power network, and local traditional practices [3.3]. Grid code technical requirements can be divided into regulations for continuous operation and special requirements under network disturbances [3.4]. The most significant factors that need to be set for continuous operation are voltage and frequency operating ranges, active and reactive power regulation, and power-frequency response. As for operation during network disturbances, fault ride through capability and reactive power response are regarded as the most important aspects. In the following sections, the 1.5 MW WECS performance is investigated to meet continuous operation requirements as specified by UK grid codes. Subsequent chapters will focus more on system capability for fault ride through.

3.2.1 Active Power Step

The purpose of this section is to examine the PMSG WECS capabilities for extracting different power when the wind speed changes. First the WT MPPT algorithm using the ORB technique described in Chapter 2 has been utilized for optimal extraction of wind

power at any given wind speed. The WT performance has been determined offline where the data for optimal dc-power, P_{dc} versus dc-voltage, V_{dc} is recorded at different wind speeds, V, where P_{dc} corresponds to the output power from the diode rectifier unit and V_{dc} is the rectified PMSG voltage. Figure 3.2 shows the P_{dc} versus V_{dc} relation from which a V_{dc} versus I_{dc}^{*} relation is determined, where I_{dc}^{*} is the boost chopper inductor reference current for power extraction. Since MPPT extraction is not the main focus of this thesis, the data for V_{dc} and I_{dc}^{*} might lack some degree of accuracy as the main objective of the work is studying the LVRT behaviour on the simulated wind turbine system. For simulation purpose the generator speed is assumed to be 1 pu.

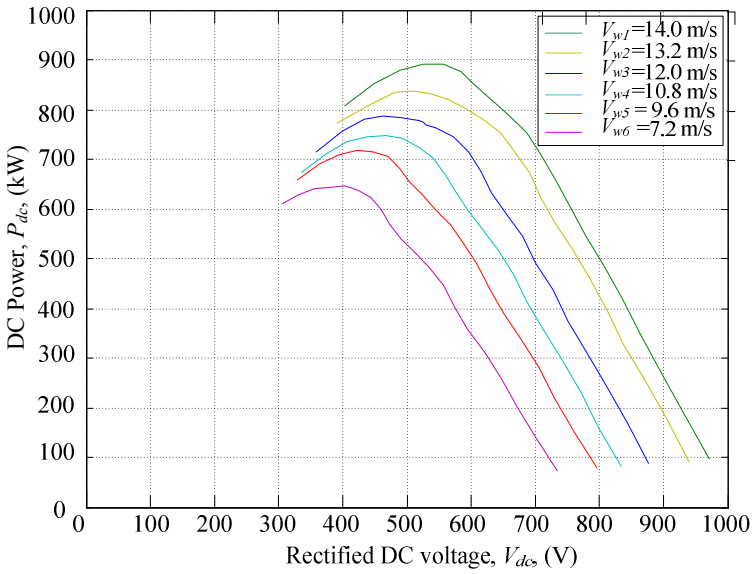

Figure 3.2. Power versus dc voltage curves for different wind speeds.

As explained earlier, since $\widehat{v_{gen}}$ is 600 V, the voltage behind the rectifier V_{dc} will be approximately 500 V. As shown in figure 2.3 in Chapter 2, if the wind speed is 12 m/s and the generator speed is at 1 per-unit of the base generator speed, the estimated turbine output power equals 0.65 pu of its nominal output power. At this power level and accounting for PMSG efficiency the output electrical power from the PMSG, P_{gen} will be approximately 877 kW. Thus the output dc power, P_{dc} after the rectifier stage will become 790 kW while the grid injected power P_{grid} will be 765 kW. The same assumption can be made when the wind turbine is driven at a wind speed of 10.8 m/s where the generator speed is maintained at 1 pu, the estimated output turbine power will be 0.5 pu of the

turbine nominal mechanical power. At 10.8 m/s, P_{gen} will be 675 kW and P_{grid} will be approximately 500 kW.

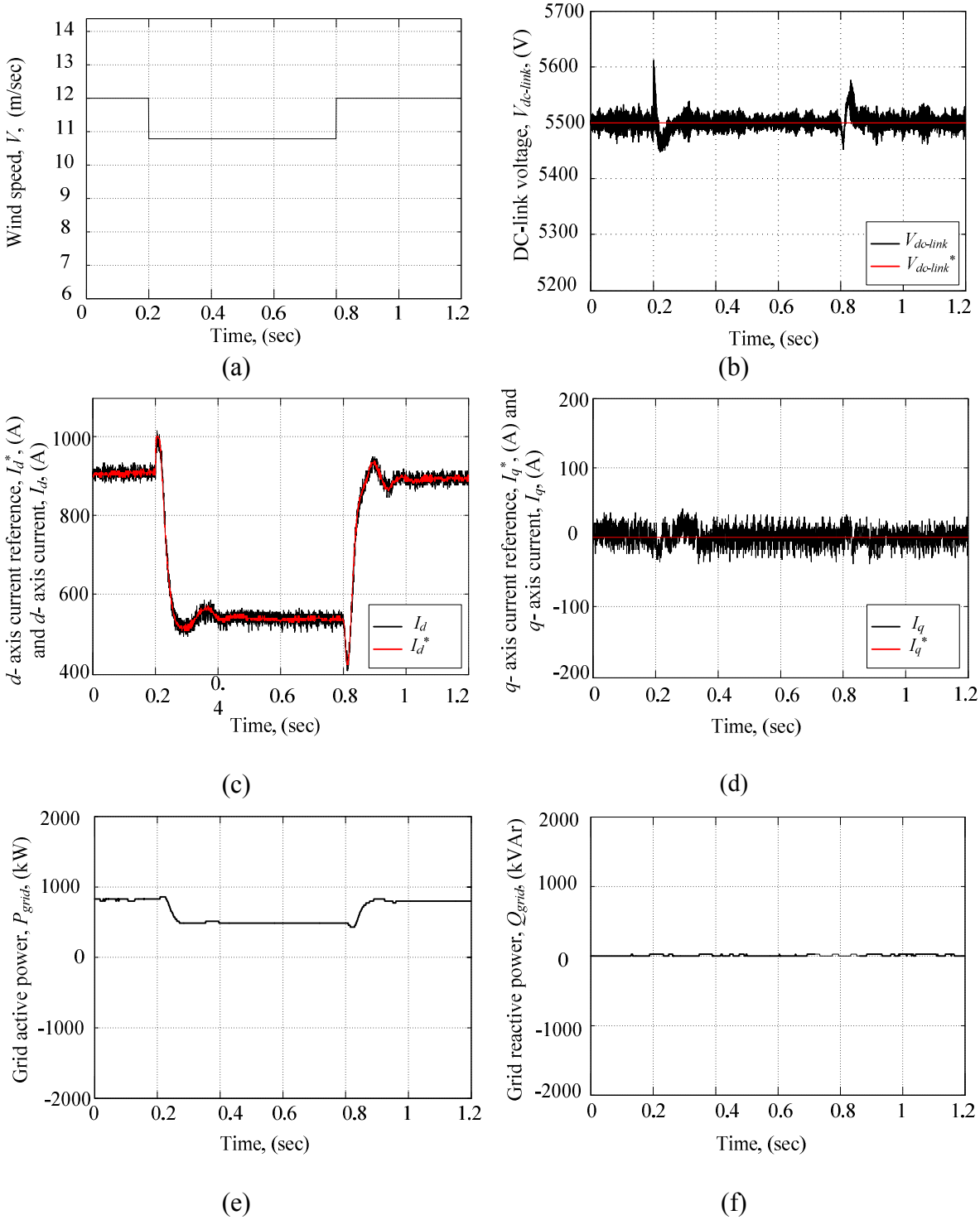

Figure 3.3. System Performance due to sudden wind change: (a) wind speed, V, (b) dc-link voltage, $V_{dc\text{-}link}$, (c) d-axis current reference and actual, I_d^* and I_d, (d) q-axis current reference and actual, I_q^* and I_q, (e) active grid power, P_{grid}, and (f) reactive grid power, Q_{grid}.

The simulation has been carried out on different wind speed step changes as shown in figure 3.3 (a) to (f), with the reactive power reference set to zero. The wind speed, V, has been changed from 12 m/s to 10.8 m/s between 0.2 and 0.8 s, then to 12 m/s as illustrated in figure 3.3(a). When the wind speed changes suddenly, the rectifier output voltage, V_{dc} changes accordingly, as explained in Chapter 2 and consequently, the boost converter current command, I_{dc}^{*} is obtained via the lookup table constructed for all wind speeds to extract the available power from the wind. Due to decreased wind speed from 0.2 to 0.8 s, the grid active current command, I_{d}^{*} decreases in an attempt to balance the generated and grid injected power to the grid as shown in figure 3.3 (c). Since the power extracted from the wind decreases, the power exported to the grid, P_{grid} will be reduced from 790 kW to 675 kW as shown in part (d). DC-link voltage, $V_{dc-link}$ is maintained constant even during sudden reduction of wind speed with slight transients exhibited as shown in part (b). The q-axis grid current, I_q and reactive power transferred to grid, Q_{grid} remain unaffected as indicated in parts (d) and (f) respectively. The fast action of the grid current controllers simulated in part (c) is quite fast as the wind turbine inertia has been neglected and the mechanical transient is still not over.

3.2.2 Reactive Power Step

Like conventional power plant, wind turbines are required to provide reactive power to the grid. Reactive power command changes either due to sudden load changes or due to special requirements by grid operators. Also, reactive power regulation capability may be exploited for voltage control at the wind farm connection point to the system, or at a more distant node [3.5]. According to the UK grid code, the following conditions apply with all plant in operation as defined in figure 3.4.

- The reactive power limits defined at rated MW at lagging power factor are valid at all active power output levels above 20% of the rated MW output.
- The reactive power limits defined at rated MW with leading power factor are valid at all active power output levels above 50% of the rated MW output.
- The reactive power limits reduce linearly below 50% of active power output unless the requirement to maintain the reactive power limits defined at rated MW at leading power factor down to 20% active power output is specified in the bilateral agreement [3.6].

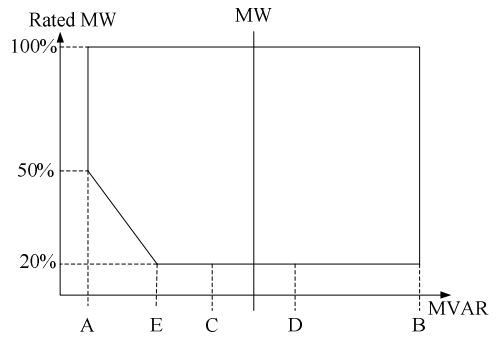

Point	Power factor/ Reactive power
A	0.95 lead at rated MW
B	0.95 lag at rated MW
C	Q = -5% of rated MW
D	Q = 5% of rated MW
E	Q = -12% of rated MW

Figure 3.4. Typical power factor variation range requirements in relation to voltage. [3.7]

The performance of the 1.5 MW PMSG WECS is demonstrated in figure 3.5 (a) to (h) for a sudden change of ±20% in the grid reactive power command, Q_{grid} based on the electrical active power. The grid reactive current controller, which is responsible for controlling the reactive power injected into the grid, has been altered for unity power factor, lagging and leading operation. As indicated in figure 3.5 (b), the grid reactive power command is set to unity during the first 0.2 s and from 0.4 to 0.8 s. Lagging power factor is required during the period 0.2 s until 0.4 s, while leading power factor is maintained from 0.8 to 1 s. Accordingly, the grid reactive current control loop acts to inject the required Q_{grid} and at the same time keeps the active power constant as defined by the grid code in figure 3.4. The d and q-axis grid currents are shown in parts (c) and (d) respectively, as well as the dc-link voltage, $V_{dc-link}$ response in part (e). The effect of changing the reactive power command on the PCC voltage is illustrated in part (f).

3.2.3 Frequency Excursion

System frequency is a continuously changing variable that is determined and controlled by real time balance between system demand and total generation. If demand is greater than generation, the frequency falls while if generation is greater than demand, the frequency rises. Generating equipment in an electric system is designed to operate within strict frequency margins in abnormal or exceptional circumstances where the developed control loop within the wind turbine is like the conventional generators' speed governor which automatically adjusts power output in response to a frequency drop [3.8]. However, due to wind variability, speed-droop control has its own limitation and the effectiveness of the proposed control scheme is dependent on the operating stability and available generating margin [3.9].

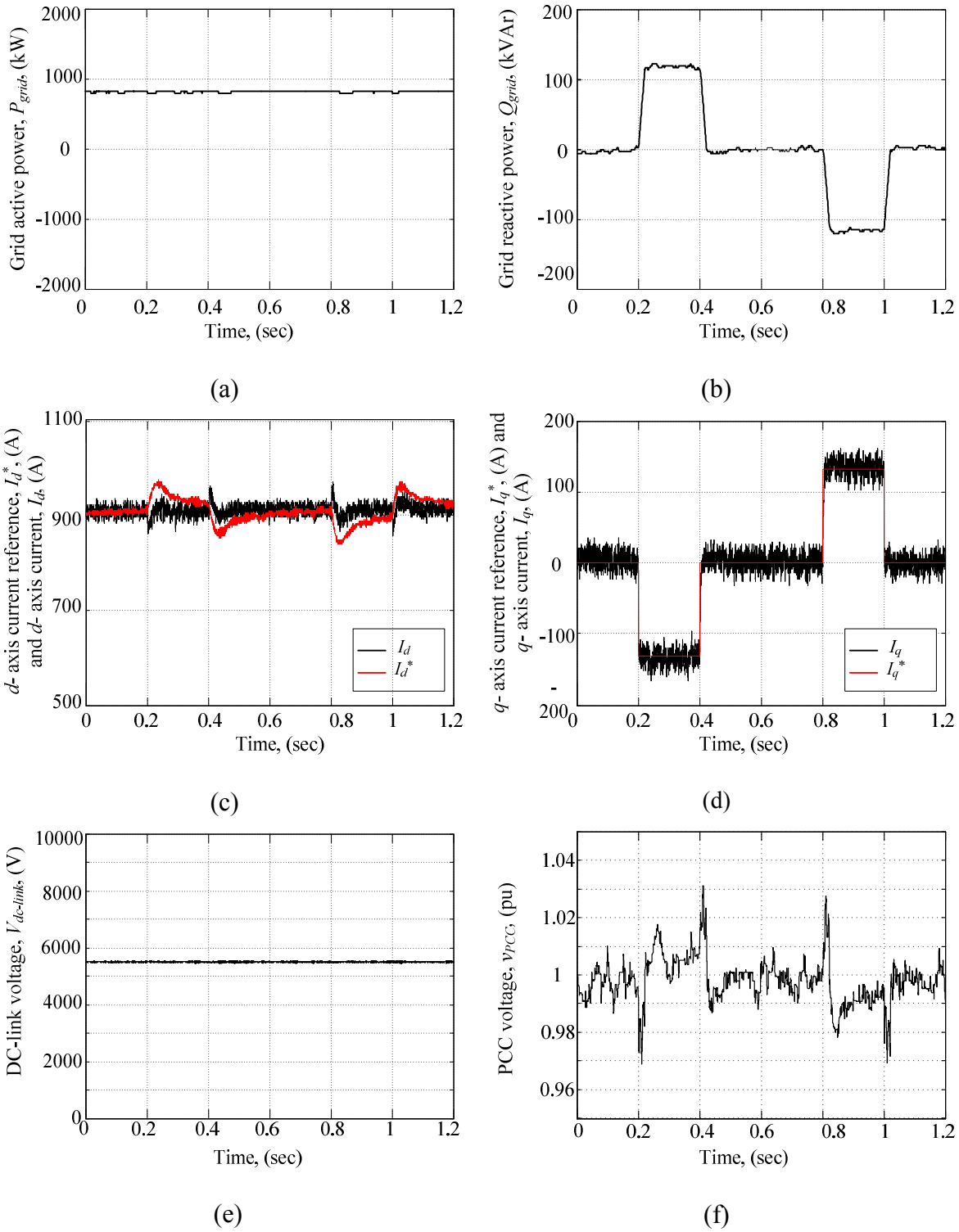

Figure 3.5. Effect of ±20% change in reactive power command: (a) Active grid power, P_{grid},(b) reactive grid power, Q_{grid}, (c) d-axis current reference and actual, I_d^* and I_d, (d) q-axis current reference and actual, I_q^* and I_q, (e) DC-link voltage $V_{dc\text{-}link}$, and (f) PCC voltage in pu.

Grid codes currently impose requirements on the regulation capabilities of the active power of wind farms. High-frequency response must be provided from full output to a reduced output when the frequency exceeds the nominal frequency and the new grid codes require that when the frequency increases above the rated value, generating plants should decrease their output at a given rate. According to the frequency guidelines in the UK grid code wind farms are required to [3.11].:

- Operate continuously with constant active power output for a system frequency within 49.5Hz and 50.5 Hz [3.10].
- The wind farm active power output should not be reduced by more than 5% for system frequency changes within the range 49.5 to 47 Hz.
- The wind farm must be capable of operation continuously between 47-52 Hz

Frequency and active power control are achieved through several modes of control which are illustrated in figure 3.6 (a) to (c) [3.5]. In the absolute power constraint strategy, active power can be regulated to a specific value even if more power can be extracted from the wind in the frequency decrease case. On the other hand, when the demand is low and with high wind power, the operator must export the excess wind power to neighbouring grids. This type of control is usually used to protect the network against overloading as shown in figure 3.6 (a). With the delta production constraint method shown in part (b), the output power can be regulated to bear a fixed relationship to the available power, such as maintaining a specified reserve. As for the power gradient constraint in figure 3.6 (c), this approach limits the maximum speed by which the active power can be changed in the event of changes in wind speed or the set points for the power plant. This function is typically used to prevent changes in active power from impacting the stability of the network. [3.5, 3.12, 3.13].

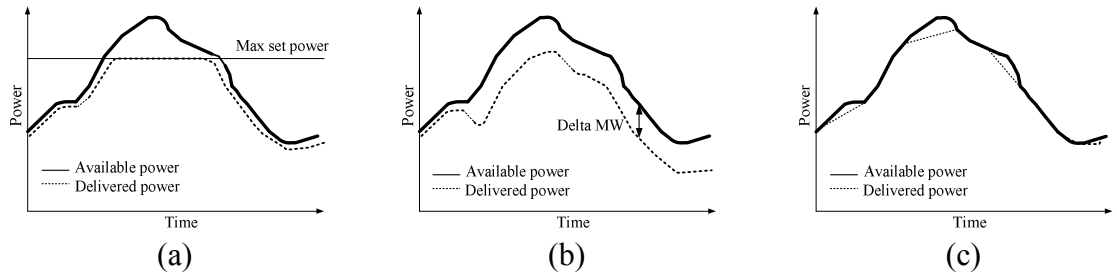

Figure 3.6. Power regulation strategies (a) absolute power constraint, (b) delta production constraint, and (c) power gradient control

The simulated system has been investigated for a ±2% change in grid frequency as shown in figure 3.7.

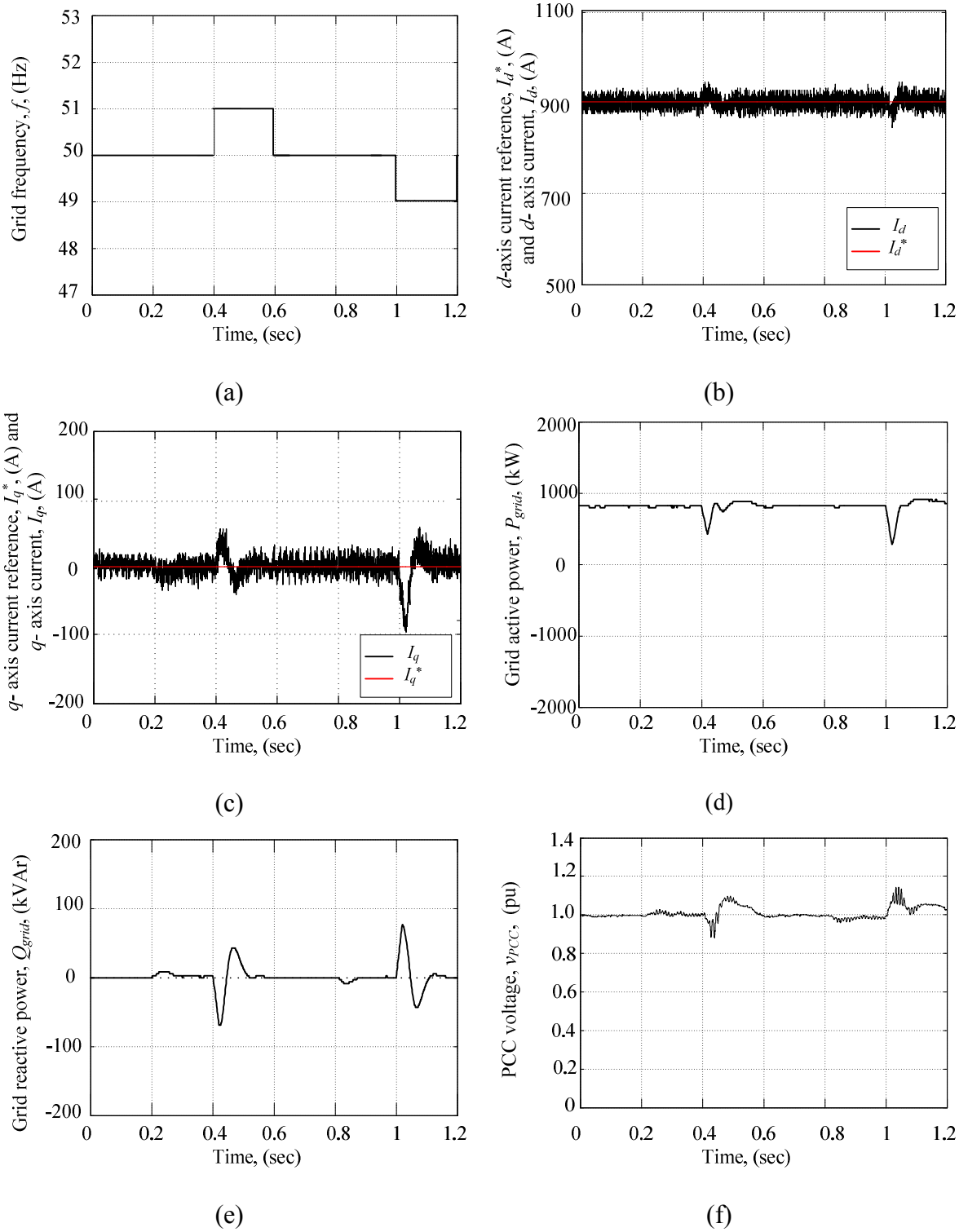

Figure 3.7. Effect of ±2% change in grid frequency: (a) Grid frequency, f, (b) d-axis current I_d^* and I_d, (c) q-axis current I_q^* and I_q, (d) active grid power, P_{grid}, (e) reactive grid power, Q_{grid}, and (f) PCC voltage, v_{PCC}.

The grid utility frequency, f, has changed from 50 Hz to 51 Hz between 0.4 and 0.6 s, and to 49 Hz between 1 and 1.2 s as indicated by the control signal applied for frequency step changes shown in part (a). The simulation has been carried out to show the effect of frequency changes on the performance of the PMSG WECS with an active power constraint strategy. Part (b) shows the response of the *d*-axis grid current, I_d, which affects the grid active power, P_{grid}, response in part (d). In the absence of an active power constraint strategy, the change in grid frequency will be accompanied by a rise in I_d accompanied by a rise in P_{grid}. The responses in figure 3.7 show that the grid current and active powers are controlled. The q-axis current, I_q in part (c) exhibits some transients which affect the grid reactive power response, Q_{grid} shown in part (e) due to the q-axis current controller response towards the frequency deviation which tends to affect the PCC voltage response shown in part (f).

3.2.4 Phase Jump

Synchronization is one of the most important issues in the control of power converters connected to the grid. The phase angle of the fundamental vector of the ac-mains voltage should be measured in real time in order to set the energy transfer between the grid and the power converter. Typical power-system phenomena related with transients in the input of the PLL are voltage variation (sag and swells), phase-angle shifts or phase jumps, and frequency deviations [3.14].The grid phase angle, θ_u is used to transform the grid currents and grid voltages needed in the vector current controller, into the *dq*-coordinate system for grid connection purposes as explained in Chapter 2. The *d*-axis of the rotating *dq*-coordinate system is synchronized with the grid voltage vector and the reference voltages from the current controller are transformed back to three-phase values. A phase shift in synchronization will result in steady-state errors, and the cross-coupling current gain will increase. In addition, poor performance or instability can occur if the synchronization is sensitive to noise or reacts too distinctly to phase steps [3.15].

The PMSG WECS has been further investigated for a change in grid voltage angle, θ_u by ±30° as seen in figure 3.8 (a). The angle is changed to +30° between 0.2 and 0.4 s, and to -30° during 0.8 to 1 s. As seen in (b) and (c), I_d and I_q current controllers try to inject the same amount of active power while keeping the reactive power set to zero even with a grid phase step change, with almost negligible effect on the active power shown in part (d). The

q-axis current exhibits more transients which are reflected onto the reactive power response in (e) as well as the voltage at the PCC as shown in (f).

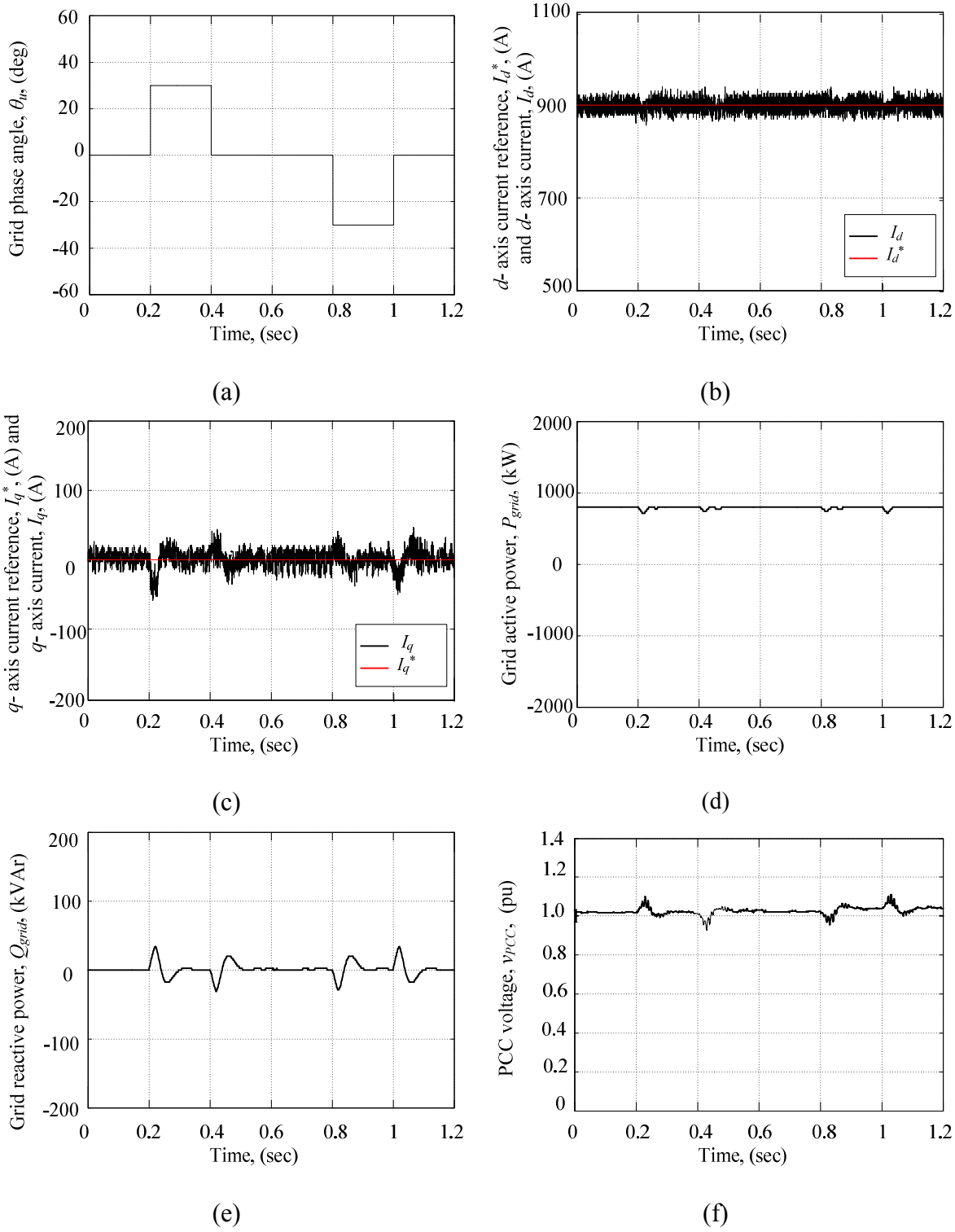

Figure 3.8. Effect of ±30° change in grid voltage angle (a) Grid phase angle, θ_u, (b) active grid power, P_{grid}, (c) reactive grid power, Q_{grid}, (d) d-axis current I_d^* and I_d, (e) q-axis current I_q^* and I_q, and (f) PCC voltage, v_{PCC}.

3.3 LVRT Capability and Grid Compliance

Voltage dip (sag) is defined as a short reduction in voltage magnitude for a duration of time, and is the most important and commonly occurring power quality issue. The definitions to characterize voltage dip in terms of duration and magnitude vary according to the authority. According to the IEEE standard (IEEE Std. 1159, 1995), voltage dip is defined as a decrease of rms voltage from 0.1 to 0.9 per unit (pu), for a duration of 0.5 cycle to 1 minute. Voltage dips are caused by faults on the system, transformer energizing, large currents drawn by arc furnaces or heavy load switching [3.16].

The interest in voltage dips is mainly due to the problems they cause on several types of equipment: adjustable-speed drives, process control equipment, and computers are notorious for their sensitivity. Some equipment trips when the root mean square (rms) voltage drops below 90% for longer than one or two cycles [3.17]. This tripping could extend to cause failure to power converters employed with WECS and might lead to total wind farm disconnection.

The increasing penetration level of wind energy can have a significant impact on the grid, especially under abnormal grid voltage conditions. When a fully rated converter wind turbine is connected to an ac-network and a network fault occurs, the dc-link voltage of the wind turbine will rapidly rise since the GSC of the wind turbine is prevented from transmitting all the generator active power while the MSC is still extracting maximum power and unaware of the voltage dip incidence. The power imbalance between the generator mechanical input power and its electrical output power could accelerate the generator, particularly in DFIG systems. Since the DFIGs rotor voltage will experience overvoltage during voltage dips, if this situation is allowed to continue, the generator is damaged by over-current and the power converters will be damage as well. Consequently, total cut-out of the wind farm occurs. If the wind farm is connected to a weak grid, loss of this large megawatt power might threaten network stability. To maintain a wind turbine's dc-link voltage below its upper limit, the excess power must be dissipated or the generator power has to be reduced. Consequently, wind farms should provide operational ability similar to that of conventional power plants. A demanding requirement for wind farms is fault ride-through (FRT) capability. According to this demand, the WT is required to survive during grid faults. The ability of a wind turbine to survive for a short voltage dip

duration without tripping is often referred to as the Low-Voltage Ride through (LVRT) capability of a turbine.

The UK's LVRT requirements apply to networks with a voltage level extending to above 200 kV. The grid code divides voltage dips in two categories:

- Those lasting less than or equal to 140 ms (seven cycles based on 50 Hz), caused by symmetrical or unsymmetrical network faults. In this case, the wind farm must stay connected for voltage drops down to 0%.
- Those lasting more than 140 ms (seven cycles), caused by symmetrical faults. In this case, disconnection is not allowed above the curve shown in figure 3.10 [3.5].

After restoration of the grid voltage, the active power must be restored to at least 90% of the level available before the dip, within 1 s. The UK grid code, unlike other codes, defines that the profile of figure 3.9 is not an RMS voltage–time response envelope that would be obtained by plotting the transient voltage response at a point on the transmission system against time. Rather, it is clarified that each point on the characteristic represents a combination of voltage level and associated time duration, which the connected wind power station must ride through [3.10]. LVRT requirements of various grid codes can be found in Appendix (E) [3.5].

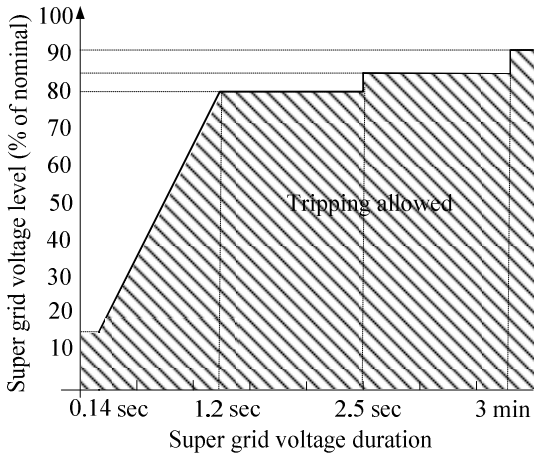

Figure 3.9. LVRT requirements of the British grid code.

3.4 System Energy Model

The energy balance equation for a grid connected PWM inverter system can be summarized as follows [3.18]

$$E_{grid} = E_{Rg} + \Delta E_{Lg} + \Delta E_{Cdc-link} + E_{gen} \quad (3.1)$$

where E_{grid} denotes the energy injected into the grid, E_{Rg} is energy consumed by an equivalent grid resistor, ΔE_{Lg} means energy exchanged in the ac inductor connected to the grid, $\Delta E_{Cdc-link}$ refers to energy exchanged in the dc-link capacitor, and E_{gen} represents generator output power. The energy flow chart of this system is presented in figure 3.10.

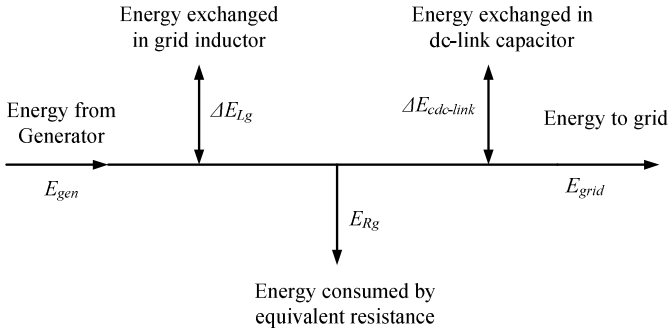

Figure 3.10. Energy flow chart in a rectifier-inverter.

Representing (3.1) in differential form

$$P_{grid} = P_{Rg} + \frac{d\Delta E_{Lg}}{dt} + \frac{d\Delta E_{Cdc-link}}{dt} - P_{gen} \quad (3.2)$$

where

$$P_{grid} = \frac{3}{2}\left(\bar{v}_{grid} \cdot \bar{\imath}_{grid}\right) \quad (3.3)$$

$$P_{Rg} = \frac{3}{2}\left(R_g . \bar{\imath}_{grid} . i_{grid}\right) \quad (3.4)$$

$$\frac{d\Delta E_{Lg}}{dt} = \frac{3}{2} L_{grid}\bar{\imath}_{grid} \cdot \frac{d\bar{\imath}_{grid}}{dt} \quad (3.5)$$

$$\frac{d\Delta E_{Cdc-link}}{dt} = \frac{1}{2} C_{dc-link} \cdot \frac{dV_{dc-link}{}^2}{dt} \quad (3.6)$$

$\bar{v}_{grid}$ and $\bar{\imath}_{grid}$ denote the voltage and current vectors of the grid, respectively.

The grid voltage vector can be replaced by the d-axis component v_d in synchronous rotating coordinates. Additionally, if the reactive power from the grid is controlled to be zero, the q-axis component of the grid current vector must be zero, and there will be only a d-axis current component i_d. Thus, the instantaneous energy balance equation is:

$$\frac{3}{2}\left(\bar{v}_d . \bar{\imath}_{grid}\right) = \frac{3}{2} R_{grid}\bar{\imath_d}^2 + \frac{3}{2} L_{grid}\bar{\imath_d} \cdot \frac{d\bar{\imath_d}}{dt} + \frac{1}{2} C_{dc-link} \cdot \frac{dv_{dc-link}{}^2}{dt} - P_{gen} \quad (3.7)$$

Thus it can be concluded from (3.7) that the dc-link stored energy is

$$\frac{1}{2}\,C_{dc-link}\cdot\frac{dv_{dc-link}{}^{2}}{dt}=\frac{3}{2}\,(\bar{v}_d.\bar{\imath}_d)-\frac{3}{2}\,R_{grid}\bar{\imath}_d{}^{2}-\frac{3}{2}\,L_{grid}\bar{\imath}_d\cdot\frac{d\bar{\imath}_d}{dt}+P_{gen} \tag{3. 8}$$

If the system is at steady state, the instantaneous energy balance equation is

$$\frac{3}{2}\,(v_d.\bar{\imath}_d)=\frac{3}{2}\,R_{grid}\bar{\imath}_d{}^{2}-P_{gen} \tag{3. 9}$$

From (3.9), it can be concluded that at steady state operation, the energy generated from the PMSG will be transformed into active power injected into the grid as well as losses in the grid resistance.

At a given wind speed, the power generated from the PMSG can be considered constant. Thus for any sudden change in grid voltage occurring due to a voltage dip, the corresponding grid voltage falls to a low value and consequently the grid current rises till reaching the thermal limits of the converter, which makes the controller limit the exported power. Consequently, there will be an energy imbalance between the generated and the grid injected powers leading to a rise in dc-link voltage as concluded from (3.8) [3.19].

3.5 WECS Response to Grid Voltage Dip

The proposed 1.5 MW system presented in figure 3.1 has been examined for grid voltage dips and assessed for ride-through capability. Before studying the impact of voltage dips on WECS behaviour, it is assumed that the WECS is connected to a 480V, 50Hz grid where the main objective of the GSC control is to deliver all the power extracted from the wind to the electrical grid at unity power factor whilst maintaining the dc-link voltage, $V_{dc-link}$ at 5500V. The boost converter is controlled for power point tracking [3.20]. Also, the wind turbine is driven at a fixed wind speed of 12 m/s at β=0, where the MSC extracts almost 800 kW power from the wind turbine at this wind speed. Only 765 kW is exported to the grid due to the PMSG, converter and cables losses.

Figures 3.11 and 3.12 show MSC performance, while figures 3.13 and 3.14 show GSC performance prior, during and after the fault is cleared, where the system has been subjected to a 90% symmetrical grid voltage dip at 0.2 s for a fault duration of 140 ms. As shown in figures 3.11 and 3.12, the MSC and PMSG are unaffected by the voltage dip due to the decoupling effect between MSC and GSC operation provided by the dc-link capacitor $C_{dc-link}$ [3.21]. The PMSG is driven by the wind turbine at a constant speed of 1.8 rad/s as shown in figure 3.11 (c) where the boost converter extracts generator current,

i_{gen} of 1000 A peak from its terminals, as shown in figure 3.11 (b), at a PMSG terminal voltage, v_{gen} of approximately 600 V peak as shown in part (a). The addition of a six pulse rectifier unit with smoothing output capacitor C_{dc} affects the PMSG line currents and produces a current waveform with two pulses every half cycle of supply frequency [3.22].

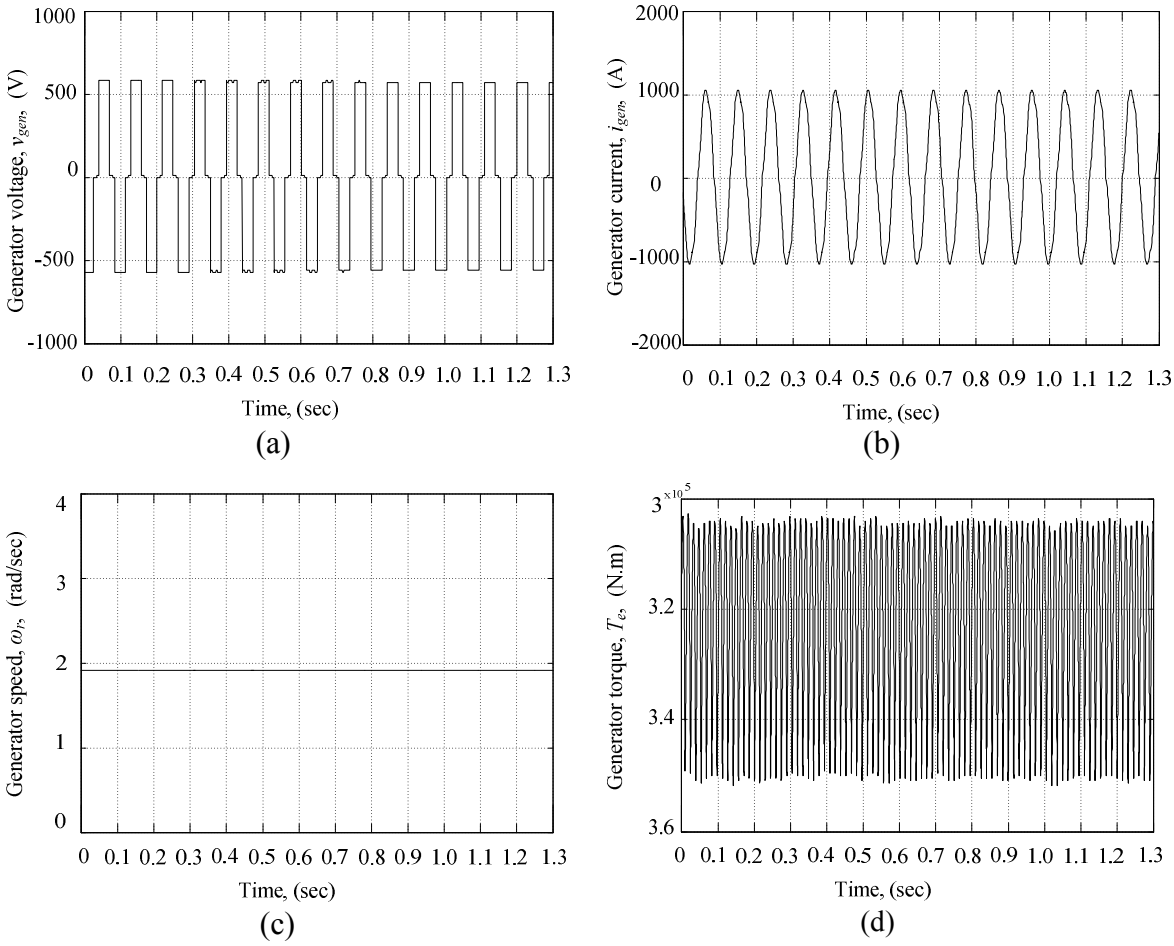

Figure 3.11. PMSG and MSC response to voltage dip: (a) PMSG voltage, v_{gen}, (b) PMSG current, i_{gen}, (c) PMSG rotational speed, ω_r, and (d) PMSG electromagnetic torque, T_e.

To smooth the generator output current i_{gen} waveform, series line filter inductance between the diode rectifier and the PMSG terminals, L_{gen} is added. However, the series line inductance distorts the PMSG line voltage v_{gen} waveform shown in figure 3.11 (a). The PMSG electromagnetic torque, T_e is approximately 340 kN.m as presented in figure 3.11 (d). The boost chopper current, I_{dc} flowing in the boost chopper inductor L_{dc} is shown in figure 3.12 (a) along with a magnified view. The chopper inductor current, I_{dc} is

set to 1000A, representing the maximum power that could be extracted from the wind turbine and the PMSG at a wind speed of 12 m/s, which in turn corresponds to 820 kW active power, P_{gen} and 600 kVar reactive power, Q_{gen} extracted from the generator as indicated in figure 3.12 (d).

Due to the decoupling effect, the generator side (including the converters) does not experience any PMSG effects during the voltage dip event which started at 0.2 seconds and remains for 140 ms. Consequently, no voltage or current stresses are experienced by the 6 pulse rectifier diodes as indicated in parts (b) and (c) of figure 3.12 which represents the voltage applied on the diode switch, v_{D1} and the current i_{D1} in diode D_1.

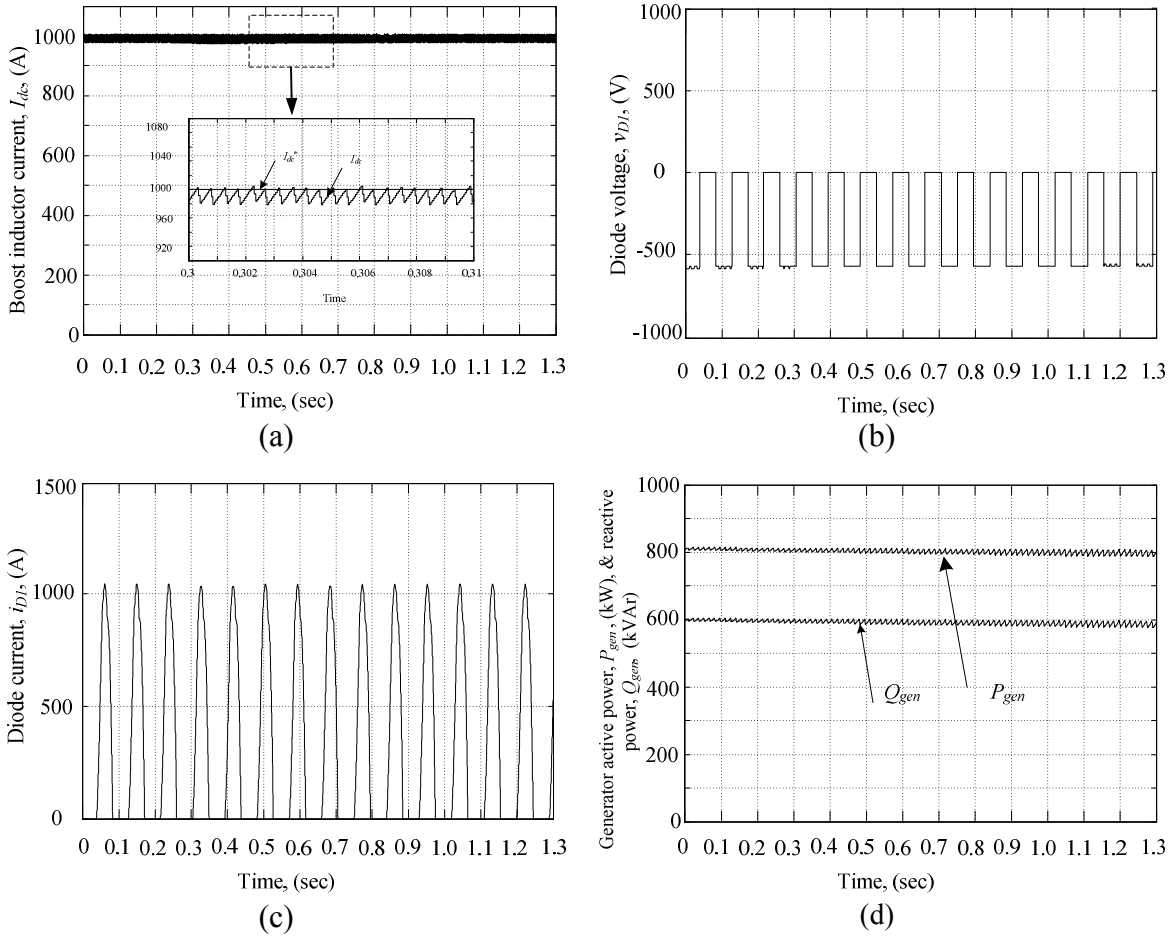

Figure 3.12 PMSG and MSC response to voltage dip (a) boost inductor current, i_{dc} and magnified view, (b) diode voltage, v_{D1}, (c) diode current, i_{D1}, and (d) generator active and reactive power, P_{gen} and Q_{gen} respectively.

As for the grid and GSI response to the sudden voltage dip, at 0.2 s the rms value of the grid voltage v_{grid} dropped suddenly from 480V to 48V for 140 ms duration as shown in figure 3.13 (a) where the grid current i_{grid} starts rising reaching almost 1000A in 0.05 s. Consequently, the power injected into the grid, P_{grid}, decreases from 765 kW prior to the fault instance to 100 kW during the fault as indicated in figure 3.14 (d). The energy imbalance between the maximum energy extracted from the PMSG and the energy being delivered to the grid will cause a dc-link voltage $V_{dc-link}$ rise, as explained previously [3.23].

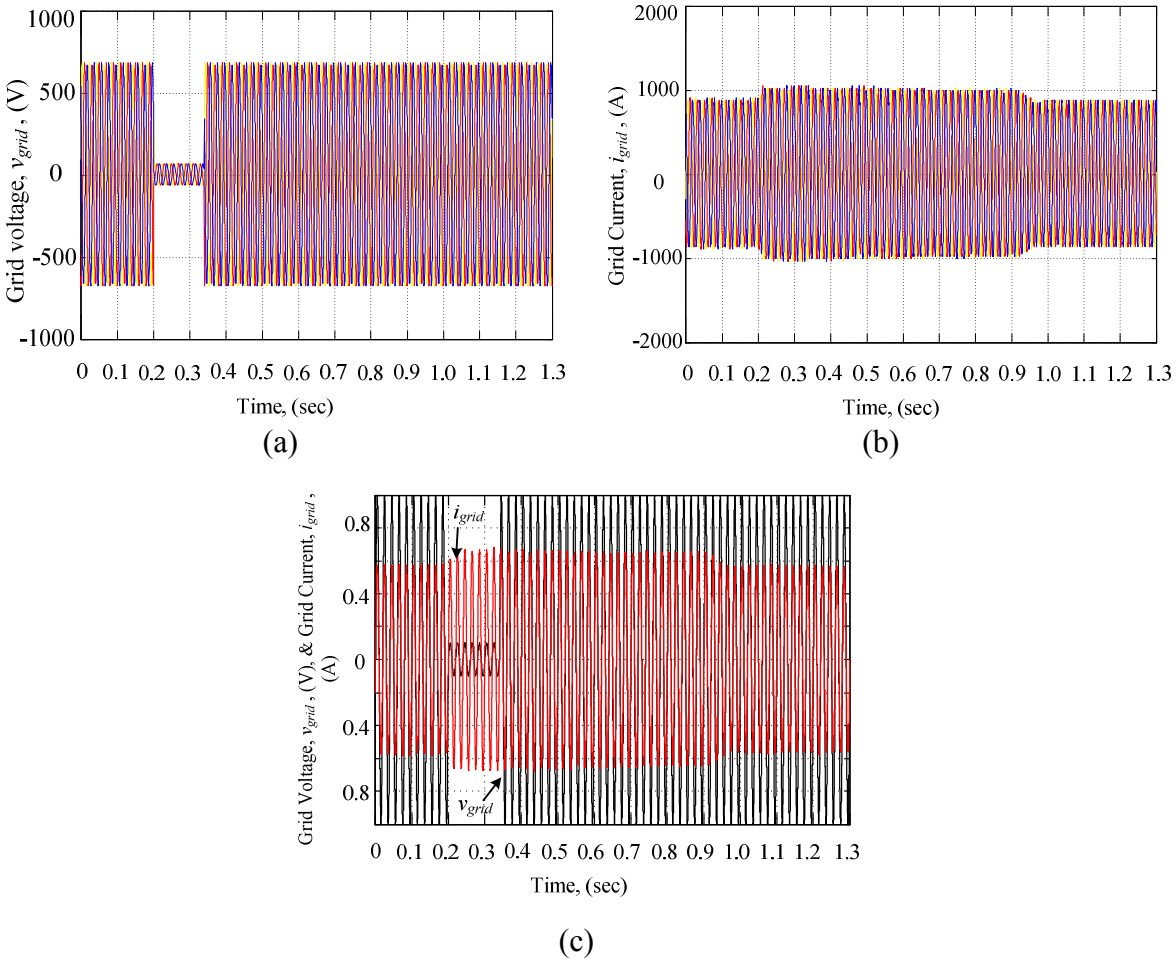

Figure 3.13. Grid and GSC response to voltage dip (a) grid voltage, v_{grid}, (b) grid current, i_{grid}, and (c) per unit v_{grid} and i_{grid}.

The dc-link voltage $V_{dc-link}$ response is shown in figure 3.14 (a), rising from 5500V, reaching 6500 V in the 140 ms duration. A longer fault duration will cause the dc-link voltage to reach higher values, depending on the dc-link capacitance $C_{dc-link}$.

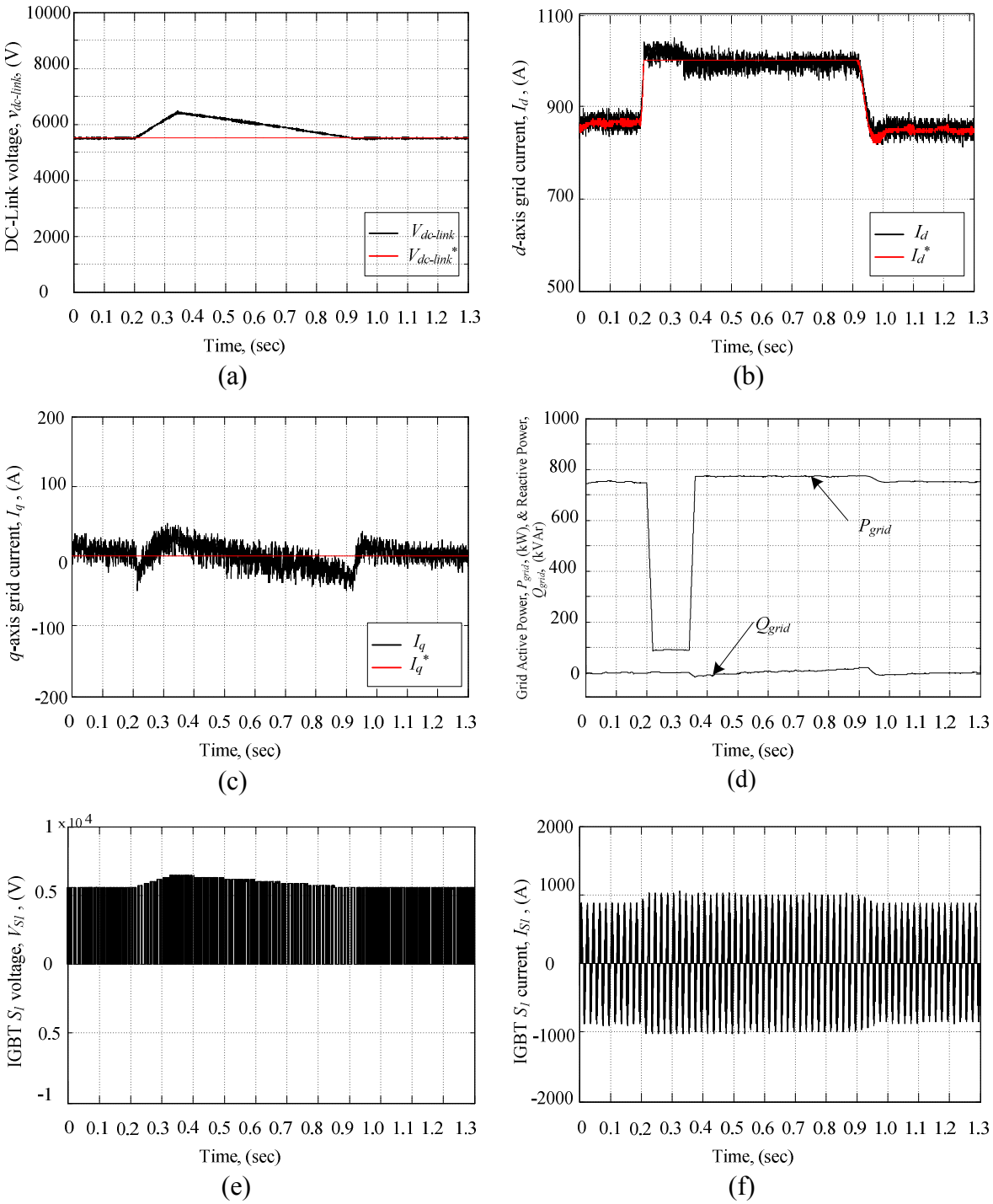

Figure 3.14. Grid and GSC response to voltage dip (a) dc link voltage, $V_{dc-link}$, (b) d-axis grid current, i_d, (c) q-axis grid current, i_q, (d) grid active and reactive power, P_{grid} and Q_{grid} respectively, (e) IGBT S_1 voltage, V_{S1}, and (f) IGBT S_1 current, I_{S1}.

In response to the dc-link voltage rise, the *d*-axis current I_d^* controller command rises, tending to deliver all the energy stored in the dc-link capacitor to the grid in an attempt to maintain the energy balance as shown in figure 3.14 (b), thus rises from 900A to 960 A, hitting the grid current thermal limit [3.24]. The dc-link voltage rise will in-turn cause voltage and current stresses in the inverter power module IGBT switches as in parts (e) and (f) of figure 3.14.

After the voltage dip is cleared, the $V_{dc-link}$ restoration time is longer and is governed by the control action of the dc-link voltage control loop and the capacitance of the dc-link capacitor $C_{dc-link}$. As seen from the responses of $V_{dc-link}$ and I_d in figure 3.14 (a) and (b) respectively, it takes approximately 0.7 s for $V_{dc-link}$ and I_d to be restored to their corresponding post fault values. Since the dc-link control loop sets the *d*-axis current command I_d^*, the grid current i_{grid} will also take longer to recover. The *q*-axis control loop action satisfies unity power factor operation during the fault by keeping the *q*-axis current I_q close to zero as indicated by in figure 3.14 (c). Since the VSI IGBT switches are affected by the rate of rise of $V_{dc-link}$ and i_{grid} as pointed out in figure 3.15 (e) and (f), the converter could mal-function if the switches were not designed to handle such voltage and current stresses, and the protection systems did not take appropriate action.

System failure to ride-through grid voltage dips needs to be properly addressed through the use of LVRT capability enhancing features. The following chapter will review the state-of-art techniques for fault ride-through, as well as briefly introduces a fault ride-through technique suggested by this author.

3.6 Summary

As more renewable energy sources are installed in the power system, grid codes for wind power integration are being created to sustain stable power system operation with non-synchronous generation. A 1.5 MW WECS based on PMSG technology was investigated for proper grid interconnection through the use of MATLAB simulation. The simulated system has been validated during sudden changes in active and reactive power, as well as frequency excursion and grid voltage phase angle jump. The results obtained are in compliance with UK grid requirements. Next, the 1.5 MW system was further explored for ride-through capability during a symmetrical grid voltage dip of 90% for a 140 ms

duration. The simulation results showed that the basic system failed to comply the UK grid requirements for successful ride-through, due to the lack of any LVRT capability enhancement technique. Consequently, dc-link voltage and grid current rises were experienced which might cause damage to the power converters employed, leading to wind farm total disconnection from the utility grid.

References

[3.1] H. Li and Z. Chen, 'Overview of Different Wind Generator Systems and their Comparisons', IET Renewable Power Generation, Vol. 2, 2008. pp. 123-138.

[3.2] H. Geng, *et al.*, 'Unified Power Control for PMSG-Based WECS Operating Under Different Grid Conditions', IEEE Transaction on Energy Conversion Vol. 26, 2011. pp. 822 - 830

[3.3] N. R. Ullah, T. Thiringer, and D. Karlsson, 'Voltage and Transient Stability Support by Wind Farms Complying With the E.ON Netz Grid Code', IEEE Transactions on Power Systems, Vol. 22, 2007. pp. 1647-1656.

[3.4] E. M. Rodrigues, A. W. Bizuayehu, and J. P. S. Catalao, 'Analysis of Requirements in Insular Grid Codes for Large-Scale Integration of Renewable Generation', IEEE PES T&D Conference and Exposition, 2014. pp. 1-5.

[3.5] M. Tsili and S. Papathanassiou, 'A Review of Grid Code Technical Requirements for Wind Farms', IET Renewable Power Generation, Vol. 3, 2009. p. 308.

[3.6] M. Barlow, M. Theodoridis, and M. T. Bishop, 'The Design of Wind Plant Reactive Compensation System Alternatives to Meet Grid Code Requirements', 2nd IEEE PES International Conference and Exhibition on Innovative Smart Grid Technologies (ISGT Europe), 2011. pp. 1-8.

[3.7] S. Chondrogiannis, *et al.*, 'Modelling and GB Grid Code Compliance Studies of Offshore Wind Farms with Doubly-Fed Induction Generators', The 3rd IET International Conference on Power Electronics, Machines and Drives, 2006. pp. 22-26.

[3.8] G. Lalor, A. Mullane, and M. O'Malley, 'Frequency Control and Wind Turbine Technologies', IEEE Transactions on Power Systems, Vol. 20, 2005. pp. 1905-1913.

[3.9] C.-C. Le-Ren, L. Wei-Ting, and Y. Yao-Ching, 'Enhancing Frequency Response Control by DFIGs in the High Wind Penetrated Power Systems', IEEE Transactions on Power Systems, Vol. 26, 2011. pp. 710-718.

[3.10] N. G. E. T. plc. The Grid Code - Issue 4 Revision 2 [Online].

[3.11] O. A. Giddani, *et al.*, 'Control Strategies of VSC-HVDC Transmission System for Wind Power Integration to Meet GB Grid Code Requirements', International

Symposium on Power Electronics Electrical Drives Automation and Motion (SPEEDAM), 2010. pp. 385-390.

[3.12] W. Murrell, R. Li, and W. Jihong, 'Modelling UK Power System Frequency Response with Increasing Wind Penetration', IEEE Innovative Smart Grid Technologies - Asia (ISGT Asia), 2014. pp. 1-6.

[3.13] T. Ackermann,'Wind Power in Power Systems', Wiley, 2005.

[3.14] F. D. Freijedo*, et al.*, 'Tuning of Phase-Locked Loops for Power Converters Under Distorted Utility Conditions', IEEE Transactions on Industry Applications, Vol. 45, 2009. pp. 2039-2047.

[3.15] J. Svensson, 'Synchronisation Methods for Grid-Connected Voltage Source Converters', IEE Proceedings- Generation, Transmission and Distribution Vol. 148, 2001. pp. 229-235.

[3.16] G. R. Rey and L. M. Muneta. Electrical Generation and Distribution Systems and Power Quality Disturbances [Online]. Available: www.intechopen.com

[3.17] M. H. J. Bollen,'Understanding Power Quality Problems (Voltage Sags And Interruptions)', A JohnWiley & Sons, 2001.

[3.18] Y. Lu*, et al.*, 'An Improved DC-Link Voltage Fast Control Scheme for a PWM Rectifier-Inverter System', IEEE Transactions on Industry Applications, Vol. 50, 2014. pp. 462-473.

[3.19] T. Ji*, et al.*, 'Performance Analysis and Research on LVRT of PMSG Wind Power Systems with SDBR', 33rd Chinese Control Conference (CCC), 2014. pp. 6953-6958.

[3.20] M. H. Ali,'Wind Energy Systems: Solutions for Power Quality and Stabilization', Taylor & Francis, 2012.

[3.21] L. Jianlin*, et al.*, 'Study on Low Voltage Ride through Characteristic of Full Power Converter Direct-Drive Wind Power System', IEEE 6th International Power Electronics and Motion Control Conference, IPEMC '09 2009.

[3.22] B. Wu,'High-Power Converters and AC Drives', Wiley, 2006.

[3.23] J. Li*, et al.*, 'A Novel Power-flow Balance LVRT Control Strategy for Low Speed Direct Drive PMSG Wind Generation System', 36th Annual Conference on IEEE Industrial Electronics Society IECON 2010 2010.

[3.24] W. Wenliang, *et al.*, 'Energy Storage Based LVRT and Stabilizing Power Control for Direct-Drive Wind Power System', International Conference on Power System Technology (POWERCON), 2010. pp. 1-6.

CHAPTER FOUR

Low Voltage Ride Through of a PMSG WECS

As the scale of wind farms increases, the grid connection condition of the wind turbine becomes more important. Recently, some countries have issued dedicated grid codes for wind turbine system interconnection to the utility grid [4.1]. However, loss of a considerable part of WECS cannot be accepted in case of network faults [4.2]. Therefore, ride-through control of the wind power generation system is needed for abnormal grid conditions. Several solutions have been proposed for LVRT in variable-speed wind turbine systems which vary based on grid and turbine variables such as voltage during a fault, voltage overshoot and response time during recovery, rotor speed, rotor current, and dc-bus voltage. In this chapter, a survey study is undertaken of low voltage ride-through capability enhancement techniques. Merits and demerits of each approach are explained with special focus on PMSG WECS.

The use of magnetic amplifiers as a technique for fault ride-through capability enhancement is suggested in this research. The theory of operation and available configurations are highlighted with focus on use as a series voltage compensator in the case of grid voltage dips. Two configurations are tested and validated in subsequent chapters.

4.1 LVRT Capability Enhancement Technique Classification

Methods for LVRT capability enhancement can be divided into those requiring additional hardware to the WECS and those requiring change in the control system as to satisfy grid code requirements for successful ride through operation. Figure 4.2 lists the most commonly used techniques that can be applied to each individual wind turbine or for a group of wind turbines if extended to the wind farm level.

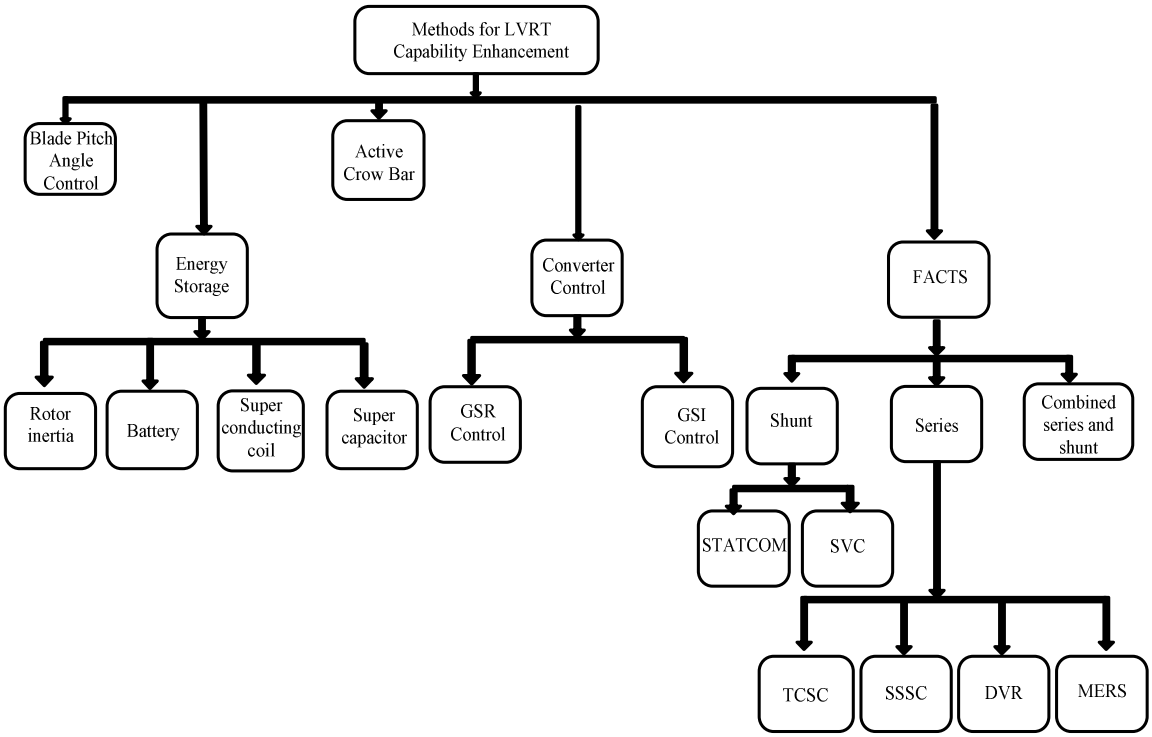

Figure 4.1. Techniques for LVRT Capability Enhancement for PMSG Wind Turbines.

4.1.1 Blade Pitch Angle Control

When the wind velocity is invariant, the power extracted from the wind P_w is directly proportional to the power co-efficient C_p which in turn varies with both the TSR and the blade pitch angle (BPA) as explained in Chapter 2. Maximum C_p is achieved at optimized rotational speed ω_{opt} when the BPA, β, is equal to zero at point (A) in figure 4.2 [4.3]. During a grid voltage dip event, kinetic energy is stored in the rotor inertia causing the wind turbine generator to exhibit a change (increase) in its rotational speed, shifting the operating point from point (A) to point (B). This occurs since the MSC cannot control the extracted wind power as quickly as the GSC power causing a mismatch between the extracted and exported power to the grid [4.4]. To avoid the over speeding effect, a BPA controller is needed where the pitch controller pitches the BPA to reduce the performance coefficient of the turbine above rated rotational speed and rated power of the generator. The BPA is adjusted to reduce the wind power to keep the rotational speed from increasing, shifting operation away from its maximum value (β =0) to along the vertical line, thus shifting the operating point from point (B) to point (C). When the voltage

recovers, the BPA is adjusted to bring the wind turbine back to where $\beta = 0$ i.e. back to point (A). Pitch control is primarily employed to limit the active power generation or the rotor speed when the wind speed is high.

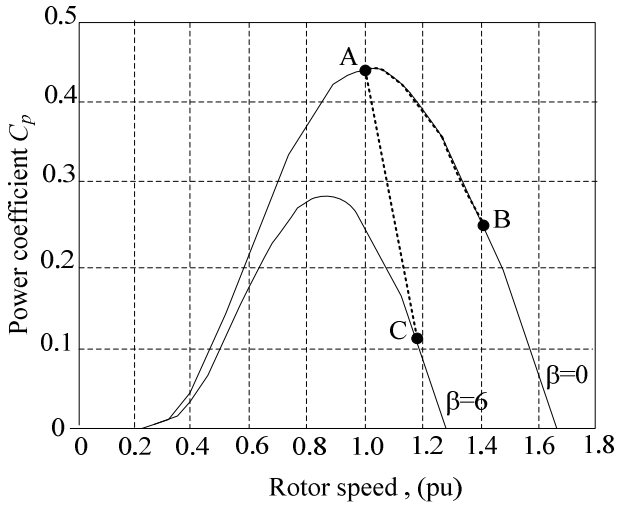

Figure 4.2. Blade pitch angle control.

There are significant response limitations when a BPA technique is employed with weak power grids as the dynamic forces resulting from restoring power at a high rate during a fault are high, even though the blade pitch actuators are powerful enough to fully pitch the blades in a short time (many seconds) [4.5].

4.1.2 Crowbar Approach

The initial solution implemented by manufacturers to protect the generator and the converter was to use a bypass resistor, configured to short-circuit the generator windings with the braking resistors or crowbar and to disconnect the turbine from the grid [4.6]. By providing an alternative path for the PMSG stator currents through a set of resistors, excess energy is dissipated in the crowbar resistors. Two crowbar topologies are common, namely passive and active as shown in figure 4.3 (a) and (b) respectively. A passive crowbar is implemented with a diode rectifier or two thyristors in anti-parallel to be activated during fault. The second option is an active crowbar using IGBT switches; this allows crowbar deactivation and, consequently, faster recovery of PMSG control [4.7]. The crowbar resistance magnitude and deactivation time affect the current behaviour; large crowbars result in better damping of stator over-currents and torque overshoot reducing also the reactive power consumption. Also, delay time for crowbar removal can completely remove

the current and torque spikes, however, it can delay the active power restoration. Also, large crowbars can cause current spikes upon deactivation resulting in voltage stress on the stator winding. The dc-link chopper shown in figure 4.3 is another crowbar circuit which keeps the dc-link voltage within acceptable limits [4.6, 4.8]. Although the crowbar technique is considered the simplest technique among LVRT methods, it can minimize power and voltage fluctuations, and for that reason it can be used along with other methods for LVRT capability improvement, such as energy storage for superior and better performance [4.9].

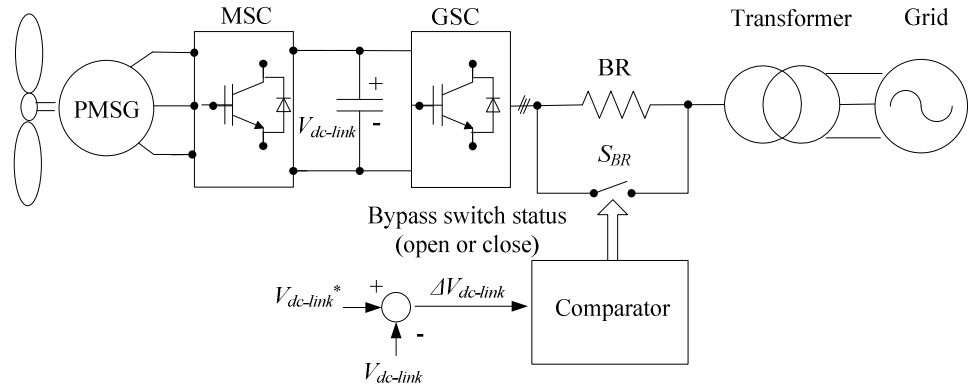

(a)

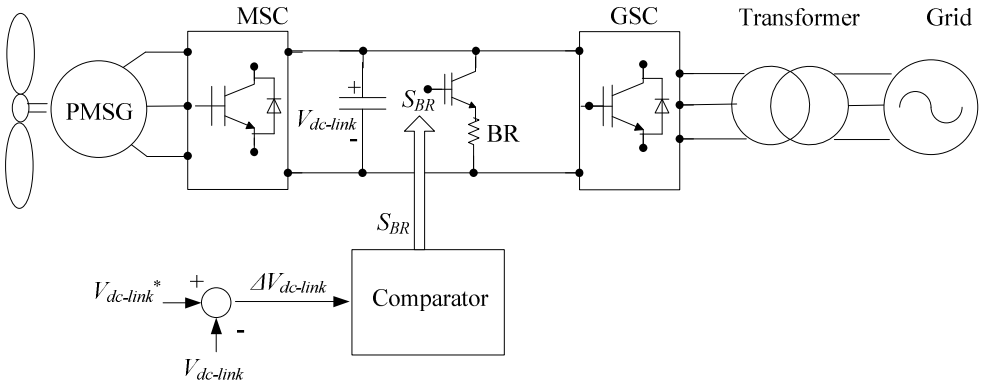

(b)

Figure 4.3. Crow bar approach with chopper: (a) grid side crowbar and (b) dc-link crowbar.

4.1.3 Energy Storage Systems

An energy storage system (ESS) can be used to manage the energy during a voltage disturbance. The energy is stored and subsequently exported to the grid once the voltage returns to its nominal value.

i- Stored Energy in Rotor Inertia

The flywheel is a mechanical device that stores kinetic energy in a rotating mass, where the energy stored varies linearly with the moment of inertia of the flywheel and the square of its angular velocity [4.10]:

$$E_{ke} = ½\, J\, \omega_r^2 \tag{4.1}$$

where E_{ke} is stored kinetic energy, J is the moment of inertia, and ω_r is the rotor angular velocity.

An electric motor is employed to 'flywheel' during off-peak periods to store electric energy in the form of kinetic energy, and then the kinetic energy is released during peak demand. Flywheel energy storage (FES) systems have been used in off-grid applications to regulate frequency and to mitigate power fluctuations, offering fast transitional response and a long life cycle. A flywheel can provide ride-through of deep voltage sags and full power outages, however, maintenance and safety are the main concerns [4.11, 4.12]

ii- Battery Based Energy Storage Systems

Batteries such as Lead-Acid Batteries (LAB) are popular since they can be charged and discharged frequently, and are readily availability at low cost. However, they have a limited life time which depends mainly on how deeply they are discharged, require high maintenance, and are heavy [4.13]. Other batteries such as sodium sulphur (NaS) are available with higher power density, good efficiency, and long life cycles. NaS needs high temperatures to operate thus the battery construction requires a special arrangement to prevent heat loss. This is considered to be a major disadvantage. The Vanadium Redox flow Battery (VRB) is well suited for ESS in large-scale power energy storage because of its high scalability, long life, low materials price, maintenance requirements, and fast response. In practice, the LAB is more dominant in the market but VRB have superior characteristics such as higher energy and power density, lower maintenance cost and longer life time in stand-alone systems [4.14-17]. By adding a VRB-based ESS on the dc-link bus, energy can be stored or released to smooth the grid-injected power as well as to absorb excess energy from the dc-link bus to improve LVRT capability, as shown in figure 4.4[4.18]. The ESS method is more sensitive to fault severity than fault type, and requires an additional dc converter and appropriate sizing of the power converters [4.19, 4.20].

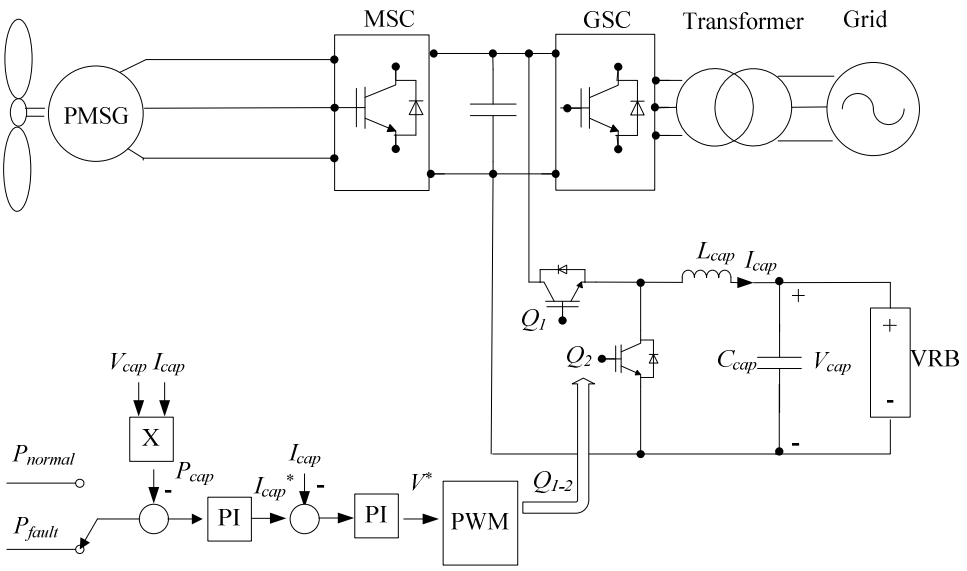

Figure 4.4. Energy storage system with Vanadium Redox Flow Battery [4.21].

iii- Super Conducting Coil

A Super Magnetic Energy Storage (SMES) system stores energy in the magnetic field created by direct current in a Super Conductor Coil (SCC). With liquid helium or nitrogen, the conducting coil is cooled cryogenically below its superconductive critical temperature, at which it exhibits zero resistance [4.22]. The energy E_{SMES} stored in the SMES is:

$$E_{SMES} = ½ i_{SMES}^2 L_{SMES} \tag{4.2}$$

where i_{SMES} is the SMES current and L_{SMES} is the SMES coil inductance [4.23, 4.24].

SMESs are known for their high efficiency, quick response and lack of deterioration; for this reason they have been applied in load fluctuation compensation [4.25]. Despite cooling losses, the most distinct SMES feature is a high power density that can reach approximately 10 times higher than that of the LAB, the NaS battery, and the double-layer capacitor [43]. Although SMES capital cost is higher than other energy storage devices, the annual cost (defined as the life cycle cost divided by the lifetime) is much lower (better) than other energy storage devices due to its higher efficiency, enabling its use in high power applications [4.26]. SMES are extended to the wind farm level by their connection at the point of common coupling, as shown in figure 4.5 [4.24, 4.27].

Superconducting fault current limiters (SFCL) can suppress short circuit currents by using unique quench characteristics of superconductors, where at the fault, the superconductor

undergoes a transition into its normal state (i.e., quenching). After quenching, the current is commutated to a shunt resistance and is then limited rapidly [4.28]. SFCL exist in many configurations and are an efficient means for improving power system stability [4.29]. The resistive type SFCL has been investigated due to its compact size and simple operating principle. With state-of-art conductors, a high current density SFCL with fast transition and recovery has been realised [4.30]. The simple resistive SFCL structure is shown in figure 4.6. The total SFCL resistance during a fault depends on the total number of units in figure 4.6. Studies show that the higher the SFCL resistance, the better the FRT capability. Nevertheless, high resistance results in high energy loss during the fault current limitation period [4.31].

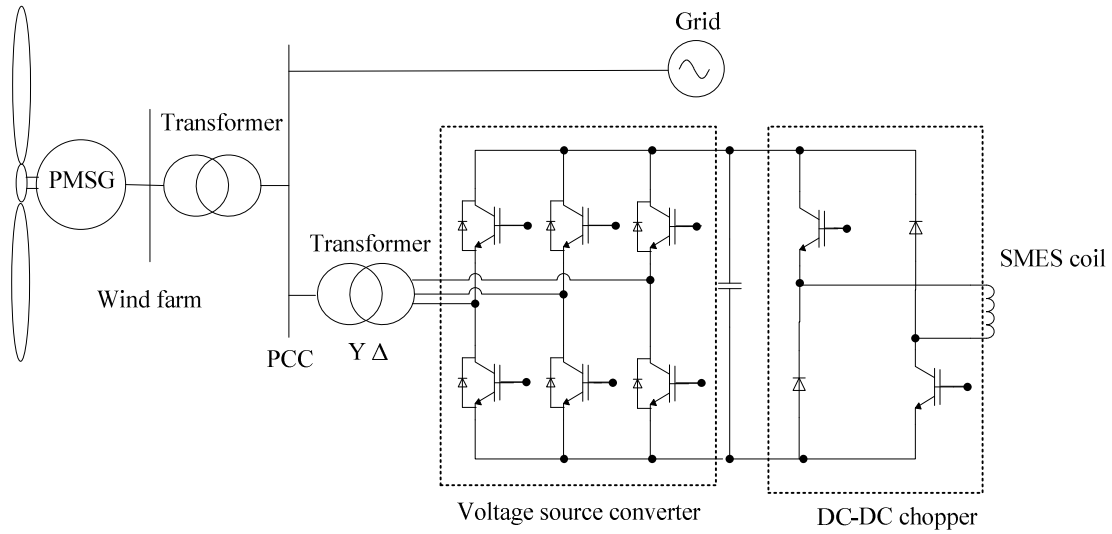

Figure 4.5. Grid connected wind turbine with SMES.

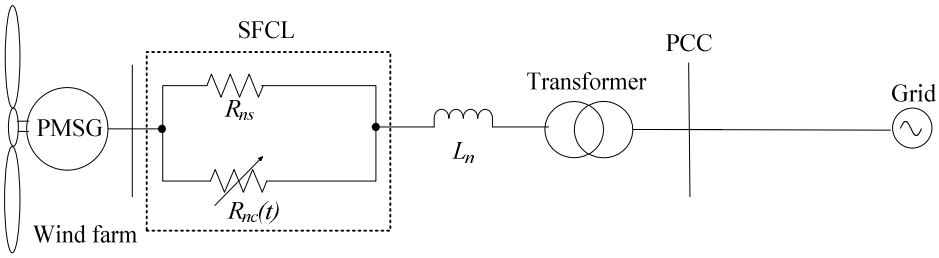

Figure 4.6. SFCL at the farm scale level.

Combining the features of both the SMES and SFCL will result in superior characteristics. The key idea of Short Circuit Fault Current Limiter-Magnetic Energy Storage (SFCL-

MES) is to utilize the SCC as the energy storage device and fault-current limiting inductor simultaneously and to thus help enhance LVRT capability [4.32].

iv- Super Capacitor

Instead of dissipating energy in a dump resistor, energy can be stored in a larger capacitor, as indicated by:

$$\int P_c dt = ½C_{dc-link}\left(V_{dc-link}^2 - V_{dc-link(0)}^2\right) \tag{4.3}$$

where P_c is the power transfer in the capacitor, $C_{dc-link}$ is the capacitance in Farad, $V_{dc-link}$ is the capacitor voltage at the voltage dip event, and $V_{dc-link(0)}$ is the capacitor voltage during normal operation. From (4.3) the required capacitor power P_c is directly proportional to the dip voltage [4.5]. Also, the required capacitance increases if the voltage-dip duration increases, requiring a larger area for the plates and permittivity of dielectric as well as smaller distance between the two plates. Hence, the resultant capacitor size may make it an impractical solution.

The super capacitor/ultra capacitor or boost-capacitor, significantly increases electrode surface area. Such capacitors use two layers of metal filaments or porous carbons made from foils to form anode and cathode that are perfuse in dielectric material of electrochemical liquid unlike conventional capacitors which uses metal for the anode or cathode [4.22, 4.33]. Super capacitors (SC) exist with high power density storage, long cycle life and good environmental performance, which make them viable for coping with transient grid failure [4.34, 4.35]. When using SCs as energy storage elements during a transient voltage dip, a dc-dc converter is employed to charge and discharge the SC, as seen in figure 4.7. When the link voltage is less than the referenced power requirement, the SCs deliver energy to grid to compensate the voltage sag through series inductance, L_{SC}. When the link voltage is higher than the referenced power requirement, which is the case during grid voltage dips, the SCs charges up [4.34]. The SC has low heat dissipation and does not produce any hazardous substances. Although SCs are known for high efficiency, charging and discharging unlimited number of times lasting up to 10 years [4.36], their energy density is low and has a high self-discharge so they are good for short time compensation for stabilization and fluctuation and are not oriented for long-term applications [4.37]. Their typical 1s RC time constant implies inefficient energy transfer during a 140ms fault ride through period.

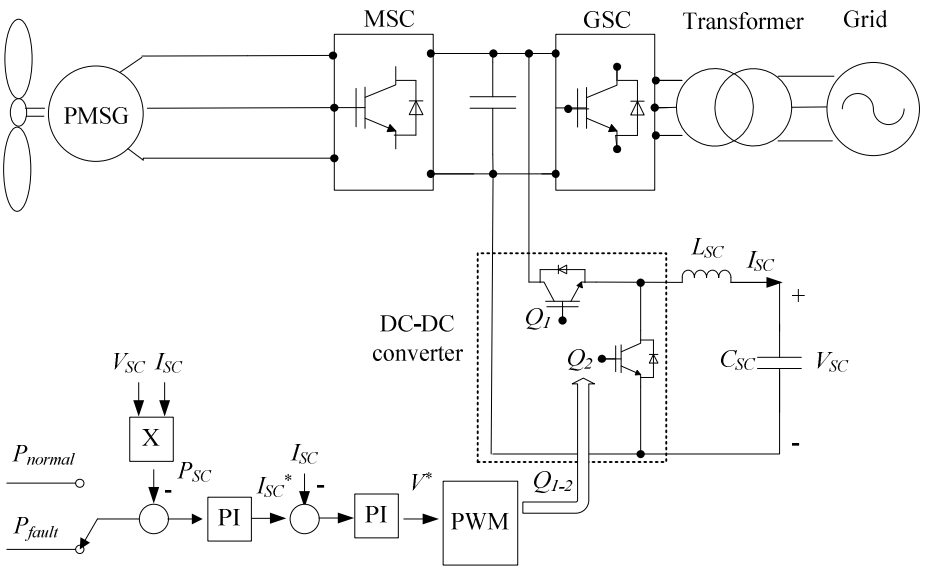

Figure 4.7. Energy storage using super capacitors.

4.1.4 Converter Control

The dc-link voltage can be reduced by 'de-loading' the wind turbine. Fully rated converter wind turbines can be de-loaded in many ways for fault ride through. This can be achieved by reducing the generator torque via MSC control, blocking the output powers via the wind turbines' GSC control or via a boost converter if employed on the dc-link. For PMSG WECS employing a diode rectifier and dc-dc chopper, enhanced LVRT capability can be achieved through control of the boost chopper [4.38].

i- Control of Machine Side Converter (MSC):

In this type of control, the generator power is rapidly reduced (de-loaded) by reducing the generator's torque as soon as the dc-link voltage rises to a certain threshold. The reduction in generator torque follows a de-loading droop characteristics which must be fast enough to de-load a large megawatt wind turbine in a few milliseconds. As the wind turbine's dc-link voltage drops, the grid side controller reduces the wind farm grid side active power current, thus reducing the active power from the wind farm. This approach is illustrated in figure 4.8. Electromagnetic torque is managed through controlling the armature current, and thus the generator speed is controlled. Decoupling the *dq*-axes armature current components is employed to independently manage the PMSG active and reactive powers. For this reason, two control loops are utilized with MSC control. In the inner control loop,

the generator d-axis reference current I_{dgen}^{*} is set to zero to obtain maximum torque at minimum current to minimize the resistive losses in the generator. Equation (2.24) is rewritten as:

$$T_e = \frac{3}{2}\left(\frac{P}{2}\right)\left(\varphi_d i_{qgen}\right) \tag{4.4}$$

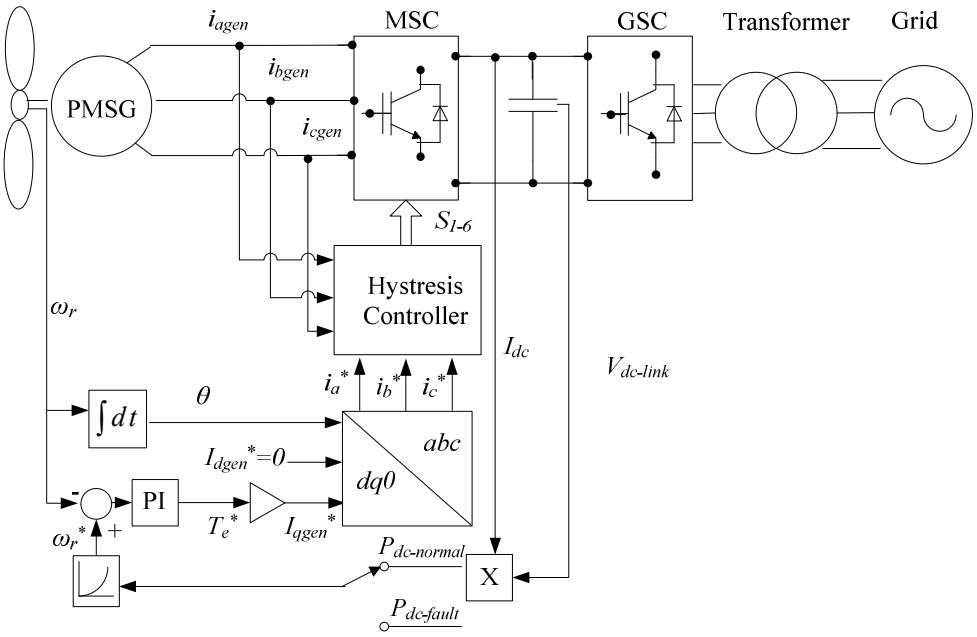

Figure 4.8. MSC Control for LVRT capability enhancement.

The mechanical rotational speed ω_r is determined by the torque electromagnetic torque T_e and the load torque T_m using (2.25).

$$\frac{d\omega_r}{dt} = \frac{(T_e - T_L - \omega_r B_m)}{J} \tag{4.5}$$

where B_m is the damping co-efficient.

The q-axis reference current I_{qgen}^{*} is obtained from the outer power loop. Since the maximum power at different wind velocities is proportional to the cubic function of generator speed as explained by (2.2), the generator speed is controlled to follow the power-speed characteristic. For this purpose, the power at the dc-link is used to obtain the reference speed by using the power-speed curve. The error signal is then used to obtain the generator reference torque.

ii- Control of Grid Side Converter (GSC):

De-loading via the GSC means that the wind turbine's grid side active power current, I_d is reduced to block wind turbine output power. The GSC is responsible for dc-link voltage regulation so that the power balance can be maintained under fluctuating wind and grid disturbances. A block diagram of the GSC control system is presented in figure 4.9. The inner control loop is used in reactive power or harmonic compensation while the outer loop is a voltage loop that sets the current reference for active power control [4.3]. The controllers in figure 4.9 function well in normal operation, however in the case of a grid fault, the dc-link voltage increases rapidly because the generator active power is prevented from being transferred to the grid and instead feeds into the dc-link capacitor. Using the de-loading droop approach shown in figure 4.10, it is possible to suppress any dc-link over voltage. The dc-link capacitor should absorb the energy until the inverter side power reference is reduced, hence the dc-link capacitance should be properly sized to handle this energy and prevent an over-voltage problem [4.3, 4.39]. Controllers are often designed to operate in a specific range so when the terminal voltage drops below the nominal level, the operating point may stray outside the designed range, resulting in an unexpected response which could cause converter transient currents to exceed their limits.

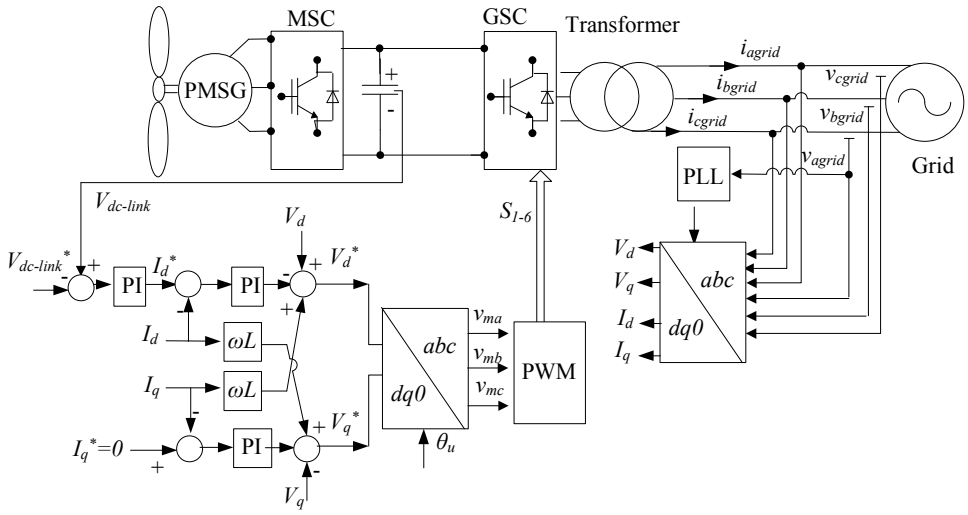

Figure 4.9. GSC Control for LVRT capability enhancement.

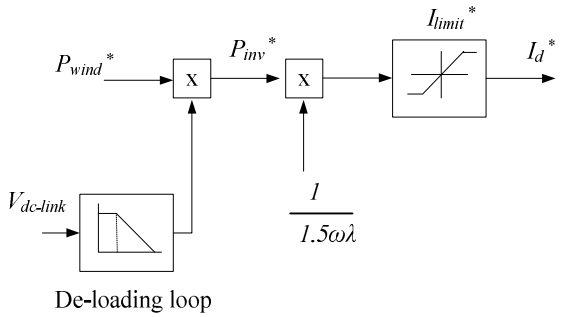

Figure 4.10. De-loading droop characteristics [4.39].

4.1.5 FACTS and Compensation Techniques:

All previously reviewed solutions tend to overcome problems associated with voltage dips for individual WTs through implementation before the point of common coupling, thus tackle the LVRT problem from the wind turbine perspective. This section is aimed to review other techniques applied at point of common coupling applied for individual WTs or at the wind farm level. The proposed solutions aim for reactive power and voltage recovery at the point of common coupling (PCC) using FACT compensation techniques from the grid stability perspective [4.40]. Generally, FACTS devices can be divided into three major categories: series, shunt and combined (series and shunt) devices. With shunt compensation, a large reactive current is injected where the reactive current size is decided by the difference between the wind farm consumption requirement and the amount of reactive power that can be transferred from the grid with the given voltage conditions. Series compensation is based on increasing the reactive power transfer from the grid by injecting capacitive voltage.

i- Shunt Compensation:

Shunt FACTS are connected in parallel with the power system. A shunt controller can be a variable source, variable impedance or a combination of both. Their principle of the operation is to inject current into the power system. There are two types of shunt compensation: static Var compensators and STATCOM.

- **Static VAR Compensator (SVC)**

A Static Var Compensator (SVC) consists of a thyristor controlled reactor, and thyristor or mechanically switched capacitors. By means of phase angle modulation control of the

thyristors, the reactor is variably switched into the circuit providing a variable VAr injection (or absorption) to the electrical network as shown in figure 4.11 [4.41]. SVCs can significantly enhance the LVRT capability without significant cost increase and can maintain the transient stability of the wind farm [4.42].

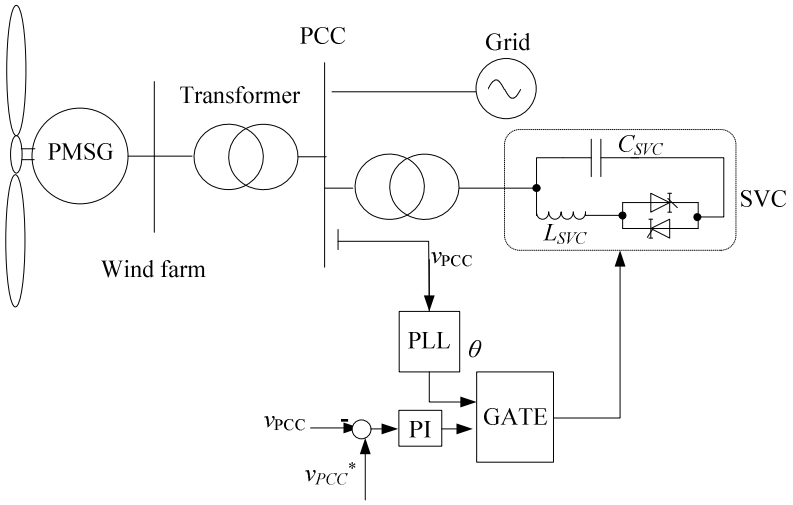

Figure 4.11. Grid connected wind farm with static Var compensator.

- **STATCOM**

The STATCOM shown in figure 4.12 is a self-commutating voltage source inverter which converts dc-voltage into a three-phase set of output voltages with desired amplitude, frequency, and phase.

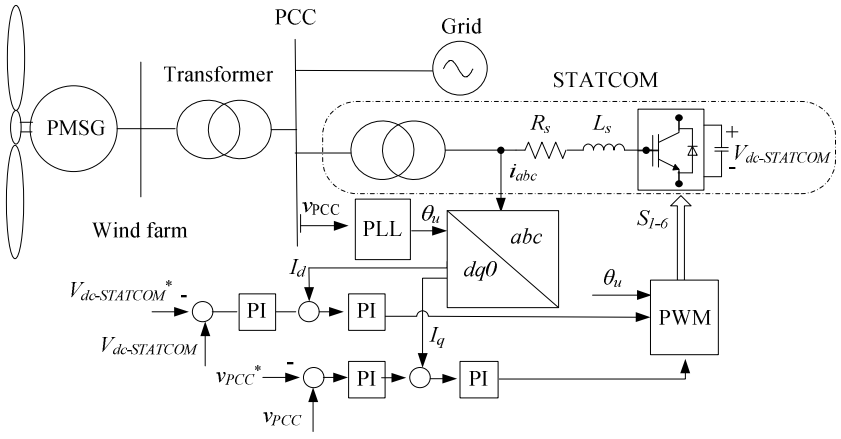

Figure 4.12. STATCOM Connection for grid connected wind farm.

A STATCOM is faster, smaller and has higher control bandwidth than a SVC and with additional capability of injecting high currents at low voltage levels. As for LVRT, the most relevant feature of the STATCOM is its inherent ability to increase the transient stability margin by injecting a controllable reactive current independent of the grid voltage [4.43]. shows a basic STATCOM used for LVRT capability with wind turbines [4.44]. STATCOMs are often used to improve power factor and voltage stability at network nodes. Because of the switching devices employed, it can react faster than an SVC and can vary its response continuously. Battery storage may also be incorporated onto the DC bus to allow for active power regulation as well.

ii- Series Voltage Compensation:

- **Thyristor Controlled Series Capacitor (TCSC):**

The basic structure of a TCSC is shown in Figure 4.13 [4.45]. It is constituted by three parts: series compensating capacitor *C*, bypass inductance *L*, and bi-directional thyristors $T_1$and T_2 [4.46]. When a grid fault occurs, the effective impedance of the TCSC can be increased almost immediately by controlling the firing angle of T_1 and T_2, thus increasing the power transfer capability of the line. Using a TCSC, the voltage is compensated and the short circuit current is limited. In spite of having good over-current capability, TCSCs suffers from a limited operating range. [4.47]

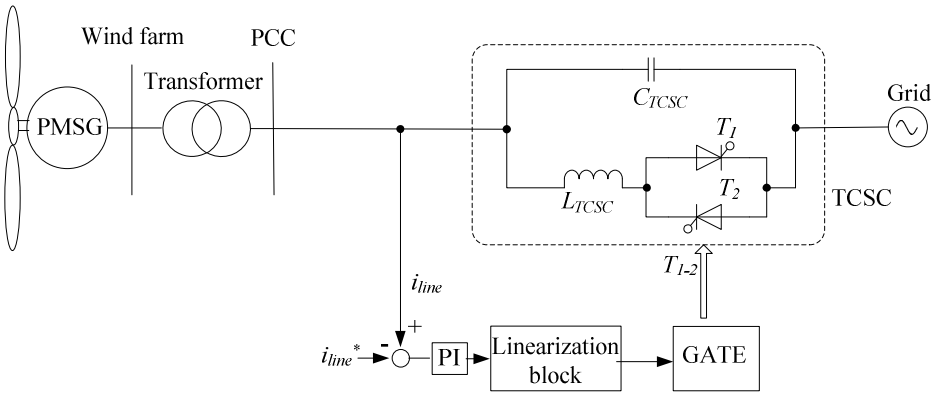

Figure 4.13 Configuration for thyristor controlled series capacitor for wind farm.

- **Static Synchronous Series Compensator (SSSC)**

As SSSC consists of a VSI connected in series through a coupling transformer to a compensated line as shown in figure 4.14 [4.48]. The SSSC creates an equal and opposite

voltage to the dc-link voltage rise experienced during the voltage dip. A source of energy is required for providing and maintaining the dc-link voltage, compensating the SSSC losses. An SSSC has a larger operating range than a TCSC, but has a complex configuration and requires additional protection arrangements to handle over-currents [4.49].

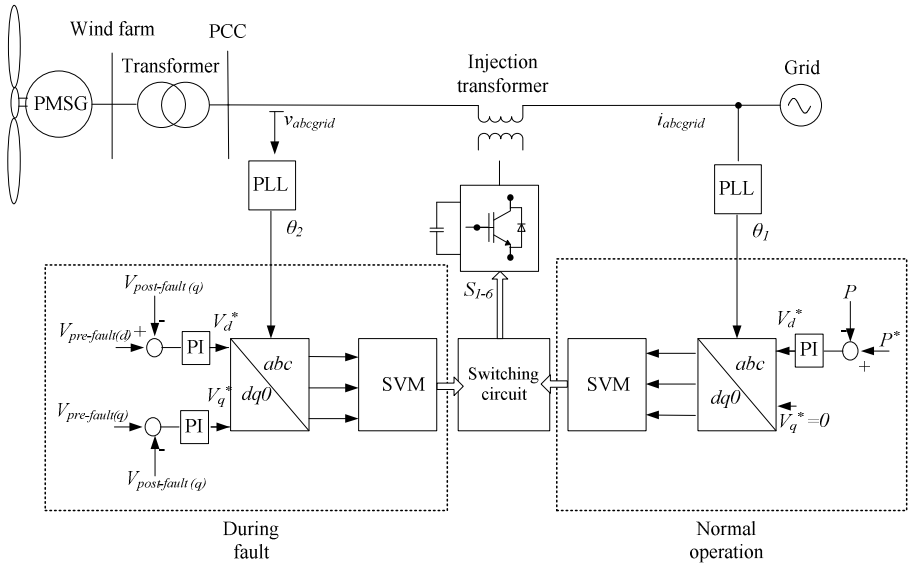

Figure 4.14. Control strategy for a static synchronous series compensator.

- **Dynamic Voltage Restorer (DVR):**

A Dynamic Voltage Restorer (DVR) is a power electronics based controller that provides flexible voltage control at the PCC with the utility distribution line for voltage quality improvement. If a dc-voltage source is connected to the DVR dc-bus, the compensator can inject both active and reactive power into the distribution system [4.50]. The DVR consists on a three-phase converter, connected via a transformer and with a load element (or source) in the dc-side of the converter, as shown in figure 4.15. When a voltage dip occurs, the DVR injects synchronized voltage which is the difference between the voltage prior to fault occurrence and the fault voltage. The injected voltage can vary in amplitude and phase allowing active and reactive power exchange between lines. The energy storage device compensates network voltage sags and improves LVRT capability [4.51-53].

- **Magnetic Energy Recovery Switch (MERS)**

A MERS is a series FACTS controller which has a simpler configuration and lower cost over-current protection with the same capacitive operating range as the SSSC [4.54]. With new low on-state voltage IGBT, MERS are attractive as the initial on state losses are low

[4.55]. One MERS is needed in each phase for a three-phase configuration, where in single-phase operation the configuration is similar to a single-phase full bridge using four switches but the control differs and the size of the capacitor is significantly smaller. The approach is shown in figure 4.16. The MERS is connected between the grid and the main wind farm transformer arm where it injects a series capacitive voltage for grid support. There is a mechanical by-pass switch that can be used during normal operation to reduce losses or for protection. The MERS could be used during steady state operation to improve the wind farm voltage profile [4.56, 4.57].

iii- Combined Series and Shunt Compensation:

A unified power flow controller (UPFC) as shown in figure 4.17 is a back-to-back combination of a shunt converter (STATCOM) and a series converter (SSSC), which are coupled by a common dc-link, to allow bi-directional flow of active power between the series and shunt terminals of the converters. The series converter injects a voltage which has two orthogonal components where the *d*-axis component contributes to magnitude variation and the *q*-axis component contributes to the phase angle. The shunt converter functionality can be a reactive source compensation (providing inductive or capacitive VAr) or a voltage regulator [4.59]. For these reasons, the UPFC can be used to enhance the LVRT capability, with energy storage [4.60].

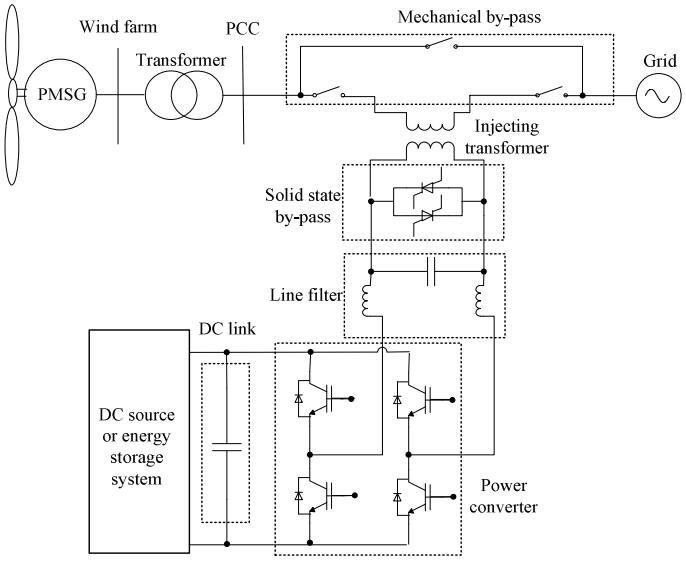

Figure 4.15. Dynamic voltage restorer in wind energy conversion systems.

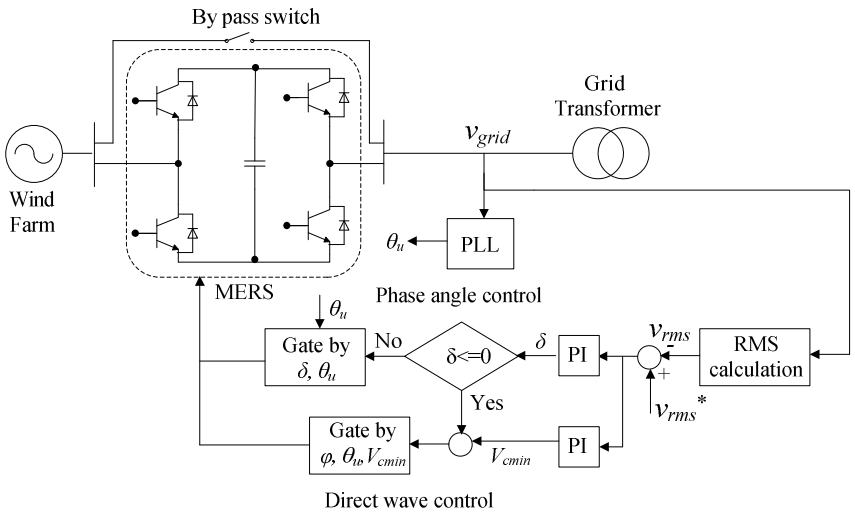

Figure 4.16. Single phase series compensating magnetic energy recovery switch [4.58].

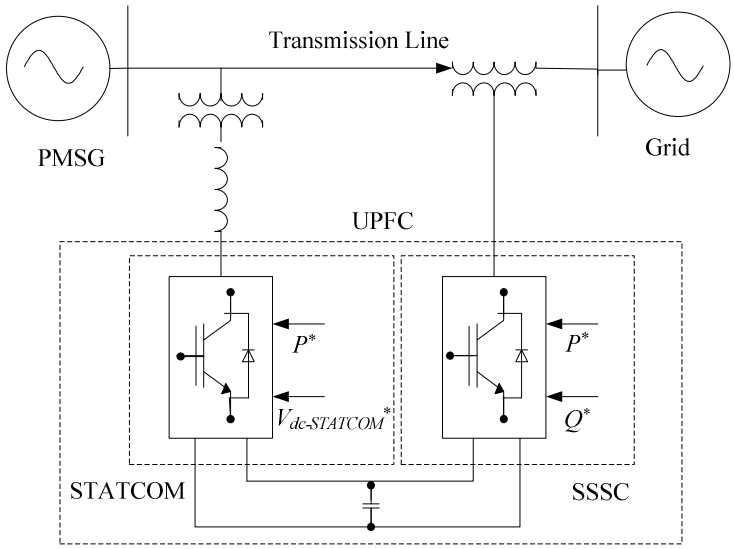

Figure 4.17. Schematic Diagram for a UPFC.

4.2 Magnetic Amplifier

Magnetic amplifiers, also known as transductors, have been used for many years in many applications such as in instrumentation, relays, position servo mechanisms, voltage and frequency control, and automatic battery chargers [4.61]. The magnetic amplifier offers high efficiency, reliability, ruggedness and high overload capability. Research has been conducted into its non-linear characteristics [4.62], steady-state and transient behaviour

[4.63], possible circuit configurations for single and three phase operation [4.64, 4.65], and designs for many applications [4.66, 4.67].

To the author's knowledge, the magnetic amplifier has not been used as a method for improving WT ride-through capability. For this reason, the following sections will explain the theory of operation, possible configurations, control aspects, and parameter determination procedures for using magnetic amplifiers as LVRT capability enhancers.

4.2.1 Theory of Operation and Possible Configurations

The simplest magnetic amplifier consists of a single ferromagnetic core having two windings, namely, a main or ac-coil winding N_1 and a dc or control winding N_2. The reactor is shown in figure 4.18. The control winding is connected to a dc- controlled source and the main winding is connected in series with the ac load. When the control current is varied, the impedance of the main winding changes, thereby affecting and determining the output voltage appearing across the load. However, an interaction between the control and main circuit exists due to the mutual induction between the dc and ac windings. For this reason, modification to figure 4.18 (a) is made and gives the new configuration shown in figure 4.18 (b). Having two separate core elements with series control and series main windings causes the induced voltage to cancel, thereby reducing the mutual effect [4.62]. N'_{1a} and N''_{1a} represent the two main winding coils, while N'_{2a} and N''_{2a} represent the two control winding coils as indicated in figure 4.19.

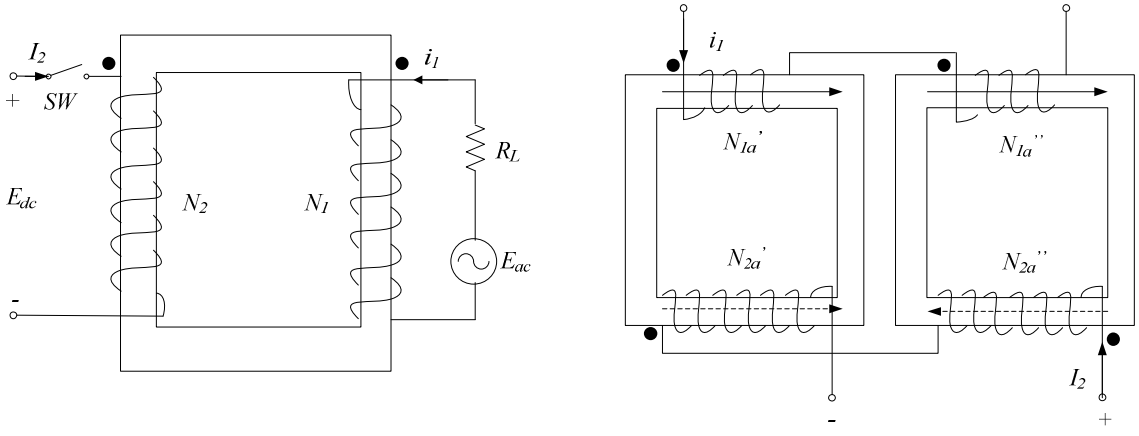

(a) (b)

Figure 4.18. Magnetic amplifier configuration: (a) simplest configuration and (b) configuration having two cores.

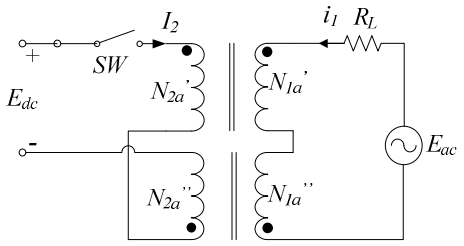

Figure 4.19. Two sections magnetic amplifier with series opposing control winding.

Assume the current flowing in control winding is I_{w2} and that in the main winding is i_{w1}. The dc-control circuit is energized from a dc-source, E_{dc} and the load resistance connected to the main winding is R_L and is excited from the main winding alternating source, E_{ac}. If the switch SW is opened, the current i_{w1} is determined by the circuit's inductive reactance, X_1 and the applied voltage E_{ac}. The total flux in this case is produced by the ac-winding only and the inductance of the coil is determined according to:

$$L = \frac{N\varphi}{I} \tag{4.6}$$

where N is the number of turns in the coil and φ is the magnetic flux linkage due to the current *I*.

Assume that the dc-control winding creates a magnetizing force in the core at H_c of figure 4.20 (a), if the magnetizing force of the main (ac) winding is represented by a sine-wave ABCDE, the resulting flux density will swing between B_2 and B_1. This small variation in flux density ΔB indicates that the flux linkage is small and thus the inductive reactance of the ac coil is low. Now assume that the dc-winding control current has decreased to point H_c of figure 4.20 (b), having the same magnetizing force as that of part (a) and operating in the linear part of the *BH* curve. Figure 4.20 (b) shows that even with the same variation in magnetizing force ΔH, large variation in the magnetizing flux density ΔB are experienced swinging between B_2 and B_1. With large flux density operating in part (b) of figure 4.20, the inductance seen by the ac winding is large thus blocking the flow of current in the main ac winding. Thus, the dc-current applied to the control winding with SW closed will create a magnetic flux and in effect will determine the magnetization of the core as shown in figure 4.21. The total flux will be the sum of the fluxes contributed by both N_1 and N_2 [4.64]. Moreover, the ac winding inductance depends on the saturation or non-saturation

condition of the core; having a high value in a non-saturated condition and a low value in the saturated region.

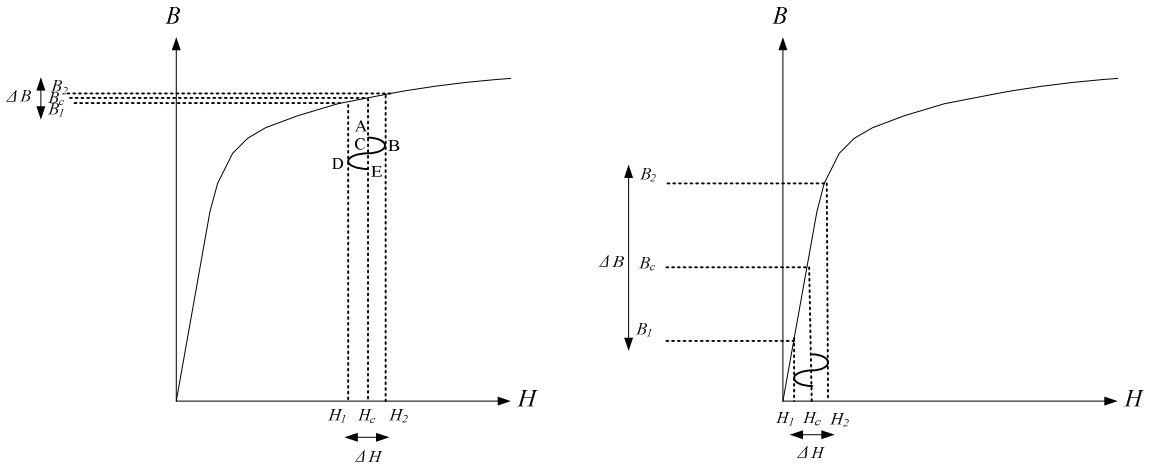

Figure 4. 20. Flux and MMF of transductor during steady-state operation (a) saturation and (b) un-saturation.

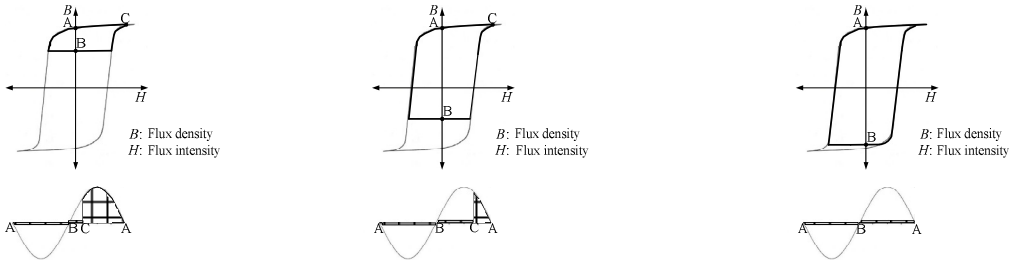

Figure 4.21. Flux control and output waveform characteristics of a simple half-wave magnetic amplifier: (a) large output, (b) small output, and (c) cut-off.

The exact method of effecting control of the reactor flux level, which in turn will determine the time at which saturation occurs, can vary. Also the exact manner of inter-connections between the magnetic amplifier, main ac supply, and load can assume different configurations. The basic principles of operation, however, remain unchanged [4.61]. Another modification can be made to the circuit which includes a diode in series with each of the two main winding coils as shown in figure 4.22. In this case, full utilization of the alternating current would give higher efficiency and better waveforms and reduce the time delay that can be up to half a cycle of the supply frequency [4.68].

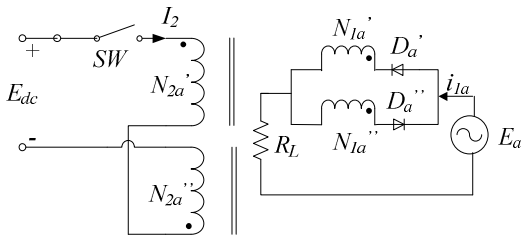

Figure 4.22. Self-saturable magnetic amplifier.

Figure 4.23 shows the basic configuration for a three phase arrangement which consists of six magnetic amplifier elements and six diodes.

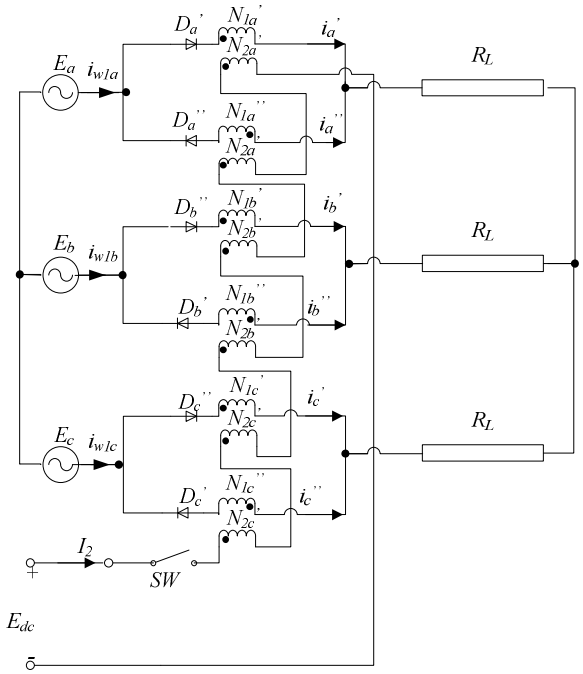

Figure 4.23. Three-phase 3-element full-wave magnetic amplifier circuit.

From the circuit arrangements, it is useful to highlight some important aspects to be considered in designing magnetic amplifiers:

1. The magnetizing curve should be steep, so that a slight change in I_{w2} produces a large change in the output power, i.e. the amplification is large. The magnetizing curve should also be as straight as possible. To achieve that, it is evident that the material should be homogeneous, and that air-gaps should be avoided [4.69]

2. Time lag: The magnetic amplifier is a resistive-inductive electrical component, so that a time lag exists between the application of the control voltage and the attainment of the full output current. Any closed circuit linking the two cores is inductively coupled to the control circuit, and increases the time lag. The time-constant and power amplification are directly related. Also, the time constant is inversely related to the effective number of turns and the control winding frequency [4.70].
3. Efficiency: Large magnetic amplifiers at low frequencies tend to have higher efficiency than smaller units. In practice, magnetic amplifiers are known for their high efficiency, as with transformers [4.71].

Other factors that might be taken into consideration when designing magnetic amplifiers are power gains and size as detailed in [4.72, 4.73].

4.2.2. Magnetic Amplifier for LVRT Capability Enhancement

This section provides an explanation as to how a magnetic amplifier within a PMSG will provide blocking capabilities during grid voltage dips to limit any dc-link voltage rise.

Each of the magnetic amplifier units will be treated as a single phase transformer, whose turns ratio is $N_1 : N_2$. The main winding of N_1 turns is designed according to

$$E_{ac} = N_1 \frac{d\varphi}{dt} \tag{4.7}$$

The control winding composed of N_2 turns is connected to an auxiliary controlled dc-current source which delivers the control winding current, I_{w2}, required to shift the magnetic amplifier operation from saturation to unsaturation:

$$N_2 I_{w2} = - N_1 I_{w1} \tag{4.8}$$

The interaction between the load current flowing in the main winding, I_{w1} and the control winding current I_{w2}, tends to saturate the core material, where no further magnetization is induced by increasing the field intensity (*H*). However, the control winding current, I_{w2} action may cancel the load current effect and demagnetize the core, thus forcing the operating point away from the saturation region to the linear region. Shifting magnetic amplifier operation from the saturation to the linear zone allows the effective impedance of the magnetic amplifier to change from a low to high value. Figure 4.24 shows the suggested magnetic topology in a 3-phase configuration where it is employed between the

generator terminals and the diode rectifier unit, while figure 4.25 is another suggested magnetic amplifier connection, inserted in the chopper circuit.

During normal operation of the electrical grid and in the absence of any grid faults, the magnetic amplifier operates in the saturation zone and effectively has low impedance (with relative permeability equal to that of air). At this point the amplifier can be treated as a filter for the generator current i_{gen} in the 3-phase topology, or as a filter in the dc-side topology for the boost current I_{dc} if inserted in the boost chopper, with minimum voltage drop across its main winding terminals. However, with a sudden voltage dip, the amplifier will sense the fault occurrence and subsequent control action will shift its operation to the linear zone where it exhibits a large impedance value (with relative permeability of the core). It is suggested that the magnetic amplifier can either be inserted between the PMSG and rectifier terminal, or in the boost chopper circuit, thus limiting the dc-link voltage rise and protecting the power converters from damage.

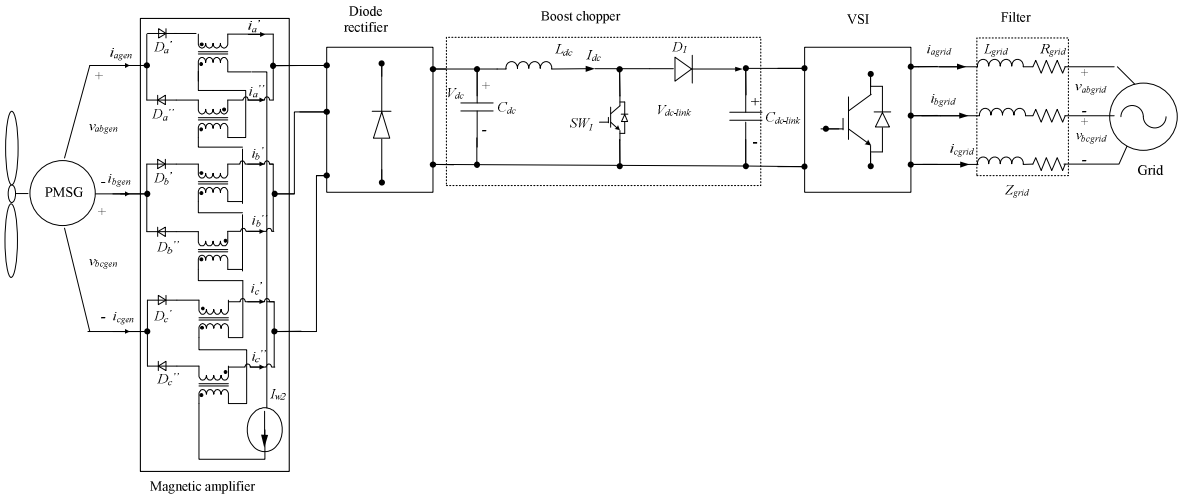

Figure 4.24. WECS with configuration #1 3-phase topology magnetic amplifier.

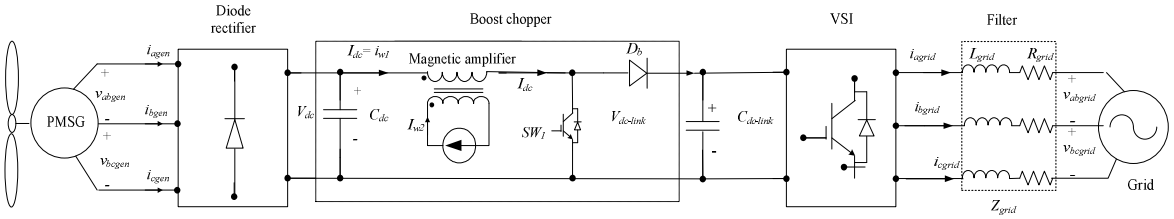

Figure 4.25. WECS with configuration #2 dc-side magnetic amplifier topology.

4.2.3. Control Circuit of Magnetic Amplifier

To shift the amplifier operation from the saturated region to the un-saturated region of the *BH* curve, a dc-chopper circuit is required. From (4.8), if the effective number of turns for the primary and secondary windings N_1 and N_2 were equal, a large control winding current I_{w2} would be required to demagnetize the magnetic amplifier core. Consequently, the converter required to source the large current would be highly rated in terms of voltage and current. Thus in order to control the magnetization process of the magnetic amplifier, the effective number of secondary turns N_2 is set higher than the primary number of turns N_1 so that a small signal I_{w2} can in fact control large current I_{w1} flowing in the main winding. Also, since the rate of change of flux $d\varphi/dt$ is inversely proportional to the effective number of turns N, choosing N_2 will affect the rate of change of the magnetic flux in the magnetic amplifier core thus affects the value of the associated inductance. The power converter responsible for controlling the magnetic amplifier current I_{w2} is a continuous current source. Different controlled current sources can be used to generate the control winding current, however a converter producing continuous output current is needed for controlling the magnetic amplifier in both configurations. Discontinuity of I_{w2} will tend to magnetize and demagnetize the core at a frequency equal to the chopper frequency, thus disrupting amplifier action. A simple class 'A' buck chopper is used as shown in figure 4.26 where V_{ch} is the input supply voltage for the chopper, I_{ch} is the input chopper current and I_{w2} is the output chopper current which is the current supplied to the control winding of the magnetic amplifier [4.74].

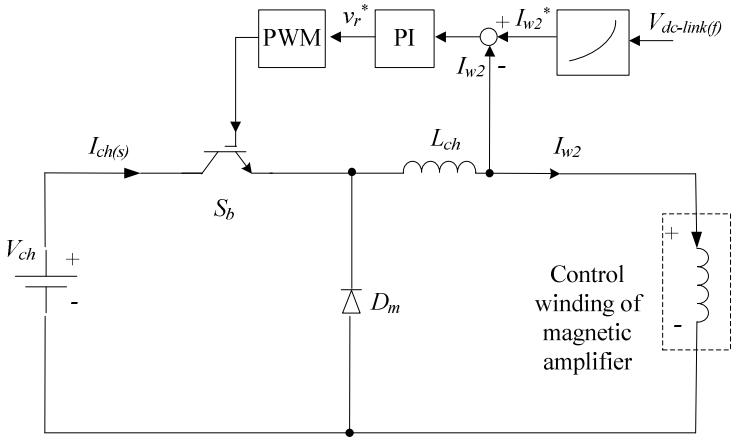

Figure 4.26. Buck chopper current source circuit.

The buck chopper switch S_b operates by comparing the reference signal v_r^* with a constant carrier triangular signal v_c whose carrier frequency is f_{ch} as shown in figure 4.27. The duty cycle D is defined by

$$\delta = \frac{t_{on}}{T} = t_{on} f_{ch} \tag{4.9}$$

This chopper topology results in discontinuous input current, $I_{ch(s)}$ as shown in figure 4.27 (c) but, as desired, continuous output current I_{w2}. The chopper input power can be calculated using (4.10):

$$P_{ch} = V_{ch}\overline{I_{ch}} = \delta\, V_{ch} I_{ch} \tag{4.10}$$

The freewheel diode D_m conducts due to energy stored in the inductor, L_{ch}, and the inductor current, which is the chopper output current, continues to flow through the control winding. The chopper output current, I_{w2}, is shown in figure 4.27 (d).

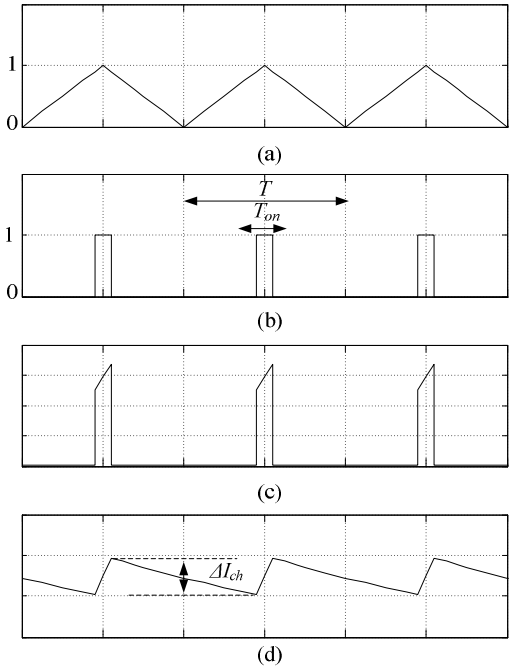

Figure 4.27. Buck chopper waveforms: (a) PWM generation, (b) gate voltage, (c) chopper input current, $I_{ch(s)}$, and (d) chopper output current, I_{w2}.

The chopper current ripple, ΔI_{ch}, depends inversely on the chopping frequency. Increasing the chopping frequency decreases the load current ripple and decreases the inductance of the smoothing series inductor, L_{ch} . To ensure continuous current, the system parameters

should be designed to satisfy the condition $L_{ch}\,T_{ch} \gg R_{ch}$, where R_{ch} and L_{ch} represent the total equivalent output impedance of the magnetic amplifier.

For the 1.5MW system, the chopper is used with the magnetic amplifier as it circulates the chopper output current in the control winding which has low resistance. This low load resistance determines the maximum steady-state chopper current when D≈1. During normal operation, D is set close to 1 where maximum steady state chopper current is injected in the control winding ensuring saturation of the magnetic amplifier. During the voltage dip event, D changes depending on the dc-link voltage, $V_{dc-link(f)}$ during the fault, which sets the control winding current reference I_{w2}^{*}. A dc-voltage source of 500 V is used to generate the control winding current, I_{ch}, of 500A when the duty cycle approaches 1 with chopping frequency, f_{ch}, of 5 kHz. A smoothing inductance, L_{ch}, of 10 mH is used to ensure continuous output current operation with a maximum ripple current of less than 1 A. The reason for the high current and voltage ratings of the control circuitry is due to the fact that the parameters chosen are for simulation purposes since no detailed design for the magnetic amplifier has been carried out and the design is based on silicon steel cores. With higher permeability materials along with an optimised design for the core and control circuit, it is believed that the power rating of both the magnetic amplifier and control circuitry will be reduced accordingly.

4.3 Discussion

Magnetic amplifiers are characterized by electrical isolation, high efficiency and high short circuit capability, and thus can be utilized as a series compensation technique for LVRT capability enhancement of PMSG WECS. Changing the magnetic amplifier control winding current alters the main winding effective impedance, thus the magnetic amplifier acts as a variable inductance if inserted between an emf source and a load. Two configurations are suggested and will be tested for LVRT capability enhancement namely a 3-phase topology (configuration #1) and a dc-side topology (configuration #2). In both configurations magnetic amplifier elements are driven into saturation by the control winding current during normal operation, while if a fault occurs, the dc-control current changes the operation of the magnetic amplifier from the saturated to the unsaturated state thus supporting a larger voltage drop across its terminals whilst presenting high inductance. It is expected that both magnetic amplifier topologies will perform the function

of blocking any dc-link voltage rise associated with a grid voltage dip incident, hence, the amplifier will limit such rise, thereby guarantying successful ride-through operation. While in the 3-phase configuration the magnetic amplifier acts as a switch between the PMSG terminals and the diode rectifier unit and maintains the energy balance during voltage dips through storing energy in the rotor inertia, the dc- side topology stores energy in the magnetic field of the magnetic amplifier which is proportional to the value of inductance and the square of the ac winding current. Both configurations are modelled and tested for ride-through capability in Chapter 5 and WECS performance is studied. Practical validation is presented in Chapter 6.

4.5 Summary

Grid disturbances such as severe voltage dips caused by short-circuit faults can lead to power-generating units being disconnected from the grid, which may cause grid instability. To avoid this, the grid code requires power-generating units to remain connected and continuously operated even if the voltage dips reaches low values. This chapter reviewed the methods for LVRT capability enhancement applied to individual turbines and at a wind farms level. Among the techniques reviewed are: blade pitch angle control, active crow bar techniques, energy storage systems using flywheels, super capacitors, batteries and super conducting coils. Other methods for LVRT improvement can be through de-loading of the WT by MSC and GSC control. At the wind farm scale, FACTS have been utilized which are divided into series, shunt and combined configurations.

Historically, magnetic amplifiers have been used in many applications owing to their high efficiency, reliability, simplicity, and ruggedness. They have the ability to control a large current signal (either ac or dc) flowing in the main winding using a small dc-signal in the control winding to control the magnetization characteristics of the magnetic core. The magnetic theory of operation and available configurations were explained in this chapter, with a recommendation for use as a technique for LVRT capability enhancement. Two configurations were suggested for PMSG WECS. Configuration #1 is a three-phase magnetic amplifier topology based on using six magnetic elements and six diodes inserted between the generator terminals and the diode rectifier unit. Configuration #2 uses only one magnetic element inserted in a boost chopper. Both configurations will be tested for successful ride through operation in the following chapter.

References

[4.1] K. Ki-Hong, *et al.*, 'LVRT Scheme of PMSG Wind Power Systems Based on Feedback Linearization', IEEE Transactions on Power Electronics, Vol. 27, 2012. pp. 2376-2384.

[4.2] F. Tang, *et al.*, 'A Novel LVRT Strategy for Direct-Drive Wind Turbines Based on Permanent Magnet Synchronous Generator', 7th International Power Electronics and Motion Control Conference (IPEMC), 2012. pp. 2228-2233.

[4.3] Y. Xiao-ping, *et al.*, 'Low Voltage Ride-Through of Directly Driven Wind Turbine with Permanent Magnet Synchronous Generator', Power and Energy Engineering Conference (APPEEC), March 2009.

[4.4] L. Jun, *et al.*, 'A Novel Power-Flow Balance LVRT Control Strategy for Low-Speed Direct-Drive PMSG Wind Generation System', 36th Annual Conference on IEEE Industrial Electronics Society (IECON), 2010. pp. 748-753.

[4.5] J. F. Conroy and R. Watson, 'Low-Voltage Ride-through of a Full Converter Wind Turbine with Permanent Magnet Generator', IET Renewable Power Generation, Vol. 1, 2007. p. 182.

[4.6] A. H. Kasem, *et al.*, 'An Improved Fault Ride-through Strategy for Doubly Fed Induction Generator-Based Wind Turbines', IET Renewable Power Generation, Vol. 2, 2008. pp. 201-214.

[4.7] M. Tsili and S. Papathanassiou, 'A Review of Grid Code Technical Requirements for Wind Farms', IET Renewable Power Generation, Vol. 3, 2009. p. 308.

[4.8] M. Rizo, *et al.*, 'Low Voltage Ride-through of Wind Turbine Based on Interior Permanent Magnet Synchronous Generators Sensorless Vector Controlled', IEEE Energy Conversion Congress and Exposition (ECCE), 2010. pp. 2507-2514.

[4.9] R. Cardenas, *et al.*, 'Overview of Control Systems for the Operation of DFIGs in Wind Energy Applications', IEEE Transactions on Industrial Electronics, Vol. 60, 2013. pp. 2776-2798.

[4.10] S. Samineni, *et al.*, 'Modeling and Analysis of a Flywheel Energy Storage System for Voltage sag Correction', IEEE Transactions on Industry Applications, Vol. 42, 2006. pp. 42-52.

[4.11] O. C. Montero-Hernandez and P. N. Enjeti, ‘A Low Cost Approach to Provide Ride-through for Critical Loads’, Sixteenth Annual IEEE Applied Power Electronics Conference and Exposition (APEC), 2001. pp. 917-923 vol.2.

[4.12] R. S. Weissbach, G. G. Karady, and R. G. Farmer, ‘Dynamic Voltage Compensation on Distribution Feeders using Flywheel Energy Storage’, IEEE Transactions on Power Delivery, Vol. 14, 1999. pp. 465-471.

[4.13] D. Rekioua,‘Wind Power Electric Systems Modeling, Simulation and Control’, Springer, 2012.

[4.14] L. Barote*, et al.*, ‘Stand-alone Wind System with Vanadium Redox Battery Energy Storage ’, 11th International Conference on Optimization of Electrical and Electronic Equipment (OPTIM), 2008.

[4.15] L. Barote, C. Marinescu, and M. Georgescu, ‘VRB Modeling for Storage in Stand-alone Wind Energy Systems ’, IEEE Bucharest PowerTech, Bucharest 2009.

[4.16] L. Barote and C. Marinescu, ‘A New Control Method for VRB SOC Estimation in Stand-alone Wind Energy Systems ’, International Conference on Clean Electrical Power, 2009.

[4.17] W. Wenliang*, et al.*, ‘Energy Storage Based LVRT and Stabilizing Power Control for Direct-Drive Wind Power System’, International Conference on Power System Technology (POWERCON), 2010. pp. 1-6.

[4.18] W. Wang*, et al.*, ‘Energy Storage based LVRT and Stabilizing Power Control for Direct-Drive Wind Power System’, International Conference on Power System Technology (POWERCON), 2010.

[4.19] G. Joos, ‘Wind Turbine Generator Low Voltage Ride through Requirements and Solutions’, IEEE Power and Energy Society General Meeting - Conversion and Delivery of Electrical Energy in the 21st Century, 2008.

[4.20] C. Abbey*, et al.*, ‘Power Electronic Converter Control Techniques for Improved Low Voltage Ride Through’, 37th IEEE Power Electronics Specialists Conference, (PESC), 2006.

[4.21] M. H. Ali,‘Wind Energy Systems: Solutions for Power Quality and Stabilization’, Taylor & Francis, 2012.

[4.22] F. A. Bhuiyan and A. Yazdani, 'Energy Storage Technologies for Grid-Connected and off-Grid Power System Applications', IEEE Electrical Power and Energy Conference (EPEC), 2012. pp. 303-310.

[4.23] A. M. S. Yunus, A. Abu-Siada, and M. A. S. Masoum, 'Improvement of LVRT Capability of Variable Speed Wind Turbine Generators using SMES Unit', IEEE PES Innovative Smart Grid Technologies Asia (ISGT), 2011. pp. 1-7.

[4.24] A. M. S. Yunus, A. Abu-Siada, and M. A. S. Masoum, 'Effect of SMES Unit on the Performance of Type-4 Wind Turbine Generator during Voltage Sag', IET Conference on Renewable Power Generation (RPG), 2011. pp. 1-4.

[4.25] Z. Caihong*, et al.*, 'Development and Test of a Superconducting Fault Current Limiter-Magnetic Energy Storage (SFCL-MES) System', IEEE Transactions on Applied Superconductivity, Vol. 17, 2007. pp. 2014-2017.

[4.26] S. Nomura*, et al.*, 'Technical and Cost Evaluation on SMES for Electric Power Compensation', IEEE Transactions on Applied Superconductivity, Vol. 20, 2010. pp. 1373-1378.

[4.27] S. M. Said, M. M. Aly, and M. Abdel-Akher, 'Application of Superconducting Magnetic Energy Storage (SMES) for Voltage Sag/Swell Supression in Distribution System with Wind Power Penetration', IEEE 16th International Conference on Harmonics and Quality of Power (ICHQP) 2014. pp. 92-96.

[4.28] M. H. Ali and R. A. Dougal, 'Comparison of SMES and SFCL for Transient Stability Enhancement of Wind Generator System', IEEE Energy Conversion Congress and Exposition (ECCE), 2010. pp. 3382-3387.

[4.29] A. A. Hussein and M. H. Ali, 'Comparison between DVR and SFCL for Fault Ride Through Capability Improvement of Fixed-Speed Wind Generator', IEEE PES T&D Conference and Exposition, 2014. pp. 1-5.

[4.30] M. E. Elshiekh, D. A. Mansour, and A. M. Azmy, 'Improving Fault Ride-Through Capability of DFIG-Based Wind Turbine Using Superconducting Fault Current Limiter', IEEE Transactions on Applied Superconductivity, Vol. 23, 2013. pp. 5601204-5601204.

[4.31] I. Ngamroo and T. Karaipoom, 'Cooperative Control of SFCL and SMES for Enhancing Fault Ride Through Capability and Smoothing Power Fluctuation of

DFIG Wind Farm', IEEE Transactions on Applied Superconductivity Vol. 24, 2014. pp. 1-4.

[4.32] G. Wenyong, X. Liye, and D. Shaotao, 'Enhancing Low-Voltage Ride-Through Capability and Smoothing Output Power of DFIG With a Superconducting Fault-Current Limiter- Magnetic Energy Storage System', IEEE Transactions on Energy Conversion, Vol. 27, 2012. pp. 277-295.

[4.33] A. Abedini and A. Nasiri, 'Applications of Super Capacitors for PMSG Wind Turbine Power Smoothing', 34th Annual Conference of IEEE Industrial Electronics (IECON), 2008. pp. 3347-3351.

[4.34] L. Qicheng and L. Yuping, 'An Integration of Super Capacitor Storage Research for Improving Low-Voltage-Ride-Through in Power Grid with Wind Turbine', Power and Energy Engineering Conference (APPEEC), 2012. pp. 1-4.

[4.35] C. Abbey and G. Joos, 'Supercapacitor Energy Storage for Wind Energy Applications', IEEE Transactions on Industry Applications, Vol. 43, 2007. pp. 769-776.

[4.36] C. Farcas*, et al.*, 'Modeling and Simulation of Supercapacitors', 15th International Symposium for Design and Technology of Electronics Packages (SIITME), 2009. pp. 195-200.

[4.37] Q. Li*, et al.*, 'On the Determination of Battery Energy Storage Capacity and Short-Term Power Dispatch of a Wind Farm', IEEE Transactions on Sustainable Energy, Vol. 2, 2011. pp. 148-158.

[4.38] F. Deng and Z. Chen, 'Low-Voltage Ride-through of Variable Speed Wind Turbines with Permanent Magnet Synchronous Generator', 35th IEEE Annual Conference on Industrial Electronics (IECON) 2009.

[4.39] S. Hojoon, J. Hyun-Sam, and S. Seung-Ki, 'Low Voltage Ride Through (LVRT) Control Strategy of Grid-Connected Variable Speed Wind Turbine Generator System', IEEE 8th International Conference on Power Electronics and ECCE Asia (ICPE & ECCE), 2011. pp. 96-101.

[4.40] M. Singh, V. Khadkikar, and A. Chandra, 'Grid Synchronisation with Harmonics and Reactive Power Compensation Capability of a Permanent Magnet Synchronous Generator-based Variable Speed Wind Energy Conversion System ', IET Power Electronics, Vol. 4, 2011. pp. 122 - 130

[4.41] Z. Junjie, *et al.*, 'Enhancement Voltage Stability of Wind Farm Access to Power Grid by Novel SVC', 4th IEEE Conference on Industrial Electronics and Applications (ICIEA), 2009. pp. 2262-2266.

[4.42] L. Huan-ping and Y. Jin-ming, 'The Performance Research of Large Scale Wind Farm Connected to External Power Grid', 3rd International Conference on Power Electronics Systems and Applications (PESA), 2009. pp. 1-5.

[4.43] M. Molinas, J. A. Suul, and T. Undeland, 'Low Voltage Ride Through of Wind Farms With Cage Generators: STATCOM Versus SVC', IEEE Transaction on Power Electronics Vol. 23, 2008. pp. 1104-1117.

[4.44] M. H. Ali and B. Wu, 'Comparison of Stabilization Methods for Fixed-Speed Wind Generator Systems', IEEE Transaction on Power Delivery Vol. 25, JANUARY 2010. pp. 323-331.

[4.45] R. K. Varma, Y. Semsedini, and S. Auddy, 'Mitigation of Subsynchronous Oscillations in a Series Compensated Wind Farm with Thyristor Controlled Series Capacitor (TCSC)', Power Systems Conference: Advanced Metering, Protection, Control, Communication, and Distributed Resources (PSC), 2007. pp. 331-337.

[4.46] M. Khederzadeh, 'Application of TCSC to Enhance Power Quality', 42nd International Universities Power Engineering Conference (UPEC) 2007. pp. 607-612.

[4.47] E. V. Larsen, *et al.*, 'Characteristics and Rating Considerations of Thyristor Controlled Series Compensation ', IEEE Transactions on Power Delivery Vol. 9, Apr 1994. pp. 992 - 1000

[4.48] S. Raphael and A. M. Massoud, 'Compensator for Low Voltage Ride through Capability of Wind Energy Systems', IET Conference on Renewable Power Generation (RPG), 2011. pp. 1-6.

[4.49] S. Zhang, *et al.*, 'Advanced Control of Series Voltage Compensation to Enhance Wind Turbine Ride-through', in IEEE Transaction on Power Electronics ed, 2011, p. 1.

[4.50] G. Nicolaescu, H. Andrei, and S. Radulescu, 'Dynamic Voltage Restorer Response Analysis for Voltage Sags Mitigation in MV Networks with Secondary Distribution Configuration', 14th International Conference on Environment and Electrical Engineering (EEEIC), 2014. pp. 40-45.

[4.51] M. H. Haque, 'Compensation of Distribution System Voltage Sag by DVR and D-STATCOM', IEEE Porto Power Tech Proceedings, 2001.

[4.52] C. Wessels, F. Gebhardt, and F. W. Fuchs, 'Fault Ride-Through of a DFIG Wind Turbine Using Dynamic Voltage Resotrer', IEEE Transaction on Power Electronics Vol. 26, 2011. pp. 807-815.

[4.53] M. N. Eskander and S. I. Amer, 'Mitigation of Voltage Dips and Swells in Grid-Connected Wind Energy Conversion Systems', ICCAS-SICE, 2009. pp. 885-890.

[4.54] J. A. Wiik, F. D. Wijaya, and R. Shimada, 'Characteristics of the Magnetic Energy Recovery Switch (MERS) as a Series FACTS Controller', IEEE Transactions on Power Delivery, Vol. 24, 2009. pp. 828-836.

[4.55] G. Wenming, *et al.*, 'A Survey on Recent Low Voltage Ride-Through Solutions of Large Scale Wind Farm', Power and Energy Engineering Conference (APPEEC) 2011.

[4.56] J. A. Wiik, O. J. Fonstelien, and R. Shimada, 'A MERS type Series FACTS Controller for Low Voltage Ride Through of Induction Generators inWind Farms', 13th European Conference on Power Electronics and Applications (EPE), 2009.

[4.57] T. Isobe, *et al.*, 'A Simple and Reliable Rectifier for PMSG Wind Turbines by Using Series Reactive Compensator Named MERS', 15th International Conference on Electrical Machines and Systems (ICEMS), 2012. pp. 1-6.

[4.58] C. Miao-miao, *et al.*, 'Voltage Control of Induction Generator Powered Distributed System using a New Reactive Power Compensator SVC-MERS', 15th International Power Electronics and Motion Control Conference (EPE-PEMC) 2012. pp. DS3b.7-1-DS3b.7-8.

[4.59] M. e. A. Kamarposhti, *et al.*, 'Comparison of SVC, STATCOM, TCSC, and UPFC Controllers for Static Voltage Stability Evaluated by Continuation Power Flow Method', IEEE Electrical Power & Energy Conference, 2008.

[4.60] S. Raphael and A. Massoud, 'Unified Power Flow Controller for Low Voltage Ride through Capability of Wind-Based Renewable Energy Grid-Connected Systems ', 8th International Multi-Conference on Systems, Signals & Devices 2011.

[4.61] C. W. Lufcy, 'A Survey of Magnetic Amplifiers', Proceedings of the IRE 1955. pp. 404-413.

[4.62] R. Feinberg, ‘A Review of Transductor Principles and Applications’, Journal of the Institution of Electrical Engineers,, Vol. 1951, 1951. pp. 40-41.

[4.63] C. S. Hudson, ‘A Theory of the Series Transductor’, Power Engineering Proceedings of the IEE - Part II Vol. 97, 1950. pp. 751-755.

[4.64] K. C. Parton, *et al.*, ‘Superconducting Power-System Transductor’, IEE Proceedings Generation, Transmission and Distribution, Vol. 128, 1981. pp. 235-242.

[4.65] A. U. Lamm, ‘Some Fundamentals of a Theory of the Transductor or Magnetic Amplifier’, Transactions of the American Institute of Electrical Engineers, Vol. 66, 1947. pp. 1078-1085.

[4.66] E. H. F.-. Smith,‘The Theory and Design of Magnetic Amplifiers’, Chapman and Hall 1966.

[4.67] Y. Shindo, *et al.*, ‘A Magnetic Amplifier using Nanocrystalline Soft Magnetic Material’, IEEE 8th International Conference on Power Electronics and ECCE Asia (ICPE & ECCE), 2011. pp. 1299-1306.

[4.68] S. B. Cohen, ‘Analysis and Design of Self-Saturable Magnetic Amplifiers’, Proceedings of the IRE Vol. 39, 1951. pp. 1009-1020.

[4.69] L. F. Borg, ‘Some Aspects of Magnetic Materials used in Transductors’, Journal of the Institution of Electrical Engineers, Vol. 1949, 1949. p. 138.

[4.70] H. M. Gale and P. D. Atkinson, ‘A Theoretical and Experimental Study of the Series-Connected Magnetic Amplifier’, Journal of the Institution of Electrical Engineers, Vol. 1949, 1949. pp. 161-163.

[4.71] S. Platt,‘Magnetic Amplifiers: Theory and Application’, Prentice-Hall, 1958.

[4.72] G. M. Ettinger, ‘Some Aspects of Half-Wave Magnetic Amplifiers’, Proceedings of the IEE - Part B: Radio and Electronic Engineering, Vol. 105, 1958. pp. 237-248.

[4.73] L. Austrin, D. Ribbenfjard, and G. Engdahl, ‘Simulation of a Magnetic Amplifier Circuit Including Hysteresis’, IEEE Transactions on Magnetics, Vol. 41, 2005. pp. 3994-3996.

[4.74] M. H. Rashid,‘Power Electronics: Circuits, Devices, and Applications’, Pearson Education, 2004.

CHAPTER FIVE

LVRT Capability Enhancement with a Magnetic Amplifier

According to the UK grid code reviewed in Chapter 3, a wind farm must stay connected for voltage drops down to 0% for up to 140 ms (seven cycles), caused by symmetrical or asymmetrical network faults. However, for those lasting more than 140 ms (seven cycles) caused by symmetrical faults, disconnection is not allowed above the curve shown in figure 3.10 [5.1]. Generating stations may encounter stability problems, depending on the type, magnitude and duration of the dip, as well as on the type and technology of the power station [5.2]. An abrupt drop of the grid voltage will cause a rise in the grid current and over-voltage on the dc-bus of the power converters, as demonstrated in the previous chapter. Without any protection, this will lead to the destruction of the converters. In addition, it may cause over-speeding of the wind turbine, which will threaten the safe operation of the turbine [5.3].
Use of magnetic amplifiers as a method for LVRT capability enhancement has been suggested in Chapter 4, with two possible topologies. This chapter analyzes the performance of a 1.5 MW WECS using MATLAB simulation for improving its LVRT ability when using the 3-phase and dc-side magnetic amplifier topologies.

5.1 Enhancement of LVRT Capability using Magnetic Amplifier

As demonstrated in Chapter 4, grid voltage dips can cause severe damage to the power converters due to the energy imbalance between P_{gen} and P_{grid} which must be transferred to the dc-link capacitor accompanied by a rapid rise in the capacitor's voltage [5.4]. Two proposed configurations will be introduced and investigated for ride-through capability in this research, based on a magnetic amplifier as a series voltage compensator to compensate the dc-link voltage rise.

Configuration #1; WECS using a 3-phase magnetic amplifier

Configuration #2; WECS using a dc-side magnetic amplifier

Both configurations are investigated using MATLAB simulation and tested for LVRT capability enhancement for the 1.5 MW WECS. The simulation analysis will expose any disadvantages and limitations of each approach.

5.2 Configuration #1: 3-phase Magnetic Amplifier Topology

As considered in Chapter 4, the magnetic amplifier element consists of two windings; the main winding and a control winding. They are connected so that the fluxes produced by both windings oppose each other [5.5]. The block diagram for the 1.5 MW WECS employing a magnetic amplifier with Configuration #1 is shown in figure 5.1. The main winding is inserted where the amplifier action is required and carries the normal line current, while the control winding carries dc-bias current from an isolated source (although the dc link could serve as the source). In normal operation, by feeding high dc-bias current in the control winding, the reactor operates in a saturated condition. The inductance depends on the saturated or non-saturated condition of the core, having a higher value in non-saturated condition and a lower value in saturated condition [5.6]. Thus by acting as variable impedance inserted during a fault, the magnetic amplifier blocks the excess energy stored by the dc-link capacitor during a fault and helps maintain the energy balance between the generation and grid side. Changing its control winding current I_{w2} changes the main winding effective impedance [5.7]. In this configuration, each of the three phases of the PMSG is split into two windings so as to avoid demagnetization of the magnetic amplifier during the negative half cycle of the supply voltage [5.8]. Also, each winding is connected in series with a rectifying diode which enables the amplifier cores to reach the saturation zone faster. The use of six magnetic elements and six power diodes adds extra cost and size to the WECS, and this is considered o be one of the disadvantage of this approach and any hardware approach [5.9].

The 1.5 MW system with Configuration #1 has been tested for enhancing WECS ride through capability. The same system parameters used in Chapter 4 have been used in the simulations. The results obtained are divided into machine and MSC side results found in figures 5.2 and 5.3, and grid side and GSC responses found in figures 5.4 and 5.5. The system has been

subjected to a 90% drop in the grid voltage for a 140 ms duration, starting at 0.3 s and ending at 0.44 s.

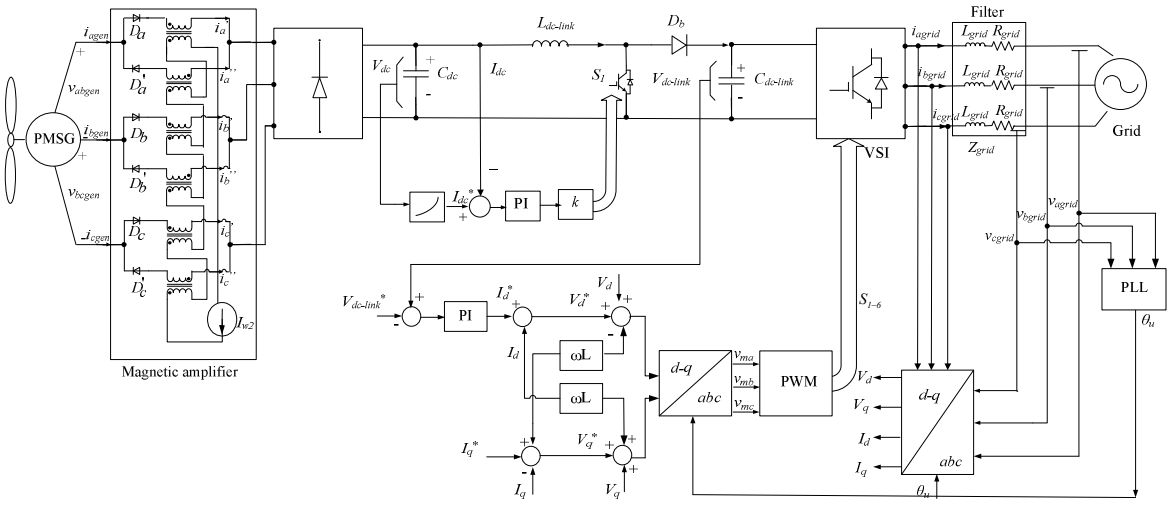

Figure 5.1. WECS with Configuration #1.

It is noticed that using magnetic amplifier Configuration #1 during the grid voltage dip event affects the performance of the generator. Figure 5.2 (a) and (b) present waveforms for the PMSG terminal line-to-line voltage v_{gen} and current i_{gen} respectively, and show changes in both the magnitude and shape of v_{gen} and i_{gen}. This is due to the high reflected magnetic amplifier impedance accompanied by the magnetic amplifier action in response to the network grid fault. A high impedance inserted between the generator terminals and the diode rectifier unit limits the generator current i_{gen} and at the same time alters the generator output voltage v_{gen}. With the change of v_{gen}, the associated generator rotational speed ω_r will increase while the electromagnetic torque T_e will decrease due to the increase in stored the rotor inertia during the fault as shown in figure 5.2 (c) and (d) [5.10]. Due to the large inertia of the wind turbine, this results in a slow change of the rotor speed as observed in figure 5.2 (c) [5.11]. This could be considered as another drawback for Configuration #1, since pitch control cannot respond sufficiently within 140ms to limit the increased speed effect. The active power, P_{gen} , and reactive power Q_{gen} curves shown in figure 5.2 (e) and (f) also support this, where P_{gen} and Q_{geen} are both calculated at the generator terminals.

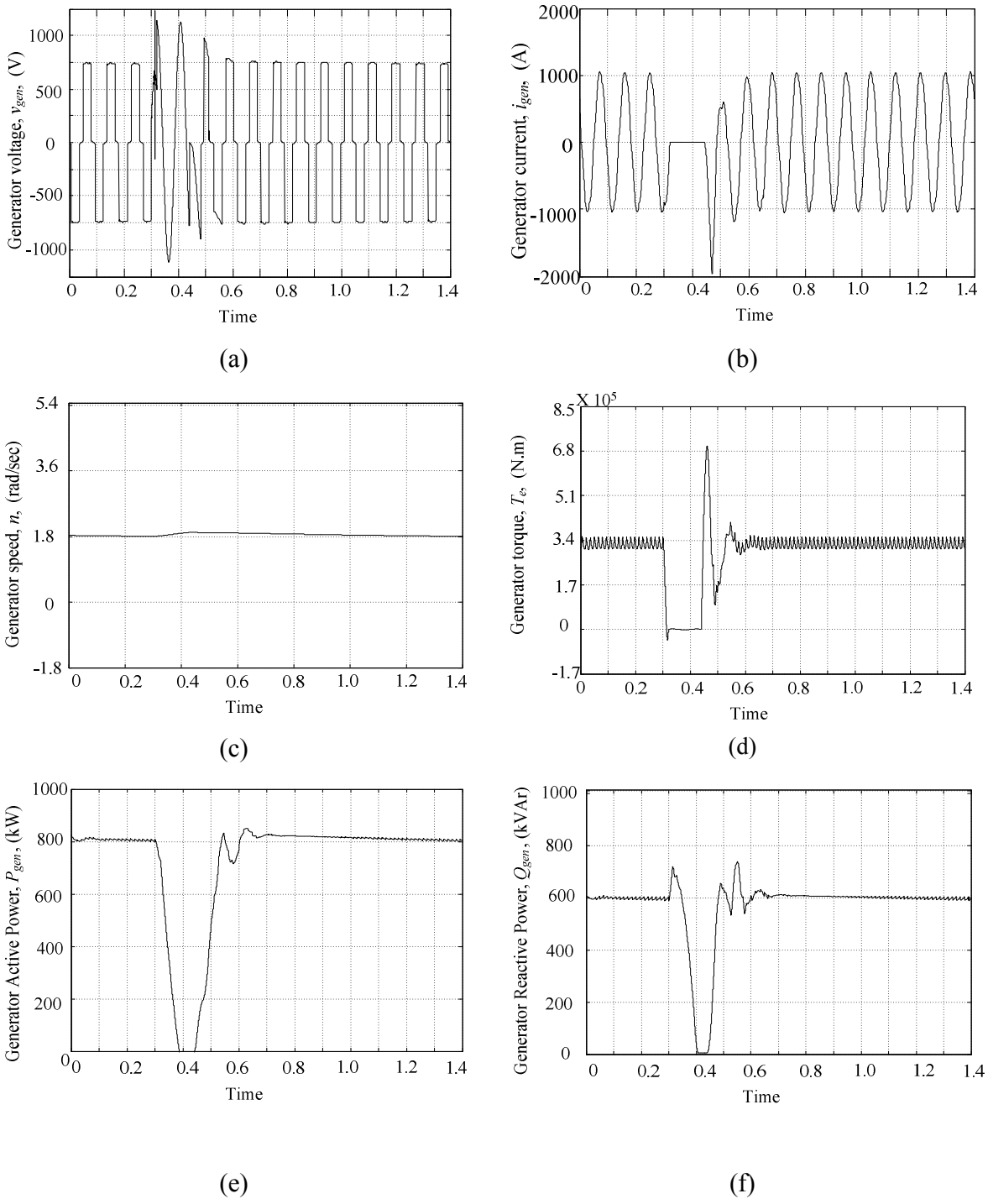

Figure 5. 2. Simulation results for Configuration #1: (a) PMSG voltage, v_{gen}, (b) PMSG current, i_{gen}, (c) PMSG angular speed, n , (d) electromagnetic torque, T_e, (e) generator active power, P_{gen}, and (f) PMSG reactive power, Q_{gen}.

As for the MSC power converter responses for Configuration #1, since i_{gen} has fallen to a low value as shown in figure 5.2, the capacitor current, i_{cdc} contributes to the majority of the boost chopper current I_{dc} shown in figure 5.3 (a) which could be considered as another disadvantage for Configuration #1.

To demonstrate whether the rectifier unit will exhibit any voltage or current stresses on their semiconductors, the rectifier diode voltage, v_{D1} and current, i_{D1} are shown in figure 5.3 (b) and (c). The current and voltage responses imply that power is prevented from being transmitted to the rectifier unit due to the energy stored in the rotor inertia.

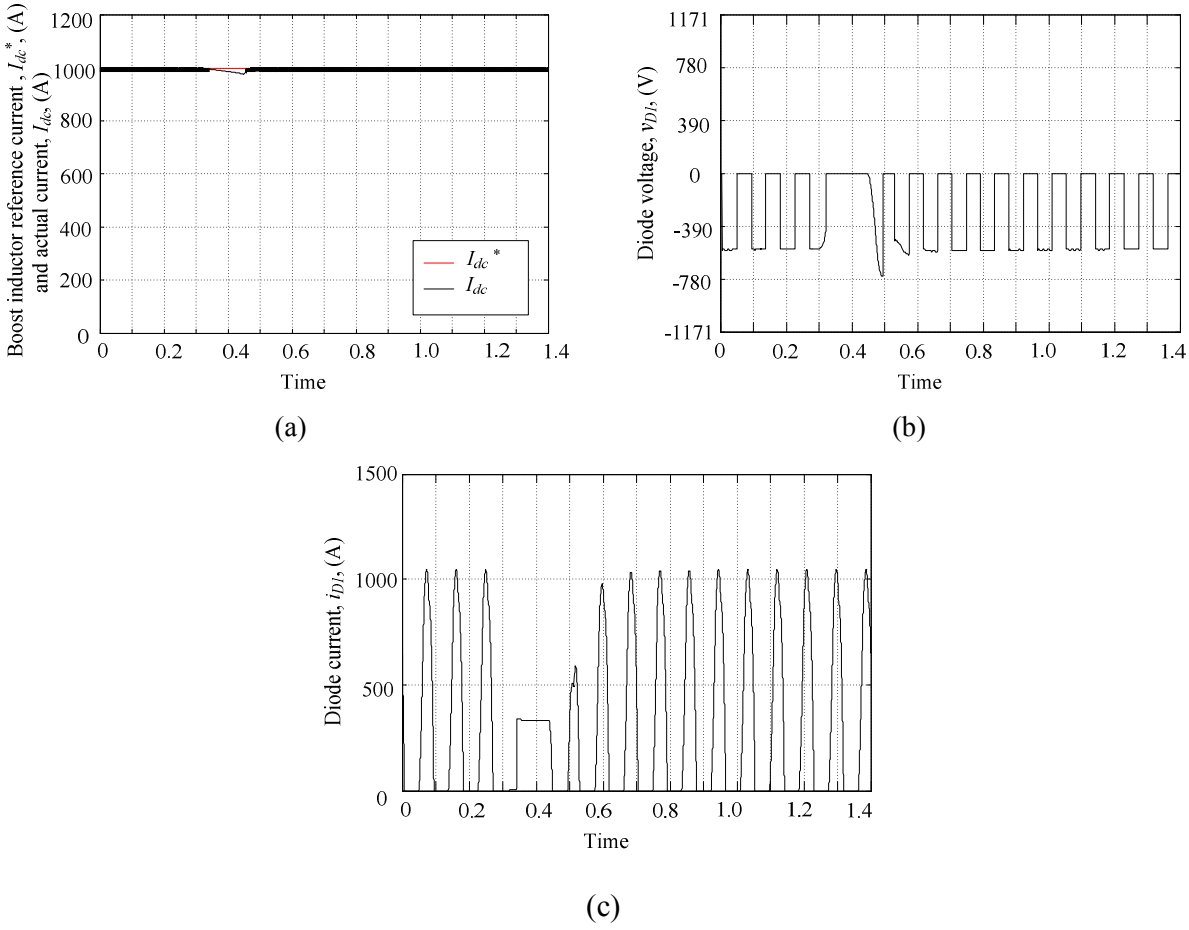

Figure 5.3. Simulation results for Configuration #1: (a) boost inductor current, I_{dc} , (b) diode voltage, v_{D1}, and (c) diode current, i_{D1}.

The grid side response for Configuration #1 is shown in figures 5.4 and 5.5. The grid voltage v_{grid} in figure 5.4 (a), shows at 0.3 s, the RMS value of v_{grid} suddenly falls to 0.1 per unit for the fault duration of 140 ms, as specified by grid operators. Consequently, the three-phase grid current i_{grid} will experience an increase in its rms value as shown in figure 5.4 (b). Using Configuration #1, the grid current i_{grid} still exhibits increase during the voltage dip incident, reaching 1 per unit of the nominal grid current, which corresponds to 1000 A . The grid current i_{grid} remains high for the whole dip duration, post dip, and after grid voltage recovery, for a total period of 0.34 s. The reason for the delayed grid current recovery is related to the dc-link voltage response $v_{dc-link}$.

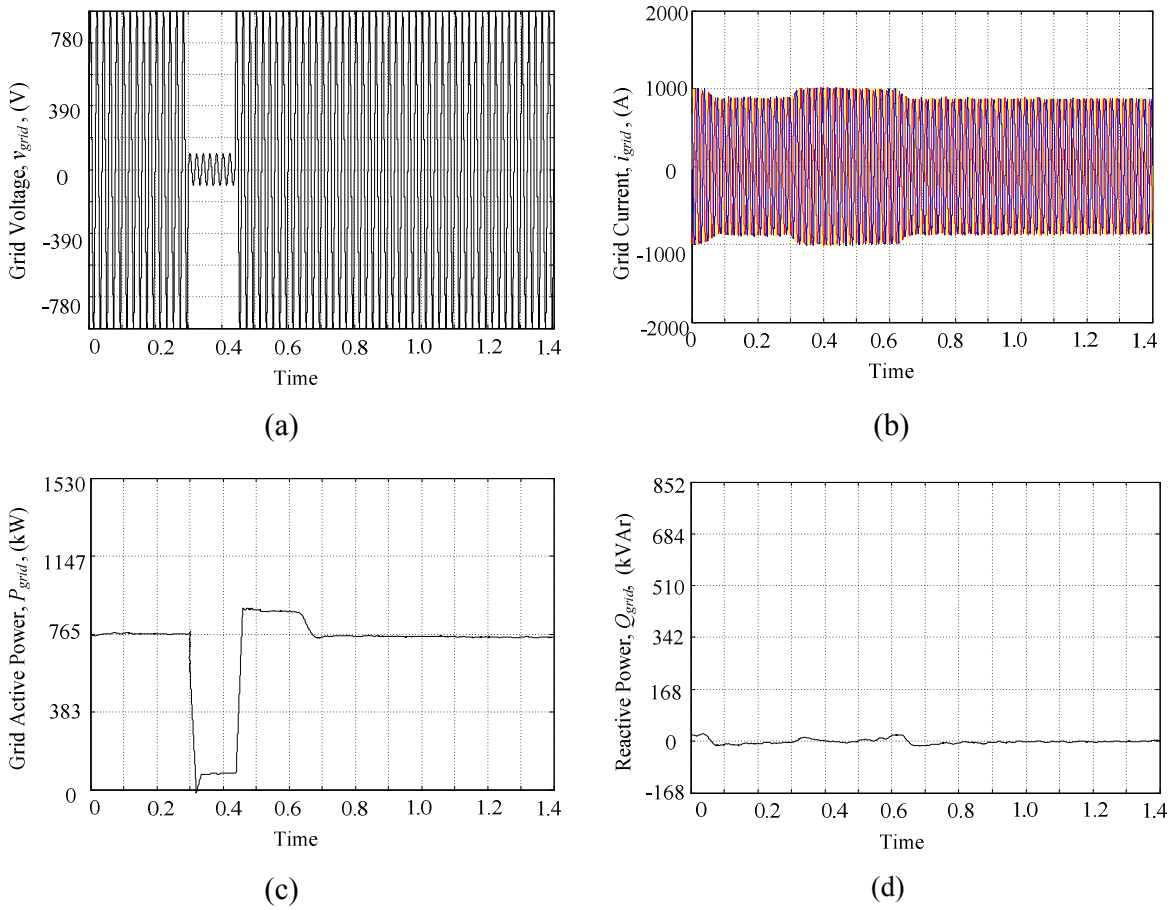

Figure 5.4. Simulation results for Configuration #1: (a) grid voltage, v_{grid}, (b) grid current, i_{grid} , (d) grid active power, P_{grid}, and (g) grid reactive power Q_{grid}.

The grid active power P_{grid} and reactive power Q_{grid} are shown in figure 5.4 (c) to (d).

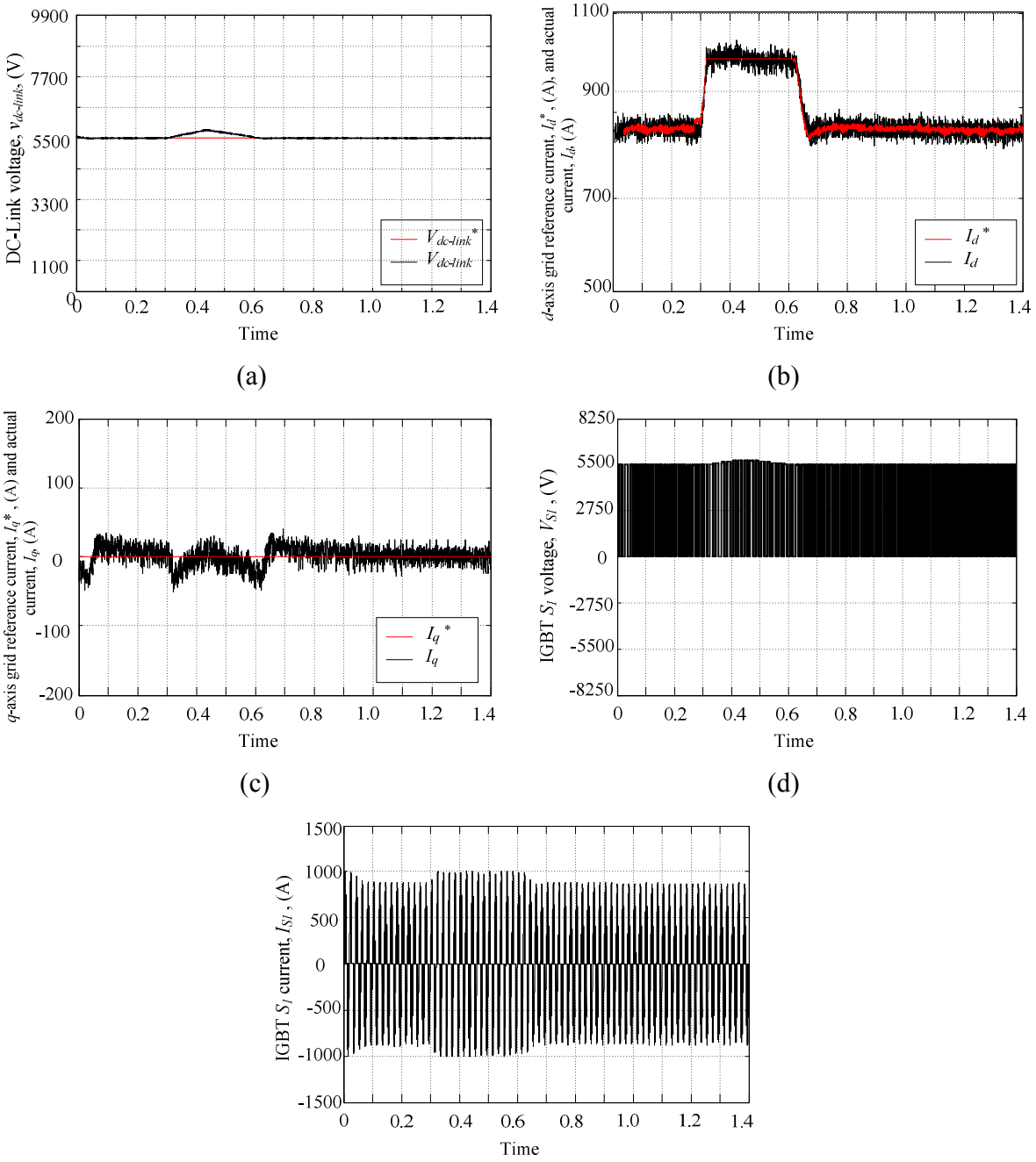

Figure 5.5. Simulation results for Configuration #1: (a) dc-link voltage, $V_{dc-link}$, (b) d-axis grid current, I_d , (c) q-axis grid current, I_q, (d) IGBT S_1 voltage, V_{S1}, and (e) IGBT S_1 current, I_{S1}.

For Configuration #1, the GSC controller for q-axis current, which will in turn control reactive power Q_{grid}, tends to hold the grid power factor at unity by keeping Q_{grid} close to zero, as shown in figure 5.4 (d). However, the grid injected active power P_{grid} experience a rise after grid voltage recovery in response to the high grid current and high dc-link voltage. Configuration #1 is able to limit the dc-link voltage rise during the dip duration to below 1.1 per unit as shown in figure 5.5 (a), taking 0.26 s after grid voltage recovery to restore $V_{dc-link}$ to 1 per unit. This corresponds to a blocking capability of 725 V from the total of 1000 V increase in the $V_{dc-link}$ during fault as shown in Chapter 3, figure 3.15 (a). Since the grid current will not change rapidly when the grid voltage recovers, the d-axis current will take longer to be restored to its prior fault value, as shown in figure 5.5 (b). As mentioned, q-axis current I_q is maintained at zero for unity power factor operation as demonstrated in figure 5.5 (c).

Finally, the VSI-IGBT S_1voltage, V_{S1}, and current, I_{S1}, waveforms are shown in figure 5.5 (d) and (e) respectively. These show that minimum voltage and current transients are experienced by the IGBT switches due to the application of the magnetic amplifier, with minor effects generally exhibited with the use of magnetic amplifier of Configuration #1.

5.3 Configuration #2: DC-side Magnetic Amplifier

Modifications have been made to the 3-phase magnetic amplifier topology so as to minimize the number of magnetic elements yet still serve the same purpose of dc-link voltage limiting. The six magnetic amplifiers and six diodes are replaced by a single magnetic amplifier circuit inserted in the boost converter (Configuration #2), as shown in figure 5.6. Also, the boost inductor L_{dc} has been eliminated from the boost chopper, thus the magnetic amplifier serves as a boost chopper filter inductor for current smoothing and filtering, as well as a component for LVRT capability enhancement. Although magnetic amplifiers have been used in high frequency dc-dc converters [5.12, 5.13], they have not have been reported for LVRT capability enhancement use. Since magnetic amplifiers are characterized by high efficiency and ruggedness compared to semi-conductors operating at high switching frequency [5.14], proving their ability for enhancing the LVRT would make them a preferred choice.

With the magnetic amplifier inserted in the boost chopper, its main function is to store energy during fault duration thus maintaining the required energy balance between the generated and grid injected power.

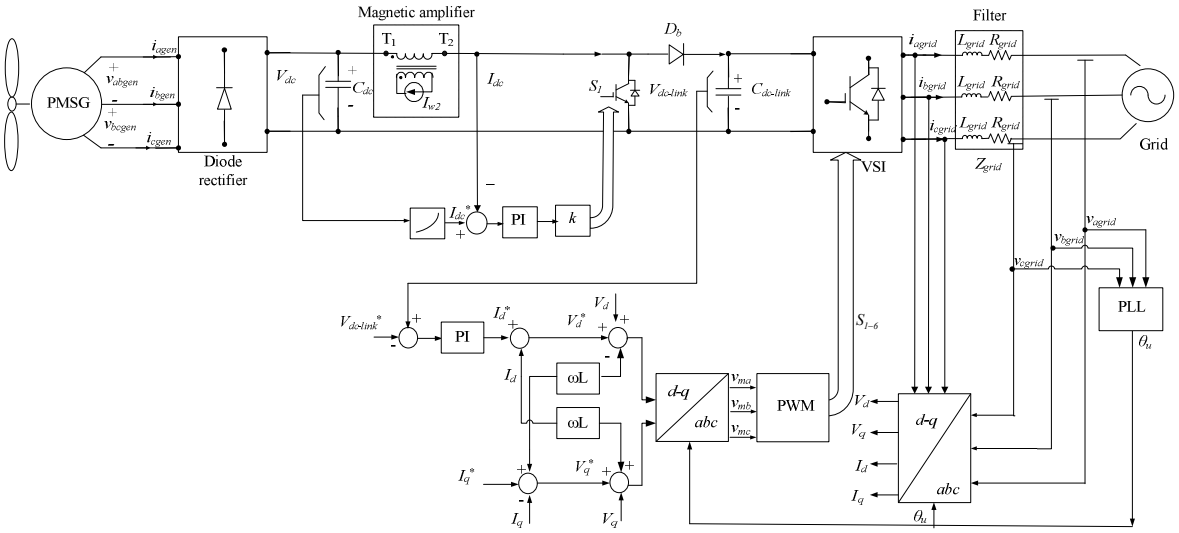

Figure 5.6. WECS with Configuration #2.

The magnetic amplifier response in Configuration #2 is shown in figures 5.7 to 5.10. For the generation side, no change is exhibited in the PMSG line voltage, v_{gen} or in the PMSG current, i_{gen} even during the grid voltage sag, as shown in figure 5.7 (a) and (b) respectively. Also, no changes are seen in the generator rotational speed n, electromagnetic torque T_e, active power P_{gen} or reactive power Q_{gen} curves shown in figure 5.7 (c)-(f) indicating the absence of any stored energy in the PMSG during the fault duration.

As for the MSC response using Configuration #2, the boost chopper continues to extract the same power from the PMSG during fault. The actual chopper current I_{dc} tracks the reference boost converter current I_{dc}^{*} which has been determined based on a maximum power extraction criteria, as shown in figure 5.8 (a). The diode rectifier stresses are demonstrated in figure 5.8 (b) and (c) where the rectifier unit does not experience any voltage or current transients that might cause damage to the power converter unit, as indicated in the waveforms for v_{D1} and i_{D1}.

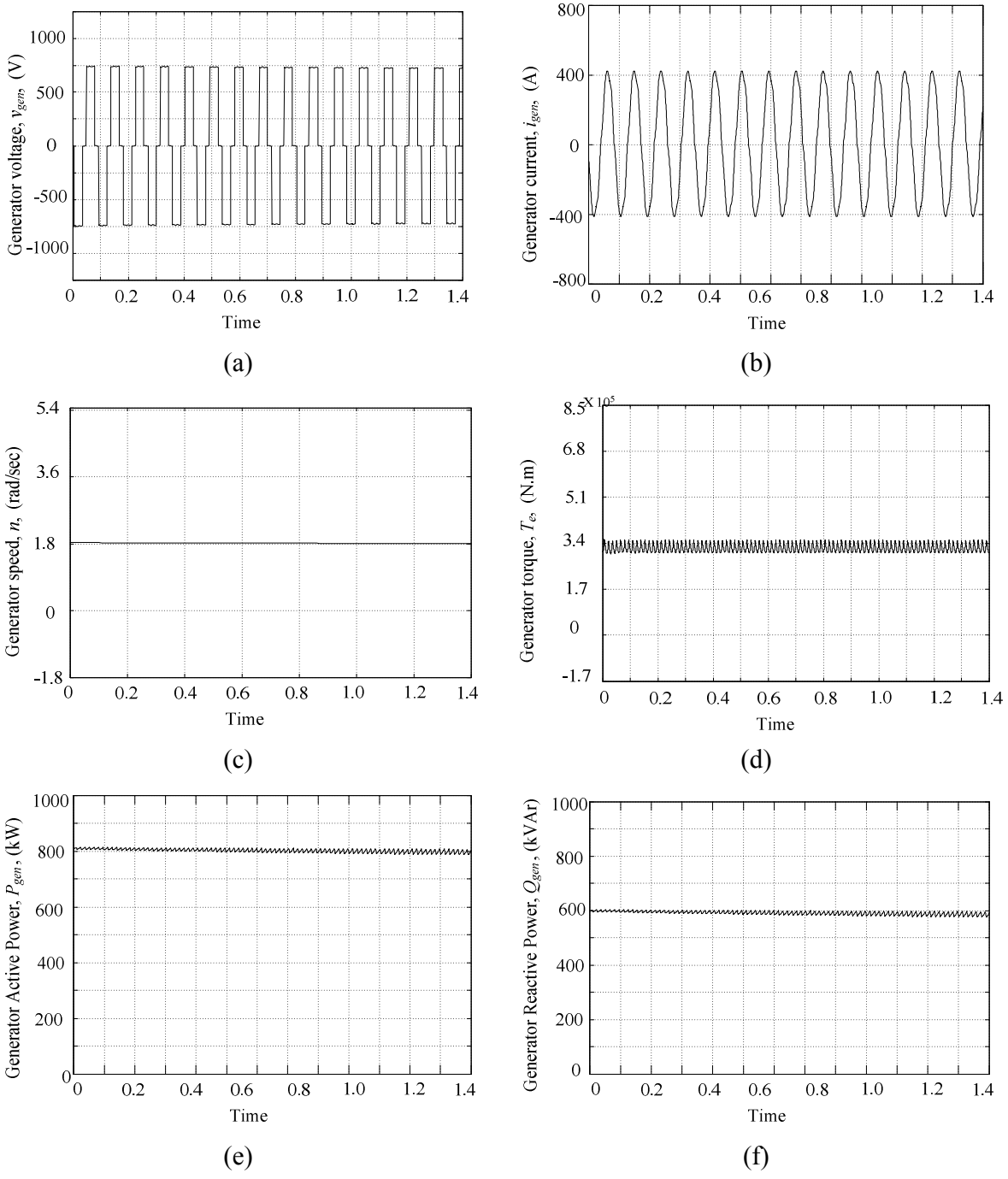

Figure 5. 7. Simulation results for Configuration #2: (a) PMSG voltage, v_{gen}, (b) PMSG current, i_{gen}, (c) PMSG angular speed, n , (d) electromagnetic torque, T_e, (e) generator active power, P_{gen}, and (f) PMSG reactive power, Q_{gen}.

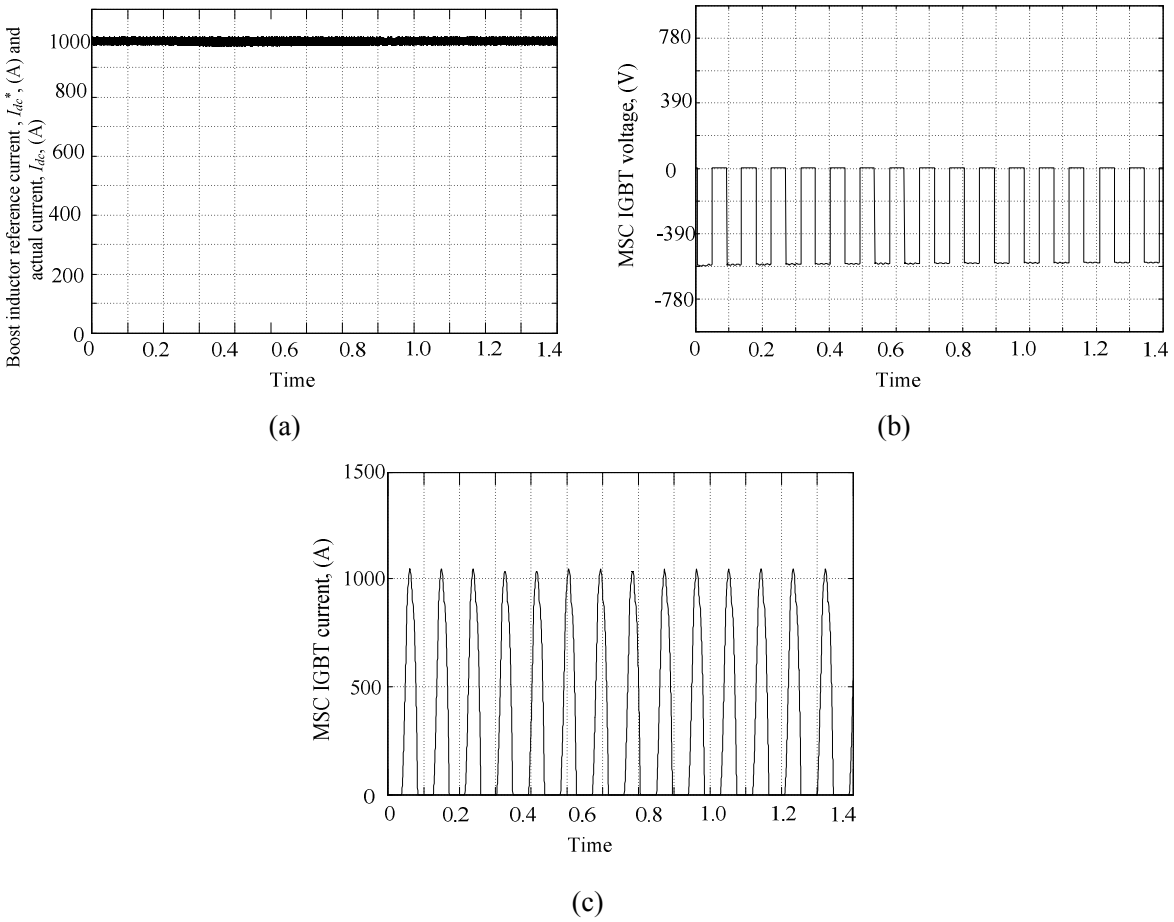

Figure 5.8. Simulation results for Configuration #2 (a) boost inductor current, I_{dc} , (b) diode voltage, v_{D1}, and (c) diode current, i_{D1}

The grid and GSC performance can be studied from figure 5.9 and figure 5.10 respectively. The grid current, i_{grid} experiences a current rise to 960 A during the fault reaching its thermal limits as defined by the current controller. Figure 5.9 (b) shows that i_{grid} recovery after the fault is more rapid than grid current recovery using Configuration #1. Since the magnetic amplifier is Configuration #2 relies on storing energy in the magnetic amplifier's magnetic field, it is also observed that after grid voltage recovery the amplifier releases power to the grid with a transient behavior which can be observed in the grid active power P_{grid} response of figure 5.9 (c). Reactive powers Q_{grid} response is demonstrated in figure 5.9 (d).

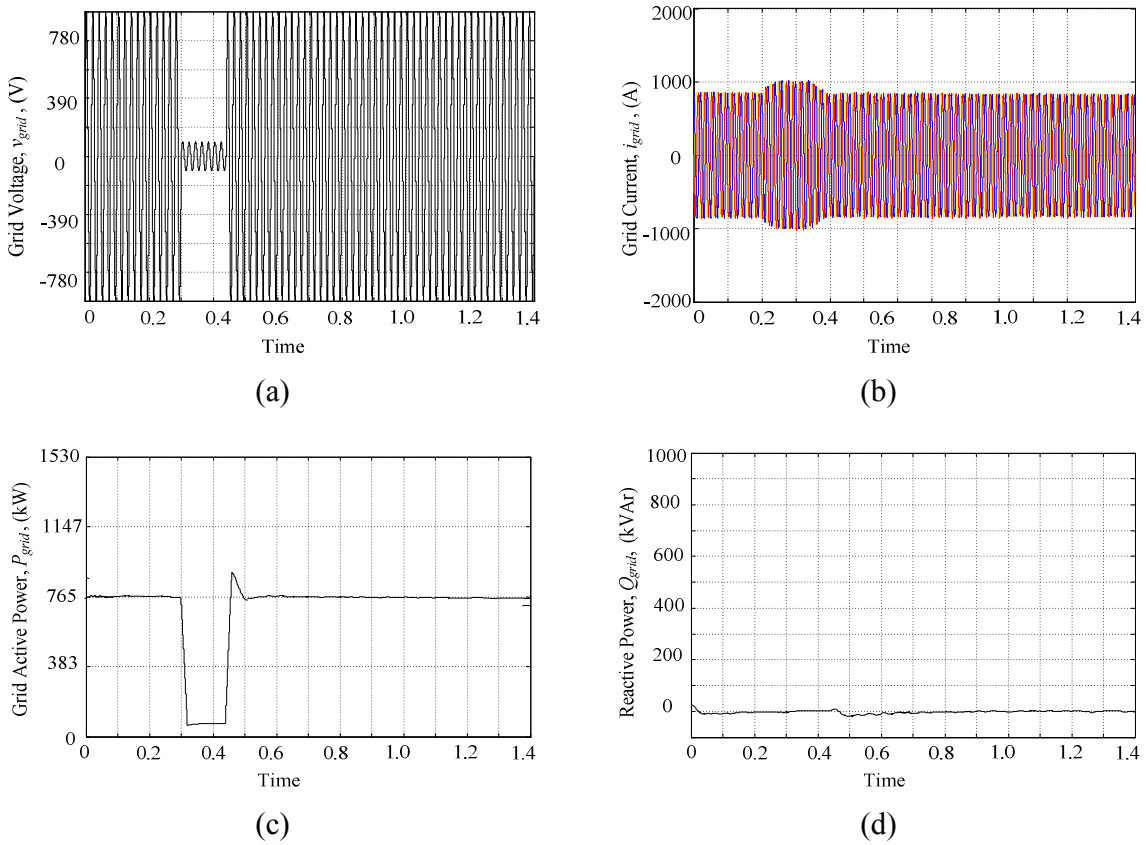

Figure 5.9. Simulation results for Configuration #2: (a) grid voltage, v_{grid}, (b) grid current, i_{grid} , (c) grid active power, P_{grid}, and (d) grid reactive power, Q_{grid}.

The GSC response in figure 5.10 (a) indicates that the magnetic amplifier is able to limit the $V_{dc-link}$ rise. Configuration #2 response for $V_{dc-link}$ shows better performance than that of Configuration #1, where $V_{dc-link}$ is better limited. Since the $V_{dc-link}$ response affects d-axis grid current control action, it can be noticed from figure 5.10 (b) and (c) that the d-axis grid current I_d rises due to the sudden drop in grid voltage to 0.1 per unit, while the q-axis current, I_q is maintained close to zero. Limiting $V_{dc-link}$ reduces the power converters voltage and current stresses on the IGBT switches as shown in figure 5.10 (d) and (e) respectively.

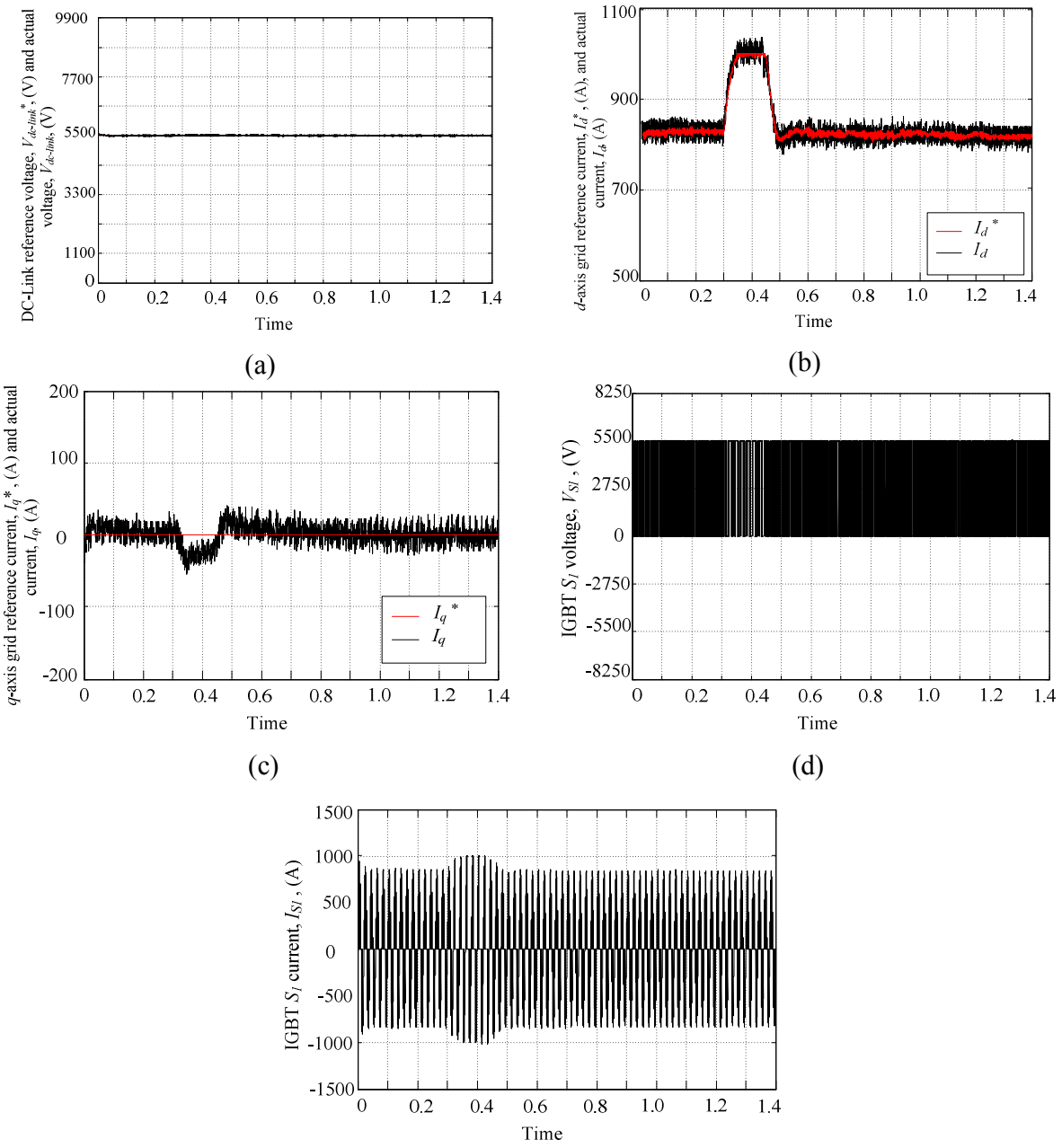

Figure 5.10. Simulation results for Configuration #2: (a) dc link voltage, $V_{dc-link}$, (b) d-axis grid current, i_d , (c) q-axis grid current, i_q, (d) IGBT S_1 voltage, V_{S1}, and (e) IGBT S_1 current, I_{S1}.

5.4 Discussion

The use of magnetic amplifiers has been suggested in this research to overcome the problem of dc-link voltage rise which in turn may cause damage to the power converters. The first approach was to use a 3-phase amplifier topology (Configuration #1), where six magnetic elements along with six diodes are placed between the PMSG terminals and the six-pulse diode rectifier unit, to compensate for the dc-link voltage rise. System performance was investigated and results showed that the amplifier was able to limit the dc-link voltage rise to 1.05 pu of its nominal value, compared to 1.2 pu without the amplifier addition. Also, dc-link voltage recovery was more rapid, taking 0.26 s with the magnetic amplifier and 0.56 s without amplifier action. However, the topology affects PMSG performance by storing energy in the rotor inertia, causing an over speeding effect as well as improper operation of the boost chopper. Possibly the overall size and cost of the topology makes it the less interesting approach.

The modification is to replace the 6 units with one single magnetic element placed in the dc-side, which simultaneously replaces the dc chopper filtering inductance (Configuration #2). The system performance improves, with the dc-link voltage limited to 1.0 per unit, which in turn improves the system's ride-through capability during significant voltage dips. System recovery time after the fault is reduced and amplifier operation do not interfere with the action of the generator side and the MSC. However, the amplifier is unable to limit the grid current rise due to the sudden grid voltage drop. The configuration has almost negligible effect on the power converters. The potential of Configuration #2 topology will be further investigated through experimental validation on a scaled prototype.

5.5 Summary

Being unable to compensate for the energy imbalance during voltage dips can lead to destruction of power converters which would lead to wind farm disconnection. This chapter investigated the use of two magnetic amplifier topologies to improve ride through capability. Configuration #1 uses a three-phase configuration of magnetic amplifiers inserted between the PMSG and the diode rectifier unit where its impact has been demonstrated on system elements. Configuration #1 improves the dc-link voltage response, but affects the generator's

performance. The large size and cost of the approach decreases its appeal. Configuration #2, which only uses one magnetic amplifier element inserted in the boost chopper, has proven to be superior to Configuration #1 due to its improved dc-link voltage response, reduced size and cost, whilst also exhibiting no detrimental effects on the generation side. Furthermore, the voltage and current stresses on the power conversion units are minimized. Configuration #2 is further explored for practical validation in the next chapter.

References

[5.1] S. Chondrogiannis*, et al.*, 'Modelling and GB Grid Code Compliance Studies of Offshore Wind Farms with Doubly-Fed Induction Generators', The 3rd IET International Conference on Power Electronics, Machines and Drives, 2006. pp. 22-26.

[5.2] M. Tsili and S. Papathanassiou, 'A Review of Grid Code Technical Requirements for Wind Farms', IET Renewable Power Generation, Vol. 3, 2009. p. 308.

[5.3] A. Yousef, A. Nasiri, and O. Abdelbaqi, 'Wind Turbine Level Energy Storage for Low Voltage Ride through (LVRT) Support', IEEE Symposium Power Electronics and Machines for Wind and Water Applications (PEMWA), 2014 2014. pp. 1-6.

[5.4] F. Deng and Z. Chen, 'Low-Voltage Ride-through of Variable Speed Wind Turbines with Permanent Magnet Synchronous Generator', 35th IEEE Annual Conference on Industrial Electronics (IECON) 2009.

[5.5] A. Boyajian, 'Theory of D-C. Excited Iron-Core Reactors and Regulators', Transactions of the American Institute of Electrical Engineers, Vol. XLIII, 1924. pp. 919-936.

[5.6] K. M. Salim*, et al.*, 'Preliminary Experiments on Saturated DC Reactor Type Fault Current Limiter', IEEE Transactions on Applied Superconductivity, Vol. 12, 2002. pp. 872-875.

[5.7] S. Platt,'Magnetic Amplifiers: Theory and Application', Prentice-Hall, 1958.

[5.8] A. G. Milnes, 'Three-phase Transductor Circuits for Magnetic Amplifiers', Proceedings of the IEE - Part II: Power Engineering, Vol. 99, 1952. pp. 615-619.

[5.9] 'Discussion on "Three-phase transductor circuits for magnetic amplifiers"', Proceedings of the IEE - Part IV: Institution Monographs, Vol. 100, 1953. pp. 1-2.

[5.10] S. Alepuz*, et al.*, 'Use of Stored Energy in PMSG Rotor Inertia for Low-Voltage Ride-Through in Back-to-Back NPC Converter-Based Wind Power Systems', IEEE Transactions on Industrial Electronics, Vol. 60, 2013. pp. 1787-1796.

[5.11] D. Shuhui, W. Yi, and L. Heming, 'Coordinated Control for Active and Reactive Power of PMSG-based Wind Turbine to Enhance the LVRT Capability', 15th International Conference on Electrical Machines and Systems (ICEMS), 2012. pp. 1-4.

[5.12] K. Harada and T. Nabeshima, ‘Applications of Magnetic Amplifiers to High-Frequency DC-to-DC Converters’, Proceedings of the IEEE, Vol. 76, 1988. pp. 355-361.

[5.13] V. Yaskiv, ‘Using of High-Frequency Magnetic Amplifier in Switch Mode DC Power Supplies’, IEEE 35th Annual Power Electronics Specialists Conference (PESC), 2004. pp. 1658-1662 Vol.2.

[5.14] V. Yaskiv*, et al.*, ‘Performance Evaluation of MagAmp Regulated Isolated AC-DC Converter with High PF’, ELEKTRO, 2014. pp. 411-416.

CHAPTER SIX

Practical Implementation and Results Verification

Utilisation of a magnetic amplifier for LVRT capability enhancement of a 1.5 MW WECS was investigated in the previous chapter. The suggested magnetic amplifier can have two topologies; 3-phase and dc-side topologies. Both configurations limit the dc-link voltage rise associated with sudden grid voltage sags. The line side magnetic amplifier topology's main disadvantage is the use of large number of magnetic elements and semiconductors, as well as its adverse effect on the PMSG performance and operation. The DC-side topology is thus recommended as it reduces the overall size and cost yet serves the same function in limiting the dc-link voltage rise, consequently reducing the stresses on the power converters. LVRT using the dc-side topology, on a scaled down system prototype emulating a MW WECS, is investigated in this chapter. Simulation results of the scaled system performance, with and without the amplifier, are experimentally verified.

6.1 The Proposed System Prototype

A scaled down system of the proposed WECS is modelled and simulated using MATLAB and the performance is verified experimentally. Figure 6.1 represents the block diagram of a low-voltage, low-power system used to emulate the 1.5 MW system. Operation of the prototype is described in the following sections.

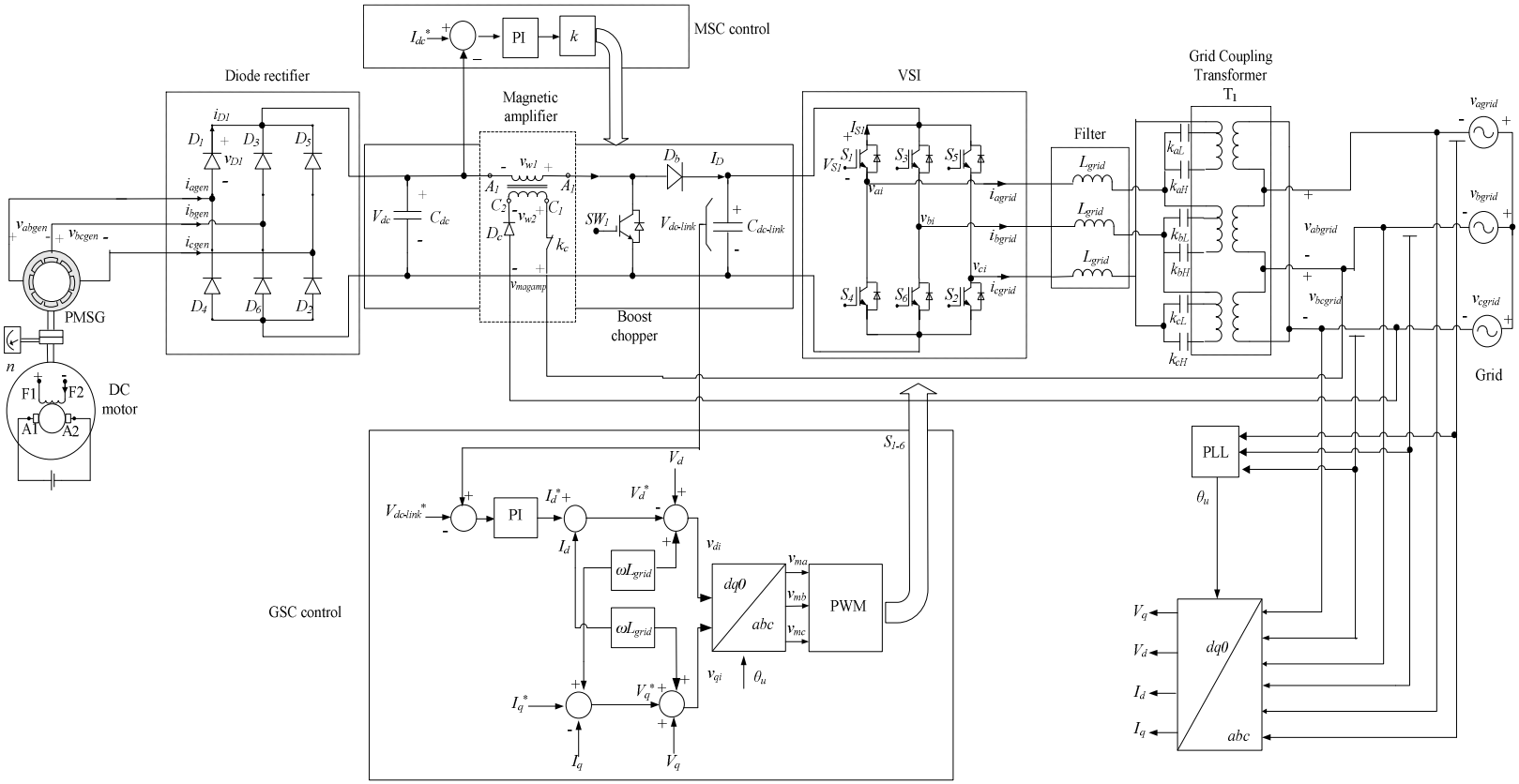

Figure 6.1. Block diagram of scaled down system with dc-side magnetic amplifier.

6.2 Generator and MSC

The scaled down system parameters are shown in Table 6.1 where the simulation and experimental parameters will be the same.

Table 6.1 Scaled down system parameters

Parameter	Variable name	Value
Generator power (kW)	P_{gen}	0.31
Rated voltage at 1500 rpm (V)	$v_{gen(nom)}$	200
Rated frequency at 1500 rpm(Hz)	$f_{gen(nom)}$	50
Pole pairs	P	2
Rated generator torque (Nm)	T	2
Operating Generator speed (rpm)	n	900
Generator frequency at operating speed (Hz)	f_{gen}	30
Operating generator line voltage (V)	v_{gen}	50
PWM switching frequency (Hz)	f_c	5000
Boost converter inductance (mH)	L_{dc}	10
Boost chopper reference current (A)	I_{dc}^*	2
Input boost converter capacitor (μF)	C_{dc}	1200
DC-link capacitor (μF)	$C_{dc-link}$	2200
DC-link reference capacitor voltage (V)	$V_{dc-link}^*$	100
Grid voltage (V)	v_{grid}	40
Grid filter and coupling transformer inductance (mH)	L_{grid}	2
Grid filter and coupling transformer resistance (Ω)	R_{grid}	1.5
PWM-VSI switching frequency (Hz)	f_c	5000
Grid frequency (Hz)	f_{grid}	50
Voltage dip magnitude (% full voltage)	p.u	0.25
Voltage dip duration (s)		5

An 0.3 kW, 4 pole, 200 V, 50 Hz, 1500 rpm, Y-connected PMSG is used for the experimental test rig, whose parameters are presented in Appendix (B-2). The PMSG is to be driven with a constant wind speed from a wind turbine to study the impact of voltage dips on WECS performance. A separately excited DC motor is used as a prime mover (wind turbine) whose parameters are listed in Appendix (B-3). The armature controlled dc motor ensures that the PMSG is driven at a constant speed thus simulating a constant driven wind speed instead of using a mechanical wind turbine. The PMSG is driven at a fixed speed, n of 900 rpm, and

produces a balanced 3-phase, line-to-line voltage, v_{gen} of 50 V at a frequency, f_{gen} of 30 Hz. The difference between the prototype and full sized system generator frequency is the reduced number of poles available in the scaled down system's generator.

The PMSG terminals are connected to a six pulse diode rectifier with an 1100μF smoothing capacitor followed by a boost chopper serving as the machine side converter. A 10 mH boost chopper inductor, L_{dc} is selected for minimum inductor current ripple and an output filtering electrolytic capacitor, $C_{dc-link}$ of 2200 μF, 400V is the dc-link capacitor. $C_{dc-link}$ provides the required dc-bus voltage for the GSC as well as a path to accept energy recovery from the VSI during operation of its freewheel diodes. It also decouples the MSC and GSC control action. The boost chopper extracts generator current i_{gen} of 2 A at 5 kHz switching frequency, which is the same frequency as the full sized system modelled in chapters 3 and 5. This is achieved by sensing the boost chopper inductor current, I_{dc}, and comparing it with a preset reference, I_{dc}^{*}, so that the boost chopper extracts constant current from the PMSG, even at different loading conditions. The reference boost chopper current, I_{dc}^{*}, is determined from the MPPT algorithm. Due to the constant speed operation of the PMSG, I_{dc}^{*} is set to 2 A, thus emulating MPPT when the generator speed is 900 rpm. Also, the choice of I_{dc}^{*} is based on the required power level to be injected into the grid through the GSC. With a constant speed driven PMSG and a current controlled boost chopper, the MSC acts extracting maximum power from the PMSG which will then be exported to the grid through the GSC.

6.3 Grid Representation and GSC

The GSC is a 3-phase VSI module which consists of an insulated gate bipolar transistor (IGBT) module, (IRAMX 16UP60S), which is a 16 A, 600 V inverter from International Rectifier. The PWM carrier frequency, f_c is 5 kHz, identical to the full sized system GSC carrier frequency. The inverter is an integrated power hybrid IC with internal shunt resistor for appliance motor drives applications as well as for light industrial application.

Laboratory emulation of the voltage dips can be performed by several methods, such as the starting of a large induction motor, a voltage dip generator, or through the use of different transformer outputs for normal operation and dip [6.1, 6.2]. In the proposed research, a voltage dip is emulated using a transformer by connecting the GSC to the grid through the primary

side of a multi-turn step-up transformer, where different circuit breakers are controlled to suddenly connect the GSC to the required voltage level. The GSC connection to the grid for voltage dip emulation is shown in figure 6.1. The grid coupling transformer, T_1, is a 3-phase, 2 kVA, 50 Hz, 220 V: (2x 63.5) V autotransformer; whose low voltage side terminals are connected to the GSC. The high side terminals of T_1 represent the grid, where the rms line-to-line grid voltage, V_{HS} are adjusted to 40 V.

The turns ratio, *a,* for the grid coupling transformer, T_1, between the primary number of turns, N_{1T} and the secondary number of turns N_{2T} is selected for the dip emulation. Two tap settings are used, the turns ratio, *a*, is either 1 or 0.25. Tap setting a =1 is selected if the system is required to connect at the 40 V grid, while a = 0.25 setting is chosen in case the system is tested for a sudden voltage dip of 75% of the nominal grid voltage. The transition from the full grid voltage to 75% is achieved with a set of 3-phase contactors operated by a timer labelled k_{abcL} and k_{abcH}. Prior to the fault, the VSI terminals are connected to T_1 through k_{abcH}, while during the fault the VSI terminals are connected via k_{abcL}. The system is designed to switch between contactors k_{aH} and k_{aL} to simulate a grid voltage dip event when desired through an external push button. The voltage dip duration can be varied. Transformer T_1 is connected to the 3-phase VSI module through 2 mH grid filter inductance, L_{grid} for grid current smoothing and filtering.

Both the scaled-down and full-scale systems simulated have similar control algorithms for their GSC. The PWM VSI controls both the frequency and magnitude of the voltage and current injected into the grid. Synchronous reference frame control is selected for PWM VSI operation, which transforms the 3-phase supply grid currents $i_{abcgrid}$ into a reference frame that rotates synchronously with the 3-phase grid voltages $v_{abcgrid}$. The control in this case requires two loops; an inner loop for grid current control and an outer loop for dc-link voltage control, as shown in figure 6.1.

For proper operation of the PWM-VSI, the dc-link capacitor voltage, $V_{dc-link}$ must be controlled to comply with the necessary output power needed to be injected into the grid. Also, this slow acting control loop balances the amount of energy extracted from the PMSG and the energy being exported to the grid. Failure to balance the energy will be accompanied

by a rise/fall in the energy stored in the link capacitor. A 100 V $V_{dc-link}$ has been selected in accordance with the dc-link voltage equation (2.36), to ensure safe rig operation since the dc-link voltage increases above this threshold during voltage dip, reaching over 200V.

For grid current control, the three-phase grid currents $i_{abcgrid}$ are transformed into instantaneous active I_d and reactive I_q components using a rotating frame synchronous with the positive sequence of the system voltage. The system under study is a three-wire system where the zero sequence component are neglected, so only I_d and I_q are considered. The dq-axes grid currents, I_d and I_q are decoupled to independently control the active and reactive power components injected to the grid. For decoupled control, the fundamental phase angle θ_u of grid voltage, v_{agrid} used by the $abc \rightarrow dq$ transformation has to be locked with the PLL technique described in Chapter 2. In the inner active current control loop, I_d^* is set in relation to the dc-link voltage, $V_{dc-link}$ which is controlled via the outer control loop. Controlling I_d controls the active power injected in the grid P_{grid} in relation to $V_{dc-link}$. I_q is compared to a zero reference for unity power factor operation. Using PI controllers, the output of both grid current loops v_{di} and v_{qi}, are transformed back to synchronous rotating quantities to issue the gating signals for the GSC. For a three-phase SPWM inverter, the maximum amplitude of the fundamental phase voltage in the linear region (m_a< 1) is ½$V_{dc-link}$, and the maximum amplitude of the fundamental ac output line voltage is given by (2.37) [6.3]. The modulation index for the fundamental voltage, m_a, should be specified prior to setting the inverter dc-side reference voltage, $V_{dc-link}^*$, so as to avoid over-modulation which occurs when the peak of the overall modulating signal exceeds 1. The magnitude of the fundamental modulating signal, m_a, is set to 1 to avoid over-modulation under the accepted dc-bus voltage, $V_{dc-link}$. Decreasing m_a helps avoiding over-modulation but requires an increase of the dc-side voltage for improved grid current shaping.

6.4 Parameter Determination of the PMSG

Determining the PMSG parameters is essential to estimate the performance of the whole WECS. Four parameters are determined which include the stator winding resistance R_s, dq axis inductances L_d and L_q respectively, and the permanent magnet (PM) flux linkage φ_f.

The armature resistance has been measured by a dc test with subsequent correction to obtain the ac value. Since R_a is the line-to-neutral resistance, R_a is a half of the measured line-to-line resistance [6.4]. Therefore

$$R_a = \frac{1}{2}\frac{V_s}{I_s} \tag{6.1}$$

where V_s is the dc-voltage applied to the PMSG terminals and I_s is the dc-current flowing in the windings. The results obtained from the test are shown in figure 6.2 and R_a is 12.5Ω.

To compute the PM flux linkage, φ_f, the PMSG no-load line-to-line r.m.s voltage V_{nl} is recorded when driven at a constant speed, *n,* as indicated in figure 6.3. While running the PMSG on no load, the no-load voltage V_{nl} versus rotational speed, *n* relationship is obtained [6.5]. The relationship is modified to include the maximum no-load phase voltage, $\hat{V}_{nl}$ versus the angular speed of rotation ω_e as illustrated in figure 6.4. The slope of the curve equals φ_f where φ_f= 0.36 Wb.

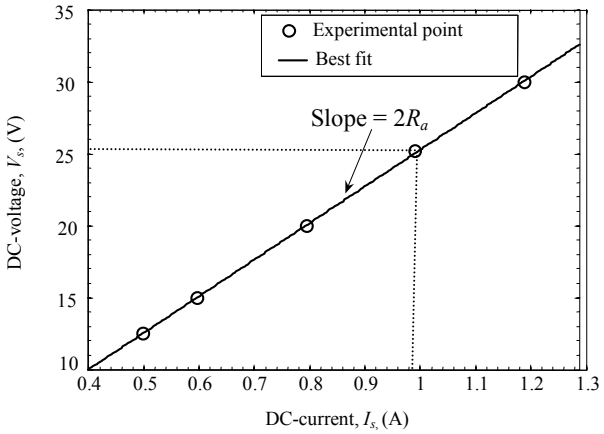

Figure 6.2. Relationship between voltage and current resulting from the dc test.

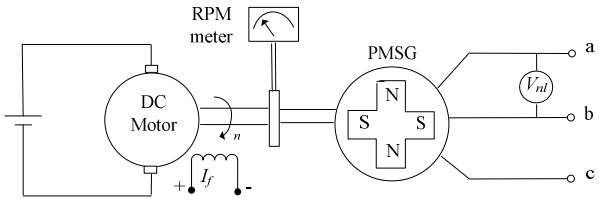

Figure 6.3. Connection diagram of the no-load test used to measure PMSM flux linkage.

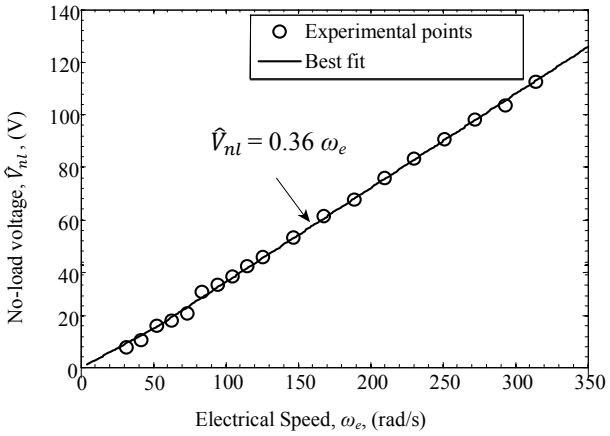

Figure 6.4. Relationship between electrical speed and maximum phase voltage for PMSG no-load test.

The dq axis inductances, L_d and L_q are determined from the load angle δ of the machine by coupling the PMSG with a dc motor from one side and with an externally excited synchronous machine (EESG) from the other side, as shown in figure 6.5. Thus, the dc motor drives two synchronous generators, where the no-load voltage, V_{nl} of the two machines is recorded and synchronized on a dual beam scope. The no-load EMF's, E of the PMSG and EESG operating as generators should be in phase. Thus, the same positions for the PMSG and EESG rotors, with regard to the same phase windings, can be found. When the PMSG is loaded with a resistive load, and in the absence of a wattmeter, the load angle (which indicates rotor position) will be the difference between the output load voltage of the PMSG machine, V_{nl} and the no load voltage of the EESG, E.

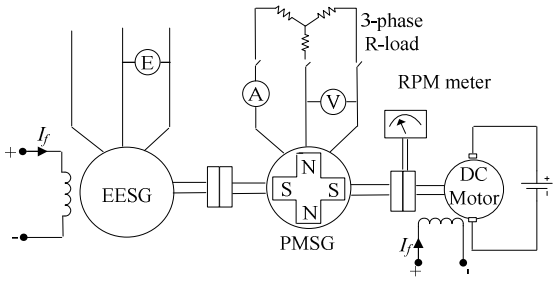

Figure 6.5. Connection diagram of the proposed method to measure the load angle δ.

Referring to the PMSG model in Chapter 2, the PMSG *dq* stator voltage equations at steady state are:

$$v_{dgen} = -R_a i_{dgen} + \omega_e L_q i_{qgen} \tag{6.2}$$

$$v_{qgen} = -R_a i_{qgen} + \omega_e \varphi_f - \omega_e L_d i_{dgen} \tag{6.3}$$

The relationship between load angle δ and *dq* axis stator voltages, v_{dgen} and v_{qgen}; and currents i_{dgen} i_{qgen} are:

$$[v_{dgen} \quad v_{qgen}]^T = v_{gen}[\sin\delta \quad cos\delta]^T \tag{6.4}$$

$$[i_{dgen} \quad i_{qgen}]^T = i_{gen}[sin\,\delta \quad cos\delta]^T \tag{6.5}$$

Thus, the *dq* axes inductances can be calculated as follows:

$$L_d = \frac{\omega_e \varphi_f - v_{qgen} - R_s i_{qgen}}{\omega_e i_{dgen}} \tag{6.6}$$

$$L_q = \frac{v_{dgen} + R_s i_{dgen}}{\omega_e i_{qg}} \tag{6.7}$$

Using these results, the relationship between the *d*-axis flux linkage φ_d and the *d*-axis current i_{dgen} at speeds of 1500 rpm and 1000 rpm are shown in figure 6.6.

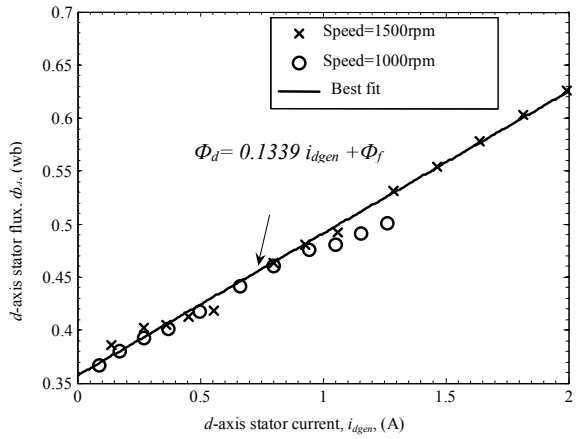

Figure 6.6. Relationship between measured *d*-axis flux linkage φ_d and *d*-axis current i_{dgen}.

Taking the best fit of the two curves in figure 6.6, at both speeds, the relation between φ_d and i_{dgen} can be described by:

$$\varphi_d = 0.134\, i_{dgen} + 0.375 \tag{6.8}$$

Therefore, the measured value of the *d*-axis inductance L_d is 0.134 H.

Similarly, the relationship between the *q*-axis flux linkage φ_q and the *q*-axis stator current i_{qgen} is plotted, as shown in figure 6.7. The measured PMSG *q*-axis inductance is shown in figure 6.8. L_q depends on the *q*-axis current, thus before magnetic saturation (i_{qgen}< 0.4 A), L_q is almost constant. Since

$$\varphi_q = L_q\, i_{qgen} \tag{6.9}$$

Therefore, the average value of the measured *q*-axis inductance L_q is 0.379 H. Whereas, before magnetic saturation (i_{qgen} < 0.4 A), L_q can be simply modelled by (6.9) as a function of i_{qgen}. Hence (6.10) describes the relation between measured *q*-axis inductance and *q*-axis current after magnetic saturation.

$$L_q = 0.466 - 0.186\, i_{qgen} \tag{6.10}$$

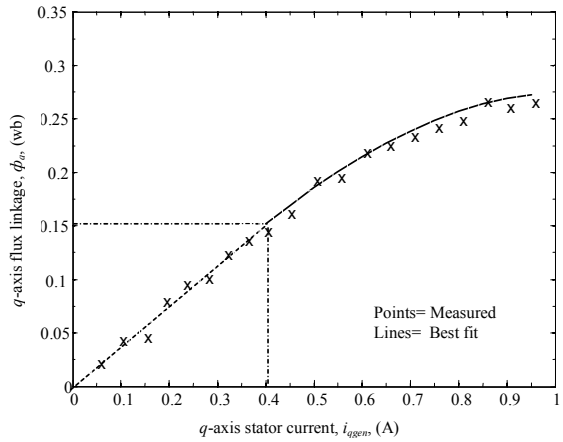

Figure 6.7. Relationship between measured *q*-axis flux linkage φ_q and *q*-axis stator current i_{qgen}

At the full-load operating condition, the *q*-axis current i_{qgen} is equal to 1.23 A and i_{dgen} is 1.248 A. Thus, from figure 6.8 the corresponding value of L_q is 0.239 H.

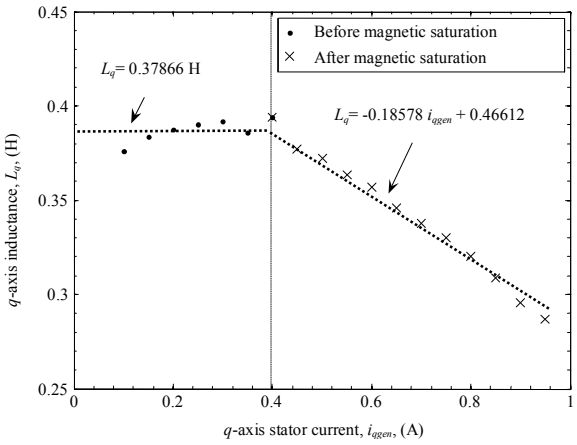

Figure 6.8. Relationship between measured q-axis inductance L_q and q-axis stator current i_{qgen}.

6.5 Parameters Selection for Magnetic Amplifier Prototype

A multi-tap, silicon steel core magnetic amplifier has been fabricated for system experimental verification [6.6, 6.7]. The magnetic amplifier adopted is rated as a 500 VA, 200 V and is designed from silicon steel laminations with data listed in Appendix (C-1).The magnetic amplifier is designed with a primary winding with two taps and a secondary with 4 taps. Figure 6.9 shows the main connection diagram as well as the notation used in the magnetic amplifier design. Silicon steel laminations have been selected for their low cost and relatively high permeability.

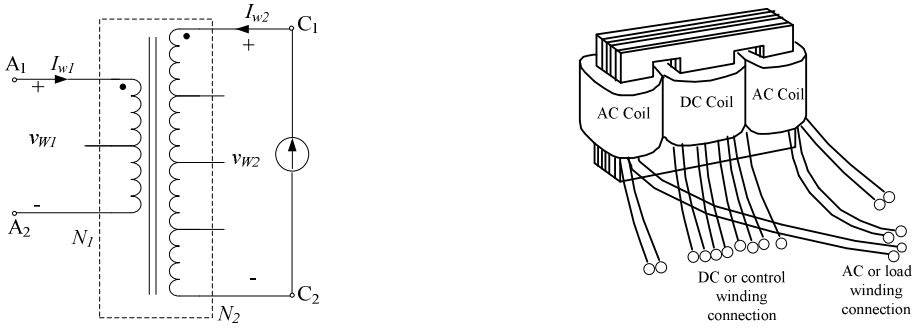

(a) (b)

Figure 6.9. Magnetic amplifier: (a) winding arrangement and (b) core structure.

The turns ratio, a_m, between magnetic amplifier primary winding turns, N_1, and the secondary number of turns, N_2 is 1. The primary winding is tapped at 100 turns while the secondary winding has four taps.

Assume the primary winding current, I_{w1}, carries 2 A, and is of stranded copper wire with cross sectional area, A_1, of 3mm^2 from El Seweedy Cables chart number CPD-S001-U07 found in Appendix (F).

Assume secondary winding current, I_{w2}, to be 8 A, and that the winding is constructed of solid copper wire with cross sectional area, A_2, of 3mm^2 from El Seweedy Cables chart number CPD-T001-U07 Appendix (F).

Therefore, the total copper wire area in the window, W_c, can be calculated using

$$W_c = N_1 A_1 + N_2 A_2 \tag{6.11}$$

Choosing a window utilization factor, k_u, according to the apparent power, S, of the magnetic amplifier which is 500 VA, $k_u = 0.28$ which is the smallest possible k_u.

The emf per turn, E_t, is calculated using

$$E_t = K\sqrt{S} \tag{6.12}$$

where $K = 1$ and S is in VA for a single phase shell type transformer.

Also

$$E_t = 4.44 f B_{sat} A_c. \tag{6.13}$$

For silicon steel, $B_{sat} = 1.8$ T, then according to (6.13) the core area can be calculated.

Using this design criteria, silicon steel *EI* laminations with available cross sectional area closest to the designed core cross section, as shown in figure 6.10 (a), is used; with the *BH* characteristics for silicon steel found in figure 6.10 (b) [6.8]. The magnetic amplifier magnetizing current, I_m versus flux φ_m characteristics are also shown in figure 6.10 (c) [6.9].

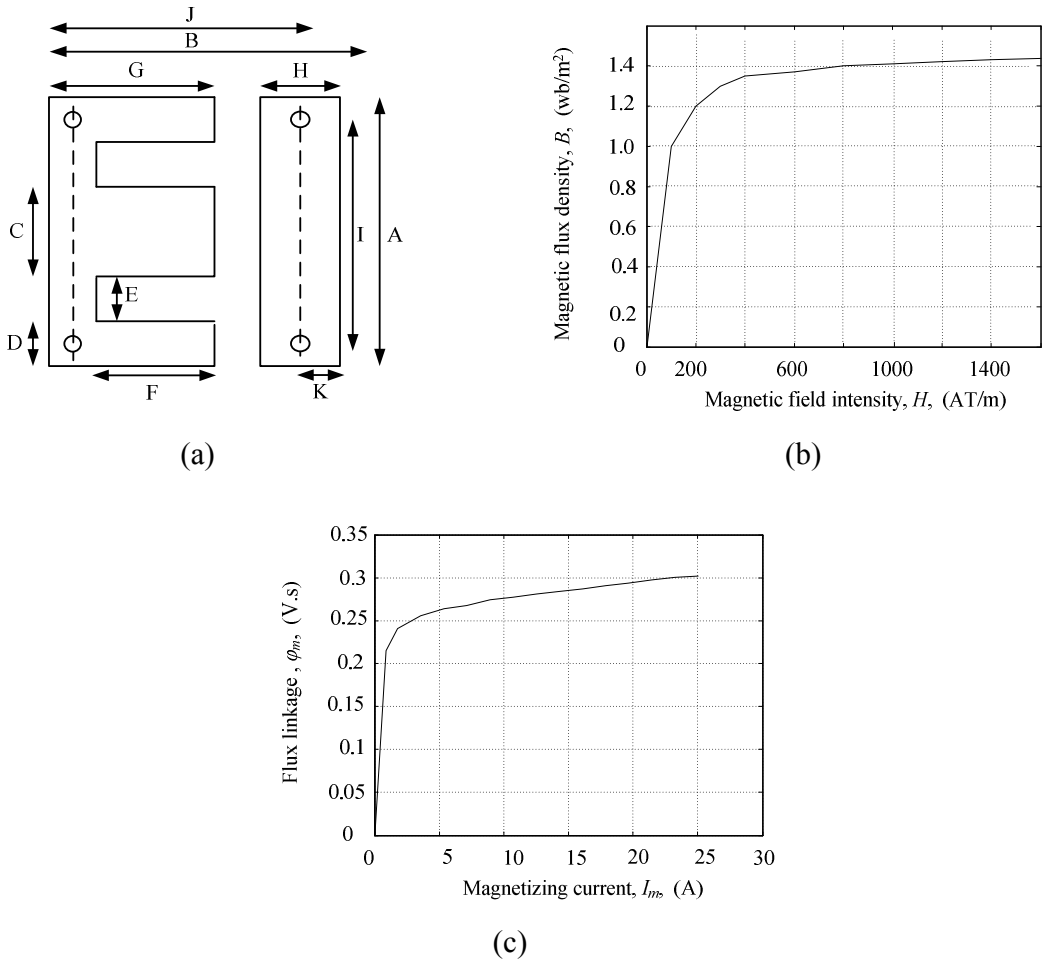

Figure 6.10. Silicon steel *EI* core: (a) construction, (b) *BH* characteristics, and (c) magnetizing current-flux linkage characteristics.

6.6 Control Circuit of Magnetic Amplifier Prototype

The method of controlling the magnetic amplifier flux level, which in turn determines the time at which saturation occurs, can vary [6.10]. One of the main aims is to minimize the number of passive elements, controllers and power electronic switches, to reduce the overall cost when using the magnetic amplifier dc-side approach. For this reason, one diode element D_c, is connected to the control winding circuitry as shown in figure 6.11. Before testing the performance of the proposed magnetic amplifier within the scaled down WECS, simulation

analysis of the magnetic amplifier when embedded in the boost chopper is tested separately and explained in the following section.

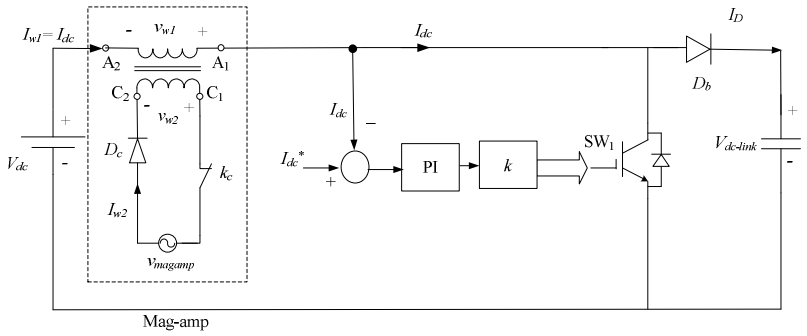

Figure 6.11. Magnetic amplifier in a boost chopper.

The simulation results for figure 6.11 are found in figures 6.12 to 6.14, where the ability of the designed amplifier to change the output dc-link voltage, $V_{dc-link}$ is tested in response to a change in the secondary winding current, I_{w2}. Being able to change $V_{dc-link}$ according to I_{w2} implies that the designed magnetic amplifier can compensate for the $V_{dc-link}$ rise during voltage sag. For the simulated system in figure 6.11, the boost chopper operates in a current control mode, where the reference chopper inductor current, I_{dc}^* is compared with the actual chopper inductor current, I_{dc} and the dc-link voltage, $V_{dc-link}$ is set at 100 V. Amplifier operation has been studied and is divided into two main regions:

Region #1: where the secondary winding control current signal, I_{w2} is present and contactor k_c is closed.

Region #2: where the secondary winding control current signal, I_{w2} is absent and contactor k_c is opened.

Figure 6.12 shows the magnetic amplifier voltage waveforms for the primary and secondary windings, v_{w1} and V_{w2} respectively; while figure 6.13 shows the amplifier current waveforms, I_{w1} and I_{w2}.

Region 1: Operation with contactor k_c closed

For the first 2 s of operation, the magnetic amplifier secondary winding, W_2 is connected to an ac -source v_{magamp} through diode D_c. With a normally closed contactor k_c and a low voltage

ac-supply v_{magamp}, the half wave rectified secondary winding current I_{w2} is set to 5 A. For the first part of every half cycle, the magnetic amplifier core is driven into saturation, where the corresponding flux linkage level reaches 0.27 V.s, which is marked as point 'A' on the *BH* curve in figure 6.14 part (c). The core is driven away from saturation in the second half cycle, moving from point 'A' to 'B', where the flux linkage level is reset to 0.14 V.s. As long as k_c remains closed, the core flux moves back and forth between points 'A' and 'B', where the change of flux linkage, $\Delta\varphi_m$ is determined by the difference between that at points 'A' and 'B' [6.11]. If $\Delta\varphi_m$ is small, the magnetic amplifier quickly saturates and most of the supply voltage appears across the load [6.12], where at this stage the amplifier transmits power to the load, and the dc-link voltage $V_{dc-link}$ remains unchanged, as observed in figure 6.14 (d).

Region 2: Operation with contactor k_c opened

Between 2 s and 7 s, the contactor k_c is opened and the secondary control winding current I_{w2} falls to zero. The core flux level moves from point 'A' to point 'C' and the flux level holds at 0.12 V.s, where $\Delta\varphi_m$ is near zero. Consequently, the magnetic amplifier blocks portion of the power delivered by the source to the dc-link due to the large reflected impedance on its primary side, as shown in figure 6.14 (d). If contactor k_c is closed after 7 s, operation is repeated.

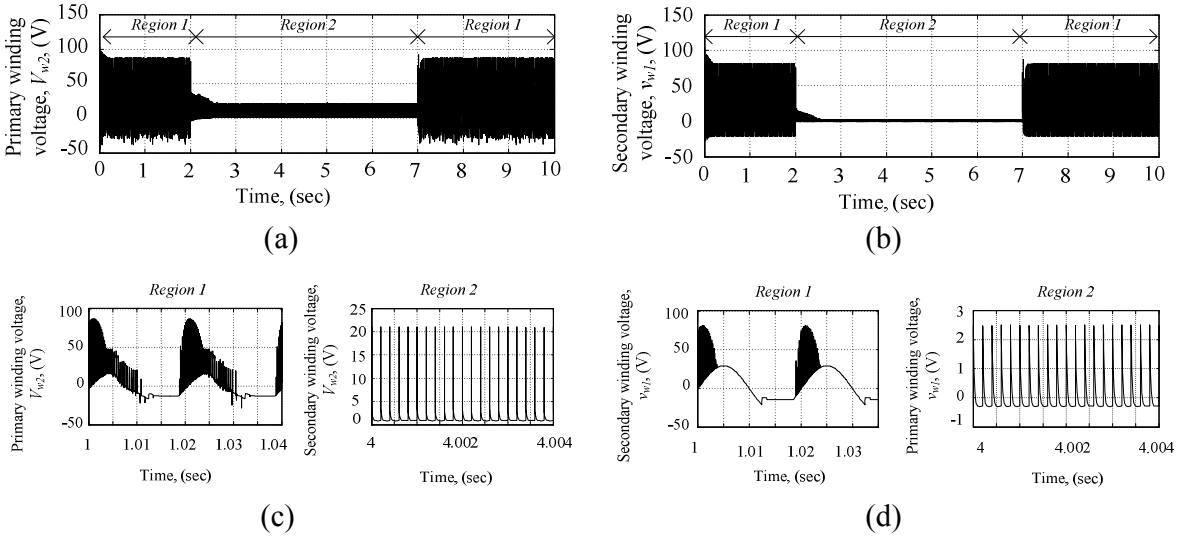

Figure 6.12. Magnetic amplifier voltage waveforms: (a) primary winding voltage, v_{w1}, (b) secondary winding voltage v_{w2}, (c) magnified view v_{w1}, and (d) magnified view of v_{w2}.

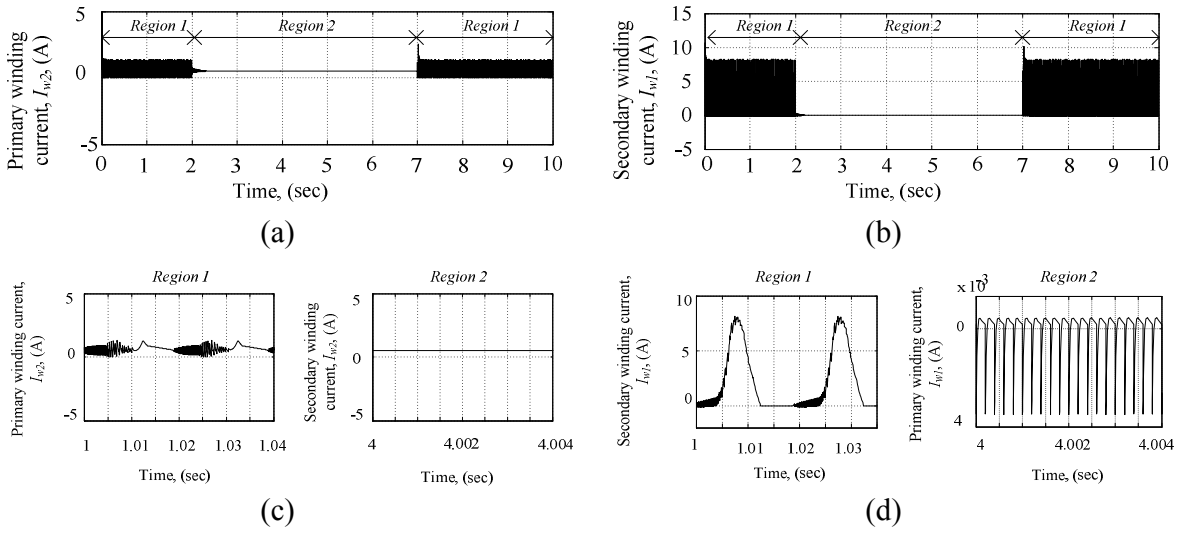

Figure 6.13. Magnetic amplifier current waveforms: (a) primary winding current, I_{w1}, (b) secondary winding current I_{w2}, (c) magnified view I_{w1}, and (d) magnified view of I_{w2}.

The difference between the control circuit used with the full scale and scaled down systems is due to the lower power level of the experimental prototype. A slight change in the control winding current I_{w2} causes a change in the flux linkage level $\Delta\varphi_m$ of the magnetic amplifier which effectively changes the reflected impedance created by the main winding.

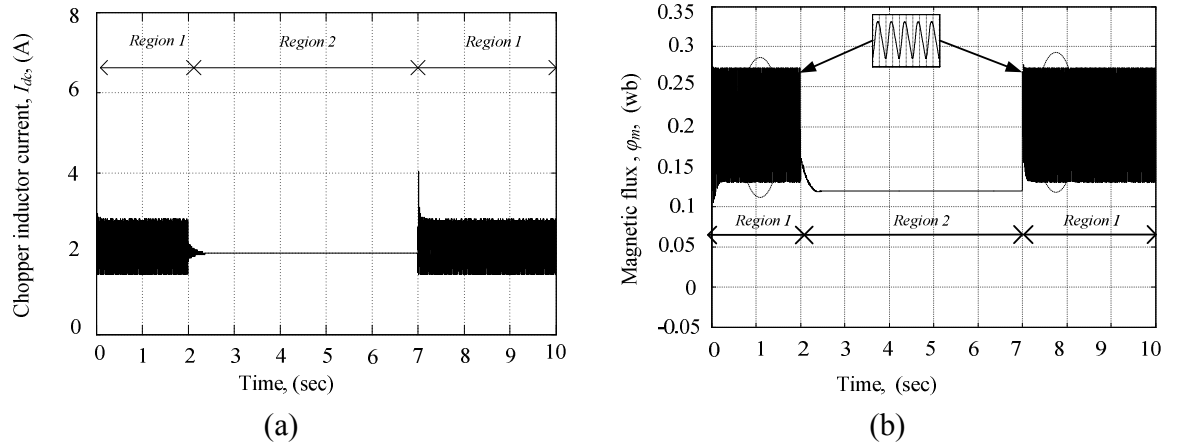

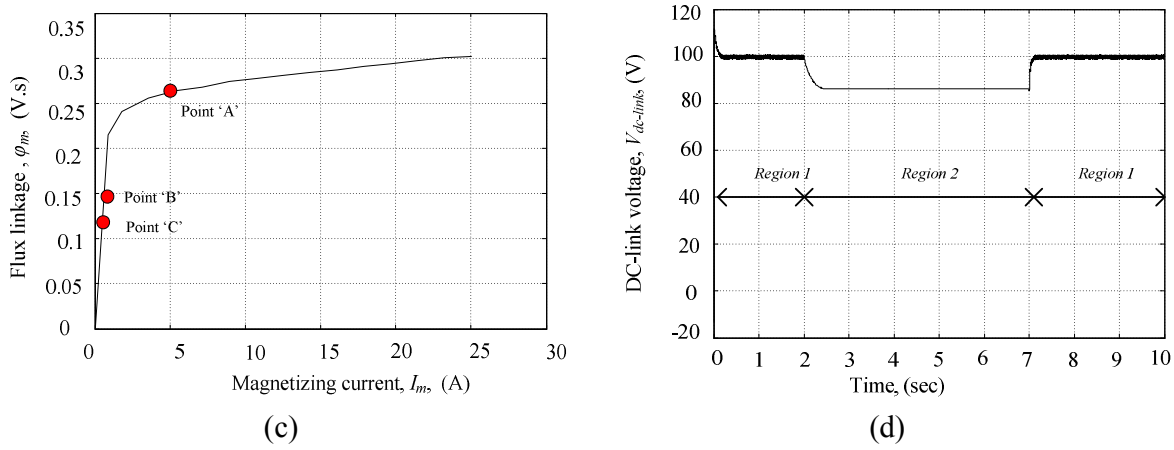

Figure 6.14. Magnetic amplifier effect when added to the boost chopper: (a) chopper inductor actual current, I_{dc}, (b) flux linkage in magnetic amplifier, φ_m, (c) magnetizing current – flux linkage characteristics, and (d) dc-link voltage, $V_{dc-link}$.

6.7 System Performance to Grid Voltage Dips

The scaled-down system in figure 6.1 is investigated by simulation and experimentation. The performance has been investigated for a sudden 75% voltage dip occurring on the grid for 5 s. The dip incidence takes place at 2 s, until 7 s after which the system is restored with the dip absent. The system waveforms for both simulation and experimental verification studies three cases: prior to a grid voltage dip, during the dip, and after the dip is cleared.

Due to the limited power level of the experimental test rig, the simulated scaled down system was investigated for a 75% voltage dip for a duration of 5 s. For smaller durations, the dc-link rise was not noticeable due to the use of large dc-link capacitance $C_{dc-link}$. Also, the energy imbalance caused by the difference between the generated and injected grid power during the voltage sag, is not high.

6.7.1. Simulation Results without the DC-Side Magnetic Amplifier

The PMSG is driven at 900 rpm using the dc motor as a prime mover coupled to its mechanical shaft. The PMSG outputs 3-phase, balanced voltages and currents are at a frequency of 30Hz. Figure 6.15 (a) to (d) show the PMSG response to grid interconnection as well as the application of symmetrical 75% voltage dips. Figure 6.15 (a) and (b) show the 3-

phase generator outputs, v_{gen} and i_{gen} respectively while figure 6.15 (c) and (d) show magnified views of v_{gen} and i_{gen}. Figure 6.16 (a) and (b) show the generator speed, n and the PMSG electromagnetic torque, T_e, respectively.

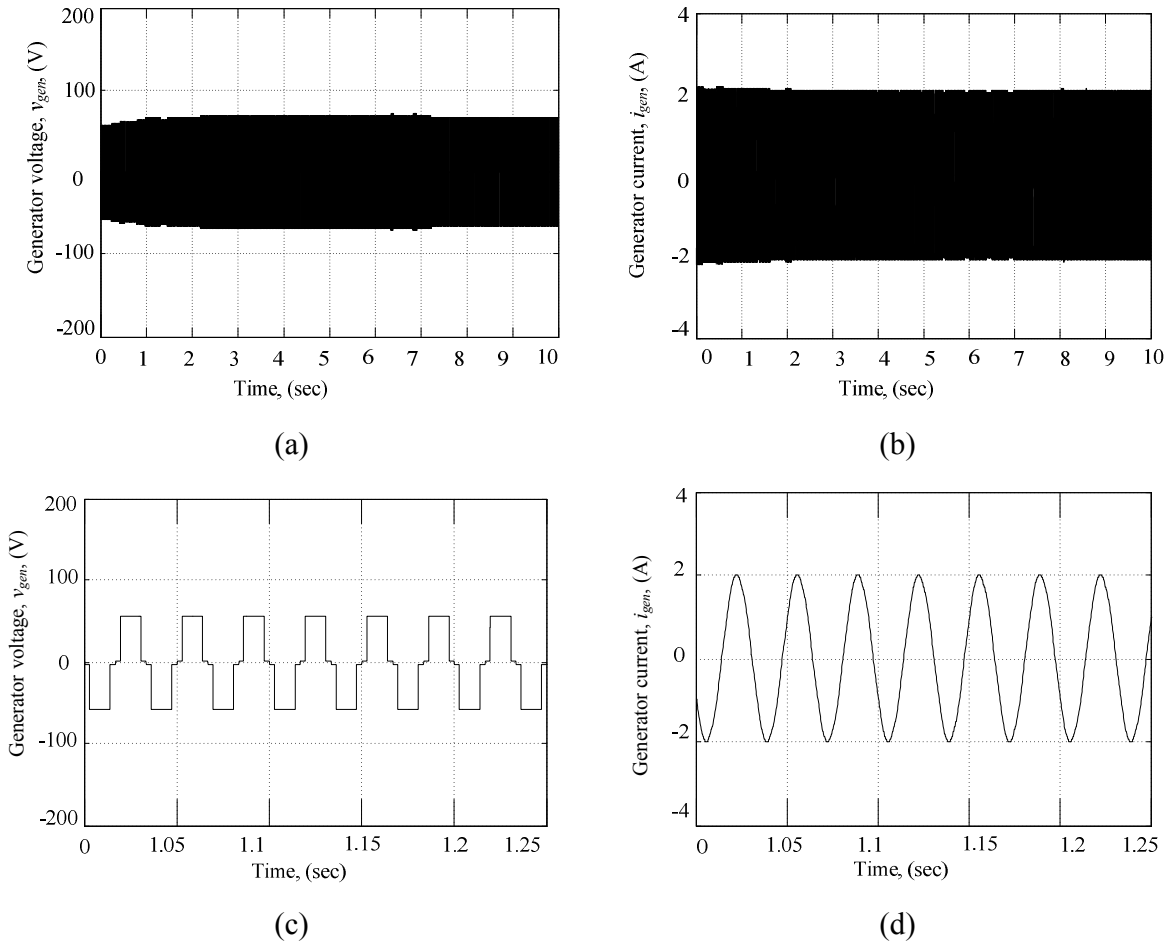

Figure 6.15. Simulation results of the scaled down system without dc-side magnetic amplifier: (a) generator voltage, v_{gen} (b) generator current, i_{gen} (c) magnified view of generator voltage, v_{gen}, and (d) magnified view of generator current, i_{gen}.

As shown in figures 6.15 and 6.16, even with the occurrence of the voltage dip incidence, the generator exhibits no change in its performance due to the total decoupling between the machine and grid side action.

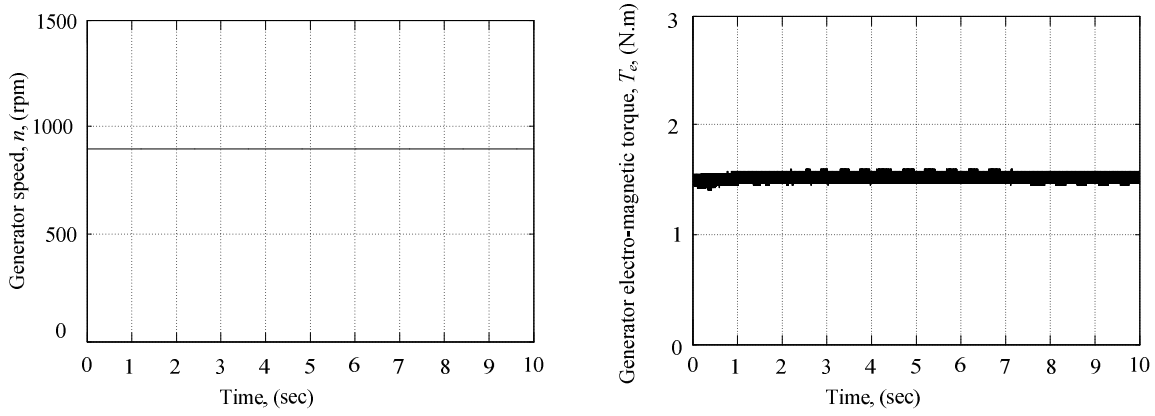

(a) (b)

Figure 6.16. Simulation results of the scaled down system without dc-side magnetic amplifier: (a) generator speed, n, and (b) generator electromagnetic torque, T_e.

The active and reactive powers supplied by the PMSG need to be measured to ensure that the same power and reactive power are extracted from the PMSG during the fault. Figure 6.17 (a) shows the active power supplied by the PMSG, P_{gen}; while part (b) shows the reactive power, Q_{gen}. Figure 6.17 (a) and (b) both indicate that even with the presence of a three-phase symmetrical dip, the same active and reactive powers are delivered by the PMSG. The value for P_{gen} is 100 W and Q_{gen} is 70 VAr.

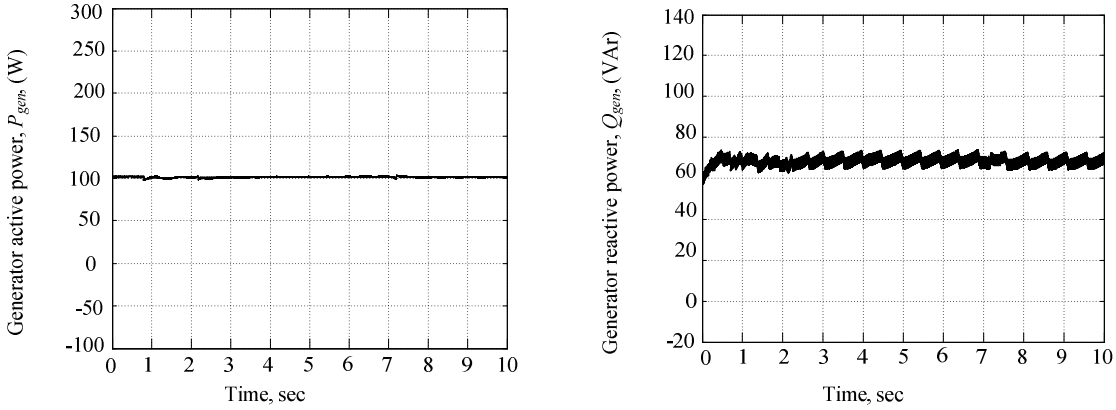

(a) (b)

Figure 6.17. Simulation results of the scaled system without dc-side magnetic amplifier: (a) active power, P_{gen}, and (b) reactive power, Q_{gen}.

As for the MSC, figures 6.18 and 6.19 show the power converter response. The MSC consists of a 6 pulse diode rectifier and a boost chopper circuit; where the main MSC objective is to extract maximum wind power at a given wind speed. With a constant speed driven PMSG, the diode rectifier output voltage, V_{dc}, remains constant provided the PMSG speed does not change. The 6 pulse diode rectifier waveforms presented in figure 6.18 (a) and (b) show the diode rectifier output voltage and current, V_{dc} and I_r respectively. A magnified view of I_r is shown in figure 6.18 (b). The V_{dc} waveform is smooth and I_{dc} is continuous with a peak value of 2 A.

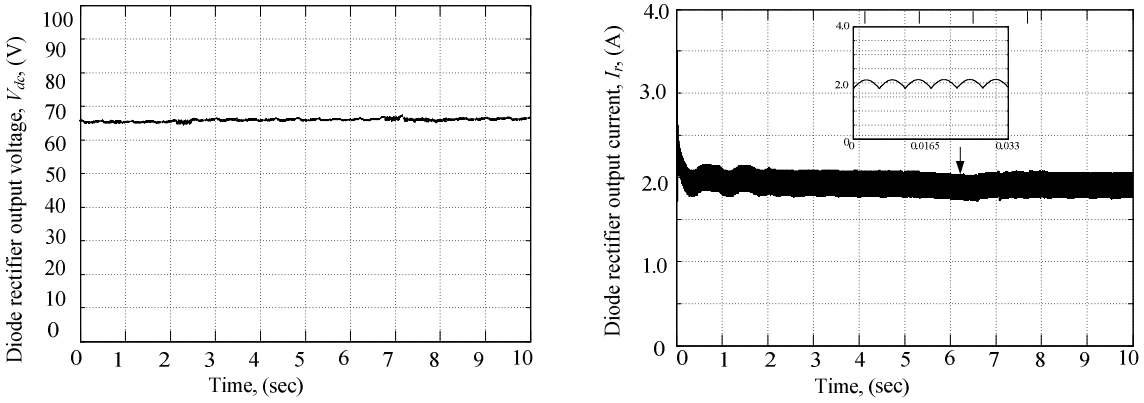

(a) (b)

Figure 6.18. Simulation results of the scaled system without a dc-side magnetic amplifier: (a) rectifier output voltage, V_{dc} and (b) rectifier output current, I_r.

As for the boost chopper, the current controlled chopper extracts constant current, I_{dc}, from the PMSG, where the reference chopper current, I_{dc}^* is 2 A. The chopper will not only extract maximum power at the given generator speed, but will also boost the output dc-link voltage, $V_{dc-link}$ for proper grid connection. Figure 6.19 (a) and (b) show the chopper inductor current reference, I_{dc}^*, actual chopper current, I_{dc}, and a magnified view of I_{dc}. Chopper inductor current, I_{dc}, is continuous with a current ripple of ±0.2 A, and tracks the reference current, $I_{dc}{}^*$, 2 A.

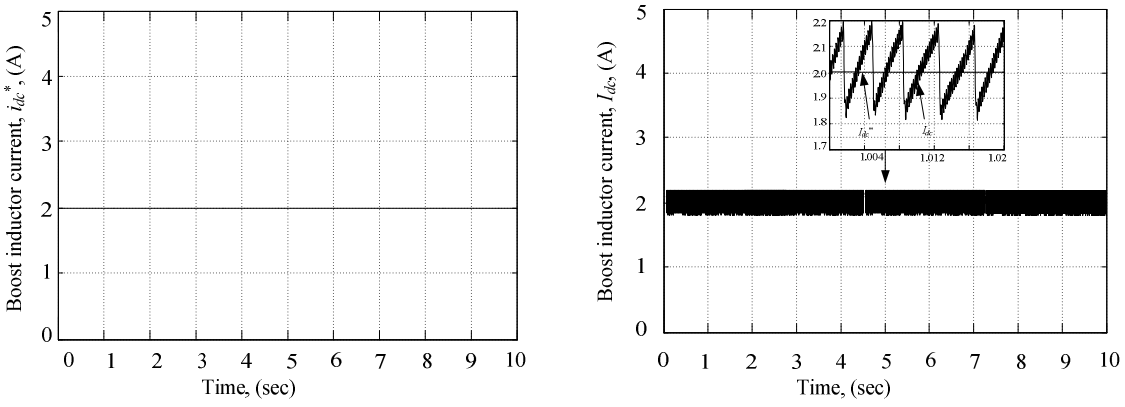

(a) (b)

Figure 6.19. Simulation results of the scaled system without a dc-side magnetic amplifier: (a) boost inductor current reference, I_{dc}^* and (b) boost chopper actual inductor current, I_{dc} .

For the GSC, the carrier based sinusoidal PWM VSI is connected to a 3-phase, balanced, 50 Hz, 40 V ac grid through resistance and a filter inductance, R_{grid} and L_{grid} respectively for grid coupling and grid current smoothing. The two-level PWM-VSI supplied from the electrolytic capacitor, $C_{dc-link}$, which acts as an energy storage element, needs a constant and ripple free voltage for proper grid interconnection and operation. Thus it is necessary to control the dc-link capacitor voltage, $V_{dc-link}$ to maintain energy balance between the extracted energy from the generator side and the energy exported to the grid side. The regulated $V_{dc-link}$ must be higher than the peak line-to-line grid voltage for grid current controllability with minimum grid current distortion. For these reasons, $V_{dc-link}^*$ is set to 100 V for both the simulation and experimental prototype. Accordingly, the maximum line-to-line inverter voltage $\widehat{v_{ab}}$ will approximately be 78 V given m_a is close to 1. The maximum line-to-line inverter voltage $\widehat{v_{ab}}$ is sufficient to inject 2 A active current, I_d, at unity power factor, into the grid. The dc-voltage level is controlled with a proportional controller and $C_{dc-link}$ is 2200μF.

Figure 6.20 shows the grid side response to a sudden voltage dip, reflected in the grid voltage, v_{grid}, and grid currents, i_{grid}. Figure 6.20 (a) show v_{grid} prior, during, and after a 75% symmetrical voltage sag: a magnified view is shown in figure 6.20 (c). Due to the

sudden grid voltage decrease, grid currents, i_{grid}, will rise as presented in figure 6.20 (b). From figure 6.20 (b) and (d), the SPWM VSI inverter injects three phase sinusoidal current, i_{grid}. According to IEEE Standard 519 which defines harmonic current limits for individual customers at a PCC, large customers are capable of causing higher voltage distortion than smaller ones. Thus, the standard allows a higher current total harmonic distortion (THD) for smaller customer loads. For customers whose short circuit current I_{sc} to full load current I_{fl} ratio falls between 20-50, the current THD level must not exceed 8% [6.13]. The grid current i_{grid} THD is 5% and is within the IEEE regulation limits.

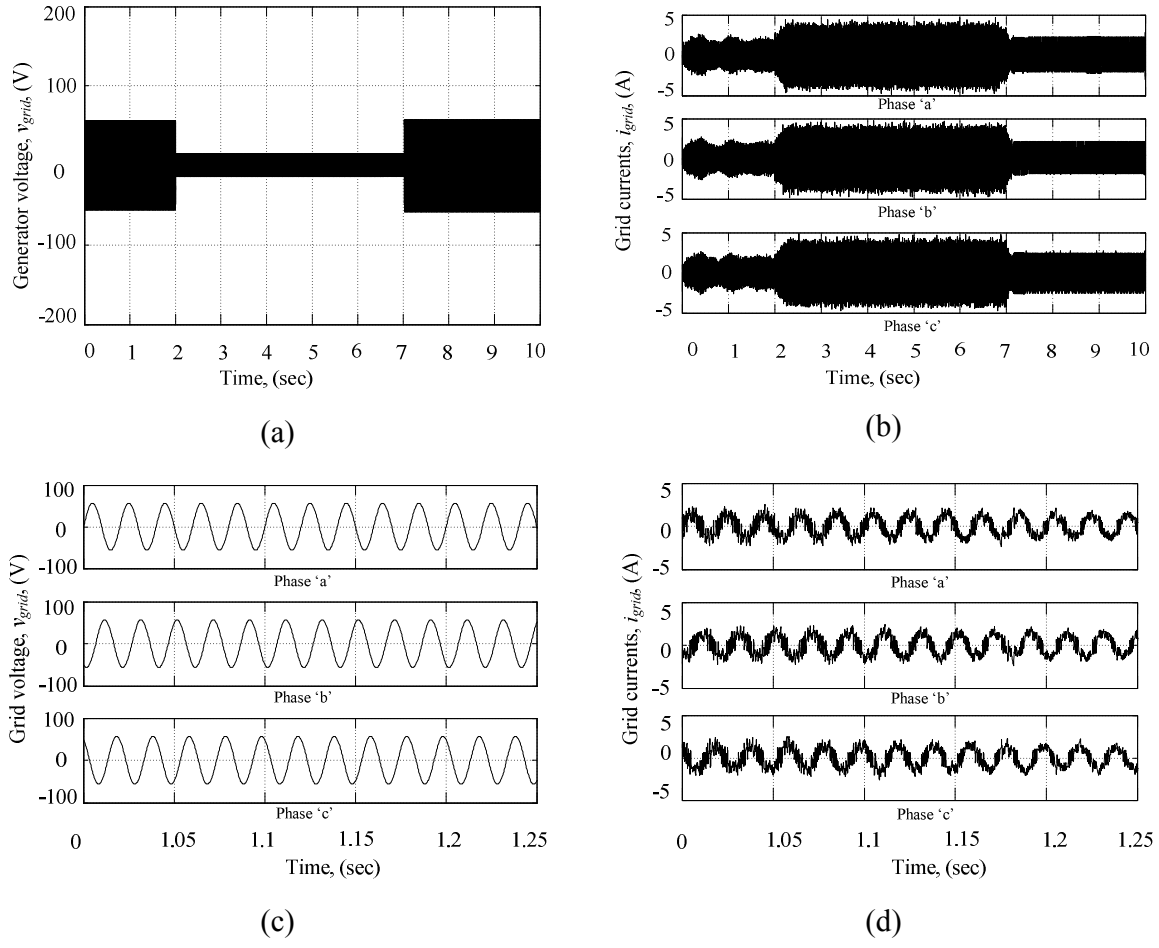

Figure 6.20. Simulation results of the scaled system without dc-side magnetic amplifier: (a) grid voltage, v_{grid}, (b) grid current, i_{grid}, (c) magnified view of v_{grid}, and (d) magnified view of grid current i_{grid}.

The PLL outputs are shown in figure 6.21 where the grid phase angle θ_u, and $\sin\theta_u$, are shown in (a), and (b), respectively. The angle changes linearly and the output is a pure sinusoid and is unaffected by the voltage dip. The PLL output locks at the fundamental frequency of the PCC voltage. The PLL output frequency is 50 Hz, as shown in figure 6.21 (b).

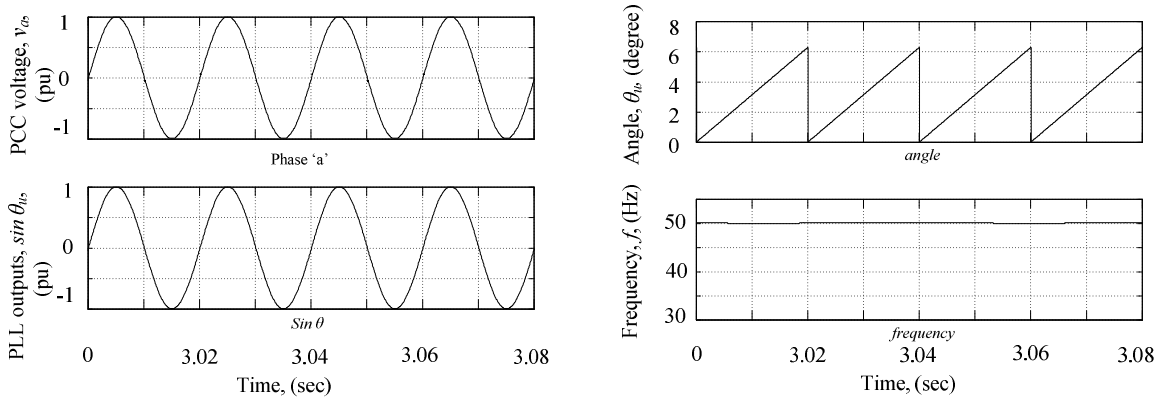

(a) (b)

Figure 6.21. Simulation results of the scaled system without dc-side magnetic amplifier: (a) PCC voltage and sin θ_u and (b) the PLL outputs, θ_u and frequency, f.

The amount of active power, P_{grid}, and reactive power, Q_{grid} transferred to the grid are demonstrated in figure 6.22 (a) and (b) respectively. Normally, 80 W are injected into the grid at unity power factor, but during the fault, P_{grid} drops to 50W while Q_{grid} remains unchanged. The difference between P_{gen} in figure 6.17 (a) and P_{grid} in figure 6.22 (a) leads to energy imbalance that will cause serious problems for the GSC.

The GSC response is presented in figure 6.23. The dc link voltage $V_{dc-link}$ rises from 100V to 150V as shown in figure 6.23 (a). Initially it is observed that the $V_{dc-link}$ experiences transient which is due to the dc-link voltage controller action. Such response is not noticed in the simulated full scale system due to difference in terms of switching and controller action. The dc-link over-voltage and oscillation caused by grid disturbances cause stress on the VSI IGBTs and may cause semiconductor switch breakdown and failure of the GSC converter. Since the outer dc-link voltage loop sets the current reference for the inner current control loop, the direct axis current, I_d^* rises in response to the $V_{dc-link}$ surplus as shown in figure

6.23 (b), where it rises from 1.2 A to 2.8 A. Due to system decoupling of d and q axis current components, the q-axis current, I_q is kept constant, with unity power factor.

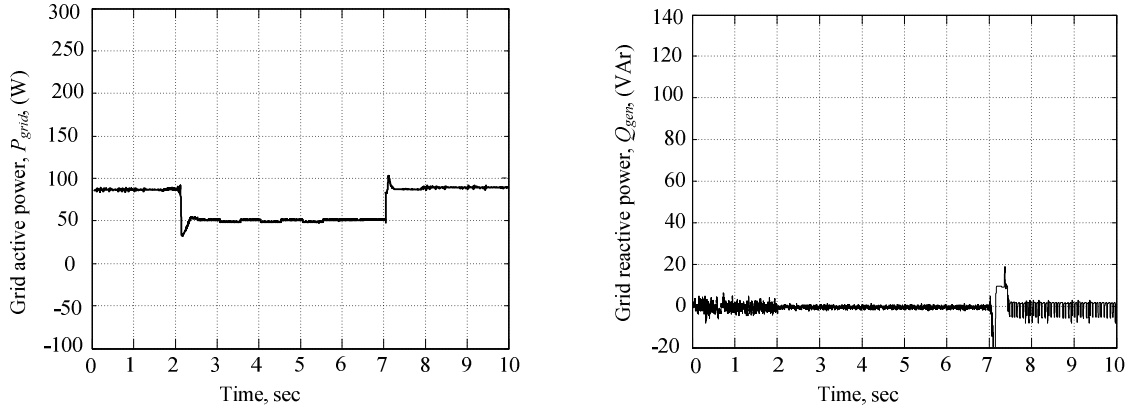

(a) (b)

Figure 6.22. Simulation results of the scaled system without a dc-side magnetic amplifier: (a) active power, P_{grid} and (b) reactive power, Q_{grid}.

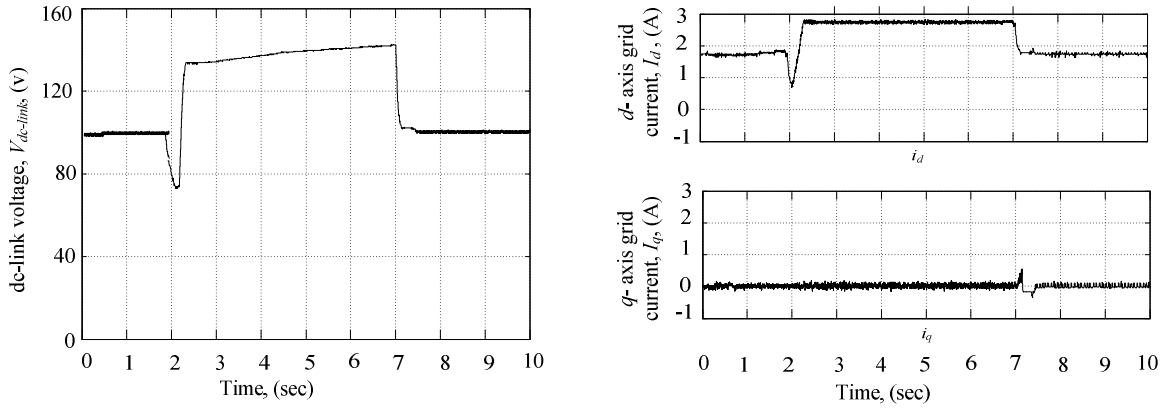

(a) (b)

Figure 6.23. Simulation results of the scaled system without a dc-side magnetic amplifier: (a) dc-link voltage, $V_{dc-link}$ and (b) grid current components, I_d and I_q.

The simulation results for both the full size and scaled down systems correlate, indicating that the scaled system response is similar to the responses obtained for large MW WECS.

6.7.2 System Response to Grid Voltage Dips using a DC-Side Magnetic Amplifier

For the scaled down system prototype, the dc-link voltage $V_{dc-link}$ will rise when the utility grid experiences a voltage dip event as indicated in figure 6.23. The longer the sag duration, the more the energy is stored in the dc-link and the higher the dc-link voltage excess. The active current component, I_d will also rise.

The pre-designed magnetic amplifier has been simulated using MATLAB for enhancing the ride through capability when added to the investigated scaled down system in response to voltage dips prior to practical validation.

Referring to figure 6.1, the boost chopper inductor L_{dc} has been removed and is replaced by the magnetic amplifier. Normally, contactor k_c is closed allowing 5 A to flow in the secondary windings of the magnetic amplifier, driving it into saturation as explained previously. In this case, the function of the magnetic amplifier is to replace L_{dc} by acting as a filtering inductor for smoothing the chopper current I_{dc}. In the event of a sudden voltage dip, the continuously sensed dc-link voltage $V_{dc-link}$ is compared to a certain threshold which detects if $V_{dc-link}$ exceeds a preset value. In this case $V_{dc-link}$ exceeds this limit, whence contactor k_C is opened forcing the magnetic amplifier to act as larger inductance inserted in the dc-link and limiting the $V_{dc-link}$ rise. When the fault is cleared, contactor k_c is closed.

The simulation results for the scaled system prototype with the magnetic amplifier are found in figures 6.24 to 6.28. Figures 6.24 to 6.26 show the PMSG and MSC responses, while figures 6.27 and 6.28 show the grid side and GSC responses. Figure 6.24 (a) and (b) show that the generator behaves similarly even with the addition of the magnetic amplifier, where the PMSG will continue to rotate at the speed, n, of 900 rpm and the electromagnetic torque, T_e, will correspond to 1.5 N.m even in the presence of the grid voltage dip. Also, the generator balanced line-to-line voltage, v_{gen}, and current i_{gen}, are 50 V and 2 A peak, respectively, at a frequency of 30 Hz as found in figure 6.25 (a) and (b): and their magnified views are shown in figure 6.25 (c) and (d). The generator line-to-line voltage is rectified through the 3-phase diode bridge rectifier whose output voltage is shown in figure 6.26 (a). Before 2 s and with the absence of any voltage sag, the magnetic amplifier operates in the saturation zone, where the secondary winding current I_{w2} is adjusted to 5 A.

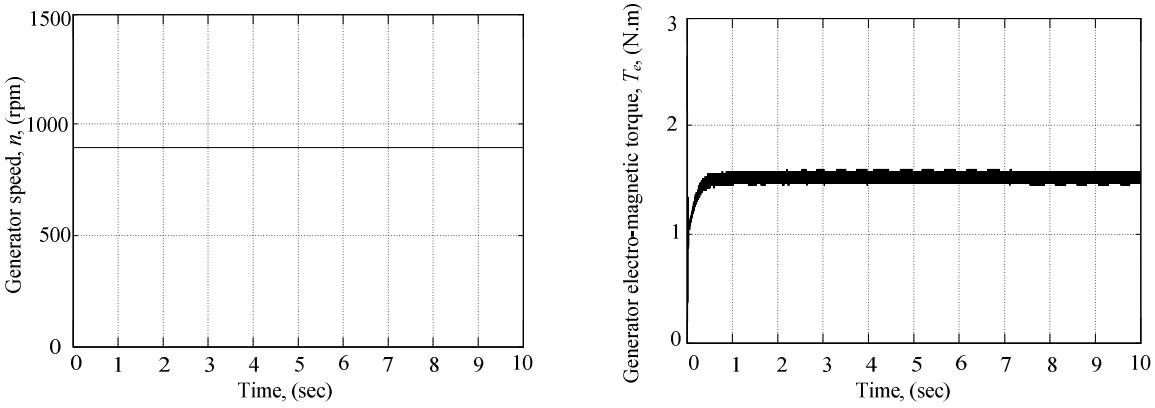

(a) (b)

Figure 6.24. Simulation results of the scaled system with dc-side magnetic amplifier: (a) speed, n and (b) electromagnetic torque, T_e.

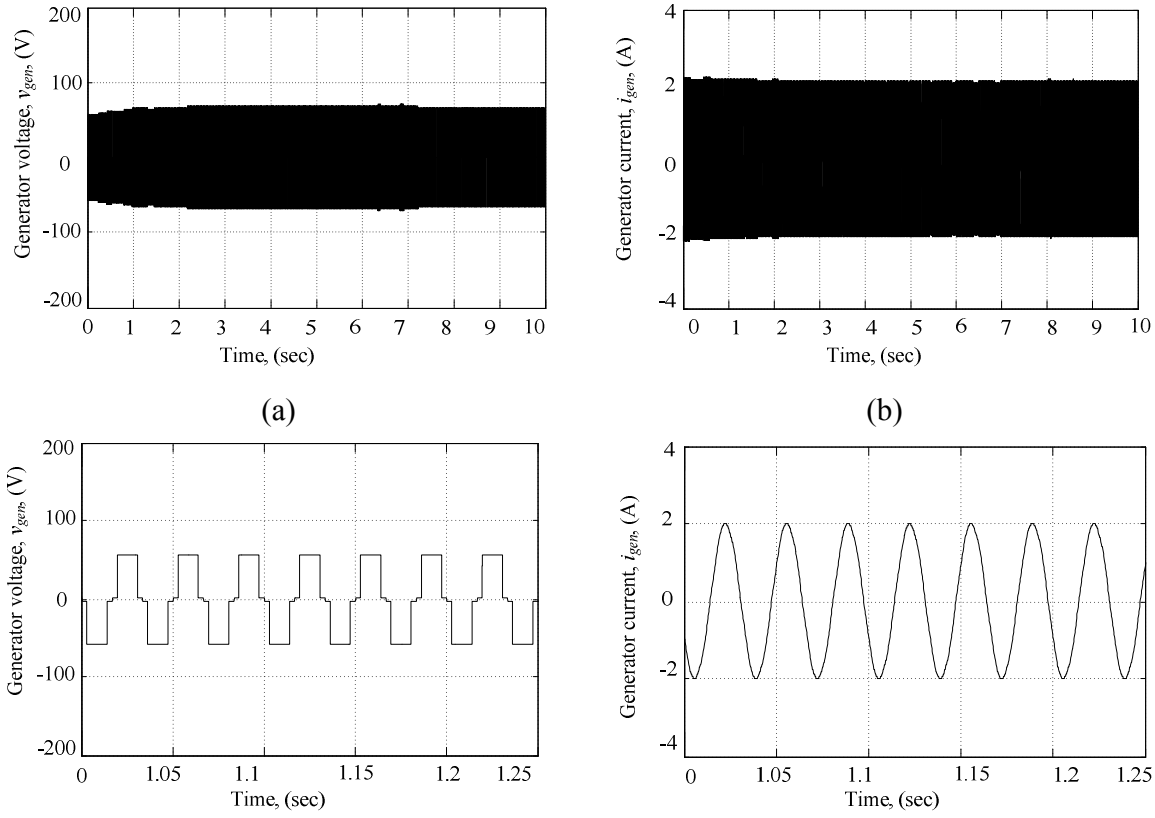

(a) (b)

(c) (d)

Figure 6.25. Simulation results of the scaled system with dc-side magnetic amplifier: (a) generator voltage, v_{gen}, (b) generator current, i_{gen}, (c) magnified view of v_{gen}, and (d) magnified view of i_{gen}.

The magnetic amplifier effectively replaces the chopper inductor L_{dc} whose action is to smooth and filter the inductor current I_{dc}. At this given PMSG speed, the MSC is selected to extract I_{dc} of 2 A from the amplifier, corresponding to the maximum extracted power at that given speed as shown in figure 6.26 (b). Before 2 s, the generator and MSC extract 100 W of active power P_{gen} as well as approximately 70 VAr of reactive power Q_{gen} as shown in figure 6.26 (c) and (d) respectively. The MSC continues to extract the same active and reactive powers even with the occurrence of the voltage dip until 7 s, after which the dip is cleared.

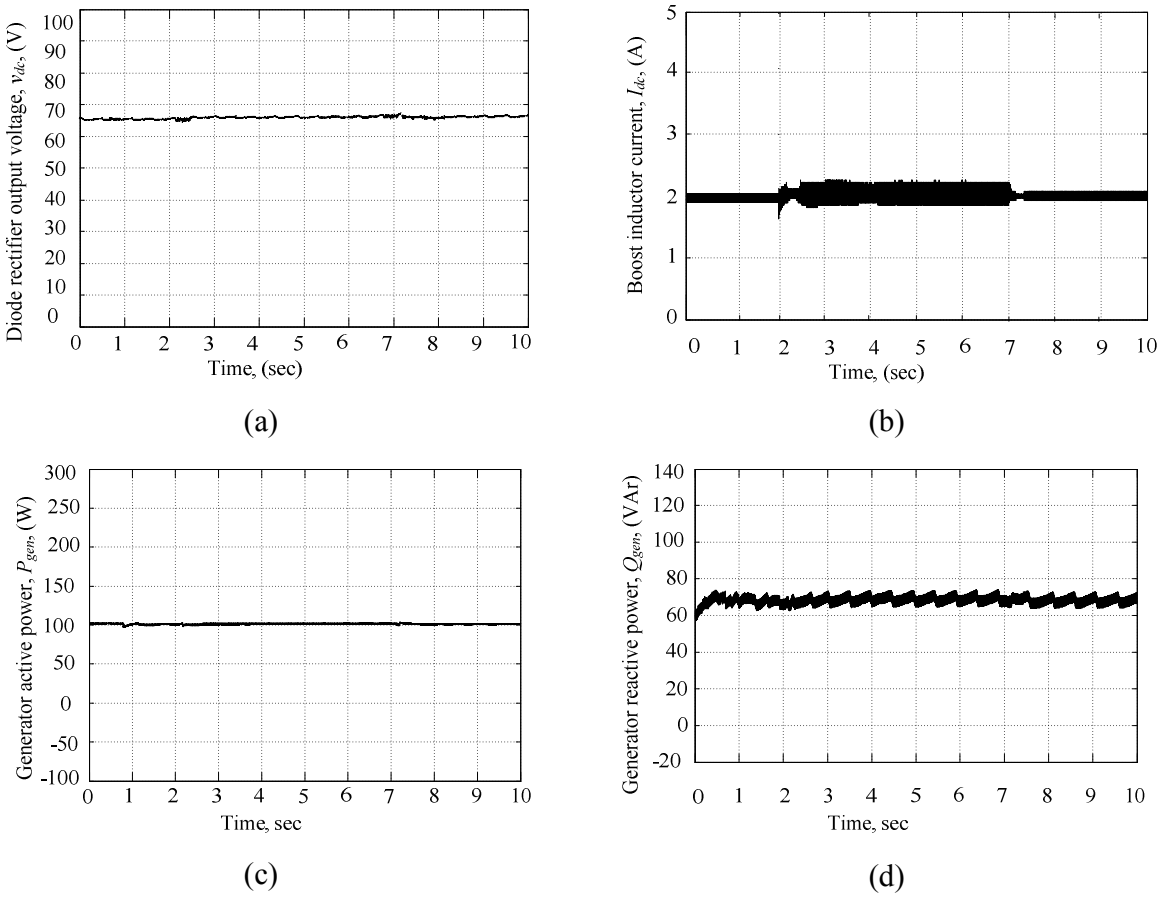

Figure 6.26. Simulation results of the scaled system with dc-side magnetic amplifier: (a) diode rectifier output voltage, V_{dc}, (b) boost chopper inductor current, I_{dc}, (c) generator extracted active power, P_{gen}, and (d) generator extracted reactive power, Q_{gen}.

The grid side and GSC responses in figures 6.27 and 6.28 show that when the voltage dip occurs at 2 s, when the grid voltage, v_{grid} suddenly falls to 75% of its nominal value, as indicated in figure 6.27 (a), the dc-link voltage, $V_{dc-link}$, starts rising and reaches the preset threshold margin, which indicates the presence of a fault as shown in figure 6.28 (a). The grid current, i_{grid}, starts rising due to the $V_{dc-link}$ rise as well as the change in the grid voltage, as indicated in part (b).

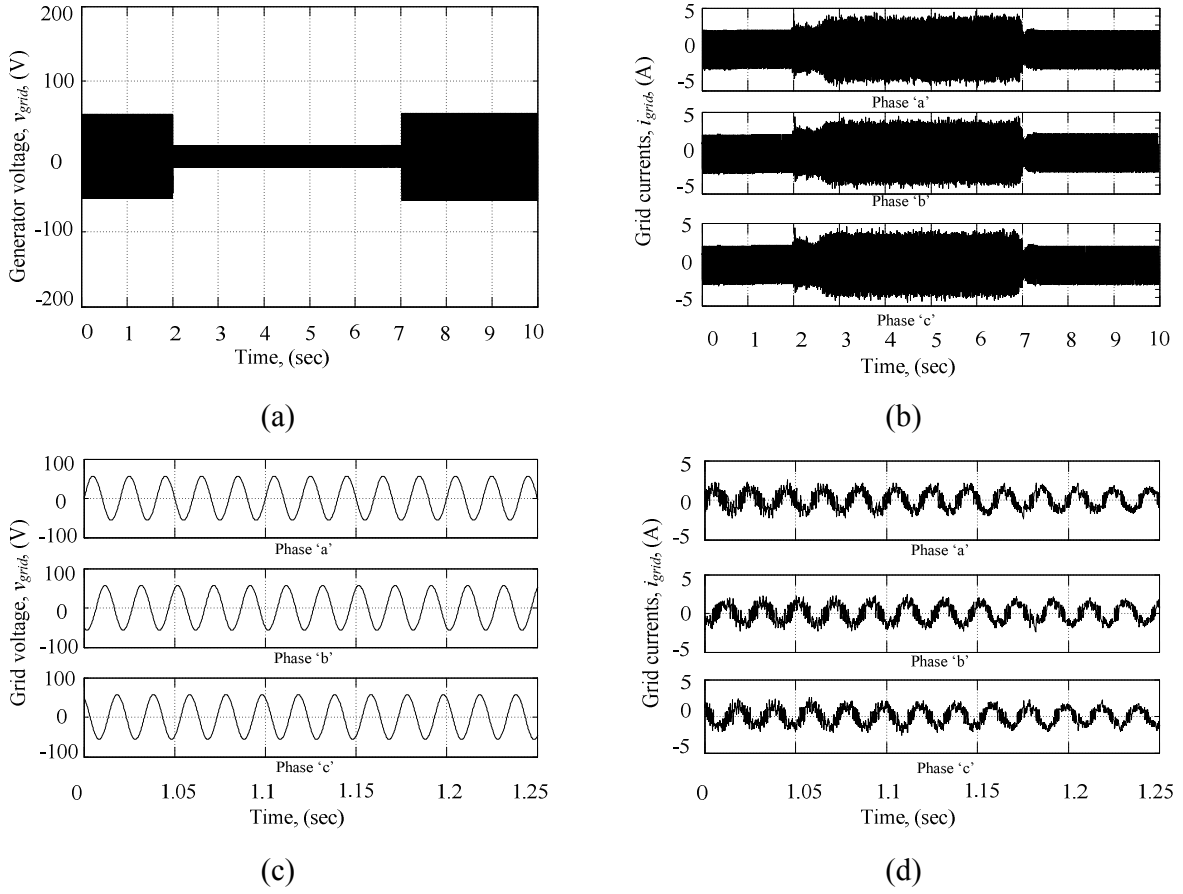

Figure 6.27. Simulation results of the scaled system with dc-side magnetic amplifier: (a) grid voltage, v_{grid}, (b) grid current, i_{grid}, (c) magnified view of v_{grid}, and (d) magnified view of i_{grid}.

The grid active power, P_{grid} falls from 80 W to 50 W as shown in part (c) of figure 6.28, while the grid injected reactive power, Q_{grid}, remains zero as indicated in figure 6.28 (d). In response to the $V_{dc-link}$ rise, magnetic amplifier control action takes place by changing the

secondary winding current, I_{w2}, from 5 A to almost zero for the fault duration, thus changing the effective impedance seen by the boost chopper and limiting the $V_{dc-link}$ voltage excess. Using the magnetic amplifier at the fault instance decreased the dc-link capacitor, $C_{dc-link}$, voltage rise by 30 V as well as slightly reducing the grid current active power component, I_d seen in figure 6.28 (b). q-axis control action is maintained even with the incorporation of the amplifier, as concluded from figure 6.28 (b) ensuring successful unity power factor operation by keeping the q-axis grid current I_q close to zero.

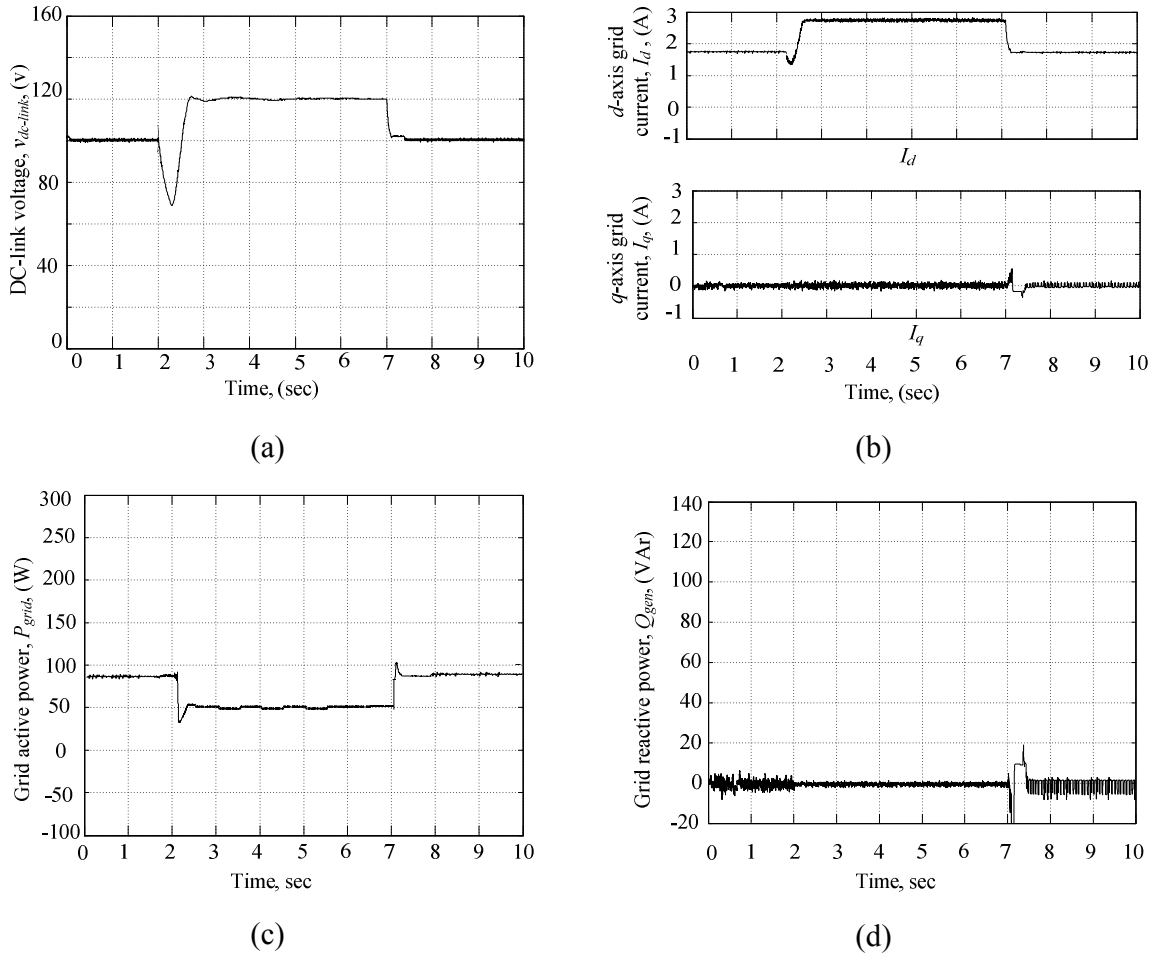

Figure 6.28. Simulation results of the scaled system with dc-side magnetic amplifier: (a) dc-link voltage, $V_{dc-link}$, (b) grid current components, I_d and I_q, (c) grid injected active power, P_{grid}, and (d) grid injected reactive power, Q_{grid}.

6.8 Experimental Verification

An experimental prototype is used to investigate the ability of the proposed system to mitigate voltage dip associated problems and ensure that the WECS can ride through the grid fault, having validated the approach using simulation analysis. The following section describes the system performance with and without the amplifier as demonstrated in figures 6.29 to 6.36. The system parameters are chosen to be the same as those used in the simulations.

Active and reactive powers (at generator and grid sides) are plotted offline as well as generator speed. For grid side active and reactive power measurements, three phase grid voltage v_{grid} and current i_{grid} where stored in 2D tables for a 10 s period corresponding to the pre, during and post fault periods. The stored data is then put into MATLAB for active power, P_{grid} and reactive power, Q_{grid}, off-line calculation. The same technique is used to calculate P_{gen} and Q_{gen} for active and reactive generator powers respectively through recording the generator line-to-line voltage, v_{gen} and the generator current, i_{gen}. As for the PMSG driven speed, a tacho-generator is used in which the induced voltage, E_{PMSG} is proportional to its driven speed.

Experimental results show that the generator speed in figure 6.29 (a) and (b), generator line to line voltage and current in figure 6.30 (a) to (c), and generator active and reactive powers in figure 6.32 (a) to (d) behave similar to the cases with or without the amplifier.

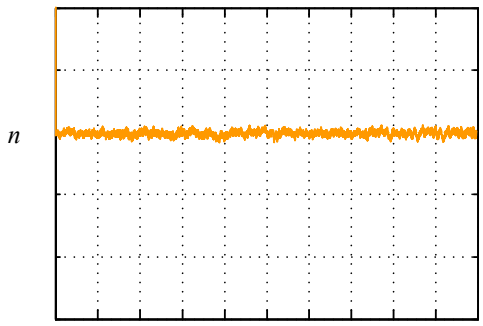

1 s/div, ch1: 300 rpm/div

(a)

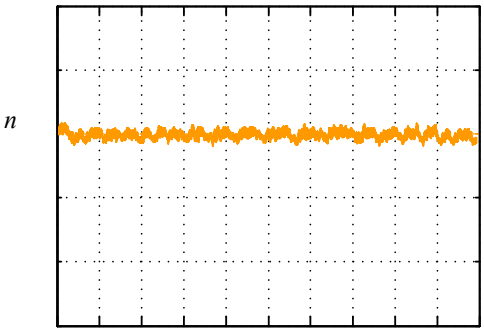

1 s/div, ch1: 300 rpm/div

(b)

Figure 6.29. Experimental results with and without the magnetic amplifier: (a) PMSG speed, n, without amplifier and (b) n with amplifier.

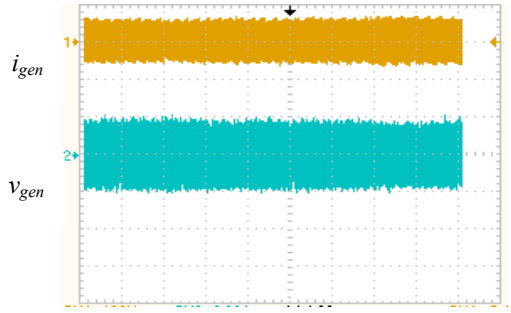

1 s/div, ch1: 100 V/div, ch2: 2A/div

(a)

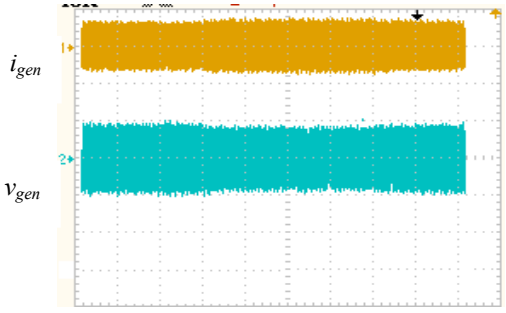

1 s/div, ch1: 100 V/div, ch2: 2A/div

(b)

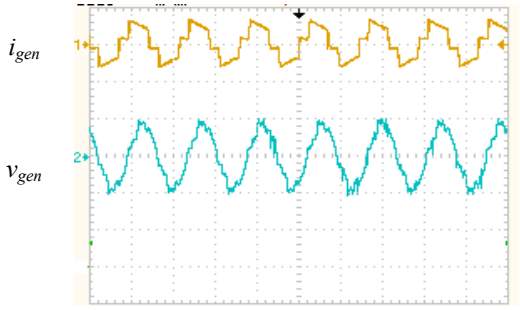

25 ms/div, ch1: 100 V/div, ch2: 2A/div

(c)

Figure 6.30. Experimental results with and without the magnetic amplifier: (a) PMSG voltage and current, v_{gen} and i_{gen} respectively without amplifier, (b) v_{gen} and i_{gen} with amplifier, and (c) magnified view of v_{gen} and i_{gen} for both conditions.

As for the boost inductor current, the waveform shapes are different as shown in figure 6.31 (a) without the magnetic amplifier and figure 6.31 (b) with the magnetic amplifier, due to the influence and interaction between the boost inductor current in the primary winding I_{w1} of the magnetic amplifier with the rectified secondary winding current I_{w2} which will allow second low order harmonic current content to circulate in the magnetic amplifier. The chopper current I_{dc} tracks the reference current I_{dc}^{*} for maximum power extraction, as shown in figure 6.31 (a). The grid and GSC responses are shown in figures 6.33 to 6.36. Figure 6.33 (a) through (c) demonstrate the effect of adding the magnetic amplifier onto dc-link voltage $V_{dc-link}$ at different power levels.

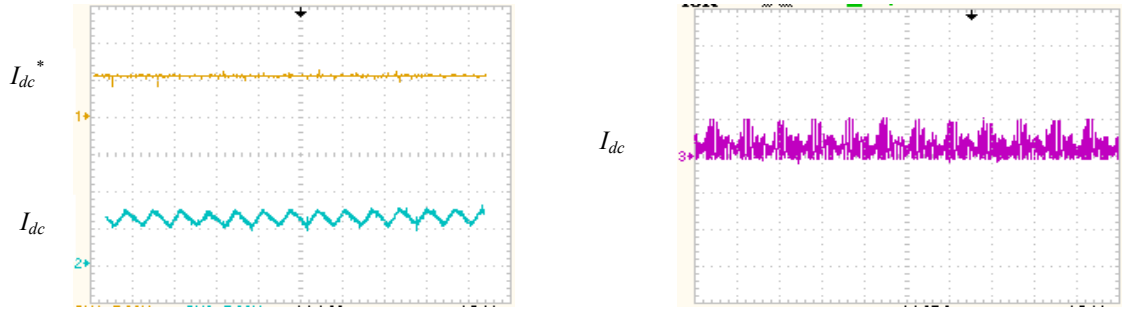

1 s/div, ch1: 2 A/div, ch2: 2 A/div

(a)

25 ms/div, ch1: 5 A/div

(b)

Figure 6.31. Experimental results with and without the magnetic amplifier: (a) boost chopper reference I_{dc}^* and actual inductor current without amplifier I_{dc} and (b) I_{dc} with amplifier.

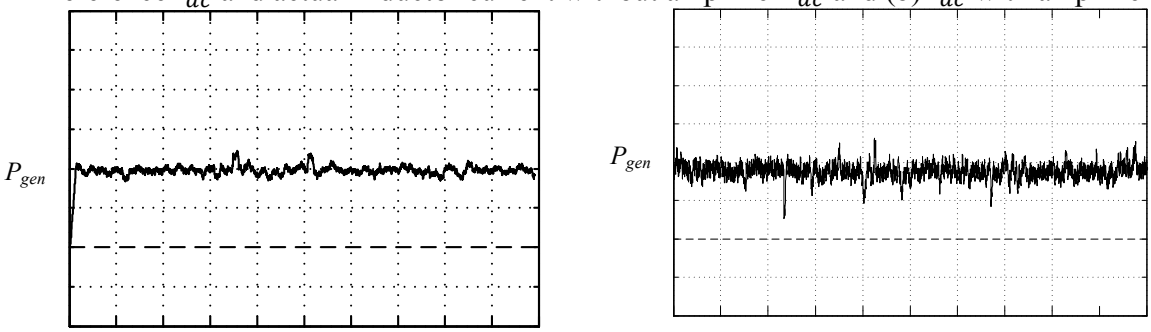

1 s/div, ch1: 50 W/div, ch2: 50 W/div

(a)

1 s/div, ch1: 50 W/div, ch2: 50 W/div

(b)

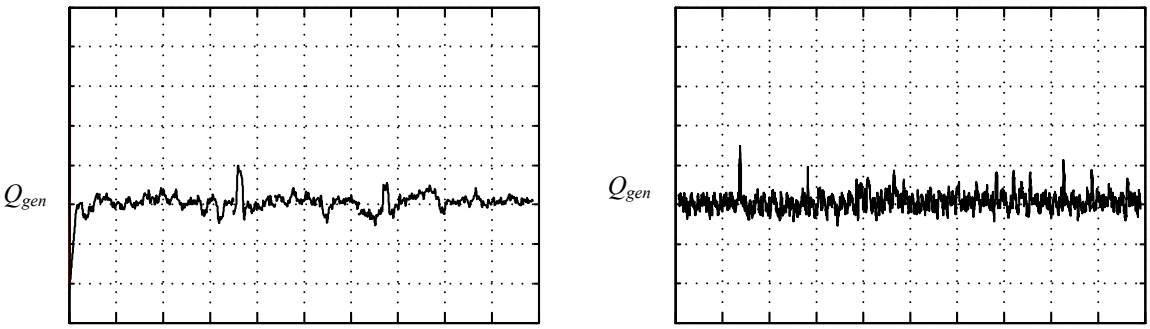

1 s/div, ch1: 20 VAr/div, ch2: 20 VAr/div

(c)

1 s/div, ch1: 20 VAr/div, ch2: 20 VAr/div

(d)

Figure 6.32. Experimental results with and without the magnetic amplifier: (a) generator active power without amplifier, P_{gen}, (b) P_{gen} with amplifier, (c) generator extracted reactive power without amplifier, Q_{gen}, and (d) Q_{gen} with amplifier.

Without the magnetic amplifier, $V_{dc-link}$ increases to 1.6 times its nominal value and upon restoration of the grid voltage, $V_{dc-link}$ recovers in 5 s. With the magnetic amplifier incorporated, the increase in $V_{dc-link}$ is reduced to 1.2 times its nominal value, and recovery is in 2.5 s, for the given power level. If the power level of the PMSG is reduced, $V_{dc-link}$ response is limited as in figure 6.33 (c). The dq axes grid current components, I_d and I_q, responses are shown in figure 6.34, showing a slight reduction in the d-axis current in (b) when compared to (a), while the q-axis is maintained at zero for unity power factor operation in both (a) and (b).

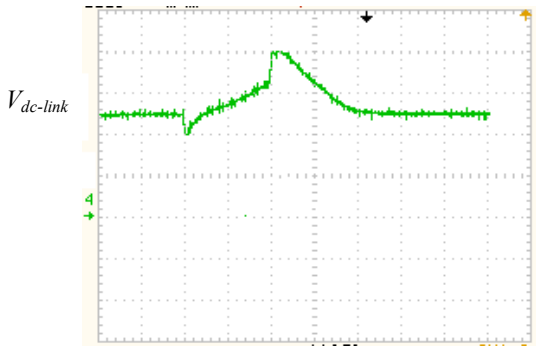

2.5 s/div, ch1: 40 V/div

(a)

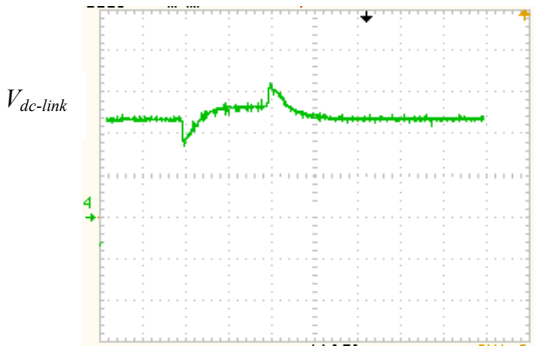

2.5 s/div, ch1: 40 V/div

(b)

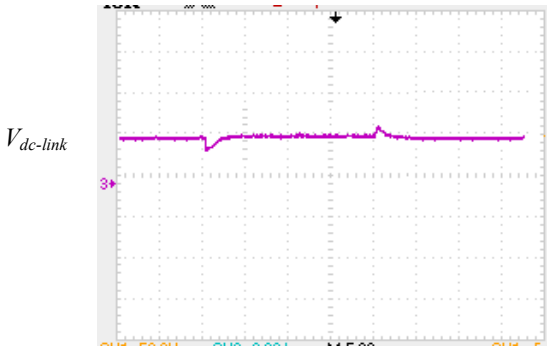

2 S/div, ch1: 100 V/div

(c)

Figure 6.33. Experimental results with and without the magnetic amplifier: (a) dc-link voltage, $V_{dc-link}$, without magnetic amplifier, (b) $V_{dc-link}$, with magnetic amplifier, and (c) $V_{dc-link}$,with magnetic amplifier at reduced power level.

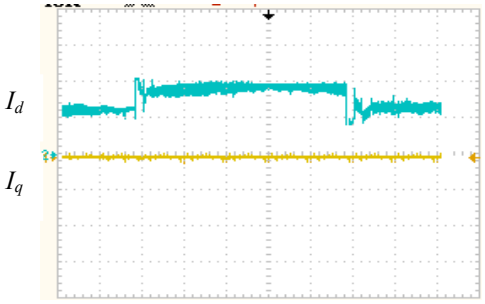

1 s/div, ch1: 2 A/div, ch2: 2 A/div

(a)

1 s/div, ch1: 2 A/div, ch2: 2 A/div

(b)

Figure 6.34. Experimental results with and without the magnetic amplifier: (a) grid current components, i_d and i_q, without magnetic amplifier and (b) i_d and i_q with magnetic amplifier.

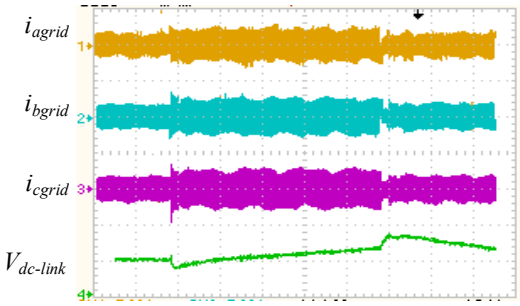

1 s/div, ch1: 5 A/div, ch2: 5A/div, ch3: 5 A/div, ch4: 100v/div

(a)

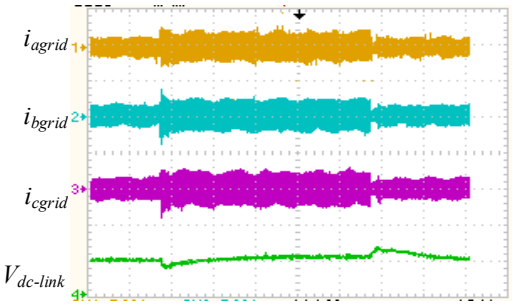

1 s/div, ch1: 5 A/div, ch2: 5A/div, ch3: 5 A/div, ch4: 100v/div

(b)

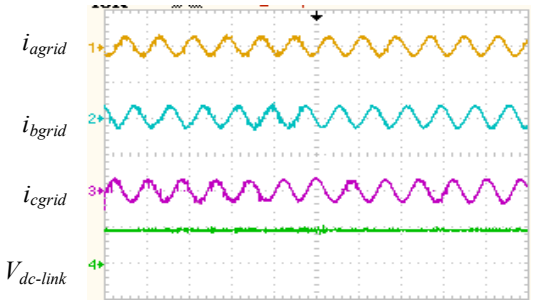

25 ms/div, ch1: 5 A/div, ch2: 5A/div, ch3: 5 A/div, ch4: 100v/div

(c)

Figure 6. 35. Experimental results with and without magnetic amplifier: (a) grid current, i_{grid}, and dc-link voltage, $V_{dc-link}$ without magnetic amplifier, (b) i_{grid}, and $V_{dc-link}$ with magnetic amplifier, and (c) magnified view of i_{grid}.

Grid active current components could be altered to satisfy certain power requirements during fault by forcing the d-axis current controller to inject a specific amount and the q-axis is calculated accordingly. Three phase grid currents, i_{grid}, are demonstrated in figure 6.35 (a) and (b), as well as their magnified view in figure 6.35 (c).

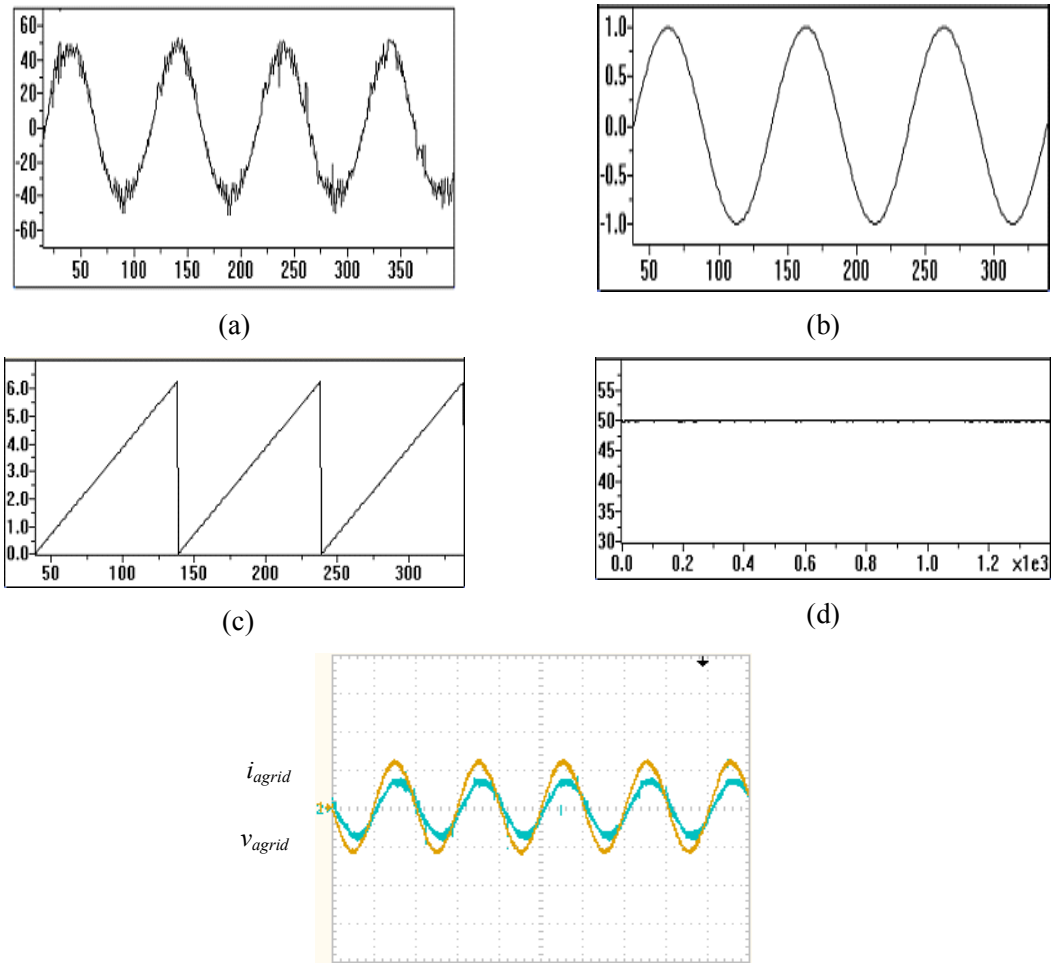

(a) (b)

(c) (d)

10 ms/div, ch1: 50 V/div, ch2: 2A/div

(e)

Figure 6.36. PLL practical results: (a) PCC voltage, (b) the PLL outputs, θ_u, (c) $sin\,\theta_u$, (d) output frequency, f_{grid}, and (e) synchronizing grid voltage and grid current, v_{agrid} and I_{agrid}.

Figure 6.36 (a) to (d) show the practical results recorded using the DSP interfacing program. The voltage measured at the PCC, v_{agrid} is shown in figure 6.36 (a). The PLL outputs, θ_u, and $\sin\theta_u$, are shown in figure 6.36 (b) and (c) respectively. The angle changes linearly and the output is a pure sinusoid, and locked at the fundamental frequency of the PCC voltage. The frequency of the PLL output, f_{grid} is 50 Hz, as shown in figure 6.36 (d). The synchronizing voltage, v_{agrid} and current i_{agrid} are in phase and satisfy unity power factor operation. Active power and reactive powers injected to the grid, P_{grid} and Q_{grid} are outlined in figure 6.37 (a) and (b) respectively.

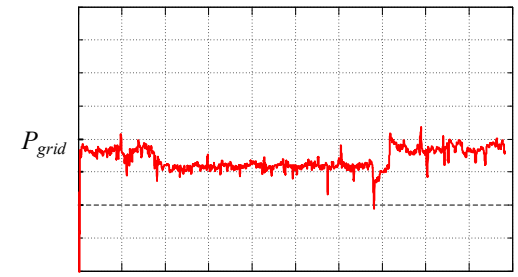

1 s/div, ch1: 50 W/div, ch2: 50 W/div

(a)

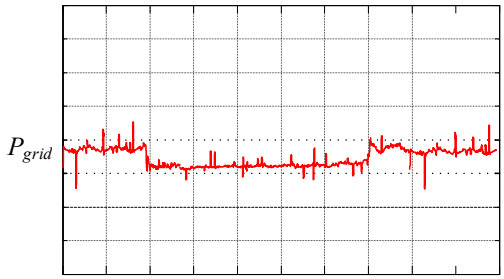

1 s/div, ch1: 50 W/div, ch2: 50 W/div

(b)

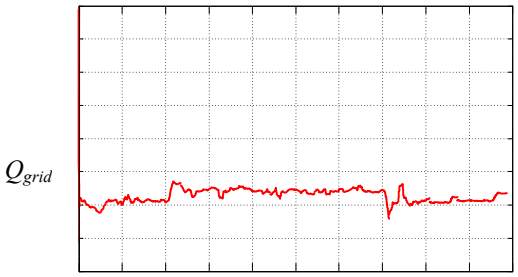

1 s/div, ch1: 20 VAr/div, ch2: 20 VAr/div

(c)

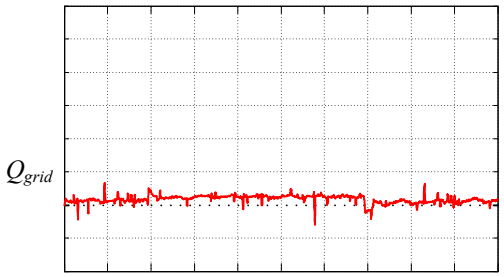

1 s/div, ch1: 20 VAr/div, ch2: 20 VAr/div

(d)

Figure 6.37. Experimental results with and without the magnetic amplifier: (a) grid injected active power, P_{grid}, without magnetic amplifier (b) P_{grid}, with magnetic amplifier, (c) grid injected reactive power, Q_{grid}, without the magnetic amplifier, and (d) grid injected reactive power, Q_{grid}, with the magnetic amplifier.

6.9 Discussion

Using magnetic amplifiers for LVRT capability improvement has been investigated for application with a high power of 1.5 MW PMSG wind turbine system in Chapter 5. Employing a single magnetic amplifier element embedded in the boost chopper, replacing the chopper inductor, L_{dc} has successfully enhanced the LVRT capability of the simulated 1.5 MW WT. The magnetic amplifier was able to limit the dc-link voltage $V_{dc-link}$ rise to approximately 1000 V during the voltage dip incidence, with improved grid recovery characteristic after fault clearance.

For experimental verification, a scaled down system prototype was implemented and a magnetic amplifier tested for ride-through capability. Comparing the results for the dc-link voltage $V_{dc-link}$ without the magnetic amplifier in figure 6.33 (a) and with the magnetic amplifier in figure 6.33 (b), it is concluded that the amplifier successfully block almost 30 V, reducing the dc-link voltage rise to 60%. Under reduced loading conditions, the magnetic amplifier was able to totally block any rise in the dc-bus voltage as indicated by figure 6.33 (c). Also, with the resultant better regulation of $V_{dc-link}$, the d-axis grid current, I_d is slightly enhanced and reduced as shown in figure 6.34 which in turn reflects on the 3–phase grid current i_{grid} being exported to the grid as in figure 6.35. Enhancing the pre-designed amplifier parameters as well as the control system's ability to induce a rapid change in the magnetic amplifier flux ensures improved dc-link voltage blocking capability and could totally limit the dc-link rise.

Figure 6.38 (a) to (c) compares the full size system, simulated scaled down system, and experimental prototype. The results show improvement in the dc-link voltage magnitude reduction during the fault, reduction in the injected grid current during the fault as well as improved recovery time for all three systems. Results shown for the simulated scaled down system and the corresponding experimental prototype correlate.

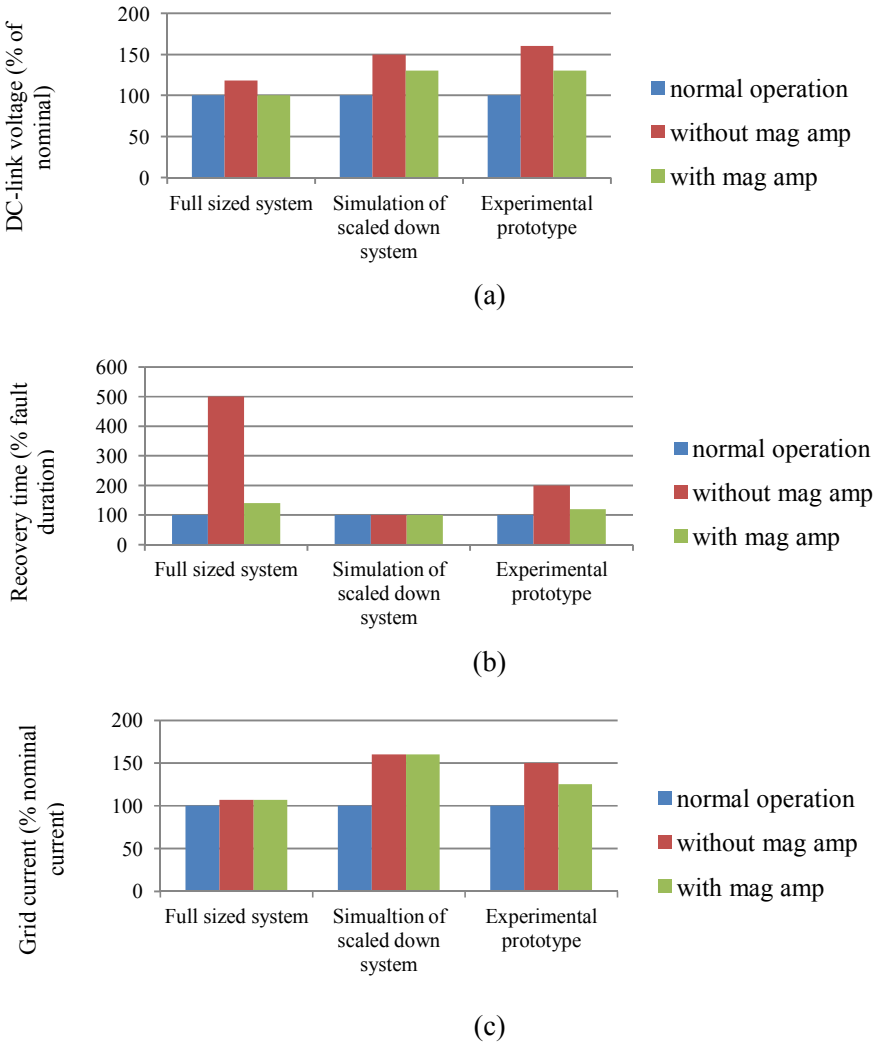

Figure 6.38. Comparison between full sized systems, scaled down system simulation and experimental prototype response: (a) DC-link voltage, $V_{dc-link}$, (b) recovery time, and (c) grid current, i_{grid}.

6.10 Summary

WECS experience dc-link voltage rise in response to grid voltage dip which may reflect serious stresses on the power converters and which may eventually lead to disconnection of the wind farm. Compensating the dc-link voltage rise through the use of a magnetic amplifier inserted in the boost chopper has been investigated on a scaled down system prototype. System performance has been studied through simulating the scaled down system as well as

through practical validation. The magnetic amplifier design had been carried out and tested for validity, which has proven its ability for enhancing the low voltage ride through capability for PMSG based WECS. Using the magnetic amplifier as a solution for enhancing the LVRT capability of wind turbines shows promise due to its reduced size and overall costs, as well as its ability to block the dc-link voltage rise and help maintain the power balance between the generation and grid sides. The proposed design was unable to fully compensate the dc voltage surplus as the blocking capability is parameter dependant and is affected by the control circuitry of the magnetic amplifier. Further modifications to the design criterion of the amplifier are needed to ensure total compensation capability. This would involve using nanocrystalline core material (as opposed to steel), which offers permeabilities 30 times higher than steel.

References

[6.1] A. Morales, *et al.*, 'Advanced Grid Requirements for the Integration of Wind Farms into the Spanish Transmission System', IET Renewable Power Generation, Vol. 2, 2008. pp. 47-59.

[6.2] J. Niiranen, 'Experiences on Voltage Dip Ride through Factory Testing of Synchronous and Doubly Fed Generator Drives', European Conference on Power Electronics and Applications, 2005. pp. 11 pp.-P.11.

[6.3] F. L. Luo and H. Ye,'Advanced DC/AC Inverters: Applications in Renewable Energy', Taylor & Francis, 2013.

[6.4] B. S. Guru and H. R. Hiziroglu,'Electric Machinery and Transformers', Harcourt Brace Jovanovich, Technology Publications, 1988.

[6.5] W. Theodore,'Electrical Machines , Drives And Power Systems', Pearson Education, 2007.

[6.6] A. A. Aboushady, *et al.*, 'Performance Analysis of a New Modular Nano-Crystalline Core Transformer based Converter for Medium Voltage DC Transmission Applications', 5th IET International Conference on Power Electronics, Machines and Drives (PEMD), 2010. pp. 1-6.

[6.7] J. C. Fothergill, P. W. Devine, and P. W. Lefley, 'A Novel Prototype Design for a Transformer for High Voltage, High Frequency, High Power Use', IEEE Transactions on Power Delivery, Vol. 16, 2001. pp. 89-98.

[6.8] B. W. Williams,'Power Electronics: Devices, Drivers Applications and Passive Components', MacMillan, 1987.

[6.9] T. C. Monteiro, *et al.*, 'Transformer Operation at Deep Saturation: Model and Parameter Determination', IEEE Transactions on Industry Applications, Vol. 48, 2012. pp. 1054-1063.

[6.10] C. W. Lufcy, 'A Survey of Magnetic Amplifiers', Proceedings of the IRE 1955. pp. 404-413.

[6.11] G. M. Ettinger, 'Some Aspects of Magnetic Amplifiers', Proceedings of the IEE - Part B: Radio and Electronic Engineering Vol. 105, 1958. pp. 237 - 248

[6.12] K. M. Salim, *et al.*, 'Preliminary Experiments on Saturated DC Reactor Type Fault Current Limiter', IEEE Transactions on Applied Superconductivity, Vol. 12, 2002. pp. 872-875.

[6.13] T. L. Skvarenina,'The Power Electronics Handbook', Taylor & Francis, 2001.

CHAPTER SEVEN

CONCLUSION

7.1 General Conclusion

Grid stability and supply security are the most important aspects of energy supplies to prevent power outages. Thus it is necessary that power generating plants have control capabilities and protection mechanisms to overcome these problems. In the past, these requirements were mainly fulfilled by conventional power plants. However, with the increased contribution made by renewable energy sources to the total amount of electricity generated, these sources too must contribute to grid stability. An important part of these requirements is LVRT capability of generating plants which requires that wind farms continue to operate through short periods of low grid voltage and to not disconnect from the grid. Short-term voltage dips may occur when large loads are connected to the grid or as a result of grid faults and transformers energizing. Power converter loss, generator over-speeding and failure, dc-bus voltage rise, and high grid inrush currents are the most common phenomena associated with voltage dips. For these reasons LVRT requirements have been introduced to guarantee that generating plants stay connected to the grid to avoid blackouts which might occur due to the consecutive disconnection of generating plants. LVRT capability enhancement technologies offer a range of solutions for successful ride-through of generating plants which not only are suitable for individual turbines, but also are applicable at the wind farm level.

The thesis outcomes can be described as follows:

- WECS modelling is important to examine system behaviour during normal and fault conditions. For this reason, a 1.5 MW PMSG based WECS has been simulated and mathematically modelled. The model includes the mechanical wind turbine, PMSG, and ac-dc-ac conversion units, as well as grid coupling and grid representation. The control algorithms used for controlling the power converters satisfy the maximum power extraction criterion, dc-bus voltage regulation, and active and reactive grid power control.

- Grid codes developed by grid operators involve rules and regulations for operation of wind plants. The modelled WECS has been tested in compliance to UK grid codes in terms of active and reactive power sudden changes, frequency excursion and phase jumps. The modelled system complies with UK grid requirements for interconnection in terms of the mentioned criteria.
- LVRT capability reflects the WECS behaviour to short duration grid voltage disturbances. Methods of LVRT capability enhancement were reviewed, outlining their limitations and advantages. The technologies being reviewed are suitable for individual wind turbines as well as for whole wind farms, with attention to techniques applicable to PMSG based WECS.
- The effect of symmetrical voltage dips on the 1.5 MW have been investigated. The study showed that a 90% voltage dip magnitude for 140 ms significantly affects system performance. The dc-link voltage rise accompanied by an abrupt grid current increase leads to abnormal system behaviour as well as severe current and voltage stresses on the power converters. Also system recovery after fault clearance is affected.
- Magnetic amplifiers are devices used in a variety of applications such as instrumentation, servo mechanisms, and battery chargers. They offer flexible configurations in terms of connection and control and are characterised by their reliability, high current capacity, inherent control isolation, and long life time. Magnetic amplifiers are proposed in this research as a method for LVRT capability enhancement using two suggested configurations. The rectifier line-side configuration is a 3-phase topology based on magnetic amplifiers inserted between the PMSG winding terminals and the diode rectifier unit, while the dc-side configuration is a single topology inserted into the boost chopper circuitry.
- Both configurations were studied and examined within the 1.5 MW system for ride-through grid voltage disturbances. In spite of limiting the dc-link voltage rise, the 3-phase topology negatively affects the generator's performance during the fault by storing energy in the rotor inertia, which in turn (depending on the turbine's mechanical inertia) may cause unacceptable over speeding of the PMSG as well as disruption of boost chopper operation. The grid currents show no change due to the

addition of the amplifier, and the system overall size, cost and weight make the rectifier line-side solution a less attractive approach.

- The dc-side configuration however, has the ability to limit the dc-link voltage rise which in turn slightly improves the grid current's response. The topology has no effect on the generator and MSC performance, and with improved dc-link response, the current and voltage stresses on power converters are limited. System recovery after fault clearance are also improved. The reduced size feature, reliability and dual action of serving as a boost chopper inductor during normal grid operation as well as an LVRT solution during short term faults, establish that the dc-side magnetic amplifier topology is viable for enhancing LVRT capability of a PMSG WECS.

7.2 Author's Contribution

- Two configurations are suggested based on magnetic amplifiers: a 3-phase and dc-side topologies for LVRT capability enhancement of PMSG wind turbines. Both configurations have been tested and their performance has been investigated using simulation, when applied to a 1.5 MW PMSG WECS.
- The dc-side topology limits the dc-link voltage rise associated with severe grid voltage dip without affecting the generator or MSC performance. The configuration also features a more rapid recovery after fault clearance for grid currents and dc-link voltage stabilization with a minimum number of magnetic elements and semiconductors. The 3-phase topology affects the generator performance by storing energy in the rotor inertia, even though dc-link voltage rise blocking capability has been improved.
- The use of dc-side topology for improving LVRT of a scaled-down PMSG WECS prototype has been practically validated. Practical results have been verified and correlate with the associated simulations.

7.3 Suggestions for Future Research

- Investigate the performance of the dc-side magnetic amplifier for LVRT capability enhancement during asymmetrical voltage dips on PMSG wind turbines.

- Optimize the design of the magnetic amplifier with the aid of finite element analysis and investigate its ability to supply reactive power to the power system during a fault as a grid supporting feature.
- Investigate the reduction of magnetic amplifier size and co-ordinated control for fault current limitation in wind turbines with back-to-back converters.
- Investigate the use of nanocrystalline core materials (replacing the steel core), which have relative permeabilities of up to 80,000.

Appendix A: Wind Turbine

1.5 MW Wind turbine parameters

Parameter	value	
Rated Power	1.5	MW
Rated wind speed	13	m/s
Rotor diameter	54.4	m
Swept area	2324.27	m^3
Number of blades	3	

Appendix B: Generators parameters

Appendix B-1

1.5 MW Permanent magnet synchronous generators parameters

Parameter	value	
Rated kVA	1.5	MVA
Voltage	690	V
Frequency	11.5	Hz
Pole pairs	40	
Mechanical angular frequency	1.8	rad/s
Inertia constant	0.92	M $kg.m^2$
Generator torque	0.83	M N.m
Permanent magnet flux linkage	8	V/rad/s
d- axis inductance	3.075	mH
q- axis inductance	2.3	mH
Stator resistance	0.000317	Ω

Appendix B-2

0.31 kW Permanent magnet synchronous generators parameters

Parameter	value	
Rated power	0.31	kW
Stator Resistance	12.5	Ω
Field Flux linkage	0.36	V/rad/s
Rated Speed	1500	rpm
Load Torque	2	N.m
Moment of Inertia	$0.68*10^{-3}$	$kg.m^2$
Nominal Voltage	200	V
Frequency	50	Hz
Number of poles	4	

Appendix B-3

1.5 kW Direct current motor

Parameter	value	
Rated power	1.5	kW
Armature Resistance	2. 5	Ω
Armature inductance	3	mH
Field Resistance	220	Ω
Rated Speed	1500	rpm
Moment of Inertia	$0.68x10^{-3}$	$kg.m^2$
Field Voltage	220	V
Armature Voltage	220	V

Appendix C: Transformers parameters

Appendix C-1

Grid coupling Transformer parameters

Parameter	value	
Rated kVA	2	kVA
Frequency	50-60	Hz
Primary	0-133-230	V
Secondary	2x 66.5V windings per phase, Available tap settings for 0-38.4-44-66.5 (± 5 %)	V
No load losses	35	W
Impedance voltage	8	pu
Resistance voltage	3	pu

Appendix C-2

Magnetic amplifier Prototype

Parameter	value	
Rated kVA	500	VA
Primary	2 x 100	V
secondary Voltage	4x45	V
Equivalent winding resistance	4	Ω
Leakage inductance	3.9	mH
Core losses	14	W

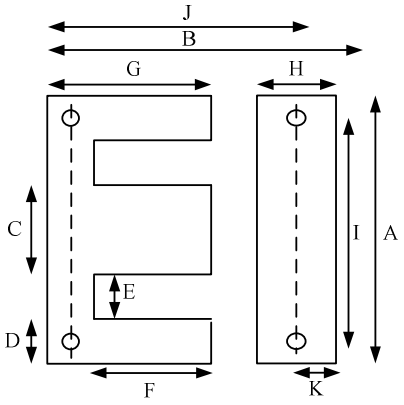

Dimension	A	B	C	D	E	F	G	H	I
Length (cm)	5.7	2.9	2.8	5.7	8.5	2.8	14.2	8.5	1.4

Appendix. D: Current Harmonic Limits in IEEE Std. 519-1992

Table I: Current Harmonic Limits

Maximum Harmonic Current Distortion in % of I_L						
Individual Harmonic Order (Odd Harmonics)						
I_{SC} / I_L	<11	11≤h<17	17≤h<23	23≤h<35	35≤h	TDD
<20*	4.0	2.0	1.5	0.6	0.3	5.0
20<50	7.0	3.5	2.5	1.0	0.5	8.0
50<100	10.0	4.5	4.0	1.5	0.7	12.0
100<1000	12.0	5.5	5.0	2.0	1.0	15.0
>1000	15.0	7.0	6.0	2.5	1.4	20.0
Even harmonics are limited to 25% of the harmonic limits, TDD refers to Total Demand Distortion and is based the average maximum demand current at the fundamental frequency, taken at PCC.						
*All power generation equipment is limited to these values of current distortion regardless of I_{SC}, I_L.						
I_{SC} = Maximum short current at the PCC I_L = Maximum demand load current (fundamental) at the PCC h = Harmonic number						

Appendix E: Low voltage ride-through Regulations

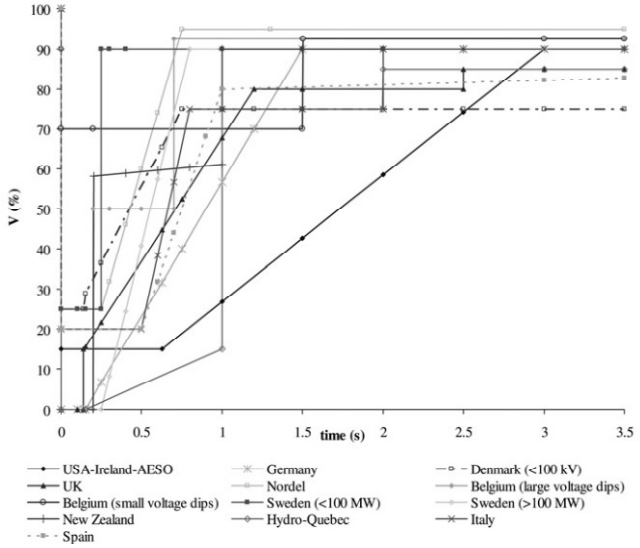

LVRT requirements of various grid codes

Characteristics of fault ride-through in various grid codes

Grid code	Fault duration (ms)	Fault duration (cycles)	Min voltage level (% of nominal)	Voltage restoration (s)
Germany (Eon)	150	7.5	0	1.5
UK	140	7	0	1.2
Ireland	625	31.25	15	3
Nordel	250	12.5	0	0.75
Denmark (<100kV)	140	7	25	0.75
Denmark (>100kV)	100	5	0	10
Belgium (large voltage dips)	200	10	0	0.7
Belgium (small voltage dips)	1500	75	70	1.5
Canada (AESO)	625	37.5	15	3
Canada (Hydro-Quebec)	150	9	0	1
USA	625	37.5	15	3
Spain	500	25	20	1
Italy	500	25	20	0.8
Sweden (<100 MW)	250	12.5	25	0.25
Sweden (>100 MW)	250	12.5	0	0.8
New Zealand	200	10	0	1

300/500 V & 450/750 V

Single Core Cables with Solid or Stranded Copper Conductors and PVC Insulated

Description

- Soft annealed solid or stranded Copper conductors insulated with PVC compound rated 70 °c or 85 °c according to IEC 60227 & BS 6004.

Application

- For indoor fixed installations in dry locations, laid in conduits, as well as in steel support brackets.

Egytech - code	Nominal cross sectional area		Max. Conductor resistance		Current rating in air		Approx. overall diameter	Approx. weight
			DC at 20 °C	AC at 70 °C	Free	In pipes		
	mm²		Ω/km		A	A	mm	kg/km
a - 300 / 500 V cables								
CPC-S001-U01	0.50	re	36.0	45.00	2	2	2.0	8
CPC-S001-U02	0.75	re	24.5	30.77	10	7	2.2	11
CPC-S001-U03	1.00	re	18.1	22.73	13	10	2.5	15
b - 450 / 750 V cables								
CPD-S001-U04	1.5	re	12.1000	14.600	17	13	2.8	20
CPD-T001-U04	1.5	rm	12.1000	14.600	17	13	3.0	21
CPD-S001-U05	2	re	9.1500	10.900	19	15	3.2	27
CPD-T001-U05	2	rm	9.1500	10.900	19	15	3.4	28
CPD-S001-U06	2.5	re	7.4100	8.890	24	19	3.4	31
CPD-T001-U06	2.5	rm	7.4100	8.890	24	19	3.6	33
CPD-S001-U07	3	re	6.1000	7.410	27	21	3.6	37
CPD-T001-U07	3	rm	6.1000	7.410	27	21	3.8	39
CPD-S001-U08	4	re	4.6100	5.510	32	23	3.9	47
CPD-T001-U08	4	rm	4.6100	5.510	32	23	4.2	50
CPD-S001-U09	6	re	3.0800	3.680	40	29	4.4	68
CPD-T001-U09	6	rm	3.0800	3.680	40	29	4.7	71
CPD-T001-U10	10	rm	1.8300	2.170	57	41	6.1	117
CPD-T001-U11	16	rm	1.1500	1.370	76	54	7.1	177
CPD-T001-U12	25	rm	0.7270	0.860	103	70	8.8	278
CPD-T001-U13	35	rm	0.5240	0.630	128	87	9.9	371
CPD-T001-U14	50	rm	0.3870	0.460	156	106	11.8	514
CPD-T001-U15	70	rm	0.2680	0.320	200	131	13.5	711
CPD-T001-U16	95	rm	0.1930	0.230	251	166	15.7	967
CPD-T001-U17	120	rm	0.1530	0.190	293	190	17.4	1240
CPD-T001-U18	150	rm	0.1240	0.150	335	219	19.4	1500
CPD-T001-U19	185	rm	0.0991	0.120	390	250	21.5	1852
CPD-T001-U20	240	rm	0.0754	0.092	471	300	24.7	2457
CPD-T001-U30	300	rm	0.0601	0.075	540	340	27.2	2977

The above data is approximate and subjected to manufacturing tolerance.
Delivery length tolerance is ± 5%

re : round, Solid
rm : round, Stranded

3

Low voltage cables datasheet

Appendix G: Hardware and Software Environment Introduction

G.1 Hardware Structure

The practical test-rig is implemented to emulate the MATLAB simulated 1.5 MW system and to verify the simulation results. In this appendix, hardware elements, photographs, and the software are introduced. The test-rig structure is illustrated by the block diagram shown in figure G-1. The structure can be divided into six main parts;

1. Generation system:
    - DC- motor
    - PMSG
2. ac-dc conversion system:
    - Three-phase diode bridge rectifier
    - DC-DC converter (boost chopper)
3. dc-ac conversion system:
    - DC-link filter
    - DC voltage bias (Power Supply) module
    - Three phase inverter module
    - Three phase grid coupling inductor
4. Grid:
    - Grid coupling transformer and grid variac
    - Three phase timer operated contactors
5. Grid:
    - Magnetic amplifier for LVRT testing
    - Single phase diode bridge rectifier
6. Control and measurements components. The practical system include the following components.
    - Host PC
    - DSP: 32-bit *TriCore* microcontroller TC1796 from Infineon

- Interface circuit
- Gate drive circuit for boost chopper
- Gate drive circuit for inverter module
- Current and voltage measuring
- Analogue output display

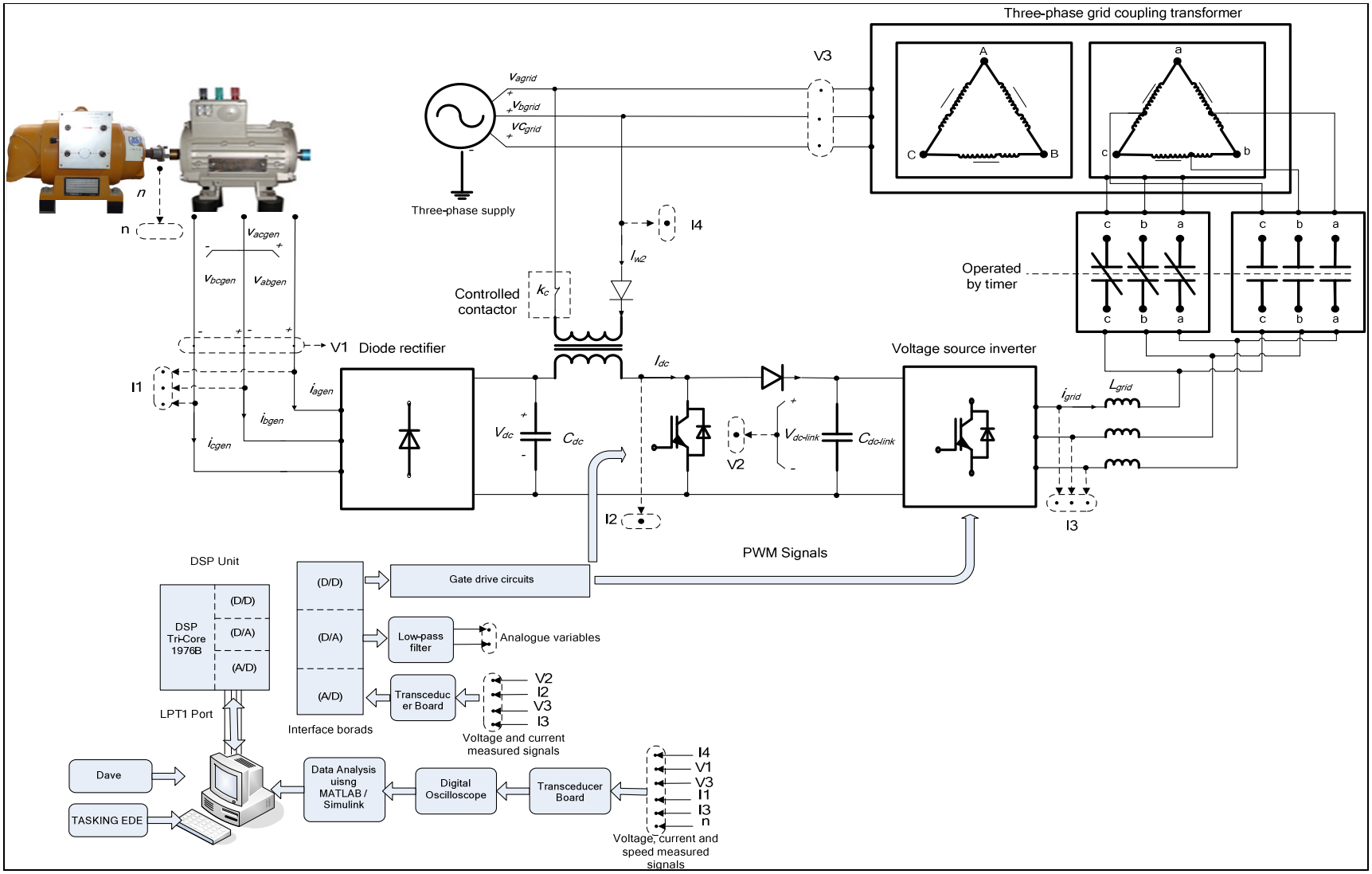

Figure G-1. Test-rig block diagram

G.2 Hardware Overview

Photographs of the test rig hardware system are shown in parts (a) to (d) of figure G.2. An overview of each component is introduced in the following subsections.

(a)

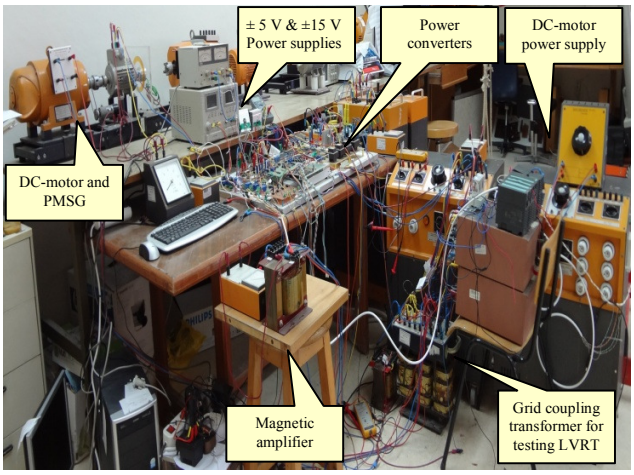

(b)

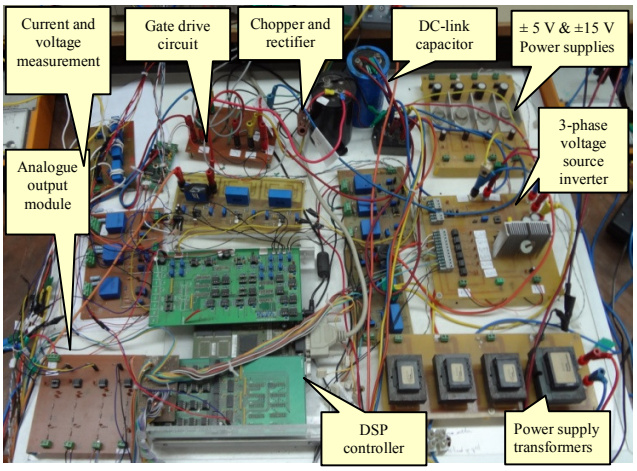

(c)

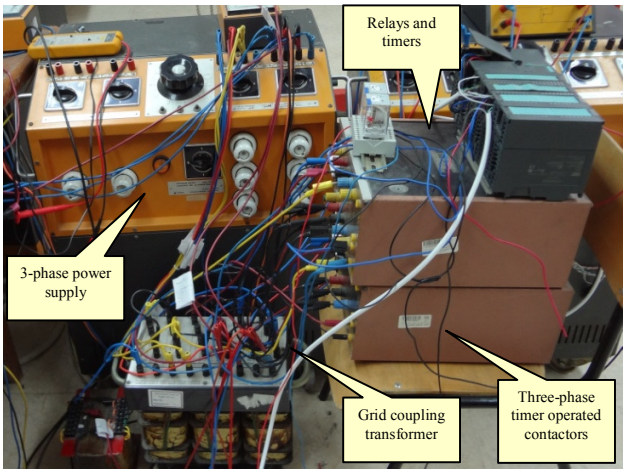

(d)

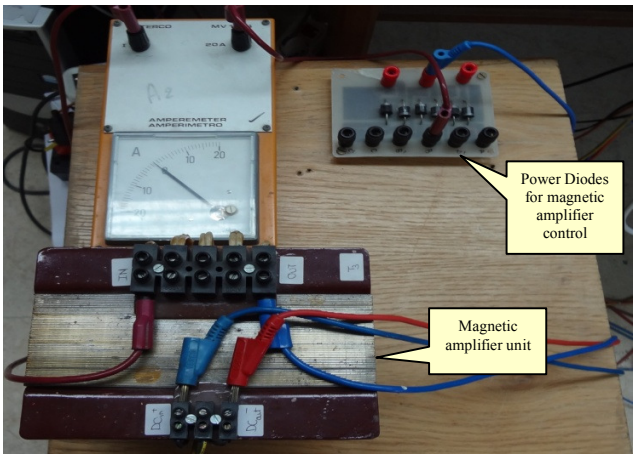

Figure G-2. Test rig photographs.

G.2.1 Permanent Magnet Synchronous Generator

The PMSG is the generating element for the wind energy system under study. A laboratory low voltage scaled motor is selected and the motor parameters are listed in Appendix B. The motor photo is shown in figure G.3. The motor is a three-phase, 4-pole, 200V, 50Hz, 1.27A, 2Nm, 0.31 kW, Y-connected motor, with an aluminium housing. The rotor is made of rare earth / ferrite magnetic material. The stator is made of iron with copper windings, as shown in figure G-3. The maximum speed is 1500 to 6000 rpm.

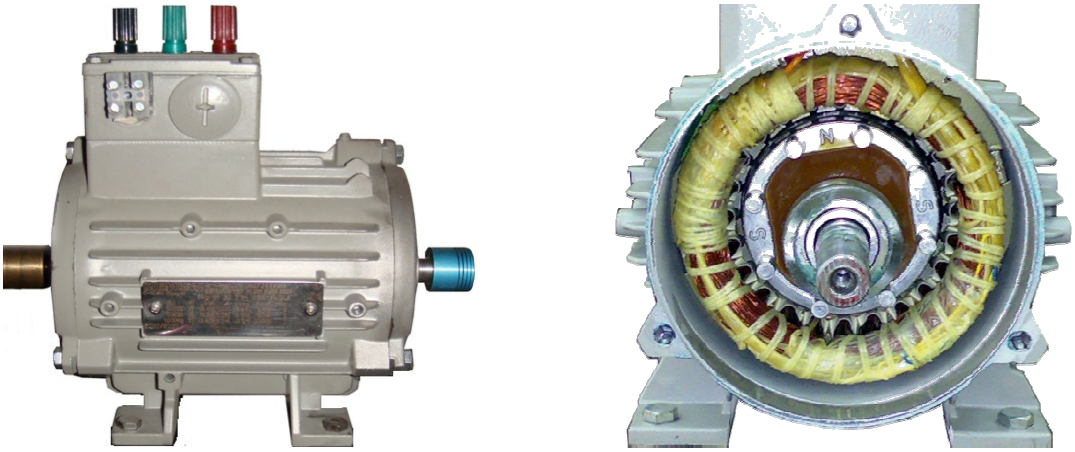

(a) (b)

Figure G-3. PMSM SIEMOSYN (a) overall picture, (b) internal picture of stator and PM rotor.

G.2.2 Separately Excited DC-Motor

A separately excited dc-motor is used as the prime mover for the PMSG. The dc-motor's parameters associated with figure G-4 of are found in appendix B-3.

(a)

Figure G-4. TERCO DC-motor picture

G.2.3 Three-phase Diode Bridge Rectifier

For ac-dc conversion, a three-phase diode bridge rectifier is employed as shown in figure G-5. The full wave rectifying unit Powersem- PSD 55/12 is available in a small sized and light module and is suitable for battery DC power supplies and as input rectifiers for PWM inverter. Table G-1 shows some important parameters of the module.

Figure G-5. Three-phase bridge rectifier picture.

Table G-1. Thee-phase bridge rectifier

Maximum input current rating	58 A
Maximum input voltage rating	1200 V

G.2.4 DC-DC Converter (Boost Chopper)

A boost chopper is employed as the dc-dc conversion unit. The chopper is composed of a current filtering inductor, an IGBT, a fast recovery diode, a group of heat sinks and a filtering capacitor. The parameters of the boost chopper items are listed in Table G-2.

Table G-2. The boost chopper specifications

Input boost capacitor	1500 μF, 400 V
Boost chopper inductor	6.13 mH, 1.7 Ω
Ultrafast IGBT (IRG4PH50KDPbF)	1200 V, 24 A
Fast recovery diode (BY229-400)	400V, 8A

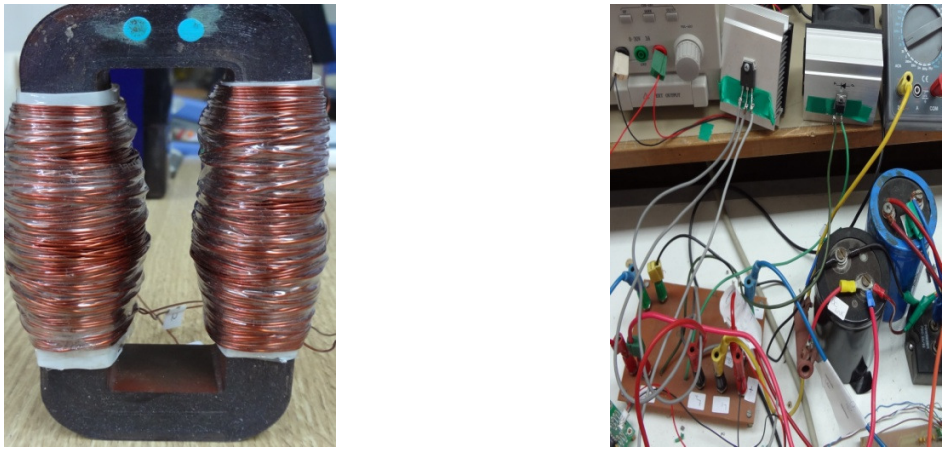

(a) (b)

Figure G-6. Boost chopper circuit: (a) chopper inductor and (b) chopper circuit

G.2.5 DC-link Filter and Grid Filtering Inductance

For the VSI operation, a 2200 μF, 450 V capacitor is utilized to maintain the DC-link voltage constant, as shown in figure G-7. A three-phase, 2mH filtering inductor is used for grid current smoothing.

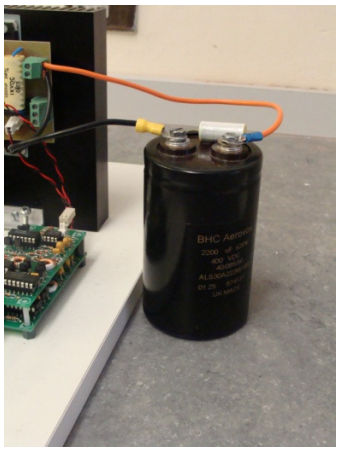

(a)

(b)

Figure G-7. DC-Link and grid filtering: (a) DC-link capacitor and (b) grid coupling inductance

G.2.6 Three-phase Inverter Module (IRAMX 16U P60B-2)

The IRAMX 16U P60B-2, shown in figure G-8, consists of switching insulated gate bipolar transistor (IGBT) modules, used at a PWM carrier frequency of 20 kHz. The module is a 16A, 600V integrated power hybrid IC. The inverter module features:

- Internal Shunt Resistor
- Integrated Gate Drivers and Bootstrap Diodes
- Temperature Monitor
- Under voltage lockout for all channels
- Matched propagation delay for all channels
- Lower $^{di}/_{dt}$ gate driver for better noise immunity
- Motor Power range 0.75~2.2kW / 85~253 Vac

Table G-3 highlights some of the electrical characteristics of the inverter module

Table G-3. Three-phase inverter module specifications

IGBT/Diode Blocking Voltage	600 V
Positive Bus Input Voltage	450 V
RMS Phase Current (@ 25°C)	16 A
PWM Carrier Frequency	20 kHz

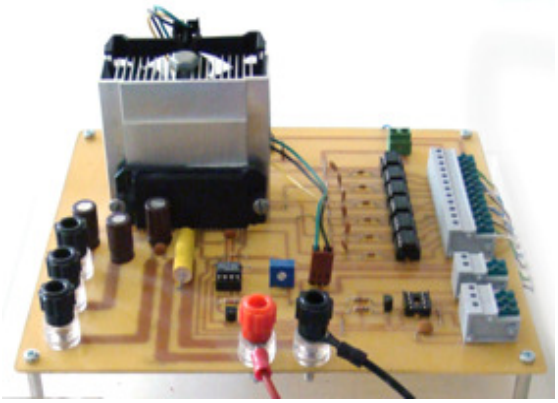

Figure G-8. Six pulse three phase inverter

G.2.7 DC voltage bias (Power Supply) module

The three-phase inverter circuit contains discrete components that need to be biased from a fixed dc-source. A dc-power supply is designed to provide these circuits with ±5V and ±15V as shown in figure G-9.

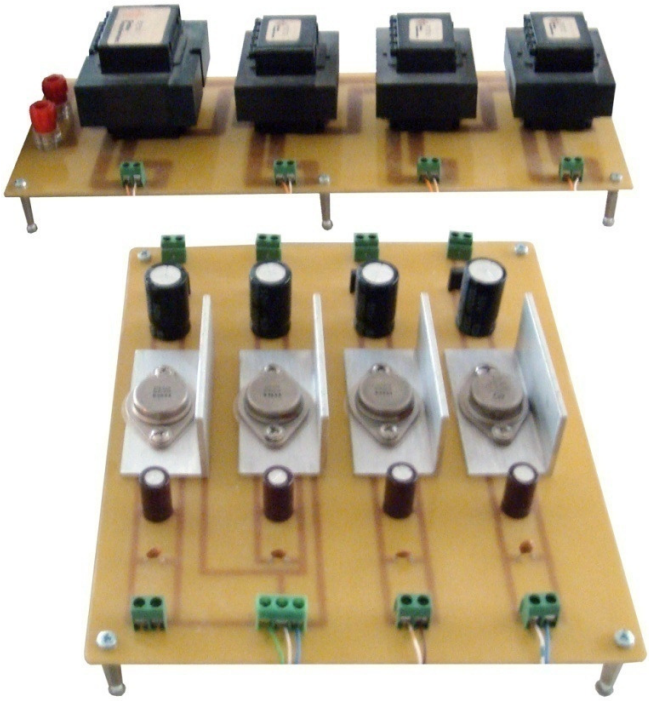

(b)

Figure G-9. DC-voltage bias (Power supply) module

G.2.8 Grid Coupling Transformer and Grid Variac

For grid representation and voltage dip emulation, an MV1300 Power Pack by TERCO is used along with transformer MV1915 whose parameters are shown in Appendix C-1. The grid coupling transformer and grid Variac are shown in figure G-10 (a) and (b).

(a) (b)

Figure G-10. Grid coupling transformer and grid variac: (a) coupling transformer (b) variac

G.2.9 Magnetic Amplifier and Control

The magnetic amplifier shown in figure G-11 along with the control circuits was fabricated and the parameters can be found in Appendix C-2.

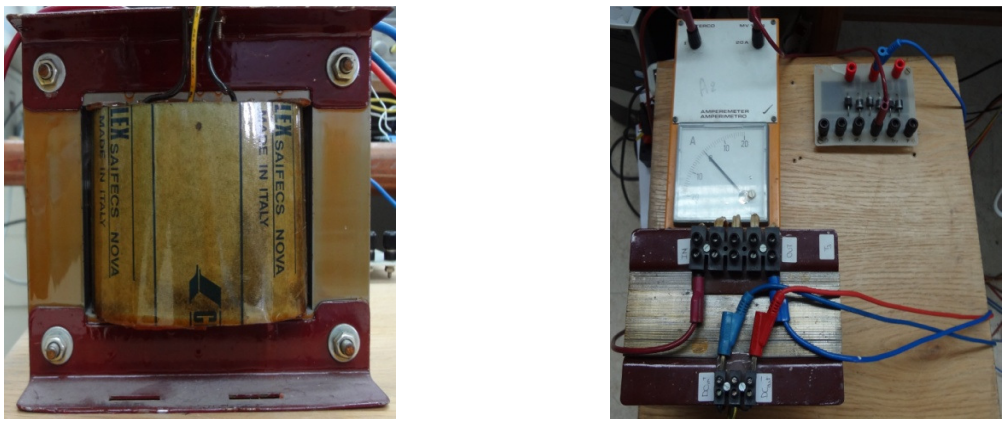

(a) (b)

Figure G-11. Magnetic amplifier: (a) core, and(b) control

G.2.10 DSP Unit with Interfacing Boards

The DSP unit with the input and output interfacing boards are shown in figure G-12.

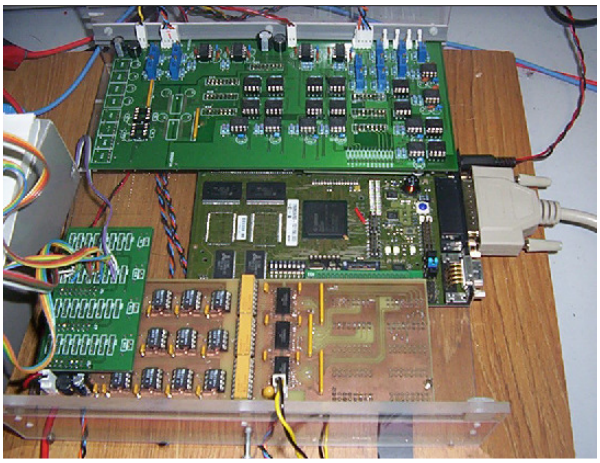

Figure G-12. DSP with interfacing boards.

i. DSP unit

The DSP unit is considered as the brain of the control system. It is an embedded controller used in changing the control strategy during the practical evaluation. It should have some features as flexibility, processor speed, available storage memory, easy for programming and interface ability. The control scheme in the test rig is implemented using DSP type TriCore ™ TC1796 from Infineon. The DSP generates the switching pattern driving the switches of the inverter according to the software algorithm of the proposed system. The Infineon TriCore ™ TC1796 has 32-Bit floating point microcontroller which can operate with a maximum CPU clock frequency of 150MHz. The main features of this DSP are [1]:

- 32-Bit CPU with floating point unit and 4 Gbyte unified data, program, and I/O address space
- 16/32-bit high-efficiency instruction set
- Programmable external bus interface
- Integrated on-chip memories (programs in this work are run in the 48Kbyte Scratch-Pad RAM, which provides high accessibility.)
- Interrupt system with 181 service request node and 256 interrupt priority levels
- Peripheral control processor

- DMA controller with 16 independent DMA channels
- Parallel I/O ports with 127 digital General-Purpose I/O port lines
- On-chip peripheral units such as two General Purpose Timer Arrays (GPTA) to accomplish input/output management, two A/D Converter (ADC) units , etc
- Maximum system clock frequency: 75 MHz

Two on-chip peripheral units are essential for implementing the control: GPTA and ADC.

A. General Purpose Timer Arrays (GBTA) **[2]**

This is the unit for generating PWM signals. TC1796 contains two General Purpose Timer Arrays (GPTA0 and GPTA1) with identical functionality, plus an additional Local Timer Cell Array. The GPTA provides a set of timer, compare, and capture functionalities that can be flexibly combined to form signal measurement and signal generation units. Each of the GPTA is slit into a Clock Generation Unit (CGU) and a Signal Generation Unit (SGU). The system clock set by the CGU in this work is 40MHz, which relates to 0.1us for one count of the involved timers for generating the PWM signals. Local Timer Cells (LTC) within SGU are configured to execute the PWM counting.

There are 63 LTCs can be used in each GPTA unit: LTC0 is set to be a free-running timer, and LTC1 is filled with the switch period. When the LTC0 reaches the value in LTC1, it will be reset and its count starts from 0 again. At the same time, the value match with LTC0 causes LTC1 to trigger an interrupt request, which leads the CPU to service the interrupt routine for the application control. The mechanisms for the PWM generation for the three phase inverter are shown in figure G-11. There are two switches in each leg and two timers are required for each switch to determine the required pulse width and the deadband time between the two switches. For the switching frequency of the three phase grid tied inverter is taken 5 kHz. For protection, the LTCs mode can be changed to push the output to be zero in case of short circuit and over loading conditions.

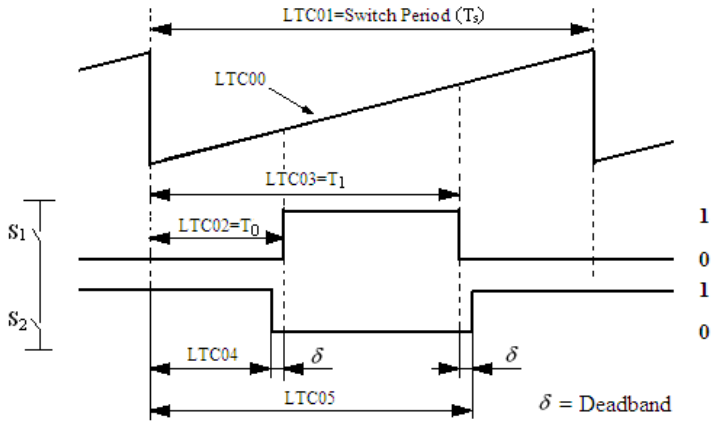

Figure G-13. Inverter PWM generation (one leg).

B. Analogue-to-Digital Converter (ADC) **[3]**

The TC1796 contains two medium-speed ADCs (ADC0 and ADC1) with identical functionality and a third fast ADC. ADC0 and ADC1 provide 2-3 µs conversion time at 10-bit resolution. The main features are:

- 8-bit, 10-bit, 12-bit A/D conversion
- conversion time below 2.5 µs at 10-bit resolution
- total unadjusted error of ± 2LSB at 10-bit resolution
- integrated sample and hold functionality
- direct control of up to 32 analogue input channels per ADC
- flexible ADC module service request control unit

ii. Interfacing Boards

The main task of the interfacing circuits is to completely isolate the TriCore ground from the test rig ground. For each DSP unit, two interfacing boards are connected as shown in figure G-14, the interfacing boards are:

1. Interfacing board between the transducer board and the ADC unit of DSP, which implements an analogue-to-analogue voltage transformation (0-10 V to 0-3.3 V). Please see Appendix for its principle diagram. The circuit layout is shown in figure G-12.

2. Interfacing board between the DSP I/O and the IGBT gate drive, which implements a Digital-to-Digital signal transformation (logic ‘1’ from 3.3V to 5V). The circuit layout is shown in figure G-15.

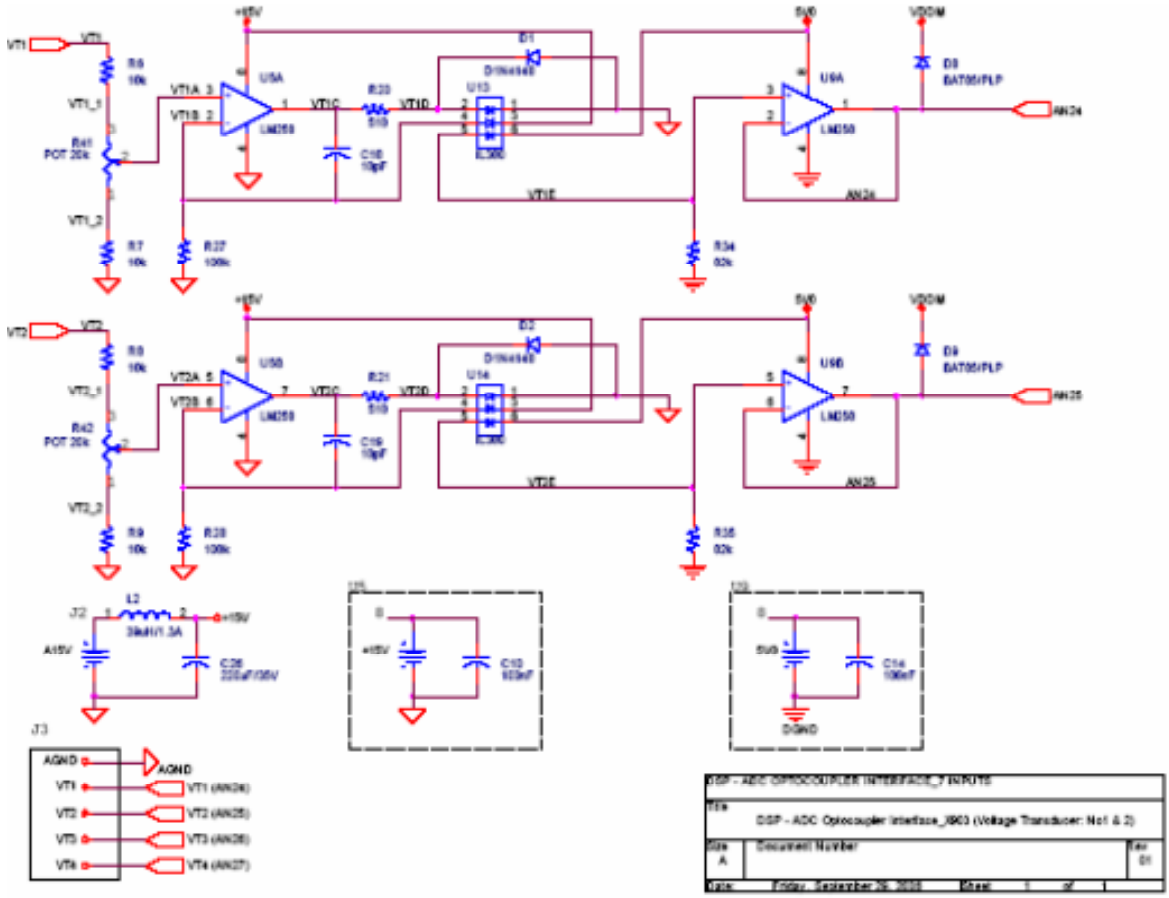

Figure G-14. Input interface circuit.

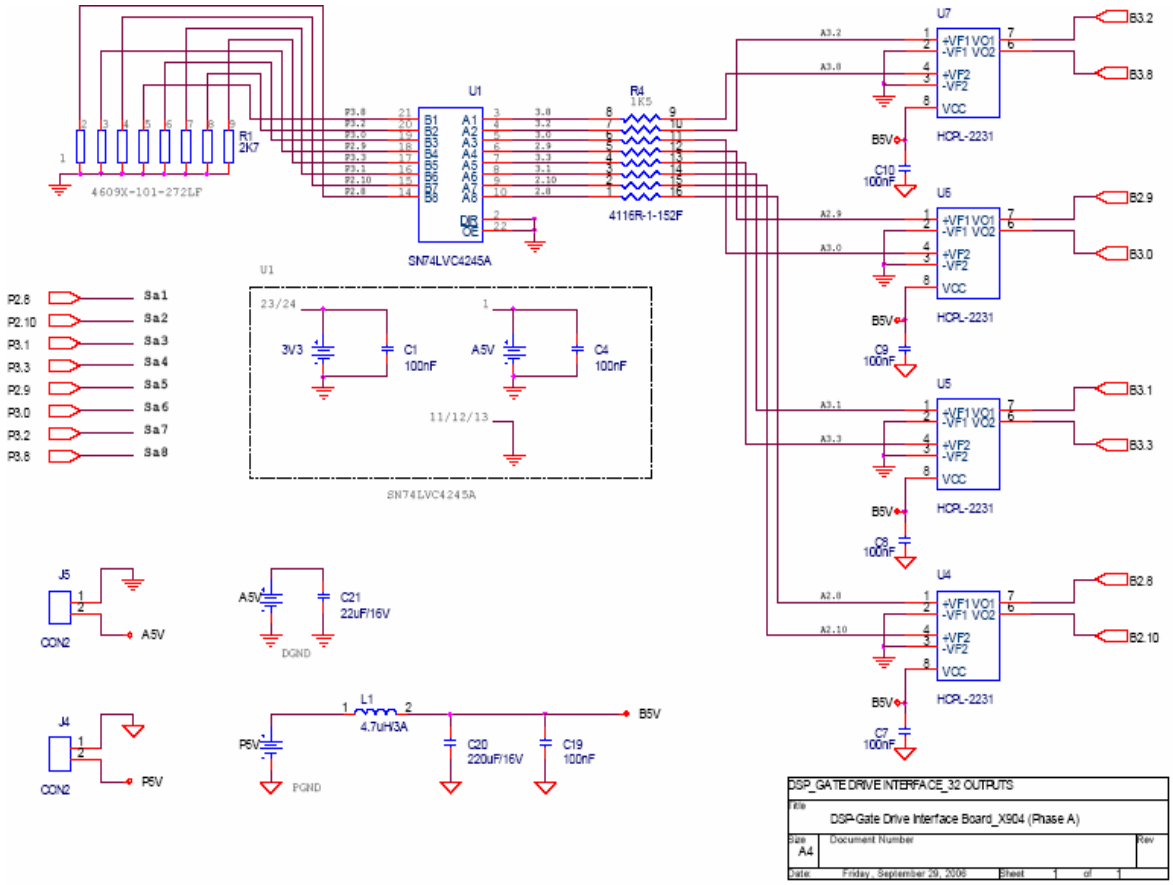

Figure G-15. Output interface board.

G.2.11 Transducer Boards

Currents and voltage sensing is required to provide the feedback signals to the controller. These are achieved using current and voltage transducer boards.

i. Current Sensing

The current sensing circuits are implemented to measure the three-phase grid currents, three-phase generator currents as well as the boost chopper inductor current. The current transducer board is shown in figure G-16. The Hall-effect current sensing devices LEM (LA-55P) were used. Table G-4 shows the parameters of the transducer used. This type of sensors has the advantage of isolation from the sensed signal and ease of implementation. This current sensor has a sensing range of each from 0 A to 50 A adjustable and a frequency range of 0 Hz to 100 kHz [4]. For proper operation, the output of the transducer is amplified through a signal

conditioning circuit and fed to the control circuit. The current transducer circuit diagram is shown in figure G-17.

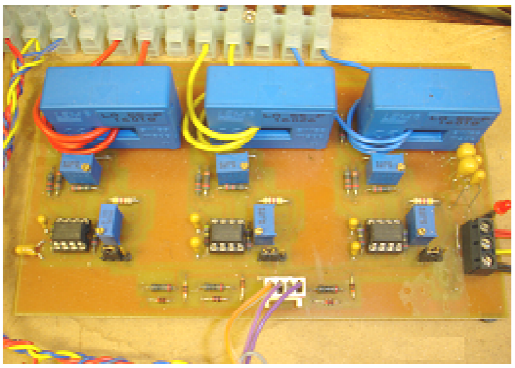

Figure G-16. Current transducer board.

Table G-4. The current transducer nominal parameter values

Nominal current	100 (rms) A
Current output	1 mA/Amp
Measuring range	0 to ± 160 A
Frequency range	DC to 100 (-1dB) kHz
di/dt	> 50 A/μs

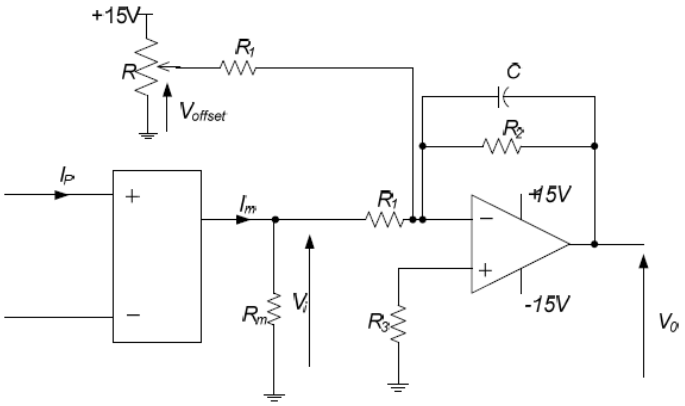

Figure G-17. Current transducer circuit diagram.

ii. Voltage measuring

The voltage sensing circuits are implemented to measure the three-phase grid voltages, three-phase generator voltages and the dc-link capacitor voltage. The voltage transducer board is shown in figure G-18. The LEM voltage transducer LV25-P uses the Hall-effect to measure ac

and dc signals with a galvanic isolation between the primary circuit (high voltage) and the secondary circuit (electronic circuit) [5]. Table G-5 shows the nominal parameters of the transducer used. This sensor can sense a range up to 500 V and a high frequency bandwidth, but dependent on the series connected external resistor in the primary circuit of the transducer. The transducer output is amplified through a signal conditioning circuit and fed to the control circuit. The voltage transducer circuit diagram is shown in figure G-19.

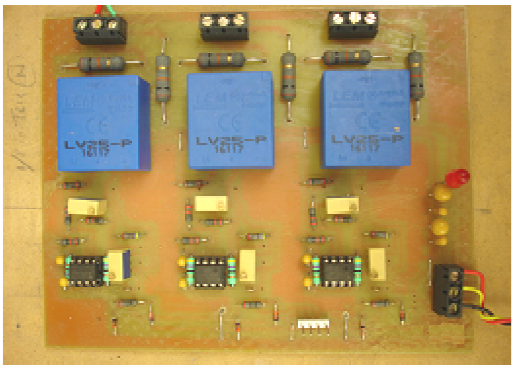

Figure G-18. Voltage transducer board.

Table G-5. The voltage transducer nominal values

Primary nominal current	10 (rms) mA
Primary current (measuring range)	0… ± 14 mA
Primary nominal voltage	10... 500 V
Bandwidth	Drop resistor dependent
Accuracy	± 0.8 %

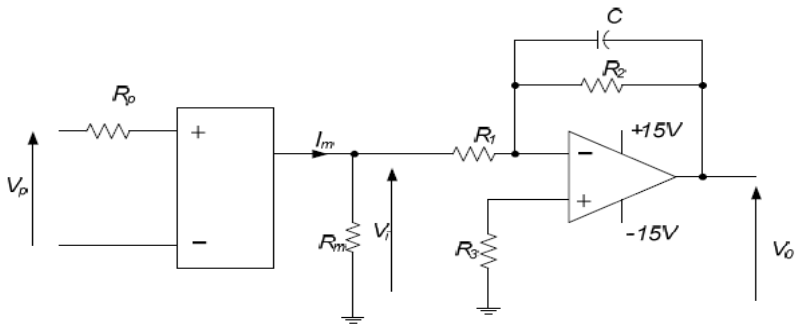

Figure G-19. Voltage transducer circuit diagram.

iii- Analogue output

This DSP evaluation board does not provide separate digital to analogue converters for analogue output measuring. Alternatively, an analogue output can be obtained by pulse width modulating the required signal with a carrier frequency of 10 kHz via PWM-module (GPTA2). Then the modulated digital output signal is passed through a third order Salen-Key low pass filter with a 1 kHz cut off frequency. Table G-6 shows the parameters of the components used in designing the analogue output module. Figure G-20 shows the schematic diagram while figure G-21 shows the analogue output board. The Bode diagrams for the filter response is shown in figure G-22.

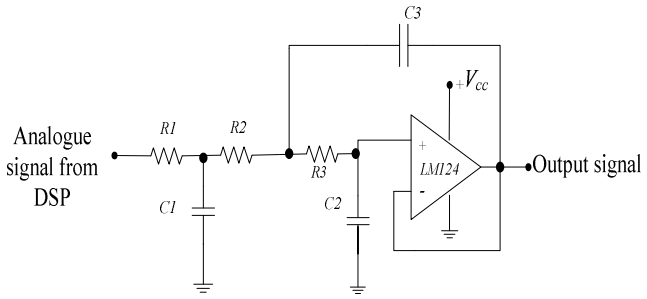

Figure G.20. Analogue low pass filter.

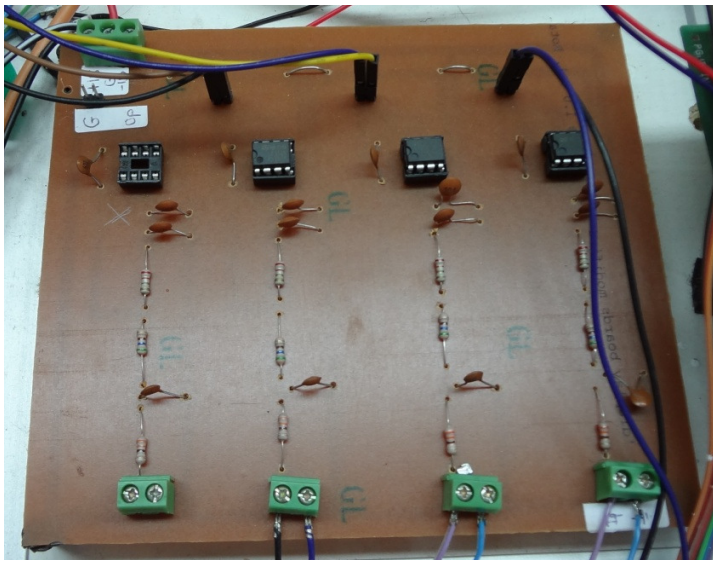

Figure G.21. Analogue low pass filter.

Table G-6. The analogue output board values

Input signal	+ 5V
Cut-off frequency	1 kHZ

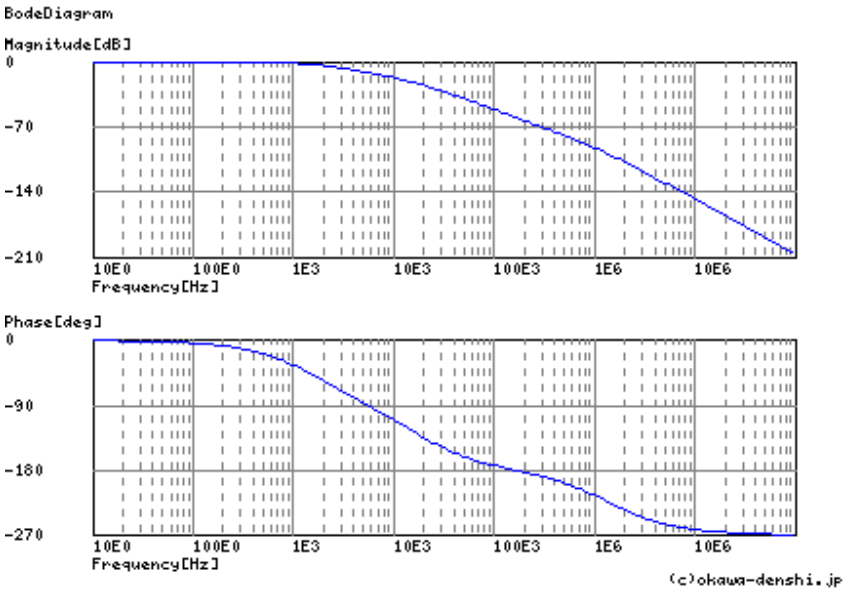

Figure G.22. Bode diagrams for analogue low pass filter.

G.2.12 Gate drive circuit

The gate drive circuit used in the test rig is shown in figure G-23. It provides isolation between the control signal and the IGBT gate by means of two transformers. One transformer is for transmitting power from the low side circuit and the other is for transmitting the gate drive signal. The maximum current that can be sunk by the control circuit is in the range of milli-amperes, while the gate terminal of the IGBT may require a large instantaneous spike of current to enable the fast charging of the gate capacitance and hence the turn on of the switch. A separate power supply is used to supply the gate drive for the boost chopper circuit. Table G-7 shows the gate drive circuit parameters.

Figure G-23. Gate drive circuit

Table G-7. Gate drive circuit parameters

Supply voltage (max)	5.25 V
$t_{d\,on}$ (typ.)	60 ns
$t_{d\,off}$ (typ.)	60 ns
Drive signal frequency (max)	75 kHz
Output voltages	0, 15 V
Output current	± 3 A

G-3 Program Development Part (Software Overview)

After collecting the measurement data inside the TriCore microcontroller, the program starts execution according to the specific written algorithm. To exploit the speed of the DSP, heavy calculations should be avoided which affects the process performance. The DSP used with the proposed system requires a PC. The PC is used to write, debug, compile and download the code to the TriCore microcontroller through the parallel port. The final code is then stored in the EPROM.

Software environment to implement the DSP control consists of two development tools; Digital Application Virtual Engineer (DAvE) and TASKING Embedded Development Environment (TASKING EDE). The operation systems can be either Windows NT, XP or 2000.

G.3.1 DAvE [6].

DAvE is the application to initially configure the TC1796 system and to generate optimized C code for the modulator. Figure G-23 shows the general configuration interface of DAvE V2.1.

The system clock is set in the GPTA Clock module, and the PWM generation timers are configured in the GPTA0. ADC0 is configured for the ADC conversion.

After configuration, the compilation of the project generates D-level template files with the resulted initial configuration parameters, such as main.h, main.c, GPTA0.h, GPTA1.c, etc. These files contain the basic program structure for the applications in TASKING EDE.

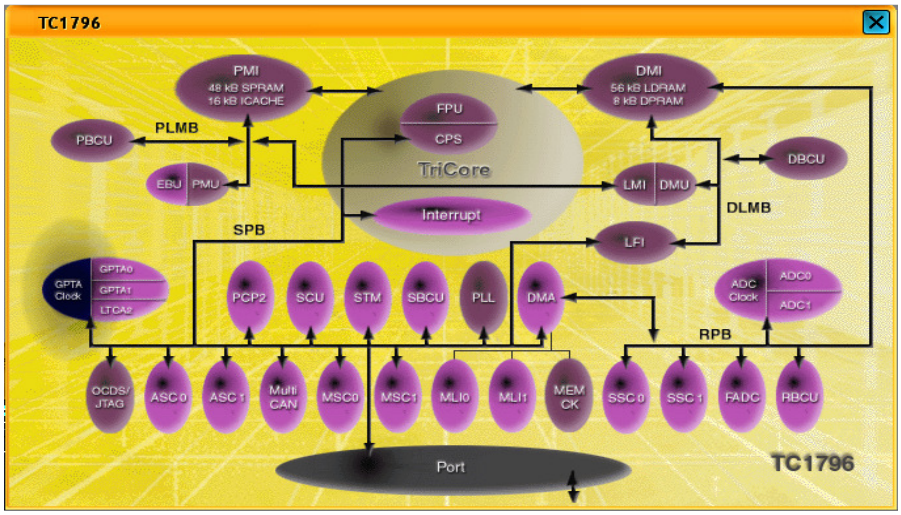

Figure G-24. Interface for DAvE V2.1.

G.3.2 TASKING EDE [6]

TASKING EDE V2.1 is a package of program building, editing, code generation and debugging tools. Options such as the format of the final built program and the used DSP on-chip memory can be further configured with TASKING EDE. Files imported from DAvE are loaded with basic program structure and the proposed user C codes are added in the specified positions. CrossView Pro Debugger is an embedded debug toll within TASKING EDE but without real time monitoring ability. Sample of C-codes for practical implementation of control operations are in Appendix H.

References

[1] TC1796 User's Manual, 'System Units', Vol. 1.0, June, 2005, pp.45-47.

[2] TC1796 User's Manual, 'Peripheral Units', Vol. 2.0, June, 2005, pp.547-612.

[3] TC1796 User's Manual, 'Peripheral Units', Vol. 2.0, June, 2005, 25-2.

[4] Current transducer, LEM, "LTA 100-P/SP1/CE - STROMWANDLER 100A"

[5] Voltage transducer, LEM, "LV25-P - SPANNUNGSWANDLER PCB MTG"

[6] Infineon Technologies, 'Hot_TC1796_Taskingv22r1_v11'

[7] Philips Semiconductors, BY229-400.

[8] International Rectifiers, IRG4PH50KDPbF.

[9] International Rectifiers, IRAMX16UP60B.

[10] POWERSEM, PSD 55/12.

Appendix H: C-codes for the implemented practical control operation

```
//*********************************************************************
// Grid Connected Wind Energy Conversion System
//*********************************************************************
USER CODE BEGIN (GPTA0_General,7)
 int R=0;
************************* Variables Setting ******************************
//store and define data from A/D for three phase voltages and currents

                int Result12,  Source12;          //ib
                int Result14,  Source14;          //ia
                int Result8,   Source8;           //vbn
                int Result9,   Source9;           //vcn
                int Result13,  Source13;          // vdc
                int Result10,  Source10;          //van
                int Result15,  Source15;          // idc

float Vz,Vh,er,Vxa_pu,Vxb_pu,Vxc_pu,vdc_ref,Va_m, Vb_m, Vc_m, Ia_m, Ib_m, Iaf_m, V_dc_m,vdc_m,
idc_m,idc_reference, id_ref, iq_reference,id_old, iq_old;
float xy=0.0, I_act_max = 0.0;
float Vdc_ref = 110.0;              // for per-unit and modulation index

************************* SVM Reference Vector*****************************
//Defining Timers, switching period and balnking time

float wt1 = 0.0 , pi = 3.141592654, wt2=0.0;
                int BL =10;                       // The blanking time
                int Tpwm = 999;                   // Tpwm is half the switching period
                int Tdta= 1999;
                int Taps , Tapr, Tans , Tanr;     // Timers_  T1   &  T4 inverter
                int Tbps , Tbpr, Tbns , Tbnr;     // Timers_  T3   &  T6 inverter
                int Tcps , Tcpr ,Tcns , Tcnr;     // Timers_  T5   &  T2 inverter
                int Tdcs, Tdcr;                   // Timers boost chopper
                int Tda1s, Tda1r,Tda2s, Tda2r;

************************* Display & Plot *********************************

float vdc_p[1000], idc_p[1000], id_act[1000], iq_act[1000];
float ma[1000], mb[1000], mc[1000], mdc[1000];
float MMA, MMB, MMC, MMDC;
float Tar[1000], Taf[1000];
float Vdca_pu[1000], Vab[1000];
float Ia_mx[1000];// ixa_pu[1000], ixb_pu[1000], ixc_pu[1000];
float Vd[1000],Vq[1000],w[1000],duty_cycle[1000], id_act_unf[1000],
iq_act_unf[1000],vdg[1000],vqg[1000],vdg1[1000],vqg1[1000], id_act_disp[1000];
float ma[1000], mb[1000], mc[1000], k[1000], z[1000];
float Va_act[1000], Vb_act[1000], Vc_act[1000];
float Ia_act[1000], Ib_act[1000], Ic_act[1000];
float vdc_act[1000], idc_act[1000];
float Vxa[1000], Vxb[1000], Vxc[1000], VLa[1000], VLb[1000], VLc[1000], Vx[1000], Vy[1000], thetaa[1000],
Vxaaa[1000];
```

```
float Vxa1[1000],Vxb1[1000],Vxc1[100], si[1000], co[1000], a_pu[1000], b_pu[1000], c_pu[1000],
id_matlab[1000];
float Vxa_1[1000],Vxb_1[1000], Vxc_1[1000], Icx_act[33], Ibx_act[66];

********************** Loading timer values ****************************

P3_OUT_P12=1;   // Start of program
// Phase a   pins 3.9 and 2.10
                    GPTA0_LTCXR16 = Taps;
                    GPTA0_LTCXR17 = Tapr;
                    GPTA0_LTCXR04 = Tanr;
                    GPTA0_LTCXR05 = Tans;
// Phase b   pins 3.3 and 2.9
                    GPTA0_LTCXR10 = Tbps;
                    GPTA0_LTCXR11 = Tbpr;
                    GPTA0_LTCXR06 = Tbnr;
                    GPTA0_LTCXR07 = Tbns;
// Phase c   pins 3.0 and 3.2
                    GPTA0_LTCXR12 = Tcps;
                    GPTA0_LTCXR13 = Tcpr;
                    GPTA0_LTCXR14 = Tcnr;
                    GPTA0_LTCXR15 = Tcns;
// Dc Boost control pin 3.1
                    GPTA0_LTCXR08 = Tdcs;
                    GPTA0_LTCXR09 = Tdcr;
// Display Digital to Analogue pin 4.0
                   GPTA1_LTCXR22 = Tda1s;
                   GPTA1_LTCXR23 = Tda1r;
                   GPTA1_LTCXR26 = Tda1s;
                   GPTA1_LTCXR27 = Tda1r;
// Display Digital to Analogue pin 4.2
                   GPTA1_LTCXR24 = Tda2s;
                   GPTA1_LTCXR25 = Tda2r;
********************** Reading and Scaling A/D ************************

wt1 = wt1+ 2*pi*50*200e-6;                    //   5 kHz switching frequency
 if (wt1 >= 2*pi) wt1 = 0;
```

```
// Read voltages
        ADC0_vGetConversionResult(10, Result10, Source10);          //Van
        ADC0_vGetConversionResult(8, Result8, Source8);             //Vbn
        ADC0_vGetConversionResult(9, Result9, Source9);             //Vcn

// Read dc- link
        ADC0_vGetConversionResult(13, Result13, Source13);          //Vdc
         ADC0_vGetConversionResult(15, Result15, Source15);         //idc

// Read currents
        ADC0_vGetConversionResult(12, Result12, Source12);          //ib
        ADC0_vGetConversionResult(14, Result14, Source14);          //ic

// Store measured values
        Va_m= (float)(Result10);
        Vb_m = (float)(Result8);
         Vc_m = (float)(Result9);
        Ib_m = (float)(Result12);
        Ia_m = (float)(Result14);
        vdc_m = (float)(Result13);
        idc_m = (float)(Result15);

//Get Actual values for voltages
        Va_act[R] =  (Va_m*0.00247- 5.0)*37.4 ;
        Va_act[R] = ((Va_m*0.00244)-4.56)*41.6;
        Vb_act[R] = ((Vb_m*0.00244)-4.5)*41.6;
        Vc_act[R] = ((Vc_m*0.00244)-4.65)*40.4;

//Get Actual values for AC currents, read two and conclude the third
        Ia_act[R] = (Ia_m*10/4096)*(1/1.057)-5.0)*(6/4.46)
         Ib_act[R] =(((Ia_m*0.00244)-4.21)*4.375);
         Ia_act[R] = (-1.0)*(Ib_act[R]+Ic_act[R]);

// Get Actual values for DC voltages and currents idc_act [R] and vdc_act[R] scaling
        vdc_act[R] = (vdc_m*0.054);
        idc_act[R] = (idc_m*0.004);
```

```
************************* Setting reference Control variables *************

//Set Reference values for DC quantities
      idc_reference= 1.5;    // reference value for boost converter current


// Set Reference values for DQ axis current control
             vdc_ref= 100.0;
             iq_reference= 0.0;

************************* Export data to Matlab ****************************

// Send values to MATLAB  (Inputs FOR PLL ALL INPUT VOLTAGES HAVE TO BE IN PER-UNIT)
             dq_rania_U.Va = (Va_act[R])/184.0; //
            dq_rania_U.Vb = (Vb_act[R])/184.0 ;
            dq_rania_U.Vc = (Vc_act[R])/184.0;
             dq_rania_U.id_ref = id_ref;
             dq_rania_U.iq_reference = iq_reference;
             dq_rania_U.id_act = id_act[R];
             dq_rania_U.iq_act = iq_act[R];
             dq_rania_U.vdc_act = vdc_act[R];
             dq_rania_U.vdc_ref = vdc_ref;
             dq_rania_U.idc_ref = idc_reference;
             dq_rania_U.idc_act = idc_act[R];
dq_rania_step( );
************************ Import data from Matlab ****************************

// Ouputs
                        thetaa[R]  = dq_rania_Y.thetaa;
                        si[R]= dq_rania_Y.si;
                        co[R]= dq_rania_Y.co;
                        duty_cycle[R] = dq_rania_Y.duty_cycle;
                        vdg[R] = dq_rania_Y.vdg;
                        vqg[R] = dq_rania_Y.vqg;
                        id_matlab[R]= dq_rania_Y.id_matlab;

************************ Calculate dq components ****************************
 id_act_unf[R]=(2.0/3.0)*(((Ia_act[R])*sin(thetaa[R]))+((Ib_act[R])*sin(thetaa[R]
(2*pi/3)))+((Ic_act[R])*sin(thetaa[R]+(2*pi/3))));
```

```
iq_act_unf[R]=(2.0/3.0)*(((Ia_act[R])*cos(thetaa[R]))+((Ib_act[R])*cos(thetaa[R]-
(2*pi/3)))+((Ic_act[R])*cos(thetaa[R]+(2*pi/3))));

********************** Filter ******************************************

 // filter for dq current
            id_act[R]=(0.3*id_old)+(0.7*id_act_unf[R]);
            iq_act[R]=(0.3*iq_old)+(0.7*iq_act_unf[R]);
            id_old=id_act[R];
            iq_old=iq_act[R];
********************** dq to abc ***************************************

Vxa_1[R]= (vdg[R]*sin(thetaa[R]))+(vqg[R]*cos(thetaa[R]));   //inverter voltage a
Vxb_1[R]= (vdg[R]*sin(thetaa[R]-(2*pi/3)))+(vqg[R]*cos(thetaa[R]-(2*pi/3)));
Vxc_1[R]= (vdg[R]*sin(thetaa[R]+(2*pi/3)))+(vqg[R]*cos(thetaa[R]+(2*pi/3)));

********************** modulating signals ********************************

Vxa_pu = (Vxa_1[R])*(2/Vdc_ref);
Vxb_pu = (Vxb_1[R])*(2/Vdc_ref);
 Vxc_pu = (Vxc_1[R])*(2/Vdc_ref);

****************** modulation index and limits signals ********************

// Reference vector for boost control
                        Vdca_pu[R] = duty_cycle[R];
                        MMA=0.5*((Vxa_pu)+1);
                        MMB=0.5*((Vxb_pu)+1);
                        MMC=0.5*((Vxc_pu)+1);
                        MMDC= Vdca_pu[R];//duty_cycle[R];

                        if (MMA > 0.92)    MMA= 0.92;
                        if (MMA < 0.08)    MMA= 0.08;
                        if (MMB > 0.92)    MMB= 0.92;
                        if (MMB < 0.08)    MMB= 0.08;

                        if (MMC > 0.92)    MMC= 0.92;
                        if (MMC < 0.08)    MMC= 0.08;
                        if (MMDC > 0.95)   MMDC= 0.95;
```

```
                    if (MMDC < 0.05)   MMDC= 0.05;
                     ma[R] = MMA;
                     mb[R] = MMB;
                     mc[R] = MMC;

                P3_OUT_P6=0;            //        End of conversion
****************** Overcurrent Protection ******************************

// overcurrent protection
                if (Ib_act[R] > 50.0)                                   //
                        {
                                xy = 100 ;
                                GPTA0_vOutputMode(GPTA0_LTC,17 ,2,1);
                                GPTA0_vOutputMode(GPTA0_LTC,05 ,2,1);
                                GPTA0_vOutputMode(GPTA0_LTC,07 ,2,1);
                                GPTA0_vOutputMode(GPTA0_LTC,11,2,1);
                                GPTA0_vOutputMode(GPTA0_LTC,13 ,2,1);
                                GPTA0_vOutputMode(GPTA0_LTC,15 ,2,1);
                        }
            else
                        {
                                Taps = ((1-MMA)*Tpwm)+BL;
                                Tapr = ((1+MMA)*Tpwm)-BL;
                                Tanr = ((1-MMA)*Tpwm)-BL;
                                Tans = ((1+MMA)*Tpwm)+BL;
                                Tbps = ((1-MMB)*Tpwm)+BL;
                                Tbpr = ((1+MMB)*Tpwm)-BL;
                                Tbnr = ((1-MMB)*Tpwm)-BL;
                                Tbns = ((1+MMB)*Tpwm)+BL;
                                Tcps = ((1-MMC)*Tpwm)+BL;
                                Tcpr = ((1+MMC)*Tpwm)-BL;
                                Tcnr = ((1-MMC)*Tpwm)-BL;
                                Tcns = ((1+MMC)*Tpwm)+BL;

                                Tdcs = ((1-MMDC)*Tpwm)-BL;
                                Tdcr = ((1+MMDC)*Tpwm)+BL;
```

```
****************** D/A analogue output ******************************

// measurment AC Quantities
          Vx[R]= 0.5*(((Va_act[R])/190.0)+1);
          Vy[R]= 0.5*(((Va_act[R])/190.0)+1);
          Tda2s = ((1-Vx[R])*(Tpwm))-BL;
          Tda2r = ((1+Vx[R])*(Tpwm))+BL;
          Tda1s = ((1-Vx[R])*(Tpwm))-BL;
          Tda1r = ((1+Vx[R])*(Tpwm))+BL;
                              }
P3_OUT_P12=0;   // End of program 3.12
                                R++;
                                if (R >=1000) R = 0;
   // USER CODE END
  }
  // USER CODE BEGIN (SRN22,8)
  // USER CODE END
} //  End of function GPTA0_viSRN22
```

Appendix I

List of Tables and Figures

List of Figures

Chapter 4: Low Voltage Ride through of PMSG WECS

Chapter 5: LVRT Capability Enhancement with Magnetic Amplifier

Chapter 6: LVRT Capability Enhancement with Magnetic Amplifier

List of Tables

Appendix I: Author's Publications

[1] R.A. Ibrahim, M.S. Hamad, Y.G. Dessouky and B.W. Williams

"A review on Recent Low Voltage ride-through Solutions of Wind Farm for PMSG Wind Turbine"

SPEEDAM 2012, International Symposium on Power Electronics, Electrical Drives, Automation and Motion, June 20-22, 2012, Sorrento, Italy.

Abstract

Research of grid connected wind turbines has gained great interest in the recent years. This led to introduce guidelines and regulations regarding the connection of large wind farms to the electrical network. One of such guidelines is low voltage ride-through capability (LVRT). In this paper, a survey on recent LVRT solutions for permanent magnet synchronous generators (PMSG) is carried out along with a brief explanation of grid codes. Among those solutions is the control of fully rated converters, blade pitch angle control and capacitor sizing. Other solutions such as active crowbar rotor circuit and the DC bus energy storage circuit are illustrated. The survey extends to provide possibilities for the development of further LVRT research at the wind farm level using high power FACT devices.

[2] R.A. Ibrahim, M.S. Hamad, Y.G. Dessouky and B.W. Williams

"A Novel Topology for Enhancing the Low Voltage Ride through Capability for Grid Connected Wind Turbine Generators"

ECCE 2012, IEEE Energy Conversion Congress and Exposition, September 15- 20, 2012, Raleigh, North Carolina

Abstract

Energy shortage and environmental pollution have led to the increasing demand of using renewable sources for electricity production. Currently, power generation from wind

energy systems (WES) is of global significance and will continue to grow during the coming years leading to concerns about power system stability where wind farms replace conventional generating technologies that use fossil fuels as the primary energy source. One of these concerns is Low-Voltage Ride-Through (LVRT). In this paper, a novel topology based on the use of magnetic amplifier for enhancing the LVRT capability for grid connected permanent magnet synchronous generators (PMSG) is presented. The system performance is investigated using Matlab.

[3] R.A. Ibrahim, M.F. Moussa, Y.G. Dessouky and B.W. Williams

"Parameters determination of grid connected interior permanent magnet synchronous generator"

EPE-PEMC 2012 ECCE Europe 15th International Power Electronics and Motion Control Conference and Exposition, September 4-6, 2012, Novi Sad, Serbia.

Abstract

Renewable energy sources are being utilized as a reliable alternative to the traditional energy sources for electricity production. Among these renewable sources, wind energy has the largest and fastest penetration into power systems. This paper introduces a method for measurement of the equivalent-circuit parameters of an interior permanent magnet synchronous generator (IPMSG) used in a wind energy system. A brief introduction on the methods used for parameter determination of IPMSG. The conventional two-axis IPMSG model is modified to include the saturation effect of the inductance in the q-axis including self-inductance values in the d- and q-axes, the stator resistance and also the PM flux-linkage.

[4] Ibrahim, R.A., Hamad, M.S., Ahmed, K.H., Dessouky, Y.G., Williams, B.W.

"Improved ride-through of PMSG wind turbine during symmetrical voltage dip using a magnetic amplifier"

2nd IET Renewable Power Generation Conference (RPG 2013)

Abstract

Direct-drive wind turbines based on permanent magnet synchronous generator with full scale back to back converters are becoming very promising due to their high power density, gearless structure and flexible control. With the remarkable growth of wind energy capacity connected to the utility grids, strict grid interconnection requirements of power plants comprising permanent magnet synchronous generators technology are essential to improve the control of electrical power system, both in steady-state and transient operation. Low voltage ride through capability enhancement is one of the grid requirements which ensures the safe operation of the wind farm during the network disturbances and avoids its shutdown. This paper proposes an improved topology based on magnetic amplifier in the boost converter circuit to enhance the ride through capability of permanent magnet synchronous generators based wind energy systems.